Title
THE ELECTRONIC STRUCTURE OF MOLECULES, SOLIDS and SOLID SURFACES

Author
Chelikowsky, James R.

Publication Date
1975-09-01

LBL-3962
c.1

THE ELECTRONIC STRUCTURE OF MOLECULES, SOLIDS AND SOLID SURFACES

James R. Chelikowsky
(Ph. D. thesis)

September 1975

Prepared for the U. S. Energy Research and
Development Administration under Contract W-7405-ENG-48

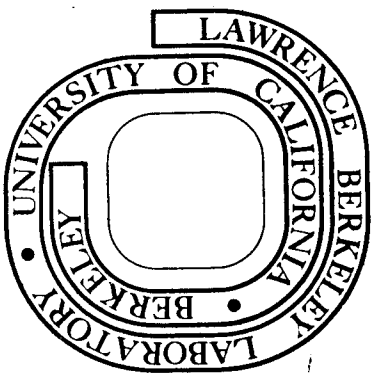

LBL-3962
c.1

DISCLAIMER

THE ELECTRONIC STRUCTURE OF MOLECULES, SOLIDS AND SOLID SURFACES

Contents

THE ELECTRONIC STRUCTURE OF MOLECULES, SOLIDS AND SOLID SURFACES

James R. Chelikowsky

Inorganic Materials Research Division, Lawrence Berkeley Laboratory
and Department of Physics; University of California
Berkeley, California 94720

ABSTRACT

A detailed study is undertaken to investigate the electronic structure of eleven diamond and zincblende semiconductors: Si, Ge, ZnSe, α-Sn, InSb, CdTe, GaP, GaSb, InP and InAs. By means of an empirical non-local pseudopotential scheme the optical spectrum, electronic density of states, and valence charge density is calculated for each compound. The theoretically required parameters are determined by comparisions with optical and photoemission experimental measurements.

In particular, the effect of a non-local potential on the electronic structure of each compound is investigated. It is found that the local pseudopotential approach can yield incorrect band topologies, optical gaps, charge densities and valence band widths. All of these defects can be corrected by the addition of a non-local term to the pseudopotential.

In addition, to the calculations performed on these bulk materials, a method for calculating the electronic structure of non periodic systems is developed. This very powerful technique allows the direct application of the pseudopotential method to such systems as solid surfaces, localized impurity and vacancy states, atomic and molecular states, finite chains or layers, adsorbates, and interfaces between solids. Here the method is applied to molecules and surfaces. Specifically

the molecular ground state energy levels and orbitals are calculated for diatomic silicon. With respect to surfaces, the technique is used to calculate the electronic structure of semiconductor and metal surfaces. The Si (111) surface is studied in detail. Calculations are performed using ideal, relaxed and reconstructed surface models with the results compared to experiment. The (110) surfaces of GaAs and ZnSe are also investigated. Finally, as an example of a metal surface the (111) surface of Al is considered.

I. INTRODUCTION

Since its introduction in the late 1950's [1] the pseudopotential method has evolved considerably. Through its application via model potentials[2] and the empirical pseudopotential method (EPM),[2] a great deal of information about solid state properties has been obtained. Band structures, optical response functions, electronic density of states and charge densities have been calculated for a wide variety of materials. Of all these materials, one of the most successful classes to which the pseudopotential method has been applied are diamond and zincblende semiconductors.

Studies on these materials, until recently, have relied upon a simplified "local" pseudopotential approach with reflectivity data used to fix the theoretical parameters. And it was observed that such an approach was sufficient to explain most of the optical data.[3] However, on purely theoretical grounds the pseudopotential should be non local and energy dependent.[3]. Thus, it was perhaps not surprising that the advent of high resolution photoemission spectroscopy, i.e. x-ray photoemission spectroscopy (XPS)[4, 5] ultraviolet photoemission spectroscopy (UPS),[6] produced detailed information on the valence bands which was in conflict with many of the existing pseudopotential calculations. This result could be explained on the basis that local approximations could suffice for the reflectivity case where only a limited energy range was involved. In particular, in reflectivity data only the highest valence bonds and lowest conduction bands are involved.

In order to accurately obtain a correct band structure for the valence band region, it was, therefore, speculated that non-locality or energy dependence must be considered. This was particularly true since other one-electron approaches, including such effects, tended to yield more accurate valence bands than a local pseudopotential approach.[7]

In addition to yielding incorrect valence band edges, it has also recently been determined that a local pseudopotential can yield incorrect bond topologies[8, 9] and valence charge densities.[10]

Therefore, an attempt to recalculate the band structures of a large number of diamond and zincblende semiconductors has been undertaken. Using an empirical non-local pseudopotential scheme we have calculated the electronic structure of Si, Ge, GaAs, ZnSe, α-Sn, InSb, CdTe, GaP, GaSb, InP and InAs. In Section II, calculations are presented for each compound yielding the optical spectrum, valence band density of states, and pseudocharge density. The non local approach has removed the discrepancies which are found to occur for the local pseudopotential with respect to the valence band widths, optical gaps, charge densities and band topologies. In addition to these properties, specific discussions are included concerning the temperature dependence of the valence charge density in Si and Ge, and the effects of local field corrections for the macroscopic dielectric function in Si.

In all of the aforementioned cases, the systems considered are infinite and periodic. This was one of the severe limitations on the pseudopotential method. While it may be easily applied to bulk

properties, there was no obvious procedure by which it could be applied to a wide variety of non periodic problems. In Section III a new technique is introduced by which the pseudopotential method may be easily extended to non periodic systems. The method allows pseudopotentials to be applied to localized combinations such as molecules, surfaces, impurities, vacancies, finite chains, adsorbates and solid interfaces. Specifically the technique is applied to the case of a molecule, and metal and semiconductor surfaces. The ground-state properties of the diatomic silicon molecule is considered. With respect to surfaces, a metal surface, Al (111), and semiconductor surfaces, Si (111), GaAs (110) and ZnSe (110) are discussed.

The Si (111) surface is covered in some detail. An ideal, relaxed, and reconstructed model for the surface is calculated with the results compared to experiment. Using a reconstructed buckled (2 x 1) surface model, all the salient experimental results can be accounted for. Finally, with respect to GaAs and ZnSe surfaces, a local density of states calculation has been performed allowing the decay of the surface features present to be directly observed. In the case of GaAs, good agreement is achieved for the dangling bond energy spectrum.

II. NON-LOCAL PSEUDOPOTENTIAL CALCULATIONS FOR DIAMOND AND ZINCBLENDE SEMICONDUCTORS

A. Non-Local Pseudopotentials

The fundamental concept involved in an pseudopotential calculation is that the ion core can be omitted or "pseudized away." Computationally this is crucial for it means that the deep ion potential has been removed and a simple plane wave basis will yield rapid convergence. There are many ways of arriving at this result,[3] but one of the most straightforward is due to Phillips and Kleinman.[1]

Simply stated, we may rewrite the one-electron Hamiltonian as

$$\mathcal{H} = p^2/2m + V_p(\underset{\sim}{r}) \tag{1}$$

where

$$V_p(\underset{\sim}{r}) = v(\underset{\sim}{r}) + \sum_{\underset{\sim}{k}} (E_{\underset{\sim}{k}} - E_t)|b_t><b_t| \tag{2}$$

$V(\underset{\sim}{r})$ is the true crystal potential and $|b_t>$ is a core state with eigenvalue E_t. This new potential has the same eigenvalues, $E_{\underset{\sim}{k}}$, but because the real potential has been cancelled in the core region by the second term in (2),[11] the resulting eigenfunctions of (1) are smoothly varying in the core region in contrast to the true eigenfunctions. While this permits the pseudoeigenfunctions to be expressed in terms of plane waves, the pseudopotential in (2) is dependent not only on the energy eigenvalues, E_k, but on the ℓ-angular momentum components present in the core states.

In spite of the face that (2) is inherently non-local and energy dependent many of the optical spectra for semiconductors can be

explained by ignoring this fact.[3] If we assume the pseudopotential is a simple function of position, then we may take,

$$V_p(\underset{\sim}{r}) = \sum_{\underset{\sim}{G}} V(\underset{\sim}{G})\exp(i\underset{\sim}{G}\cdot\underset{\sim}{r}) \tag{3}$$

where

$$V(\underset{\sim}{G}) = \sum_{\alpha} S_\alpha(\underset{\sim}{G})V_\alpha(\underset{\sim}{G})$$

$$S_\alpha(\underset{\sim}{G}) = \frac{1}{N\alpha}\sum_{\substack{\text{cell}\\ j}} \exp(-i\underset{\sim}{G}\cdot\underset{\sim}{R}_j^{\alpha}) \tag{4}$$

and

$$V_\alpha(\underset{\sim}{G}) = \frac{1}{\Omega a}\int \exp(-i\underset{\sim}{G}\cdot\underset{\sim}{r})V_p^{a}(\underset{\sim}{r})d^3r$$

where the $\underset{\sim}{G}$ are reciprocal lattice nectors and $V_\alpha(\underset{\sim}{G})$ are the atomic form factors. In such an approximation we are assuming the crystalline potential is a sum of local atomic pseudopotentials, $V_p^{a}(\underset{\sim}{r})$. Ω_a is the atomic volume and N_α is the number of atomic species, α, present. These equations may be specialized in the case of the diamond or zincblende compounds, $A^{N}B^{8-N}$ to

$$V(\underset{\sim}{G}) = V^S(\underset{\sim}{G})\cos(\underset{\sim}{G}\cdot\underset{\sim}{t}) + iV^A(\underset{\sim}{G})\sin(\underset{\sim}{G}\cdot\underset{\sim}{t})$$

where

$$V^S(\underset{\sim}{G}) = (V_A(\underset{\sim}{G}) + V_B(\underset{\sim}{G}))/2 \tag{5}$$

$$V^A(\underset{\sim}{G}) = (V_A(\underset{\sim}{G}) - V_B(\underset{\sim}{G}))/2$$

$t = a/8\ (1, 1, 1)$ where a is the lattice constant. V^S and V^A are the symmetric and antisymmetric form factors respectively.

The local empirical pseudopotential method (EPM), in fact, is based upon the above simplification. If we then take the above pseudopotentials to be spherical so that $V_p^a(\underset{\sim}{r}) = V_p^a(|\underset{\sim}{r}|)$, this means the form factors depend upon the magnitude of $\underset{\sim}{G}$, with a corresponding reduction in the number of required form factors. These form factors are the empirically determined parameters fit to experimental data such as optical gaps.

The validity of this approach rests upon two arguments: 1) $E_{\underset{\sim}{k}} >> E_t$ so that $(E_{\underset{\sim}{k}} - E_t)$ can be replaced by a mean energy in (2) such as E_F (providing one is interested in only a limited energy range) and 2) the cancellation is equal for all ℓ (or at least the ℓ-components of the valence wavefunctions which are significant). Until recently as mentioned in the introduction (e.g. comparisions with XPS and UPS data), these assumptions have been found to be satisfactory.

1. Effective Mass Approximation

If we wish to go beyond this local pseudopotential approach, the simplest procedure is to replace the actual electron mass, m, by an adjustable mass, m^*.[3] This can be illustrated by considering the diagonal matrix elements of the secular equation which we would solve for the eigenvalues and eigenvectors:

$$\frac{\hbar^2 K^2}{2m} + V(K,E) - E, \quad K = |\underset{\sim}{k} + \underset{\sim}{G}| \tag{6}$$

Following the procedure outline elsewhere,[3] we expand our potential V around the fermi-level, E_F; we get to lowest order in wavevector K, and energy E:

$$V(K,E) \simeq V(K_F,E_F) + (K-K_F)\frac{\partial V}{\partial K} + (E-F_F)\frac{\partial V}{\partial E} + \ldots \qquad (7)$$

and

$$\frac{\hbar^2}{2m}K^2-E = \frac{\hbar^2K_F^2}{2m} + \frac{\hbar^2}{m}K_F(K-K_F) - E_F - (E-E_F) + \ldots$$

Rewriting the above and neglecting constant terms we have for the diagonal elements:

$$\frac{\hbar^2}{2m}K^2[1 + \frac{1}{K_F}\frac{\partial V}{\partial K}] - E[1 - \frac{\partial V}{\partial E}]$$

Let us define the following

$$M_K = 1 + \frac{1}{K_F}\frac{\partial V}{\partial K} \qquad (8)$$

and

$$M_E = 1 - \frac{V}{E}.$$

Thus, rewriting our secular equation, by dividing everywhere by M_E, we have, for our diagonal elements,

$$\hbar^2K^2/2m^* - E \qquad (9)$$

With $m^* = M_KM_E$. In such an approach, the fit $V(\underset{\sim}{G})$, off diagonal elements, would actually include a factor M_E from the non-local and energy dependent diagonal terms, V(E,K).

This approach, while simple and leading to improved agreement for the valence band widths compared to XPS and UPS data,[12] is deficient in several respects. First, we have considered only the diagonal elements. The effect of any non-local or energy dependence

on the off-diagonal terms has been assumed small. While this may be the case for simple metals, it is not clear such an approach is applicable to semiconductors.[3] Second, another drawback is the question of the relative importance of non-locality through the ℓ-dependence in (2) and the energy dependence in (2). The m^* approach does not allow the relative importance to be seperated out. Third, the optical gaps are not improved in such fits compared to experimental data.

2. ℓ-Dependent Potentials

One procedure to avoid the difficulty in determining the relative importance of non-locality and energy dependence is to consider an explicity ℓ-dependent potential. In fact, it was first shown by Phillips and Pandey[13] that an $\ell=2$, or d-well, potential term could lead to an improved pseudoptential for Ge.

Let us consider an ℓ-dependent potential, to simulate non-locality in (2), for the form:

$$V_\ell^a(\underset{\sim}{r}) = \sum_\ell A_\ell f_\ell(\underset{\sim}{r}) P_\ell \qquad (10)$$

where A_ℓ is a constant representing the well-depth, $f_\ell(r)$ is some function simulating the "core" states, and P_ℓ projects out the ℓ-th angular momentum component. If such an atomic potential is used, we must include a $\underset{\sim}{k}$ dependence in our potential and require matrix elements of the form:

$$\langle e^{i(\underset{\sim}{k}+\underset{\sim}{G})\cdot\underset{\sim}{r}} | V_\ell(\underset{\sim}{r}) | e^{-i(\underset{\sim}{k}+\underset{\sim}{G}')\cdot\underset{\sim}{r}} \rangle \qquad (11)$$

Let us define $\underset{\sim}{K} = \underset{\sim}{k} + \underset{\sim}{G}$ and $\underset{\sim}{K}' = \underset{\sim}{k} + \underset{\sim}{G}'$ and

$$|\underset{\sim}{K}\rangle = |\exp(-i(\underset{\sim}{k} + \underset{\sim}{G})\cdot\ )\rangle$$

Then by substitution of (10) into (11) we have

$$\langle \underset{\sim}{K}|V_\ell^a|\underset{\sim}{K}'\rangle = \sum_\ell A_\ell \langle \underset{\sim}{K}|f(\underset{\sim}{r})P_\ell|\underset{\sim}{K}'\rangle \tag{12}$$

Using the well known expansion

$$e^{i\underset{\sim}{K}\cdot\underset{\sim}{r}} = \sum_{\ell=0}^{\infty}(2\ell + 1)i^\ell j_\ell(Kr)P_\ell(\cos\gamma) \tag{13}$$

with γ being the angle between $\underset{\sim}{K}$ and $\underset{\sim}{r}$, P_ℓ, the usual Legendre polynomials, $j_\ell(Kr)$ spherical Bessel functions,[3] we obtain,

$$\langle \underset{\sim}{K}|V_\ell^a|\underset{\sim}{K}'\rangle = 4\pi \sum_{\ell=0}^{\infty} A_\ell(2\ell+1)P_\ell(\cos\theta_{KK'})\langle j_\ell(Kr)f_\ell(r)j_\ell(K'r)\rangle \tag{14}$$

To obtain (14) we have made the additional assumption that $f_\ell(\underset{\sim}{r}) = f_\ell(|\underset{\sim}{r}|)$.

Let us now consider some realistic forms for f_ℓ. We wish f_ℓ to simulate the properties of core states, that it should be well localized at the atomic sites. Two appropriate choices might be a square-well or gaussian-well. The square-well has the advantage in that it is simple, but a gaussian-well is probably more realistic and is, in fact, computationally simpler.

For a square-well we require the integral,

$$\int_0^R dr\ r^2\ j_\ell(Kr)j_\ell(K'r) = F^s{}_\ell(K,K') \tag{15}$$

where we have taken

$$f(r) = \begin{cases} 1 & r<R \\ 0 & r>R \end{cases}$$

This integral is easily evaluated,[3] the result is

$$F_\ell^S(K,K') = \begin{cases} 1/2R^2\{[j_\ell(KR)]^2 - j_{\ell-1}(KR)j_{\ell+1}(KR)\} & K=K \\ \frac{R^2}{K^2-K'^2}[Kj_{\ell+1}(KR)j_\ell(K'R) - K'J_{\ell+1}(K'R)j_\ell(KR)] & K\neq K' \end{cases} \tag{16}$$

The first few $j_\ell(x)$ are given by

$$\begin{aligned} j_{-1}(x) &= \cos(x)/x \\ j_o(x) &= \sin(x)/x \\ j_1(x) &= \sin(x)/x^2 - \cos(x)/x \\ j_2(x) &= (3/x^3 - 1/x)\sin(x) - 3/x^2\cos(x) \\ j_3(x) &= (\frac{15}{x4} - \frac{6}{x^2})\sin(x) - (\frac{15}{x^3} - \frac{1}{x})\cos(x) \end{aligned} \tag{17}$$

If we take

$$f_\ell(r) = \exp(-(r/R)^2)$$

then we require the integral,

$$\int_o^\infty dr\ r^2\ j_\ell(Kr)\ j_\ell(K'r)\exp(-(r/R)^2) = F_\ell^G(K,K') \tag{18}$$

which can easily be evaluated to yield,

$$F_\ell^G(K,K') = \frac{\pi R^2}{4\sqrt{KK'}} \exp(-\frac{R^2}{4}(K^2+K'^2))\ I_{\ell+1/2}(R^2KK'/2) \tag{19}$$

The $I_{\ell+1/2}$ are modified spherical Bessel functions, the first few are given by

$$I_{1/2}(x) = \sqrt{\frac{2x}{\pi}}\,\sinh(x)/x$$

$$I_{3/2}(x) = \sqrt{\frac{2x}{\pi}}\,\left(-\frac{\sinh(x)}{x^2} + \cosh(x)/x\right) \qquad (20)$$

$$I_{5/2}(x) = \sqrt{\frac{2x}{\pi}}\,\left[\left(\frac{3}{x^3} + \frac{1}{x}\right)\sinh(x) - \frac{3}{x^2}\cosh(x)\right]$$

In both the square-well and gaussian-well cases we have assumed R to be independent of ℓ. This is not necessary and the extension of different R for different ℓ-values is trivial.

To simulate the effects of ℓ-non-locality in (2) we can simply add an ℓ-dependent term to our local potential. For example, if we wished to add a d-well correction to a local potential we could choose,

$$V^a_{NL}(\underset{\sim}{r}) = V^a_L(\underset{\sim}{r}) + A_2 f_2(r) P_2 \qquad (21)$$

with f_2 being given by a square-well or gaussian-well. This means, of course, we have added two additional parameters, A_2 and R which must be fixed by experimental or theoretical considerations. We have used just such a correction term in fitting our band structures; the results will be discussed in detail later in this section.

3. Energy Dependent Pseudopotentials

In order to understand some of the effects of energy dependence in pseudopotentials let us consider a model ion core potential devised by Heine and Abarenkov.[14]

In this model they assume that the positive ion pseudopotential

may be written as

$$V^{a}(\underset{\sim}{r}) = \left\{ \begin{array}{ll} -A_{\ell}(E) & r \leqslant R_m \\ \\ -Ze^2/r & r \geqslant R_m \end{array} \right\} \qquad (22)$$

and

$$V^{a}_{NL}(\underset{\sim}{r}) = \sum_{\ell=0}^{\infty} V_{\ell}^{a}(\underset{\sim}{r}) P_{\ell}$$

The A_{ℓ} are the well-depthes for the ℓ-angular momentum component. We shall use the script A_{ℓ} to indicate corrections to the local pseudopotential (which includes screening) and the A_{ℓ} will be reserved for the model ion core potential. P_{ℓ} projects out the ℓth angular momentum component of the wavefunction. R_m is the model radius, which is taken to be equal for all ℓ. For convenience, it is assumed that $A_{\ell}(\ell \geqslant 2) = A_2$, this can be done in most cases as the higher ℓ values are negligible in the region of interest.

To determine $A_{\ell}(E)$, after selecting a value of R_m, the spectroscopic term values are examined for an electron in the atomic ion core potential (e.g. Si^{+3}). The well depths A_{ℓ} are then adjusted to reproduce these spectroscopic terms; the behavior for the first three A_{ℓ} in Si is shown in Fig. 1. One can observe that the $\ell = 0$ and $\ell = 2$ well depths are quite dependent on the energy of the spectroscopic term to which it is fit. This should be of particular importance if one wishes to use the potential over a large energy range. To obtain the values of $A_{\ell}(E)$ for a particular energy not corresponding to a term value, an extrapolation of the A_{ℓ} to the

desired energy is required. For this purpose, as we have indicated in the figure, a linear interpolation is used, a procedure which has been justified, at least for the $\ell = 0,1$ cases by Shaw.[15]

An examination of Fig. 1 indicates quite clearly where the assumptions of a local potential may fail in silicon. While $A_1 \simeq A_2$ at E_F so p-d non-locality might be ignored, the fact that A_0 is not equal to A_1 and A_2 means that the s-non-locality probably cannot be ignored. Indeed, if one extrapolates a rydberg away from E_F as might be the case in attempting to fit photoemission data the relative value of A_0 to A_1 (or A_2) increases by a factor of two or more.

To treat such energy dependence in a rigorous fashion is quite difficult. For example, if we take an energy dependent Hamiltonian, then we have a different Hamiltonian for each eigenvalue. This means solving for as many Hamiltonians as energy bands, and also since the eigenfunctions are for different Hamiltonians, they are not orthogonal.

This problem can be circumvented by using the following simple expression to simulate an energy dependence in the well-depthes. We take,

$$A_\ell(E) \simeq A_\ell(E_F) + \frac{\partial A_\ell}{\partial E} \{[E^o(K)E^o(K')]^{1/2} - E^o(K_F)\} \quad (23)$$

for matrix elements involving K and K', E^o is given $E^o(K) = \hbar^2K^2/2m$. This approximation works quite well when compared to more rigorous techniques[16] (at least as far as the s-well corrections are concerned).

We will use such an approximation in (23) where an energy dependence may be necessary to fit experimental data and where such a need is

supported by model calculations.

4. The "On the Sphere" Approximation

Up until this point we have not made a connection between a non-local and local potential. This is, given a non-local ionic potential as in (22), is it possible to formulate some sort of local approximation which would reduce the non-local potential to a local one?

There is in fact just such a procedure.[3] In order to reduce a non-local potential to a local form, one can evaluate it at an appropriate mean energy such as E_F and use the "on-the-sphere approximation".[3] This well-known approximation converts the non-local potential to a local one by means of the following

$$V^a(\underset{\sim}{q}) = \langle \underset{\sim}{k}_F | V^a_{NL}(E, \underset{\sim}{r}) | \underset{\sim}{k}_F + \underset{\sim}{q} \rangle$$

where

$$E = E_F, \quad |k_F| = \underset{\sim}{k}_F + \underset{\sim}{q} \quad |\underset{\sim}{q}| \leq 2k_F \tag{24}$$

$$\underset{\sim}{q} \| - \underset{\sim}{k}_F \quad |\underset{\sim}{q}| \geq 2k_F$$

We now have a local ionic potential; this potential must now be screened appropriately before it can be used in calculating the electronic properties of a solid such as an optical spectrum.

In such a fashion, i.e. using the non-local ionic potential from (22), the approximation of (24), and an appropriate screening, a number of local model potentials have been constructed.[17]

B. Methods of Calculation

1. Band Structure

Once the potential is determined, it is a straight forward calculation to solve for energy band spectrum. The eigenvalue and eigenvectors are found by solving the secular equation,

$$\det\left|\mathcal{H}_{\underset{\sim}{G},\underset{\sim}{G}'}(\underset{\sim}{k}) - E(\underset{\sim}{k})\delta_{\underset{\sim}{G},\underset{\sim}{G}'}\right| = 0 \tag{25}$$

where for the local approximation we have

$$\mathcal{H}^{L}_{\underset{\sim}{G},\underset{\sim}{G}'} = \frac{\hbar^2}{2m}(\underset{\sim}{k} + \underset{\sim}{G})^2\delta_{\underset{\sim}{G},\underset{\sim}{G}'} + V_a(|\underset{\sim}{G} - \underset{\sim}{G}'|)S(\underset{\sim}{G} - \underset{\sim}{G}'). \tag{26a}$$

The form factors and structure factors are defined as in (5) for diamond and zincblende semiconductors.

For non-local corrections we may take

$$\mathcal{H}^{NL}_{\underset{\sim}{G},\underset{\sim}{G}'} = \mathcal{H}^{L}_{\underset{\sim}{G},\underset{\sim}{G}'} +$$

$$\frac{4\pi}{\Omega}\sum_{\ell}\sum_{\alpha} A^{\alpha}{}_{\ell}(2\ell + 1)\, P_{\ell}(\cos\theta_{KK'})F^{a}{}_{\ell}(K,K')\, S^{\alpha}(\underset{\sim}{G} - \underset{\sim}{G}') \tag{26b}$$

where the sum over α refers to the atomic species present. The $F_{\ell}(K,K')$ are defined as in (16) or (19). An energy dependence may be included in the A_{ℓ} as in (23).

To evaluate the optical response functions or electronic density of states it is necessary to perform a summation over wavevector $\underset{\sim}{k}$. Thus (25) is solved for a grid of 308 points in the irreducible Brillouin zone.

To achieve satisfactory convergence, typically 50 plane waves are included in the wavefunction expansion with another 50 wave treated in an approximate fashion using a scheme due to Löwdin.[3]

2. Optical Response Functions

To optical spectrum can be calculated as follows. First the imaginary part of the dielectric function is evaluated using the expression,

$$\varepsilon_2(\omega) = \frac{e^2\hbar^2}{\pi m} \sum_{n_c n_v} \int \frac{f_{n_v n_c}(\underset{\sim}{k})\, dS}{E_{n_v n_c}(\underset{\sim}{k}) |\nabla_{\underset{\sim}{k}} E_{n_v n_c}(\underset{\sim}{k})|}$$

where $E_{n_v n_c}(\underset{\sim}{k}) = E_{n_c}(\underset{\sim}{k}) - E_{n_v}(\underset{\sim}{k})$ and (27)

$$f_{n_v n_c}(\underset{\sim}{k}) = \frac{2\hbar^2}{2m} |\langle n_c, \underset{\sim}{k}|\nabla|n_v, \underset{\sim}{k}\rangle|^2 / E_{n_v n_c}(\underset{\sim}{k})$$

is the interband oscillator strength. The sum is over the initial valence band index n_v and the final conduction band states, n_c. S is a surface in k-space of constant interband energy. Four valence bands, and six conduction bands were included in the sum. The Gilat-Raubheimer scheme[18] was used to evaluate the integral. The expression for $\varepsilon_2(\omega)$ is based upon several assumptions such as neglecting excitonic effects, but has been quite satisfactory for the purpose of analyzing reflectivities. We shall discuss some corrections to (27) such as the inclusion of "local-fields", in the section on silicon. In that section we shall explicity calculate the local-field

corrections for silicon.

Once the imaginary part of the dielectric function has been evaluated, the real part may be calculated from a Kramers-Kronig transformation, and a reflectivity calculated.[3] To compare the theoretical results to the experimental derivative spectra, the logarithmic derivative of the reflectivity is computed by numerical means. Since the calculated reflectivity is susceptible to noise arising from the discrete nature of the grid over which $\varepsilon_2(\omega)$ is calculated, some averaging is usually performed.

3. Electronic Density of States

The density of states is given by

$$N(E) = \frac{1}{N} \sum_{\underset{\sim}{k}} \sum_{n} \delta(E-E_n(\underset{\sim}{k})) \tag{28}$$

where the sum is over wavevector and band index. N is the number of unit cells, so that if E(k) is in eV, then N(E) is in units of (states/eV-atom). The required sum in (28) was evaluated by a technique due to Gilat and Raubenheimer.[18] The energy gradients required in this method were calculated from $\underset{\sim}{k}\cdot\underset{\sim}{p}$ perturbation theory.

4. Pseudocharge Density

The pseudocharge density was calculated by using the special point scheme of Chadi and Cohen.[19] Instead of evaluating the sum,[20]

$$\rho(\underset{\sim}{r}) = e \sum_{\underset{\sim}{k}} \sum_{n_v} |\psi_{n_v,\underset{\sim}{k}}(\underset{\sim}{r})|^2 \tag{29}$$

over a fine grid throughout the Brillouin zone as performed by Walter and Cohen,[21] only a few representative points need by considered. The two point scheme of Chadi and Cohen, with $\underset{\sim}{k}_1 = (2\pi/a)(1/4, 1/4, 1/4)$

and $\underset{\sim}{k}_2 = (2\pi/a)(3/4, 1/4, 1/4)$ (and appropriate weighting factors), yields a valence band pseudocharge density accurate to within 1-2%,[22] as compared to a sum throughout the zone. Therefore, we have used this two point scheme. Approximately 90 plane waves were used in the calculation of the required pseudowavefunctions.

5. Spin-orbit Interactions

For the heavier elements the atomic spin-orbit splittings become rather large. This is reflected in the solids such as CdTe where the energy bands split by nearly leV at the valence band maximum. Since we are interested in obtaining precise band structures such interactions must be considered.

We have included spin-orbit by extension of a method first presented by Saravia and Brust[23] for Ge. Following the work of Weisz[24] as modified by Bloom and Bergstresser[25] we may write the spin-orbit matrix element contribution to the pseudopotential Hamiltonian as

$$\mathcal{H}^{so}_{\underset{\sim}{G},\underset{\sim}{G}'}(\underset{\sim}{k}) = (\underset{\sim}{K} \times \underset{\sim}{K}')\cdot\underset{\sim}{\sigma}_{s,s'}[-i\lambda^s\cos((\underset{\sim}{G}-\underset{\sim}{G}')\cdot t) + \lambda^A\sin(\underset{\sim}{G}-\underset{\sim}{G}')\cdot t)] \quad (30)$$

where we define

$$\underset{\sim}{K} = \underset{\sim}{k} + \underset{\sim}{G},\ \underset{\sim}{K}' = \underset{\sim}{k} + \underset{\sim}{G}'$$

as before with

$$\lambda^s = (\lambda_A + \lambda_B)/2 \qquad \lambda^A = (\lambda_A - \lambda_B)/2$$

$$\lambda_A = \mu B^A{}_{n\ell}(K)\ B^A{}_{n\ell}(K') \quad (31)$$

$$\lambda_B = \alpha\mu B^B{}_{n\ell}(K)\ B^B{}_{n\ell}(K')$$

σ are the pauli spin-states and λ^S, λ^A are the symmetric and anti-symmetric contributions to the spin-orbit Hamiltonian. μ is an adjustable parameter, and α is constrained such that the ratio of the spin-oribt contributions for the atoms A and B are the same as the spin-orbit splitting ratio for free atoms.[26]

μ is then fixed by the experimental value of the spin-orbit splittings of the energy bands.

The $B_{n\ell}$ are defined by

$$B_{n\ell}(K) = \beta \int_0^\infty j_{n\ell}(Kr) R_{n\ell}(r) r^2 dr$$

where $R_{n\ell}$ is the radial part of core wavefunction. The radial wavefunctions are taken from the Herman-Skillman tables.[27] As in Ref. 26 we only include contributions from the outermost p-core states. Contributions from inner core states or d-core states may be neglected.[26,27] β is a normalization constant as in Ref. 26.

In the Saravia-Brust method[23] spin-orbit interactions are treated by pertubation theory. If at some wavevector $\underset{\sim}{k}$ we have bands n and m such that

$$|E_n(\underset{\sim}{k}) - E_m(\underset{\sim}{k})| < E_o$$

then these bands are treated as "degenerate" and degenerate perturbation theory is used to include the spin-orbit correction. Otherwise non-degenerate pertubation theory is used.

In the degenerate perturbation technique we must solve

$$\det|\mathcal{H}^{ss'}_{mn}(k) - E(\underset{\sim}{k})\delta_{ss'}\delta_{mn}| = 0 \qquad (32)$$

where

$$\mathcal{H}^{ss'}_{mn}(\underset{\sim}{k}) = \sum_{\underset{\sim}{G},\underset{\sim}{G}'} \alpha^{m}_{\underset{\sim}{G}}(\underset{\sim}{k})\alpha^{n}_{\underset{\sim}{G}'}(\underset{\sim}{k})\mathcal{H}^{so}_{\underset{\sim}{G},\underset{\sim}{G}'}(\underset{\sim}{k}) \qquad (33)$$

$$+ E_{m}(\underset{\sim}{k})\delta_{m,n}\delta_{ss'}$$

$E_m(k)$ is the band energy without spin-orbit, $\mathcal{H}^{so}$ is given by (30) and our pseudowavefunctions by

$$\psi_{\underset{\sim}{k}}^{m}(\underset{\sim}{r}) = \sum_{\underset{\sim}{G}} \alpha_{\underset{\sim}{G}}^{m}(\underset{\sim}{k})\exp(i(\underset{\sim}{k}+\underset{\sim}{G})\cdot\underset{\sim}{r})$$

In the non-degenerate case the energy correction is simply given by the first term in (33). E_o is chosen such that it is large compared to the spin-orbit splitting. By a direct comparison with calculations which include spin-orbit exactly (rather than by pertubation theory), it is found $E_o \approx 2eV$ is quite satisfactory for the case at hand. Even with rather large spin-orbit splittings (e.g. leV) the pertubation technique is accurate to within 5% and reduces the computational time typically by almost an order of magnitude.

C. Results

In this section the results of our pseudopotential calculation are presented for eleven diamond and zincblende crystals. We shall discuss silicon and gallium arsenide in detail as prototypes for diamond and zincblende compounds respectively.

The potentials were fixed by detailed comparisons with experimental reflectivity and photoemission data. Unfortunately, the addition of a non-local correction term to a local pseudopotential increases the number of parameters rather dramatically. We have

attempted to circumvent this costraining the local part of the pseudopotential to be close to the Cohen-Bergstresser[28] values. In addition the non-local radii are fixed a follows: for an s-well the Heine-Animalu[17] model radii are used, for a d-well touching spheres are used.[29] The radii are chosen as such because the model radii should reflect an s-p admixture and thus are appropriate for an s-correction. The d-well are rather large[9] and touching spheres provide the largest radii which are physically meaningful.

Since the crystals we shall consider have wavefunctions whose character obeys

$$s + p + d \simeq 1$$

we need only consider s and d-wells. We consider s rather than p because energy dependence can be large in s, thus it need be considered explicity.

With the radii thus fixed, the only adjustable parameters we have for the non-local corrections are the well-depths.

We govern our choice for the non-local well-depthes by inspection of non-locality in the ion core potential.[2] It is expected that screening could reduce the size of the non-locality present in the core potential, but the trends are expected to be correct. Such an inspection indicates that d-well non-locality should increase from columns II to VI in the periodic table. Also s-well non-locality should become important for the heavier elements. We shall discuss this in more detail for each compound.

Finally with respect to the non-local wells it should be noted

that a gaussian well was employed for Ga, GaAs and ZnSe. A square well was used elsewhere as an s-well correction was required. The use of a square well allows us to directly apply model radii.

1. Silicon

a. Band Structure. The parameters for the potentials we used are given in Table I. We consider both a local and non-local potential. The non-local potential consists of an "energy" dependent s-well using the approximation of (23). This choice was discussed briefly with respect to Fig. 1. The s-well radius was chosen to be 1.06Å.

The eignenvalues for the local and non-local calculation at the symmetry points Γ, X and L are listed in Table II. The band structures for both cases are given in Fig. 2. The results for the local and non-local cases are quite similar, except for the lower valence band (which have a good deal of s-character), and the band ordering at for the upper conduction bands(i.e. Γ_{12}, and Γ_1).

b. Optical Spectrum. The optical spectrum can be calculated as indicated in the introduction. This procedure has been criticized in that it neglects the effects of microscopic fields (or local fields). Therefore, we shall briefly discuss the effects of such corrections with respect to silicon.

i. Local Fields. Within the linear response theory, a small perturbing electric field of frequency ω and wavevector $\underset{\sim}{q}+\underset{\sim}{G}$ in a crystal will establish responses with frequency ω and wavevectors $\underset{\sim}{q}+\underset{\sim}{G}'$, where $\underset{\sim}{G}$ and $\underset{\sim}{G}'$ are reciprocal lattice vectors. The microscopic fields of wavevectors $\underset{\sim}{q}+\underset{\sim}{G}'$ are generated from the applied perturbing field through umklapp processes. In the case of cubic crystals, the

the dielectric responses of the solid for longitudinal fields may be described by a matrix in G and G',[30]

$$\sum_{\underset{\sim}{G}'} \varepsilon_{\underset{\sim}{G},\underset{\sim}{G}'}(\underset{\sim}{q}+\underset{\sim}{G}',\omega)\, E(\underset{\sim}{q}+\underset{\sim}{G}',\omega) = E_{pert}(\underset{\sim}{q}+\underset{\sim}{G},\omega), \tag{34}$$

where E is the total field in the crystal and E_{pert} is the applied perturbing field. Microscopic-field effects (or local-field effects) are traditionally ignored by assuming the off-diagonal elements of the dielectric response matrix to be zero. However the off-diagonal elements can be important when considering local-field corrections to optical spectra,[31-33] plasmon dispersion in metals,[34,35] valence-electron density,[36] and lattice dynamics[37-41] in semiconductors and insulators.

In analyzing the optical spectrum, the incident light of frequency ω may be viewed as a perturbing field of vanishingly small wave-vector. The macroscopic dielectric function is given by[30]

$$\varepsilon(\omega) = \lim_{\underset{\sim}{q}\to 0} \frac{1}{[\varepsilon^{-1}(\underset{\sim}{q},\omega)]_{\underset{\sim}{0},\underset{\sim}{0}}}, \tag{35}$$

where ε^{-1} is the inverse of the matrix $\varepsilon_{\underset{\sim}{G},\underset{\sim}{G}'}$. Adler and Wiser[30] have derived, within the RPA, the following expression for the dielectric response matrix.[42]

$$\varepsilon_{\underset{\sim}{G},\underset{\sim}{G}'}(\underset{\sim}{q},\omega) =$$

$$\delta_{\underset{\sim}{G},\underset{\sim}{G}'} - \frac{4\pi e^2}{\Omega|\underset{\sim}{q}+\underset{\sim}{G}|\,|\underset{\sim}{q}+\underset{\sim}{G}'|} \sum_{\underset{\sim}{k}nn'} \frac{f_0[E_{n'}(\underset{\sim}{k}+\underset{\sim}{q})]-f_0[E_n(\underset{\sim}{k})]}{E_{n'}(\underset{\sim}{k}+\underset{\sim}{q})-E_n(\underset{\sim}{k})+\hbar\omega+i\hbar\alpha}$$

$$\times \langle \underset{\sim}{k}+\underset{\sim}{q},n'|\, e^{i(\underset{\sim}{q}+\underset{\sim}{G})\cdot\underset{\sim}{r}}|\underset{\sim}{k},n\rangle\langle \underset{\sim}{k},n|e^{-i(\underset{\sim}{q}+\underset{\sim}{G}')\cdot\underset{\sim}{r}}|\underset{\sim}{k}+\underset{\sim}{q},n'\rangle \ , \qquad (36)$$

where Ω is the crystal volume, f_0 is the Fermi-Dirac distribution function, and $|\underset{\sim}{k},n\rangle$ and $E_n(\underset{\sim}{k})$ are eigenstates and eigenvalues of the unperturbed Hamiltonian. $\varepsilon_{\underset{\sim}{0},\underset{\sim}{0}}(\underset{\sim}{q},\omega)$ is just the usual Cohen-Ehrenreich[43] dielectric function as given by (27).

To evaluate the required matrix elements and eigenvalues in Eq. (36), we have calculated a band structure for silicon using the local pseudopotential in Table I. The resulting band structure is in excellent agreement with the optical gaps and photoemission experiments. Each $\varepsilon_{\underset{\sim}{G},\underset{\sim}{G}'}(\underset{\sim}{q}=0,\omega)$ was evaluated in energy intervals of 0.125 eV up to 100 eV. The summation over wavevector was performed by evaluating the wavefunctions and eigenvalues on a grid of 308 $\underset{\sim}{k}$-points in the irreducible zone. The matrix size of the dielectric response matrix involved in the inversion for Eq. (35) was chosen to be 59 x 59, containing G-vectors through the set (222). Symmetry can be involked to reduce the number of $\varepsilon_{\underset{\sim}{G},\underset{\sim}{G}'}$ elements which need be calculated to 72. Convergence of the macroscopic dielectric function was confirmed by inversion of $\varepsilon_{\underset{\sim}{G},\underset{\sim}{G}'}$ including sets of $\underset{\sim}{G}$-vectors through (111), (200), (220), (311) and (222) respectively.

In order to establish the accuracy of the calculated $\varepsilon_{\underset{\sim}{G},\underset{\sim}{G}'}$, we have tested our results using the sum rules as derived by Johnson,[44]

$$\int_0^\infty \omega \, \mathrm{Im}\, \varepsilon_{\underset{\sim}{G},\underset{\sim}{G}'}(\underset{\sim}{q},\omega)\,d\omega = \frac{\pi}{2}\,\omega_q^{\,2}\left(\frac{\rho(\underset{\sim}{G}-\underset{\sim}{G}')}{\rho(0)}\right)\hat{e}(\underset{\sim}{q}+\underset{\sim}{G})\cdot\hat{e}(\underset{\sim}{q}+\underset{\sim}{G}') \ , \qquad (37)$$

where $\omega_p^{\,2} = 4\pi ne^2/m$ is the plasma frequency, $\rho(\underset{\sim}{G})$ are the Fourier transforms of the valence-electron density, and $\hat{e}(\underset{\sim}{q}+\underset{\sim}{G})$ is a unit vector in the $\underset{\sim}{q}+\underset{\sim}{G}$ direction. In Table III we list our calculated results for the specific cases $\underset{\sim}{G} = \underset{\sim}{G}'$ and $\underset{\sim}{G} = 0$, $\underset{\sim}{G}' \neq 0$. The integral appearing in Eq. (37) was evaluated over a 100 eV range in intervals of 0.125 eV. Our results demonstrate good internal consistency except for the diagonal elements for the higher $\underset{\sim}{G}$-vectors. This arises from the fact that Im $\varepsilon_{\underset{\sim}{G},\underset{\sim}{G}}(q=0,\omega)$ becomes more extended in frequency as $|\underset{\sim}{G}|$ increases and that the integrand in Eq. (37) is linearly weighted with frequency. Better results can be obtained if we extend our integrations beyond the 100 eV range. As far as the optical properties are concerned, this high energy behavior is unimportant, and our values for $\varepsilon_{\underset{\sim}{G},\underset{\sim}{G}'}$ in the region considered should be very accurate.

The calculated imaginary part of the macroscopic dielectric function with (Adler-Wiser) and without local-field (Cohen-Ehrenreich) corrections, $\varepsilon_2(\omega)$ and Im $\varepsilon_{\underset{\sim}{0},\underset{\sim}{0}}(\omega)$ respectively, is given in Fig. 3 together with the experimental measurement of Philipp and Ehrenreich.[45] From Fig. 3 we see that local-field corrections do not alter the peak position, although they do alter the strength of the dielectric function. Compared with the usual Im $\varepsilon_{\underset{\sim}{0},\underset{\sim}{0}}(\omega)$, $\varepsilon_2(\omega)$ has less strength at energies below the main optical peak, thus increasing the discrepancy with experiment. At energies higher than the main optical peak, the strength of $\varepsilon_2(\omega)$

is reduced from that of Im $\varepsilon_{\underset{\sim}{0},\underset{\sim}{0}}(\omega)$ until approximately 7 eV. Beyond this point $\varepsilon_2(\omega)$ is larger than Im $\varepsilon_{\underset{\sim}{0},\underset{\sim}{0}}(\omega)$: an event which must transpire if the well known sum rules[30] are to be satisfied. This behavior results in an overall improvement in $\varepsilon_2(\omega)$ at higher energies as compared with experiment. Excitonic effects, particularly on the lower energy side of the main optical peak, which are not included in our calculations, should further improve the agreement between our $\varepsilon_2(\omega)$ result and experiment in the low energy region. The effect of these electron-hole interactions tends to increase the oscillator strength, hence the strength of $\varepsilon_2(\omega)$, at the lower energies.

Thus, while the effects of local-field can alter the optical spectrum they do not, for example, shift the critical points nor greatly alter the peak heights. Therefore, the Cohen-Ehrenreich dielectric function should be satisfactory for our purpose of associating critical points in the band structure with reflectivity structure.[3]

To remove the discrepancies remaining between experiment and theory will probably require inclusion of higher-order corrections such as exchange[32] or dynamic correlations[31] in addition to local-field effects. Such a computation, however, would take us beyond the range of material to be covered here.

For completeness in Fig. (3b) we display the calculated and experimentally determined real part of the dielectric function, ε_1. To calculate ε_1 from ε_2 a tail function of the form

$$\varepsilon_2(\omega) = \frac{\beta\omega}{(\omega^2+\gamma^2)^2} \quad , \quad \hbar\omega > E_o$$

was used. Typically, E_o is chosen to be a few volts higher than any significant structure in ε_2. β and γ are constants. β is determined by continuity and γ is fixed such that γ is approximately the energy of the main peak in the reflectivity (e.g. $\gamma \approx 4.5$ eV for Si). With this tail function the Kramers-Kronig relations may be used with the integral required extended to infinite frequency.

The calculated ε_1 is in quite good agreement with the experimental results. In particular the static dielectric constants for the calculated and experimental results agree to within 10%. This is very suprising as for most compounds the discrepancy is larger.

We have extended our calculation to higher energies and find a plasma frequency of approximately 18 eV in agreement with experiment. Although we display the ε_1 results for our non-local potential, the local results are quite similar.

ii. Reflectivity. The calculated and experimental reflectivity spectrum is shown in Fig. 3c. The theoretical spectrum is unusual in that the caluclated reflectivity coefficient is smaller than experiment for rather high energies (i.e. 3-7 eV). This is not true for most compounds.[3] In fact, in most cases after the most prominent reflectivity peak, the discrepancy between theory and experiment is typically 50%. At present, the reason for this is unclear.[3]

In Table IV we have identified the theoretically determined structure in the reflectivity derivative spectrum, and as usual associate the structure with van Hove singularities (or critical points) in the Brillouin zone.[3] Silicon, as noted by other authors,[46] has a large number of critical points, and the identifications in

Table IV should be considered as representative for the specific energy region under consideration. Saravia and Brust[46] have done a very thorough analysis of band topologies of three model potentials for silicon. Our results are quite similar to their "Model II" and the interested reader is referred to their extensive contour maps.

A comparison between the experimental results of Ref. 47 and our calculated derivative spectra is given in Fig. 4. Overall the agreement is quite satisfactory for both the local and non-local cases. In particular, the placement of the reflectivity peak positions for both cases is accurate to within ~0.15 eV. The non-local energy dependent result is superior at the higher energies, with the E_1' structure in slightly better agreement than the local calculation. On the other hand, the local calculation is slightly superior in the E_2 region, at least as far as the placement of the 4.3 eV reflectivity structure is concerned, although both the theoretical curves have a different line shape than the experiment. In the non-local curve the reflectivity structure at 4.15 eV is in perhaps the greatest discord with the experimental results. The reason for this can be traced back to the band shape near the X_4-X_1 region. The band gap at X for the non-local case is on the order of ~0.2 eV smaller than the local case. We also note that the indirect gap is smaller for the non-local case. If we were to slightly increase the X_4-X_1 transition by ~0.2 eV the resulting reflectivity curve (and indirect gap) should be in better accord with experiment. In the E_1 region we are not able to resolve the fine structure present in the experimental results.

The first reflectivity peak at 3.45 eV has been the subject of some controversy. Piezoelectric experiments (both ac[49] and dc[50]), chemical shifts in Ge-Si alloys,[51] electroreflectance[52] and some wavelength modulation techniques[53] have suggested that the peak has Δ symmetry. However, more recent work has suggested that the peak has Λ-symmetry[54,55] and this assignment is also suggested by analogy with other zincblende structures.[53]

In both the local and non-local results this reflectivity peak arises from contributions from points near Γ, along Λ and off the Δ-direction. However, the dominant contribution arises from the Λ transition. The complexity of this peak in our theoretical calculations, that is, contributions from several critical points, has also been suggested by several authors, e.g. Welkowsky and Braunstein through an examination of experimental reflectivity data.[48] In this respect, we note that the $\Gamma_{25'}$-Γ_{15} and Λ_3-Λ_3, critical points must lie very close in energy or more widely spaced reflectivity structures would be present in our calculated reflectivities.

While the topological differences between the local and non-local calculations in this region are small, it is interesting, and perhaps significant, that our non-local calculation is "flatter" along the Λ-symmetry direction. This trend has been observed previously, in non-local calculations involving a d-well.[9,56,57] We find in the non-local calculation that from the L point midway to Γ, the energy difference between bands 4 and 5 is less than 0.01 eV, while over the same range in the local calculation the gap varies by ~0.15 eV. This means that the non-local

band structure has a nearly two dimensional M_0 point at L in agreement with recent electroreflectance data by Grover and Handler;[55] however, the transverse mass for this critical point in the non-local case is quite similar to the one calculated in the local case, and not in agreement with Grover and Handler's value. We find the transverse mass μ_t ~0.1m, whereas the experimental value found by Grover and Handler is closer to 0.02m.

Another controversial transition has been the previously mentioned $\Gamma_{25'}$-$\Gamma_{2'}$. In most diamond and zincblende semiconductors $\Gamma_{2'}$ lies below Γ_{15}. Only in silicon have theoretical calculations found the reverse to be true. This ordering, however, has been confirmed by the low field electroreflectance data of Aspnes and Studna.[58] They have been able to resolve, for the first time, the E_0 and $E_0+\Delta_0$ transitions, and find the spin-orbit critical points to occur at 4.185 ± 0.010 eV and 4.229 ± 0.010 eV at 4.2°K. This is in good accord with the theoretical value for both the local and non-local cases as can be noted in Table II.

We observe that the experimental results of Aspnes and Studna contradicts the assignment of Kunz[59] which placed $\Gamma_{2'}$ below Γ_{15}. This assignment was based upon an analysis of soft X-ray data. However, we feel the assignment of Aspnes and Studna to be more conclusive. Soft X-ray data can be difficult to interpret as the leading edge may exhibit excitonic effects.[60] In fact, one finds that the agreement between the soft X-ray spectra and the theoretical results with Γ_{15} placed lower than $\Gamma_{2'}$ are in satisfactory agreement away from the suspect leading edge.[61] Furthermore, Ge-Si alloying

experiments tend to confirm the Aspnes-Studna assignment.

c. Electronic Density of States. In Table V we compare our results for the local and non-local cases with the experimental results of photoemission measurements. The agreement is quite good for both cases, but the non-local calculation appears to be superior for the L_1 and L_2, levels. Unfortunately the ordering of the Γ_{12}, and Γ_1 conduction bands is not made clear by the experimental results, since both theoretical results are in fairly good agreement with the experimentally determined transitions. The non-local results, however, are again in slightly better accord. In Fig. 5 we compare our calculated electronic density of states to the results of XPS. We have not included the transition matrix elements, hence the theoretical peak heights do not match the experimental ones, but the peak placement for the non-local results are in excellent agreement.

d. Band Masses. We have also calculated the cylotron resonance masses using the mass parameters of Dresselhaus, et. al.[64] as modified by Kane.[65]

$$F' \simeq \frac{2}{m} \sum_n \frac{|\langle \Gamma_{25'} | P_x | \Gamma_{2'}{}^n \rangle|^2}{E_{25'} - E_2{}^n}$$

$$G' \simeq \frac{2}{m} \sum_n \frac{|\langle \Gamma_{25'} | P_x | \Gamma_{25}{}^n \rangle|^2}{E_{25'} - E_{15}{}^n} \qquad (38)$$

$$H' \simeq \frac{2}{m} \sum_n \frac{|\langle \Gamma_{25'} | P_x | \Gamma_{12'}{}^n \rangle|^2}{E_{25'} - E_{12'}{}^n}$$

where we have neglected an interaction term between Γ_{25}^{+}, and Γ_{25}^{-} which should be negligible.[64] Pseudowavefunctions were used to evaluate the required matrix elements. Contrary to comments made by other authors,[66,67] these matrix elements are quite accurate when compared to OPW calculations.[68] We have also calculated the conduction band minimum mass by directly calculating the band shape over a fine grid of points in the neighborhood of the minimum.

In Table VI the experimentally determined cyclotron mass parameters. The position, the magnitude, and transverse and longitudinal masses of the conduction band minimum as determined by experiment are also compared to the theoretical results. It is interesting that a simple three parameter purely local pseudopotential is able to so accurately reproduce the mass results and that the non-local calculation gives such excellent results. This should be contrasted with Kane's calculation in which he was unable to fit both the masses and gaps.[65] The difficulty was attributed to the failure of the local Slater exchange term, but it was observed that changes outside the linear regime" of his empirical adjustments might remedy the situation.

e. Pseudocharge Density. Finally we compare our local and non-local valence pseudocharge densities to the recent calculations of Yang and Coppens.[73] Using the results of very accurate X-ray experiments now available,[74] they were able to obtain an extremely accurate valence charge density for silicon. In Fig. 6 we present their valence charge density results which has been prepared by the removal of the core states by the use of Clementi wavefunctions.[75] They

estimate a standard deviation of 0.3 e/Ω_c in the charge density near the bonding region. However, at the nuclear sites the error is larger due to anomalous scattering, but we would not expect the pseudocharge density to be accurate in this region either. In Fig. 7 we give the theoretical pseudocharge density results for both the local and non-local calculations. The fourier coefficients of the charge density are given in Table VII for both results; these coefficients are similar to the results of an OPW calculation by Brinkman and Goodman.[75a]

Since our local calculation resembles that of Walter and Cohen's,[21] Yang and Coppen's observations[73] made regarding the Walter-Cohen calculation are valid here. A comparison of the local result to the experimental charge density shows as Yang and Coppens point out, that in both cases the maximum of the valence charge denisty occurs at the midpoint of the bond, and that the bond height maxima of 28 e/Ω_c and 26 e/Ω_c, for both experiment and theory respectively, are in very good agreement. We find similar results are also true for the non-local calculation. This is indeed quite encouraging, especially in view of recent SCOPW calculations.[76] In these calculations, while the calculated crystalline form factors are found to be an improvement over the free atom form factors, there still existed significant discrepancies.[76] Unfortunately since difference densities (i.e. $\rho_{val} = \rho_{total} - \rho_{core}$) have not been prepared for the SCOPW case, a direct comparison cannot be made between their results and our calculations.

That the pseudopotential should do so well away from the nuclear region is perhaps not as surprising as it may seem. It is in the bonding region where we would expect our wavefunctions to be most accurate. On the other hand, the fact that the agreement is so good is unexpected, as energies are always more accurate than the corresponding wavefunctions. Calculations for the temperature dependence of the "forbidden" (222) reflection in silicon, involving pseudocharge densities, have also been able to accurately reproduce the experimental results. These results will be discussed later in this section.

In the local case we do find some discrepancy with experiment: namely, the orientation of the bond. The local pseudopotential bond axis is aligned <u>perpendicular</u> to the bonding direction, while experiment finds a bond elongated <u>parallel</u> to the bonding direction. This result is outside of the experimental error quoted by Yang and Coppens.[62] But in the case of the non-local pseudopotential we find a pseudocharge density in which the bond is elongated <u>parallel</u> to the bonding direction.

The rotation of the bond from the local perpendicular orientation to the non-local parallel orientation result can be traced <u>directly</u> to the energy dependent non-local s-well's effect on the bottom valence band. A band by band comparison of the local and non-local pseudocharge densities is given in Figs. 8 and 9. The bottom valence bands in the energy-dependent non-local case see a must weaker (i.e. less repulsive) s-well than do the upper valence and conduction bands. This permits the s-like bands in the non-local case to remain the same for the upper bands, but differ for

the lower bands. Hence, in the non-local case we have, for the bottom bands, charge "leaking" into the core regions, while in the local case it remains excluded. This accounts for the "bond-like" feature appearing in the local case for the bottom bond, while in the non-local case the charge appears uniformly spaced between the atoms. The second valence band also mimics to some extent the changes occurring in the first band. But it is the major change in the first band which causes the change in bond orientation.

f. Temperature Behavior of the Pseudocharge Density. Not only have recent X-ray experiments provided an accurate charge density, but the temperature dependence of the valence charge has also been investigated. By combining neutron and X-ray diffraction studies, Roberto, Batterman and Keating[77] have been able to establish the temperature dependence of the "forbidden" (222) reflection in both silicon and germanium, and specifically, they have been able to determine the relative contributions to the forbidden reflection arising from the bonding electrons and from the anharmonic motion of the ion cores.

Early attempts[78] to account for the temperature dependence were based on inaccurate experimental results,[77] and are not in accord with the more recent data. More recent simplified models have also failed at the higher temperatures.[77] As suggested by Phillips[79] and Roberto, Batterman and Keating,[77] we find that the change in bonding charge with temperature is significant. Further, we find under the assumption of an Einstein solid, that the Debye-Waller

factor characteristic of the bond motion is one half that of the ion cores.

In establishing the temperature dependence of the bonding charge the anharmonic contribution from the ion motion must be subtracted out from the "forbidden" (222) reflection.[77] This may be accomplished through the use of neutron diffraction techniques as neutrons interact primarily with the nuclei. In such a fashion, using the simple model of Dawson and Willis[80] to account for the temperature dependence of the ion core contributions, Roberto et al. have separated out the anharmonic motion of the cores. Once this has been accomplished the resulting contributions to the forbidden reflection can arise only from non-centrosymmetric parts of the charge density, i.e. bonding charge.

Since the "forbidden" (222) reflection, corrected for the anharmonic motion of the ions, depends upon the structure factor, F^{b}_{222}, for the bond,the temperature dependence of this reflection can be analyzed in terms of this "bond" structure factor. The procedure which we shall follow in obtaining the temperature dependence of the structure factor for the bond will be analogous to the atomic structure factor case. In the atomic case the structure factor is the product of two factors: the fourier transform of the charge distribution, or scattering factor, and a Debye-Waller factor. The first factor accounts for the charge distribution, the second for thermal motion. To calculate the structure factor for the bond we first calculate the charge distribution with the ion cores in

their equilibrium positions and determine the scattering factor for the bond. Next we take the bond motion into account by an appropriate Debye-Waller factor, and obtain the structure factor for the bond by the product of the scattering and Debye-Waller factors. However, unlike the atomic case we take into consideration the effect that the bonding charge may be significantly altered by temperature as suggested by Phillips.[79] In order to account for this change in bonding charge, and the resulting change in the scattering factor, we calculate the effect of temperature on the crystalline potential. This may be done in a straight forward manner involving the use of the Debye-Waller ion core factors as indicated in Ref. 81.

In obtaining the effect of temperature on the charge density it is necessary to have a knowledge of the crystalline potential, the thermal expansion function of the solid, and the phonon spectra or Debye-Waller factors for the ion cores.[81] This data, however, is well established for both silicon and germanium. Recent calculations on both silicon[16] and germanium[8] using non-local pseudopotentials have been able to accurately obtain the optical gaps, photoemission results, and cyclotron masses, and these are the potentials which we shall use in the present calculation. Further, the thermal expansion function has been tabulated over an extensive temperature range[82] and Batterman and Chipman[83] have incorporated X-ray data on the ion core motion into Debye-Waller factors for both crystals.

After the scattering factor has been calculated in the manner outlined above, it is necessary to obtain a Debye-Waller factor for the bonding charge. Welsh has suggested that the Debye-Waller factor appropriate for the bonding charge should be smaller than the corresponding Debye-Waller factor for the ion cores.[77] However, under the physically reasonable assumption that the motion of the bond should be characterized by the motion of the midpoint of near-neighbor atoms, and the additional assumption of an Einstein solid (appropriate for the temperatures involved[83]), it is easy to demonstrate that the Debye-Waller factor for the bond is exactly one half that of the ion cores.

The temperature behavior for silicon is given in Fig. 10. The results for germanium are displayed in the next section. In Fig. 10 we indicate the results from the simple model of Roberto et al.,[77] which assumed that the valence charge density was not altered by temperature. They also assumed that the bond motion would be that of the ion cores and, hence, the same Debye-Waller factor could be used. Unlike their results, our calculations are in excellent agreement over the entire temperature range for both silicon and germanium. However, it should be pointed out that Roberto et al. recognized quite clearly the drawbacks of their model and, in fact, suggested that the temperature dependence of the scattering factor, or charge density, combined with a reduced Debye-Waller factor for the bond motion might yield the correct temperature dependence for the "bond" structure factor.

We also mention in this context that Phillips[79] has suggested that a decrease in the bonding charge, Z_b, alone could account for the observed temperature dependence of the structure factor. He has developed a theory for the magnitude of the bonding charge which states that it should very as the inverse of the optical constant squared, i.e. $Z_b \propto n^{-2}$. If we evaluate $\Delta Z_b/Z_b$ in terms of finite differences over the temperature range of interest we find $\Delta Z_b/Z_b = 0.066 \pm 0.006$ for silicon and $\Delta Z_b/Z_b = 0.13 \pm 0.05$ for germanium using the experimental values of n(T).[14] If we associate the (222) component of the charge density, ρ_{222}, as a measure of the bonding charge, and evaluate $\Delta\rho_{222}/\rho_{222}$, we find $\Delta\rho_{222}/\rho_{222} = 0.062$ for silicon and $\Delta\rho_{222}/\rho_{222} = 0.099$ for germanium in good accord with the values predicted by Phillips. The values, however, for $\Delta F^b_{222}/F^b_{222}$ are 0.10 ± 0.01 for silicon and 0.18 ± 0.02 for germanium. Therefore, we note, at least in the case of silicon where the experimental values are determined with more precision than in germanium, the decrease in Z_b alone cannot adequately explain the observed temperature dependence of the forbidden (222) reflection. However, if a Debye-Waller factor appropriate for the bond is included, then Phillips' predicted values for $\Delta Z_b/Z_b$ can adequately account for the observed behavior.

Finally we mention that the accuracy of our pseudocharge density calculation in yielding an accurate temperature dependence of the forbidden (222) reflection, and in producing an accurate valence charge density is quite encouraging. We expect the pseudocharge density to fail to reproduce the actual charge density in the core

region; however, that it is so accurate away from the core region, i.e. the bonding region, suggests that other band calculations can be refined to give similar results, e.g. self-consistent orthogonalized plane wave (SCOPW) results[76] have, thus far, not yielded accurate structure factors.

2. Germanium

a. Band Structure. For Ge a gaussian-well correction term of the form,

$$V_{NL}(\underset{\sim}{r}) = V_L(\underset{\sim}{r}) + A_2 \exp(-r^2/R^2)P_2$$

was employed. The parameters used in the calculation are given in Table VIII. The well radius, R, was chosen to be 1.22Å. The form factors we used are quite close to the ones used by Cohen-Bergstresser.[28] Unlike Si where the spin-orbit splitting is small, on the order of 0.05 eV, Ge has a splitting of 0.3 eV at the valence band maximum. Consequently, we have included spin-orbit interactions in this calculation. The eigenvalues at the high symmetry points, Γ, X and L, are given in Table IX. In Fig. 11 the band structure along symmetry lines is displayed.

b. Optical Spectrum. The reflectivity and the modulated reflectivity spectrum is displayed in Fig. 12 and Fig. 13. The reflectivity spectrum has been of interest because of the controversial nature of the E_2 peak.

Recently Aspnes[84] has proposed that the E_2 reflectivity peak, the most prominent peak, in Ge appears to arise from a localized region in the Brillouin zone (BZ) in apparent contradiction to

previous theoretical calculations.[85-89] By using our non-local pseudopotential scheme, we are able to determine that the interband transitions of interest arise from a specific BZ region; these conclusions are not at variance with the experimental results. Analysis of the calculated reflectivity reveals that the E_2 peak arises from a well defined, limited region inside the BZ which is not along lines of high symmetry. This region lies near the special point (3/4, 1/4, 1/4) determined by Chadi and Cohen.[19] These results are consistent with previous theoretical calculations and with Aspnes' suggestion that the observed structure can arise from a set of equivalent critical points. We also obtain an interband mass for the E_2 region in reasonably good accord with the experimentally determined value.

In Table X identification of the important reflectivity structure is compiled. One of the most interesting effects of the non-local potential is its effect on the critical point topologies. In particular, it has been noted[8, 9] that a non-local well "flattens" the energies bands (particularly along the Λ direction). Other critical points, which exist with a local potential, may be eliminated altogether.

In analyzing the E_2 peak we find that it originates from a specific region of the Γ-X-U-L plane. Fig. 14 indicates the energy contours of interest in this region. This very flat plateau region has large dipole matrix elements and because it is not a point of high symmetry there are[24] equivalent regions in the full Brillouin zone making up a large volume. Further, we find no critical point along Σ, and

as noted elsewhere,[88] the X_5-X_5 critical point is of little consequence due to its small volume. Such a plateau feature has been noted before in zincblende compounds[89] and Ge,[86] where it usually, but not always, is accompanied by a Σ critical point.

The plateau itself, consists of a nearly, if not completely, degenerate M_1-M_2 pair of critical points, and while it is not a "localized" region in the sense of a critical point at a symmetry point, it is still a well-defined and limited region. The dipole matrix elements and energy difference of bands 4 and 5 are nearly constant over the entire plateau. And as will be mentioned in more detail below, the interband mass in this region is also nearly constant. Finally it has been noted that the E_2 peak in the $\varepsilon_2(\omega)$ appears to arise from just such a combination,[91] and Aspnes has determined that at least one interband mass component should be negative in this region.[84] Both of these results are compatible with our calculations.

Other prominent structure arises from critical points at L and Γ. At 2.19 eV and 2.39 eV we have structure in the calculated reflectivity coming from M_1 type critical points at L. This structure corresponds to the experimental structure at 2.22 eV and 2.42 eV observed at 5°K. The structure at 3.20 eV has been the subject of some controversy.[3] Aspnes has observed structure at 3.02 eV, 3.20 eV and 3.50 eV which he attributes to transitions involving the spin-orbit split $\Gamma_{25'}$ - Γ_{15} transitions. This is in excellent agreement with our transitions:

$$\Gamma_8^v - \Gamma_6^c \quad 3.01$$

$$\Gamma_8^v - \Gamma_8^c \quad 3.22$$

$$\Gamma_7^v - \Gamma_8^c \quad 3.51$$

This suggests that the observed reflectivity structure at 3.2 eV may arise from Γ contributions, in contrast to previous speculations that the phase space at was too small to make significant contributions to any reflectivity structure. Excitonic effects could, of course, play a role in enhancing the transitions at Γ. Finally we note the structure at 5.7 and 5.9 eV does not appear to arise from spin-orbit split transitions involving L_3, - L_3, but rather the lower transition has contributions from along Δ and the higher transition involves contributions from the L region.

We conclude our discussion of the reflectivity by noting a possible relationship between the plateau region and the special point (3/4, 1/4, 1/4) of Chadi and Cohen,[19] who have developed a scheme for evaluating sums over wave vector in the Brillouin zone of a periodic function. They have found that by choosing special points in k-space, rapid convergence of the sum can be achieved (e.g. for charge density calculations).

In particular, if we have a sum

$$f = \sum_{\underline{k}} g(\underline{k})$$

they have shown that the best two point approximation which can be made is

$$f \cong \frac{1}{4}\, g(k_1) + \frac{3}{4}\, g(k_2)$$

where k_1 = (1/4, 1/4, 1/4) and k_2 = (3/4, 1/4, 1/4). It is interesting that such a two point $\varepsilon_2(\omega)$ would pick up a contribution to the E_1 and E_1' peaks from k_1 and a contribution to the E_2 peak from k_2. Of course, it is just these peaks which dominate the structure. This would seem to indicate such a scheme might be applicable in evaluating the sum over wave vector needed for dielectric function calculations.

c. Electronic Density of States. The valence band edges and other transitions of interest compared to experiment are given in Table XI. Spin-orbit interactions were not included in the calculated values; the experimental uncertainty for photoemission measurements (i.e. XPS or UPS) is larger than the spin-orbit splittings involved.

The theoretically determined electronic density of states compared to the UPS experimental results of Ref. 6 in Fig. 15. Again, we do not include transition matrix elements, and thus, do not expect the theoretical peak heights to match with the experimental spectrum. The shoulder near the top part of the valence band may be due, in part, to the presence of surface states. This aspect will be discussed later in the surface section.

d. Interband Masses. In order to compare the band masses as experimentally determined by Aspnes[84], we have calculated some interband masses from the following expression:

$$\frac{m}{m_{ij}} = \frac{2\hbar^2}{m} \sum_{\ell} \left(\frac{P^2_{j\ell}}{E_j - E_\ell} - \frac{P^2_{i\ell}}{E_i - E_\ell} \right) \qquad (39)$$

where m_{ij} is a measure of the interband mass size for the i^{th} and j^{th} bands, and $P_{i\ell}$ is the gradient matrix element. Our results for the interband masses are compared with the experimental results of Aspnes in Table XII. These results further substantiate the assignment of the E_2 structure to the "plateau" region.

e. Pseudocharge Density. The total valence charge density is given in Fig. 16. The results are quite similar to Walter and Cohen's.[21] This is to be expected as the non-local d-well potential alters only the conduction bands which, unlike the valence bands, contain significant d-character in their wavefunctions.

The temperature behavior of the bonding charge as determined from experiment is presented in Fig. 17. The melting temperature of Ge is lower than Si, thus, the departure of F_{222}^{b}(Ge) from its room temperature value is larger for an equivalent temperature. The Debye-Waller factor for the ion-cores as a function of temperature is also indicated in Fig. 17. The relatively faster fall-off of F_{222}^{b} suggests that the valence wavefunctions must alter their character with temperature. Otherwise, a simple bonding charge, Z_b, would have to oscillate faster than the ion cores to account for the difference between F_{222}^{b} and the Debye-Waller factor. This does not seem physically reasonable.

3. Gallium Arsenide

We shall discuss GaAs in some detail as it will serve as a prototype for the zircblende semiconductors. GaAs is a good choice for such a "model" III-V compound as extensive theoretical and

and experimental work has been carried out on this compound. In particular, recently Aspnes and Stadna,[94] have made electroreflectance experiments which have resulted in an order of magnitude improvement in resolution and accuracy (for higher energy gaps) over previous spectroscopic work. In addition studies by Pandey and Phillips[9] and the author[95] have resulted in extremely accurate theoretical band structures for GaAs.

a. Band Strucutre. The band structure for GaAs, including spin-oribit interactions, is given in Fig. 18. The potential included a non-local gaussian d-well as for the case of Ge. The parameters used in the calculation are given in Table XIII. The well radii are not crucial in obtaining an accurate band structure. We have therefore constrained the d-well radii to be the same for the Ga and As contributions. The radius, R, was chosen to be 1.22Å. The local symmetric form factors were constrained to remain close to Ge: the largest change being 0.01 Ry.

The eigenvalues calculated for the higher symmetry points Γ, X and L are given in Table XIV.

b. Optical Properties. In Fig. 19a we present our calculated imaginary part of the dielectric function compared to the experimental results of Ref. 45. With the exception of the doublet peak at 3 eV, the overall agreement is quite satisfactory. The 3 eV peak in experiment is nearly twice as large in magnitude as the theoretically determined peak. It has been suggested[3] that at least part of the discrepancy comes from the fact we have ignored excitonic interactions. Such interactions are known to enhance quite strongly the reflectivity peaks.

Another discrepancy is the peak placement near 5 eV, the experimental peak occurs at 4.5 eV, while the theoretical peak is near 5.1 eV. This discrepancy can be partially accounted for by the fact that the experimental measurements were taken at room temperatures, while the theoretical parameters where fit to optical gaps measured at 5°K. This would account for some, but not all of the discrepancy.

The origin of the various structure observed in the ε_2 figure will be discussed when the reflectivity spectrum is analyzed. In Fig. 19b we present the real part of the dielectric function. The real part was calculated from a Kramers-Kronig transformation. We note similar discrepancies exist as for the imaginary part of the dielectric function between the theoretical and experimental curves. The theoretical static dielectric function is smaller by nearly 20% compared to experiment. This discrepancy is also present in the reflectivity spectrum in Fig. 19c. It is interesting to note that while the dielectric functions appear to be somewhat in discord with theory, the reflectivity curve is in quite good agreement with theory (except for the magnitude). Part of this can be explained by the fact that the structure inthe reflectivity comes from critical points in the band structure. And, while many body effects may enhance the critical points they do not appear to significantly shift the critical point positions.

The reflectivity structure is identified in Table XV; in Table XVI we compare our calculated critical point energies to the experimental results of Schottky barrier electroflectence[94] and wavelength modulation[90]. The results of two recent band structures using a local

pseudopotential and an orthogonalized plane wave (OPW) calculation are also presented for comparison. We note the optical gaps for the local pseudopotential or OPW calculations can typically be in disagreement by 0.5 eV. This should be contrasted with a typical error of 0.05 eV from our non-local calculation.

The modulated reflectivity spectrum is presented in Fig. 20. In this figure we are able to resolve fine structure in the reflectivity curve. In fact by examining the energy gradients and dipole matrix elements throughout the Brillouin zone, it is possible to determine the origin of structure in the imaginary part of the dielectric function. In such a manner we have analyzed the contributions to E_o' reflectivity structure. This structure has been the subject of some discussion.[94,96] Rehn and Kyser using transverse electroreflectance observed only a Δ symmetry for this structure.[96] They attributed the structure to be derived from the pseudocrossing of the Δ_5 conduction bands. However, Aspnes and Studna have pointed out that this interpretation conflicts with band structure calculations where some Γ symmetry structure is predicted.[94] Further, they proposed that the Δ symmetry structure arises from a pair of M_1 critical points approximately 1/10th of the way from Γ to X. Our calculations agree with the Aspnes-Studna interpretation. We indeed, find two M_1 critical points along Δ at between 5 to 10% of the way from Γ to X as indicated in Fig. 21. It is these points along with contributions from Γ, which causes the structure at 4.5 eV(B) and 4.7 eV(C) in our derivative spectrum (Fig. 20). We have also found that by calculating the band structure with and without spin-orbit interactions, that these interactions

are crucial in altering the band shape near Γ and producing the critical points.

Aspnes and Studna also noted the possibility of the pseudocrossing producing some very weak structure at 4.4 eV in the electroreflectance dara.[94] This also agrees with our results. The dashed line Fig. 21. indicates an M_o critical point position near the pseudocrossing. This M_o critical point produces the weak structure near 4.4 eV(A) in Fig. 20. It should be noted, however, that there exists a companion M_o critical point due to the spin-orbit splitting of the Δ_5 valence band. Since this companion occurs at about 0.1 eV higher energy, it is nearly degenerate with the E_o' structure from Γ and Δ at 4.5 eV. In our calculated derivative spectrue it is masked by the stronger M_1 critical points, and this may also be the case in the electroreflectance measurements.

c. Electronic Density of States. In Table XVII the calculated valence band edges are given with the experimental results from XPS and UPS. In addition, we present results for some indirect transitions taken from a recent review article on GaAs.[100] Spin-orbit interactions were not included in the calculated results. The experimental values from Ref. 100 were taken at room temperature; the theoretical values were fit to the 5°K data. This accounts for the fact that the theoretical transitions are larger when compared to experiment by typically 0.1 - 0.2 eV.

In Fig. 22 the calculated density of states is compared to the results of XPS. The overall agreement is quite satisfactory. The largest discrepancy exists for the bottom valence band. Theoretically,

it is quite difficult to position this band and not affect the optical transitions. Experimentally, the resolution in this region is fairly low (0.5 eV) and removing the "background" is difficult. The UPS and XPS results disagree by approximately 0.9 eV for the position of the bottom band (with UPS results in better accord with our calculation).

The leading edge of the valence band is also difficult to place experimentally. The $L_3^v - \Gamma_{15}^v$ transition in particular is the source of some inconsistency between UPS and XPS. The XPS value is in better accord with our non-local EPM value. Surface states could play a role in the varying values between XPS and UPS. There are, in fact, rather strong surface states in this region[103], and UPS could be affected by their presence.

d. Pseudocharge Density. In Fig. 23 the calculated valence band charge density is presented band by band. In Fig. 24 the total charge density is presented. The ionic nature of GaAs is quite evident compared to Si or Ge. The bottom valence band has charge localized strongly on the As, and corresponds to the As 4s atomic level. The next three valence band show mainly As p-character. We note that this can be understood in terms of the density of states curve. The bottom peak corresponds to As s-states, the next peak (at - 7 eV) corresponds to Ga s-states with some As-p admixture. The dominant peak (-4.5 to 0.0 eV) corresponds to As p-states.

4. Zinc Selenide

Zinc selenide completes the iso-electric series Ga-GaAs-ZnSe.

This series has the same crystal structure and lattice constant. It, therefore, illustrates quite nicely the trends which may occur with increasing ionicity.

Of the three crystals, ZeSe is the least successful as far as reproducing the results from reflectivity and photoemission experiments. Part of the problem, not doubt, arises because of the existence of the Zn 3d "core" state which lies approximately 10 eV below the valence band maximum. Our pseudopotential does not explicitly include these states, and, therefore may not accurately account for any effects due to their presence.

Nevertheless, we are able to significantly improve the electronic density of states for the top three valence bands, and obtain a reflectivity with satisfactory agreement between theory and experiment using our non-local approach.

a. Band Structure. The band structure was calculated using the same type of pseudopotential as for GaAs. The parameters used in the calculation are given in Table XVIII. The well radii were chosen to be 1.22Å for both Zn and Se.[104] The more repulsive d-well for Se is consistent with the trend observed in GaAs: a more repulsive As well than Ga well. The eigenvalues for the symmetry points Γ, X and L are given in Table XIX.

The calculated band structure is presented in Fig. 25.

b. Optical Spectrum. The calculated reflectivity spectrum is presented in Fig. 26 compared to experiment. Wavelength modulation experiments would provide a better source of comparison, but such

spectra are not available. The structure present in the reflectivity spectra is identified in Table XX.

Because of its ionic character the structure is shifted to higher energy. Synchotron radiation has recently permitted the reflectivity spectrum to be measured over a 15 eV range.[105] The optical gap not listed in Table XX is 2.7 eV in good agreement with the synchotron data.

There are two prominent discrepancies between theory and experiment in Fig. 25: one is the doublet nature of the reflectivity peak at 6.7 eV which is not present in the theoretical caluclation; the other is the magnitude of the reflectivity coefficient as calculated via the non-local pseudopotential. The doublet nature of the 6.7 eV is probably missing because it is obscured in our calculation by the strong peak accurring over a plateau region (as in Ge). If one calculates a "band by band" dielectric function there is prominent structure at 6.5 eV for transitions between the top valence band and the second conduction band. However, in the total dielectric function, this structure is not discernable; it is overwhelmed by the strong "plateau" transitions from the top valence band to the first conduction band.

c. Electronic Density of States. In Fig. 27 we compare our calculated valence band density of states with the epxerimental results of ultraviolet photoemission spectroscopy (UPS)[101] and X-ray photoemission spectroscopy (XPS).[102] Previous local EPM calculations[12] were in disagreement for the top three valence band edges by an eV or more. The non-local pseudopotential calculation has removed this

discrepancy. However, the bottom valence band, which corresponds to the Se 4s states, is not in good agreement with the XPS data. In UPS the bottom band is not observed. It is not clear why our position for the bottom band is in error. OPW calculations tend to give better values than the local EPM calculations for the lowest band, and such calculations agree with our results. Further, Freeouf has recently studied the experimental reflectivity of II-VI compounds over an extended energy range by the use of synchotron radiation.[105] He observes structure in the 15-16 eV range, and notes that such structure might be associated with transitions from the group VI s-level. Our calculations agrees with this suggestion as the threshold for such a transition is 15 eV.

In Table XXI we list the experimental results from photoemission and the calculated results for the valence band edges. Except for the disagreement for the bottom band placement, the agreement is quite satisfactory, and is a considerable improvement over local pseudopotential calculations. Spin-orbit interactions are included in the experimentally measured values; the notation in Table XXI refers to experimental features. Therefore, the theoretical values listed contain the spin-orbit correction just as experimental. This practice will be important only for materials such as CdTe or InSb where the spin-orbit interactions are large.

d. Pseudocharge Density. The charge density for ZnSe is presented in Fig. 28. This result is quite different from Walter and Cohen's calculation.[21] In the Walter-Cohen result the charge density indicates

a very ionic crystal. The charge transfer from Zn to Se appears to be complete. This is not the case for the present calculation. While the valence charge is predominately localized on Se, the charge transfer is not complete.

Physically, our result is more reasonable than the local pseudopotential result.[21] ZnSe should not be very ionic. The reason the non-local result yields a less ionic crystal can be traced to the effect of the d-well on the optical gaps. The repulsive d-well increases the optical gap size without increasing the charge transfer. The optical gaps are, in fact, too small in general compared with experiment, therefore the d-well resolves this discrepancy. However, a local potential can only increase the optical gaps by increasing the antisymmetric form factors. This procedure has two drawbacks: a) the valence band widthes decrease, a trend not supported by XPS or UPS data, and b) the charge transfer increases; the crystal becomes more ionic.

5. Gray Tin

Grey tin is one of the most interesting diamond structure compounds, because it is believed to be "ideal semimetal" (i.e. a semiconductor with zero band gap). This is consistent with the trend present in Group IV elements: the band gap decreases from diamond to tin (with lead being metallic.

White tin occurs at room temperature, but does not occur in a diamond structure.

In α-Sn, InSb and CdTe it was found that a simple d-well was insufficient to fix the placement of the bottom valence band. Typically, if the optical gaps are fit, the lowest valence band differs from experiment by several volts (if only a d-well correction is employed). However, an examination of the Heine-Animalu[14] results indicates an s-well correction may become more important for the heavier elements. And if a correction term, the size of which is compatible with the Heine-Animalu calculation, is included, the placement of the bottom valence band is compatible with experiment.

In order to reduce the number of adjustable parameters, a square-well was taken from the Heine-Animalu results. The size of the d-well was given by two touching spheres of equal radii.

a. Band Structure. The band structure was calculated using the parameter in Table XXII; an s-well and d-well square well correction were used. The s-well was "energy dependent" as given by (23). The well radii were R_o = 1.06Å and R_2 = 1.41Å. The eigenvalues at the symmetry points Γ,X and L are given in Table XIII.

The band structure is given in Fig. 29. Since Γ_8^{v-c} corresponds both to the top valence band and bottom conduction band, α-Sn is an ideal semimetal. This degeneracy cannot be removed by pressure or temperature[106].

b. Optical Properties. The reflectivity spectrum is given in Fig. 30. Electroreflectence[107] and reflectivity[108, 109] experiments exist for α-Sn, but unfortunately, a wavelength modulation spectrum has not been determined. The comparison in Fig. 30 of our non-local result and the experimental result of Ref. 108 is satisfactory with

respect to peak positioning, but not magnitude. This is in part due to a poor sample,[109] but some of the error may result in the traditionally large reflectivity present at higher energies in the theory.[3]

The structure present in the reflectivity spectrum is identified in Table XXIV. The experimental data is from both electroreflectance and reflectivity measurements. There is some weak structure near 4.7 eV which we do not observe in the theory. Other than this discrepancy we are able to identify the rest of the reflectivity structure. Our identifications, for the most part are comatible with Ref. 109 (an OPW calculation).

The theoretical reflectivity below 0.5 eV is not accurate because of numerical problems associated with the vanishing band gap.

c. Electronic Density of States. Unfortunately UPS or XPS spectra are not available for α-Sn. We have, therefore, adjusted our potential to give approximate agreement with an OPW calculation. Our calculated values for the valence band edges are compared in Table XV to the OPW theoretical calculation and some experimental data near the valence band maximum. For comparison to experiment we have extrapolated α-Sn valence edges using the InSb results and by examination of the Ge-GaAs results. The extrapolation is probably good to ± 0.5 eV.

The calculated electronic density of states is displayed in Fig. 31. The band gap is observed to vanish. The overall shape and peak placement is in good accord with the calculation in Ref. 109.

d. Pseudocharge Density. In Fig. 32 the valence charge density is presented for α-Sn. The trend present from Si to Ge is present in grey tin: namely, the charge density extends into the core region to a greater extent. Tin is more metallic; therefore, the bonding charge shows a decrease in magnitude compared to silicon.

6. Indium Antimonide

a. Band Structure. As in the case of grey tin, an s-well and a d-well were employed in the band calculation for InSb. The parameters used in the calculation are listed in Table XXXVI. The radii for the s-well depths were $R_o(In) = 1.27Å$ and $R_o(Sb) = 1.06Å$. For the d-wells the radius was determined by touching spheres: $R_2 = 1.4Å$.

The eigenvalues at the symmetry points Γ, X and L are given in Table XXVII. The calculated band structure along symmetry lines is given in Fig. 33.

b. Optical Spectrum. The calculated reflectivity is compared to experimental results from Ref. 110 and Ref. 111 in Fig. 34. In Fig. 35 the calculated modulated reflectivity spectrum is compared to the experimental results of Ref. 90. The modulated reflectivity is, of course, a more accurate measure.

The structure observed in the calculated reflectivity is identified and compared to the experimental results in Table XXVIII.

With the exception of some structure near 5.2 eV, which does not appear in the theoretical calculation, the agreement is quite satisfactory.

Not shown in the experimental reflectivity is the fundamental optical gap which occurs at 0.24 eV[112]. Our theoretical value is in excellent accord with this value being 0.25 eV.

Electroreflectance measurements have been made for n-type InSb and have yielded values for the Γ_6^c-Γ_7^c, Γ_8^c transitions.[113, 114] These measurements give

$$\Gamma_6^c-\Gamma_7^c = 3.16 \text{ eV}$$

$$\Gamma_6^c-\Gamma_8^c = 3.54 \text{ eV}$$

compared to our calculated values of 2.91 and 3.34 eV. Our calculated values are slightly low, but the splitting is in good agreement with experiment.

Our theoretical identifications for the reflectivity may be compared to the results of Ref. 113. Most of the assignments are in satisfactory accord, but the non-local well has resulted in the destruction of the M_0 critical points which are known to occur for a local potential at L.

c. Electronic Density of States. The calculated valence band edges are compared to experiment in Table XXIX. XPS and UPS data are good agreement for InSb. This allows us to accurately determine the valence band density of states displayed in Fig. 36. The agreement between the theoretical density of states and experiment is excellent.

d. Pseudocharge Density. The calculated valence charge density is displayed in Fig. 37. The results are in general agreement with

that of Ref. 113. The trends observed with increasing ionicity from Ge to GaAs are similar to that of the trend observed from Sn to InSb. Attempts have been made to associate the Phillips ionicity parameter,[115] C, with the asymmetric gap.[116] These studies would seem to suggest that GaAs is more "ionic" than InSb,[116] but the charge distributions[113] observed in pseudopotential calculations would seem to suggest the opposite.

7. Cadmium Telluride

CdTe completes the isoelectric series of α-Sn, InSb and CdTe. The trends are similar to the Ge, GaAs and ZnSe series: the "antisymmetric" gap grows in the valence band density of states, the optical gaps became larger and the charge becomes localized on the anion.

Unlike ZnSe we are able to achieve good agreement with both the optical and photoemission experimental data. This fact might be attributed to the inclusion of the s-well non-local term in the pseudopotential.

a. Band Structure. A square-well non-local correction term for both s and d angular momentum components were included in our potential. The parameters used in the calculation are given in Table XXX. The non-adjustable well radii were fixed to be R_0(Cd) = 1.37Å, R_0(Te) = 1.06Å and R_2 = 1.4Å. We found it unnecessary to include a Cd d-well correction. This is similar to case of ZnSe where the Zn d-well term was of lesser importance than the Se d-well term.

The eignenvalues for the symmetry points Γ,X and L are given in Table XXXI. The spin-orbit splittings are quite large. Our calculated splitting at the valence band maximum is Δ_o = 0.89 eV compared to the experimental value of 0.91 eV.[117, 118]

The calculated band structure along symmetry lines is presented in Fig. 38.

b. Optical Spectrum. The calculated reflectivity is displayed in Fig. 39. compared to the experimental results of Ref. 118. A modulated reflectivity spectrum does not exist at present for CdTe. The theoretical reflectivity structure is identified and compared to experimental results in Table XXXII.

The identifications are basically in agreement with Ref. 118, and similar to ZnSe. Although we have not listed the transitions in Table XXXII, those occurring between the spin-orbit split Γ_{15}^{v}-Γ_{15}^{c} could play a role in creating the structure at 5.7 and 5.9 eV.

The structure occurring experimentally at 5.2 eV is not observed in the theoretical reflectivity spectrum. This was the case in ZnSe also. However, the modulated reflectivity spectrum shows some weak structure in this region. The structure arises from a well-defined M_o critical point occurring along the Δ-direction. As in the case of ZnSe, it is quite probable that this transition does not appear in the theoretical reflectivity because of the finite resolution of the theoretical caulcuation: it is obscured by the dominant peak occurring at 5.53 eV.

c. Electronic Density of States. The theoretically determined values for the valence band edges are given in Table XXXIII. They are compared to the photoemission results of UPS[101] XPS[102].

Unlike ZnSe the placement of our lowest valence band seems to be in agreement with experiment. Although the 4d Cd core states obscur the lowest valence band in experiment, an approximate position is given by UPS measurements.[101]

The theoretical electronic density of states is given in Fig. 40. The results of UPS measurements are also given indicating the approximate position of the lowest valence band.

The agreement of the non-local pseudopotential with experiment is quite good and a considerable improvement over local pseudopotential calculations. In particular, a recent local calculation[101] has yielded a valence band width for the top three bands 2 eV too small.

d. Pseudocharge Density. In Fig. 41 our calculated valence charge density is presented. While our results are similar to a recent charge density calculation[118], our results would suggest a less ionic CdTe. This is in accord with the ZnSe results with our non-local potential.

8. Gallium Phosphide

GaP is the first of four "inter-row" compounds we shall examine. Such compounds allow us to study trends obtained in descending a column of the periodic table, e.g. GaP, GaAs and GaSb.

The non-local corrections in GaP are taken into consideration by non-local s- and d-wells. Phosphorus requires a weakly energy-dependent s-well; this is a trend consistent with the observation that the heavier elements require a strongly energy-dependent well.[14,17]

Since spin-orbit interactions are small for GaP($\Delta_o \simeq 0.1$ eV), we do not consider spin-orbit corrections in this calculation.

a. Band Structure. The parameters used in this calculation are listed in Table XXXIV. The non-local well radii were not adjusted, but fixed by model radii[17] for the d-wells, therefore, R_o(Ga) = 1.27Å and R_2 = 1.18Å.

The eigenvalues at the symmetry points Γ, X and L are given in Table XXXV. The band structure is illustrated in Fig. 42.

b. Optical Spectrum. The calculated reflectivity spectrum is presented in Fig. 43 compared with the experimental results of Ref. 45. In Fig. 44 our modulated reflectivity curve is compared with the experimental results of Ref. 119.

The theoretical reflectivity structure is identified in Table XXXVI. The identifications are quite similar to those in a previous calculation.[119]

c. Electronic Density of States. The calculated density of states curve is presented in Fig. 45 compared to the experimental results of Ref. 102.

The theoretical valence band edges are compared with the experimental results of UPS[101] in Table XXXVII. Also listed are other transitions including those from a recent review article on GaP.[100] The agreement with the experimental results is quite satisfactory. The calculated indirect gap is slightly smaller than

experiment; however, the valence band edges are in excellent agreement with both XPS and UPS. Again, the bottom valence band edge as detetmined by XPS and UPS is not in accord, but this is probably due to differing methods of data reduction.[102]

d. Pseudocharge Density. In Fig. 46 we present our calculated valence charge density for GaP. The charge density indicates a rather ionic crystal: the bond and charge are displaced considerably toward anion. Such an observation is compatible with current ideas concerning the "ionicity" of a crystal.[115]

9. Gallium Antimonide

a. Band Structure. The parameters used in the band calculation for GaSb are tabulated in Table XXXVIII. The s-well radii for Ga and Sb are the same as the Ga in GaAs and the Sb in InSb. The d-well radii were determined by touching spheres.

In Table XXXIX the eigenvalues at the symmetry points Γ, L and X are given. The band structure is presented in Fig. 47.

b. Optical Spectrum. The calculated reflectivity is given in Fig. 48 compared to the experimental results of Ref. 111 and 120. The calculated derivative spectrum is given in Fig. 49 compared to the experimental results of Ref. 90.

The theoretical structure is identified in Table XL. The identifications are sililar to Ref. 89, but contain some differences due to the non-local potential, e.g. an M_1 at L instead of an M_0

and the Δ_5^v-Δ_5^c transitions occur at a higher energy.

The contour plots for the energy difference between the top valence and bottom conduction bands have been calculated in Ref. 89. The most interesting feature here is a large, but well defined, region of nearly constant energy occurring near (0.7,0.3,0.3). This plateau feature, mentioned before in the case of Ge, is responsible for the prominent reflectivity peak at 4.35 eV.

While our calculated reflectivity is in excellent agreement with the experimental structure, we do not observe weak structure at 5.5 eV measured by wavelength modulation.[90]

The fundamental gap, Γ_8^v-Γ_6^c is 0.8 eV from experimental measurements[89,121] as in the spin-orbit splitting Δ_o. Both of the values are in accord with the theoretically calculated values of Γ_8^v-Γ_8^c = 0.86 and Δ_o = 0.76.

c. Electronic Density of States. The calculated electronic density of states is presented in Fig. 50 compared to the XPS spectrum for GaSb. UPS measurements have not, to date, been performed for GaSb.

In Table XLI the observed features in the XPS spectrum are listed and compared to the theoretical results. The agreement between theory and experiment is excellent. Ohter experimentally determined transitions from Ref. 63 are also listed in the table.

d. Pseudocharge Density. The valence charge density for GaSb is displayed in Fig. 51. This charge density had not been previously calculated. It is interesting to note that GaSb is less ionic than GaP (at least from a comparison of charge densities). This

observation is not compatible with the suggestion by Chadi et al.[116] That the "ionicity" of a zincblende material should be proportional to the antisymmetric gap. Both theoretically and experimentally the antismyyetric gaps of GaP and GaSb are nearly identical. However, Phillips' "ionicity" parameter and our calculation would suggest GaP is definitely more ionic (i.e. greater charge transfer) than GaSb.

10. Indium Phosphide

a. Band Structure. The band structure of InP was calculated using non-local s-and d-wells on the phosphorus as in GaP. The use of a phosphorus d-well for InP as well as for GaP is justified by model pseudopotential calculations.[14, 17] The parameters used in this calculation are given in Table XLII. The d-well radii were determined, as usual, by touching spheres; the s-well for In was the same as in InSb, the s-well for P was the same as in GaP.

The band structure along symmetry lines is given in Fig. 52. The eigenvalues calculated for InP are given in Table XLIII for the symmetry points Γ, X and L.

b. Optical Spectrum. The calculated reflectivity spectrum for InP is given in Fig. 53 compared to the experimental results of Ref. 119 and Ref. 122. The modulated reflectivity spectrum is given in Fig. 54, and compared to the experimental results of Ref. 119.

The prominent structure in the theoretical reflectivity spectrum is identified in Table XLIV and compared to experiment.

The agreement of the calculated and experimentally determined structure is quite good. The structure at 5.25 eV observed experimentally is low by about 0.2 eV from the theoretically calculated value of 5.44 eV. However, in Ref. 119 this structure is also experimentally observed, albeit weak, and occurs at a higher energy.

The origin of the structure occurring near 5.4 eV in the theoretical calculation is unclear. A transition near 5.2 eV occurs at Γ, and could contribute to this structure. (Especially if excitonic interactions enhance this transition.)

c. Electronic Density of States. The calculated electronic density of states is given in Fig. 55 compared to the XPS spectrum of Ref. 102. The theoretical features of the density of states spectrum are compared to the experimental values in Table XLV. The agreement between our theoretical values and the experimental values is excellent.

d. Pseudocharge Density. In Fig. 56 we present the total valence charge density for InP. This charge density resembles GaP, as expected. Most of the charge density is localized on the phosphorus, and the Ga to In pertubation is not a great one. Interestingly, the charge density of InP is considerably more ionic than InSb and this would not be the case by a examination of local potential calculations.

11. Indium Arsenide

a. Band Structure. The band structure for InAs was calculated using the parameters listed in Table XLVI. The In s-well radius is the same as used for InSb and InP. The As s-well radius was the model

radius: R_o(As) = 1.06Å. The d-well radius was chosen by touching spheres, R_2 = 1.31Å.

In Table XLVII we list our calculated eigenvalues for InAs at Γ, X and L. In Fig. 57 the band structure for InAs is displayed along symmetry lines.

b. Optical Spectrum. The calculated reflectivity spectrum is given in Fig. 58 compared to the experimental results of Ref. 123. The calculated derivative reflectivity spectrum is given in Fig. 59 and is compared to the experimental results of Ref. 90.

The theoretical reflectivity structure is analysed with the results presented in Table XLVIII.

All of the theoretical structure can be identified with the experimental results, although the overall agreement is slightly less satisfactory than some of our other results.

The fundamental gap in InAs is 0.42 eV. as is the spin-orbit splitting at Γ.[124, 125] Our values are $\Gamma_8^v - \Gamma_6^c$ = 0.37 and Δ_0 = 0.43 eV in good accord with experiment.

c. Electronic Density of States. The calculated electronic density of states curve is displayed in Fig. 60 compared to the experimental results of XPS. The theoretical and experimental valence band features are compared in Table XLIX.

With the possible exception of the lowest valence band, the theoretical and experimental curves are in good agreement. Both experimentally and theoretically the lowest valence band is difficult to position. Experimentally, subtracting off the background must be

done in a precise fashion. Theoretically, one has to worry about energy dependence with a valence band minimum almost a rydberg away form the valence band maximum.

d. Pseudocharge Density. The charge density for InAs is given in Fig. 61. Compared to InSb and InP it appears to be more like InSb than InP. While this seems reasonable, recent theories[116] of "ionicity" suggest that InAs should resemble InP rather than InSb.

III. SELF-CONSISTENT PSEUDOPOTENTIAL CALCULATIONS FOR MOLECULES AND SOLID SURFACES

A. New Method of Calculating the Electronic Strucutre of Non-Periodic Systems

A method is developed which extends the pseudopotential scheme to localized configurations. The calculations are performed self-consistently and the approach is applicable to problems such as atomic and molecular states, solid surfaces, localized impurity and vacancy states, finite chains or layers, absorbates, and interfaces between solids. The scheme has many of the advantages of the pseudopotential method in that it used a simple plane wave expansion and the starting potential can be obtained from experimental data. It goes beyond the usual pseudopotential approach through the requirement of self-consistency.

Pseudopotential methods have evolved considerably since their introduction[1] in the late 1950's. The use of model potentials[2] and the empirical pseudopotential method[3] have yeilded a great deal of information about solid state properties such as band structure, optical response functions and electronic charge densities.[21] In all of these cases the systems considered were assumed infinite and periodic; and possible extensions of the method to local configurations in solids e.g. localized impurities or solids without long range periodicity were not obvious. An attempt[126] was made to use the pseudopotential scheme to study amorphous materials. Complex calls were repeated infinitely and the effects

of the complexity of the unit cells on the calculated properties yielded information about how the prominent features of the strucutre (e.g. even and odd numbered rings of bonds) influenced the properties (e.g. electronic density of states). A true amorphous system was not generated, but information gained from studies of increasingly complex cells was extremely useful.

The method discussed here is somewhat related to the above scheme, and it is directly applicable to the specific problem of interest. The method is straightforward and initially involves putting the local configuration of interest into the structure factor. In the pseudopotential formulation, the crystalline pseudopotential form factors, $V(\underset{\sim}{G})$, are written in terms of atomic potential form factors, $V_a(\underset{\sim}{G})$ through the structure factor $S(G)$,

$$V(\underset{\sim}{G}) = \sum_{\tau_a} S(\underset{\sim}{G}) V_a(\underset{\sim}{G})$$

$$S(\underset{\sim}{G}) = e^{i\underset{\sim}{G}\cdot\underset{\sim}{\tau}_a}$$

where $\underset{\sim}{G}$ is a reciprocal lattice vector and $\underset{\sim}{\tau}_a$ are the basis vectors to the various atoms in a primitive cell. The basic scheme is to include in $S(\underset{\sim}{G})$ the essential features of the local configuration. In the case of a molecule, the structure factor can be constructed to create a cell with a molecule and sufficient empty space around the molecule to provide isolation from the next molecule when the cell is repreated. For a surface, usual periodicity can be retained in two dimensions and a slab of space can be inserted to provide a surface in the third dimension. The impurity or vacancy problem requires a

of host atoms surrounding the site of interest. Ultimately the cell chosen is repreated indefinitely to allow the use of the pseudopotential method. A similar approach specifically designed for surfaces has been used by Alldredge and Kleinman[127] for Al and Li surfaces.

Self-consistency[128] is essential in obtaining realistic solutions since the calculations will start with potentials derived from bulk calculations. It is necessary to allow the electrons of react to the boundary conditions imposed by the local configuration and the resulting readjustment and screening is a fundamental part of the problem. Also, the self-consistent screening potential has to be completely general and is not necessarily a superposition of atomic potentials.

In the scheme described above, the configuration of atoms and spaces can be as complex as desired. The ultimate limitation of the number of atoms is the amount of computer time necessary to generate the eigenvalues and eigenfunctions through solution of the secular equation. The basis set is formed by Bloch waves expanded in terms of free electron eigenfunctions.

The starting potential can be an ionic model potential fit to atomic term values and screened appropriately or a potential obtained from measurements of bulk solid state properties. In both cases the results are the same once self-consistency is reached. The problems with the method come mainly via the artificial long-range symmetry imposed, but most of the consequences can be dealt with. Some examples are: the interaction between configurations;

establishing a zero of energy; the fact that the potential which should depend continuously on wavevector, q, is approximated by form factors at q's equal to the G's of the chosen lattice structure; and the symmetry of the configuration to some extent dictates the choice of lattices. Most of the above potential problems are eliminated or reduced by taking large enough cells and cells of the appropriate structure or symmetry.

To illustrate the method, the diatomic silicon molecule will first be investigated. We shall then apply the method directly to metal and semiconductor surfaces.

B. The Diatomic Silicon Molecule

We treat here the case of a silicon diatomic molecule both to illustrate the method and to demonstrate the interesting results which are possible for molecular calculations. This is the first molecular calculation using self-consistent pseudopotentials to our knowledge.

For calculations of molecular states, the main advantage of our method over more standard methods is that the properties of the core electrons need not be computed. Consequently calculations for the heavier molecules are no more difficult than for light ones except for minor complications associated with spin effects. For light molecules, standard methods are very successful, but because the computation time increases exponentially with the number of electrons, there is a paucity of calculations for molecules composed of atoms beyond the first transition series. The simplicity of the proposed

pseudopotential scheme also allows calculations for large complex molecules. At first sight the plane wave basis set used appears to be retrogressive, but there are in fact advantages to this approach. Because of the plane wave basis and the use of statistical exchange (discussed later), there is no a priori bias as to the form of the wavefunction -- its form is determined self-consistently via the potential. Also because we are using pseudopotential approach, only the valence electron charge density is computed, and the basis set need only be large enough to reproduce variations in this fairly smooth charge distribution. Specifically, the charge variation away from the cores is not large and hence the plane wave basis set and resulting matrix are easily handled by modern computers.

1. Ground State Electronic Configuration

In the diatomic molecule case which has $D_{\infty h}$ symmetry, the most convenient lattice structure is hexagonal with D_{6h} symmetry. Thus the rotational symmetry of the wavefunction is simulated by sets of six-fold "stars" of plane waves. Test calculations on the Si_2 molecule in a trigonal lattice with D_{3d} symmetry show that the self-consistent results are weakly dependent on the chosen "crystal structure" provided convergence is reached i.e. enough plane waves are taken into account.

The Si_2 molecule calculation was done in the following way. The molecule was placed in a hexagonal lattice with a c/a ratio chosen such that the distance between any two atoms not belonging to the same molecule was larger than three bond lengths. The molecule bond length was taken from experiment to be 2.25Å in the ground

state[129] which differs considerably from the 2.34Å for the Si crystal. The wavefunction was expanded in about 180 plane waves including 250 more planes waves by a second order perturbation scheme.[3] The first step in the self-consistent calculation was performed using the superposition of two atomic potentials taken from empirical crystal calculations. A continuous curve[3] of the form

$$V(q) = \frac{a_1(q^2-a_2)}{\exp(a_3(q^2-a_4))+1} \tag{40}$$

was fit to the few crystalline form factor values to provide potential values at the new "molecule $\underset{\sim}{G}$-vectors". The dispersion of the eigenvalues in k-space which is a measure of the interaction of the different molecules with each other was of the order of 0.8 eV at this stage; it decreased to about 0.2 eV in the course of self-consistency. From this starting calculation the total charge $\rho(\underset{\sim}{r})$ was evaluated in terms of its Fourier components $\rho(\underset{\sim}{G})$ and a Hartree-like screening potential

$$V_H(\underset{\sim}{G}) = \frac{4\pi e^2 \rho(G)}{\Omega_c |\underset{\sim}{G}|^2}$$

defined by

$$\nabla^2 V_H(\underset{\sim}{r}) = -4\pi e^2 \rho(\underset{\sim}{r})$$

as well as an exchange potential given by

$$V_x(\underset{\sim}{r}) = -\alpha \frac{3}{2\pi} (3\pi^2)^{1/3} e^2 \rho(\underset{\sim}{r})^{1/3}$$

with $\alpha = 0.79$ were computed. The use of a statistical exchange of the above form for atoms, molecules and solids has been proven to yield satisfactory results. The calculation of $V_x(\underset{\sim}{r})$ requires knowledge of the function $\rho(\underset{\sim}{r})^{1/3}$. For this purpose $\rho(\underset{\sim}{r})$ was evaluated on a grid of points (10,000 per unit cell), the cube root was taken at each grid point and the result was transformed back into a Fourier series resulting in $V_x(\underset{\sim}{G})$. The sum of these potentials was added to a bare ion pseudopotential obtained from empirical atomic calculations.[2] The local "on the Fermi sphere" approximation to this originally non-local potential was used and a continuous curve of the form

$$V_{ion}(q) = \frac{a_1}{q^2} (\cos(a_2 q) + a_3) e^{a_4 q^4} \qquad (41)$$

was fit to the results. The use of this atomic ionic potential in the molecular case is also justified by the following. If this potential is used in a self-consistent band structure calculation for the crystal, excellent results are obtained.

The computational procedure was then continued until self-consistency was reached. The process of reaching self-consistency can be speeded up by interpolating appropriately between output and input potentials for consecutive steps. We thus needed five steps to reach self-consistency of the eigenvalues to within 0.05 eV. The resulting potentials $V_{ion}(\underset{\sim}{r})$, $V_H(\underset{\sim}{r})$ and $V_x(\underset{\sim}{r})$ are plotted in Fig. 62 along

the line, connecting the two Si atoms. The total self-consistent potential is also shown and compared to the empirical input potential which gives the best description of Si-atoms in the crystalline phase. The interesting results are that: a) the Hartree screening potential is essentially featureless, b) the exchange potential is comparable in strength to the total self-consistent potential, c) the total self-consistent potential is considerably deeper than the empirical starting potential because of the increased exchange potential. Also indicated in Fig. 62 are the occupied molecular one-electron energy levels σ_S at -1.0 ryd, σ_s^* at -0.64 ryd, σ_p at -0.39 ryd and π_p at -0.38 ryd.

2. Molecular Orbitals

In Fig. 63 we display charge density contours for the four occupied molecular levels. The charge density values are given in $2e/\Omega_c$ where $\Omega_c = 400\text{Å}^3$ is the unit cell volume. It should be emphasized at this point that these textbook-like molecular densities were calculated using a plane wave basis. The lowest level σ_S contains mostly s-like charge in a bonding-like configuration with its maximum between the two atoms. The next higher level σ_S^* has antibonding s-like character. Some admixture of p-states quantized along the molecular axis is present. The wavefunctions of the third occupied level are predominantly p-like at the two atoms and overlap forming a σ-type bonding state. The fourth (occupied) and fifth (empty) level are "quasi-degenerate." The wavefunctions are mostly p-like in character and form π-type bonding states. The σ_p^* and

π_p^* antibonding levels lie at higher energies and are unoccupied. Experimentally[129] the ground state is found to be a Σ triplet, which is reproduced in our model assuming triplet coupling of the π electrons (as expected from Hund's rules). The inclusion of spin-dependent correlation potentials would be necessary to a-priori distinguish between singlet and triplet states. The total charge density corresponding to the four occupied levels is presented in Fig. 64; the units of the indicated values are the same as in Fig. 63. Comparison of the above orbital energies (after adjustments for the zero of energy) with results using a Hertree-Fock basis yields good agreement.[130] The Hartree-Fock calculation gives the π_p state slightly lower than σ_p and hence a singlet ground state. This probably results from the configuration choice.

To obtain a measure for the amount of charge in the bond we proceed as in Ref. 21 and integrate the charge pile-up over a region defined by the outermost closed contour. The yields a value of $Z_B = 0.138$ (in units of e) which is within computational accuracy identical to the crystalline value of $Z_B = 0.125$.

In summary we note that this method should be particularly advantageous for complex and heavy molecules. Diatomic silicon was chosen as a test case because of the detailed knowledge available for the Si pseudopotential. The results we have presented are "preliminary"; however, they illustrate the potential of the method and the possible extensions. Hopefully the scheme can be extended to give accurate values of the total energy to allow calculations of equilibrium configurations, force constants and information about the geometry of molecular systems.

C. The Electronic Structure of a Metal Surface: Al (111) Surface

The first surface to be considered is that of a metal: the Al (111) surface. While self-consistent calculations exist for simple models, e.g. jellium,[131] and have recently been performed for sodium[132] and lithium,[127] as yet, no self-consistent calculations have been performed on polyvalent metals such as aluminum. This is unfortunate because in the previous cases surface states are not found below E_F and, therefore, cannot contribute to the self-consistency process. Surface states are not, of course, observed in jellium because they are specifically excluded by the free electron nature of the band structure, while in monovalent metals, which possess no band gaps below the fermi level,[133] the observed states lie above E_F. There is also the open question of conflicting calculations between Boudreaux,[134] and Caruthers, Kleinman and Alldredge[135] (CKA). Boudreaux used a step function potential for the transition between the bulk potential and the vacuum, while in the CKA calculation an aluminum bulk potential was merged smoothly into a jellium potential[131] at some arbitrary point near the surface. Neither calculation was performed in a self-consistent fashion. Boudreaux found surface states for the (111) surface to exist only at Γ; however, CKA found surface states at Γ, K and M. In order to account for these varying results CKA examined the effect of the two different potentials on the surface properties. They concluded that the differing potentials could not reconcile their calculation with that of Boudreaux and suggested an error had been made in his calculation.

However, CKA noted in the course of their study that the behavior in the transition region between vacuum and bulk was crucial in determining an accurate picture of the surface states, thus casting some doubt on the appropriateness of the matching scheme of jellium to bulk potentials. A self-consistent calculation, not suffering from such a defect is consequently of prime importance for an understanding of the surface of Al.

The method which we have employed in this calculation was presented in our molecular calculation and, therefore, will only briefly be outlined below. The crucial point is that we periodically repreat a slab of aluminum with a (111) surface exposed to vacuum on both sides. In this sense, we retain a periodic system and, hence the usual techniques of the pseudopotential method may be applied. Specifically, we have taken a twelve layer Al slab with a vacuum region of three interlayer distances for each surface over which the wavefunctions of the slab are allowed to decay. Thus, the method is somewhat similar to the technique of Alldredge and Kleinman[127] with the principle difference being that they have the additional requirement that each plane wave component of the wavefunction must vanish at the midpoint of the vacuum region between neighboring slabs. Thus our method allows the potential in the surface region to determine the decay of the wavefunctions into vacuum without this additional, and physically unnecessary, constraint.

Although we do not have a semi-infinite crystal, the experience of Alldredge and Kleinman[127] suggests very accurate results may be

obtained from thin films with reference to the semi-infinite case. The main problems which may arise from the use of thin films are a) an interaction of surface states on opposite sides of the film may lift a degeneracy which would occur if the film were infinitely thick, and b) the surface state wavefunctions decay so slowly into the slab that the film's thickness does not permit such states to be distinguishable from bulk states. However, for a dozen or more layers these are not insurmountable problems.

1. Self-Consistent Potential

As in the molecular case, we use a Heine-Animalu[17] core potential which is then screened in a self-consistent manner using the pseudocharge density. The form of the core potential is given by (41); the parameters were

$$a_1 = -0.5176 \qquad a_3 = -0.13389$$

$$a_2 = 1.0468 \qquad a_4 = -0.02944$$

The units are such that if q is given in atomic units, V(q) from (41) will be in Ry. This core potential is normalized to an atomic volume for the case of a slab twelve layers thick separated by three layers on either side from neighboring slabs. If this potential is screened, for bulk aluminum, it yields a band structure in good agreement with experiment.

The starting potential for the self-consistency process is given by (40). The parameters, normalized as the core potential, are given by

$a_1 = 0.41$ $\quad$ $a_3 = 0.65$

$a_2 = 1.88$ $\quad$ $a_4 = -0.3$

This potential agrees with the V(o) suggested by CKA,[135] and yields an accurate bulk Al band structure.

From this starting potential, a Hartee potential is desired from the calculated charge density[136] via Poisson's equation, and exchange potential of the Slater type added. Because the bare Al^{3+} ion potential diverges as $1/q^2$ for small wavevector q, the usual iteration procedure to obtain self-consistency is not practical.[127] However, the screening potential may be altered in a systematic fashion until the "input" screening potential and the "output" screening potential are in essential agreement.

In this manner we were able to achieve agreement to within one percent for the input and output potentials. For this accuracy the eigenvalues are stable to better than 0.02 Ry.

To determine the required screening potential an accurate fermi level must be calculated. This was accomplished by calculating the eigenvalues and eigenvectors over a grid of 294 points in the two dimensional Brillouin zone. The calculated value for E_F was 0.85 Ry above the conduction band minimum in good accord with the bulk value of 0.86 Ry.

We emphasize again the importance of self-consistency. If the total pseuodpotential is taken as a superposition of linearly screened atomic pseudopotentials a negative work function will

result.[135] This can be remedied by a superposition of atomic pseudopotentials which are constructed by extrapolating a smooth curve through points determined empirically from the bulk so that a proper work function results. However, this practice is deficient in two respects. First, the rise of the resulting potential from bulk to vacuum is unphysically abrupt and second, this procedure does not incorporate any response to the Friedel oscillations which are known to occur in the screening potential.[131] In Fig. 65 we indicate our resulting self-consistent potential averaged parallel to the surface and plotted as a function of distance into the slab. We note that over the last few layers this potential actually drops below the bulk potential by approximately 0.1 Ry. This is a result of the self-consistency process and does not occur for a superposition of atomic pseudopotentials. It has also been observed in the case of Li,[127] and it casts doubt on the CKA procedure of matching jellium to bulk potentials.

2. Work Function for the (111) Surface

Once the fermi level has been determined the work function (within the one-electron approximation). ϕ, can be evaluated from

$$\phi = V(\infty) - E_F$$

as indicated in Fig. 65.

The value of $V(\infty)$ is assumed in our calculation to be negligibly different from the value of the potential at the midpoint of the vacuum region between adjoining slabs. The calculated value is 0.38 Ry,

which unfortunately cannot be compared directly to the experimental value of 0.31 Ry available for polycrystalline Al.[137] In any event such a comparison is not of great value in judging the accuracy of a surface calculation as a uniform shift in the potential at large distances would alter ϕ, but not the resulting surface states. Considering the uncertainty involved with the polycrystalline value,[138] we consider the agreement as adequate.

3. Total and Surface State Pseudocharge Densities

In Fig. 65 we display our total charge density in the (110) plane, along with the averaged charge density plotted as a function of distance into the bulk. The calculated charge density is significantly perturbed from the bulk charge only outside the second surface layer of the aluminum ions. The charge deeper into the bulk is in good accord with the bulk density.[139] Although we use this pseudocharge density to screen the ions, the actual charge density should yield similar results except within the core regions and, thus, should provide an accurate screening potential. The averaged charge density, as in the jellium case,[131] exhibits the usual Friedel oscillations in the total charge near the surface. The maximum oscillation indicates a fluctuation of about 5% above the bulk; this is larger than in jellium for the equivalent density,[131] and in accord with the trend observed in Li.[127]

To determine the existence of surface states we have examined the charge density for all eigenvalues below E_F at high symmetry points in the two dimensional zone. In this context we make use of the projected bulk band structure provided by the CKA calculation.

It is, of course, within the "projected gaps" that bona fide surface states may exist.[133, 135] In particular, we are interested in those states below E_F which could be experimentally detected.

Our results indicate the existence of surface states below E_F at Γ and at K,[140] as mentioned, in agreement with the results of the CKA calculation, but not with that of Boudreaux. At Γ the surface state occurs at 0.33 Ry below E_F and at K we have two surface states at 0.15 Ry and 0.07 Ry below E_F.

The most localized surface state is the upper state at K at 0.07 Ry. In Fig. 66 we display the averaged charge (as in Fig. 65) and a contour plot for the charge in the (110) plane. This state occurs in a rather large energy gap in the projected band structure and its decay is more rapid than the other state at K at 0.15 Ry or the surface state at Γ. From the contour plot we see that the charge density of this state is localized in a "cavity" near the surface formed by the first and second atomic layers. Since this state occurs quite near E_F and is localized very strongly near the surface, it is expected to be chemically active.[135] The 0.15 Ry surface state at K is not as localized, and is quite sensitive to the surface potential. As with the 0.07 Ry state at K it has charge localized in the cavity region, but peaks further from the surface. Finally, the surface state at Γ, which occurs in the bulk band gap at L in the three dimensional zone, decays quite slowly falling only by 10% from the peak value at the surface to the mid-point of the slab.

D. The Electronic Structure of Semiconductor Surface

In this section the Si (111) surface, and the GaAs and ZnSe (110) surfaces will be investigated. Emphasis will be placed on the Si (111) surface. This surface has been extensively explored both experimentally and theoretically and, therefore, will provide an excellent basis upon which to evaluate our calculational techniques.

1. Si (111) Surface

The electronic structure of Si (111) surfaces has been investigated in a large number of experimental studies.[141-149] Most of the experiments have been done on surfaces having either (2 x 1) or (7 x 7) superlattice structures which are the metastable and stable surface arrangements of Si (111) respectively. Very useful results, however, have been obtained from theoretical studies on unreconstructed (1 x 1) surface models.[150, 151] In spite of the usefulness of these calculations only results obtained from realistic, reconstructed surface models are consistent with all the experimental data. Two unreconstructed (1 x 1) surface models (unrelaxed and relaxed) are investigated here before studying (for the first time by a self-consistent method) a realistic (2 x 1) reconstructed surface model. We note that self-consistency in the present context means the self-consistent electronic response to a given structural model. Even through calculations of this kind can and have been carried out for several structural models (unrelaxed, relaxed and (2 x 1) reconstructed in our case) it is extremely difficult if not impossible to compare total energies to determine the most favorable surface

structure arrangement. The reasons for this are two-fold, first it is known experimentally that the surface geometry is strongly temperature dependent, therefore free energies involving entropies must be compared. Secondly, the total surface energies are large quantities which differ only slightly for the different geometries. With the present techniques they cannot be calculated with sufficient precision to yield reliable results for the energy differences. The present calculations as well as all previously existing self-consistent calculations are therefore restricted to the self-consistent determination of the electronic structure in response to a given structural model.

The only other self-consistent approach to the (111) surface is Si has been presented by Appelbaum and Hamann[150] (AH) which like our approach is based on the pseudopotential scheme. For metal surfaces, pseudopotential calculations by (AH) for Na[132] and by Alldredge and Kleinman (AK) for Al[135] and Li[127] have been carried out very successfully. In addition to the specific problems connected with a self-consistent treatment, the main difficulty arises from the absence of periodicity in treating the surface case.

AH solve this problem by expanding the electron wavefunction in a mixed representation i.e. two-dimensional plane waves to account for the periodicity parallel to the surface multiplied by functions depending on the remaining spatial coordinate, z, perpendicular to the surface. In this mixed representation the Schrödinger equation becomes a set of coupled differential equations in the spatial

coordinate, z, which can be integrated stepwise numerically obeying appropriate boundary conditions between the vacuum and a matching plane somewhere in the crystal. Numerical problems and instabilities however, turn this physically appealing concept into a rather involved procedure.

AK also start with a mixed representation, however use a series of analytic trigonometric functions describing the z-variation of the wavefunction perpendicular to the surface. Retaining a finite number of these periodic functions is equivalent to periodically repeating the surface (or better the thin film). If these films are spaced sufficiently far enough apart from each other and if they are sufficiently thick, their surfaces can be regarded as non-interacting and representative of the true crystal surface. More precisely, AK expand the z-variation of the wavefunction in a truncated set of trigonometric sine and cosine functions which individually all vanish half way between the films. We believe that these specific boundary conditions, which are not strictly imposed by the physics of the system may result in slow convergence behavior since they add an artificial symmetry to the problem.

Our method in contrast to AK's approach uses a set of periodic, trigonometric functions with arbitrary rather than fixed phases.

Using this basis set our procedure is then completely equivalent to placing the film in a periodic array and expanding the wavefunction in plane waves in the usual form as for bulk calculations. The most appealing feature of the approach is that the pseudopotential

method in its simple standard form can now be applied. In particular, non-local potentials can easily be incorporated (which is not evident in AH's method) and experience e.g. about convergence of wavefunctions gained in calculations of bulk layer crystals[152] can be used. The method adopted for the present study of the electronic structure of Si (111) surfaces however goes beyond the standard EPM through the requirement of self-consistency.

The disadvantages and also the ultimate limitations of the method in dealing with complicated systems is connected to the large number of plane waves required to describe the systems' wavefunctions. The use of symmetry adapted combinations of plane waves is a helpful tool in dealing with this problem.

Although the method of our calculation has been outlined briefly before (for the case of Al surfaces), we shall discuss it in detail below with specific application to Si surfaces.

The essence of our method of calculation is to retain (artificial) periodicity perpendicular to the surface. In other words, a large elongated unit cell is defined which in two dimensions is spanned by the shortest lattice vectors parallel to the surface i.e. for the unreconstructed surface, hexagonal lattice vectors with the length of $\sqrt{2}/2\ a_c$, where $a_c = 5.43\text{Å}$ is the lattice constant of bulk Si (the 2 x 1 reconstructed case will be discussed later) and by a long c-axis extending over M atomic layers and N layers of empty space. The numbers M and N have to be chosen such that (a) the film of material is thick enough to effectively decouple the two

surfaces on each side of the film and (b) the film surface potential can decay into the "vacuum" without perturbation arising from other periodically displaced films. Various test calculations showed that films of M = 12 atomic layers separated by N ~4 layers of empty space resulting in a lattice constant $c = \frac{5}{2}\sqrt{3}\, a_c$ fulfill these requirements well for Si. The problem thus consists of self-consistently solving the electronic structure of a "periodic" system whose hexagonal unit cell with the above mentioned dimensions contains 12 Si atoms (for the unreconstructed surface). Proceeding in the standard manner we expand the electron wavefunction in plane waves with reciprocal lattice vectors, $\underset{\sim}{G}$:

$$\psi_{\underset{\sim}{k}}^{n}(\underset{\sim}{r}) = \sum_{\underset{\sim}{G}} a_{\underset{\sim}{k}}^{n}(\underset{\sim}{G}) e^{i(\underset{\sim}{k}+\underset{\sim}{G})\cdot\underset{\sim}{r}}$$

In order to account well for the "structure" in the large unit cell (i.e. the individual atoms or bonds) this expansion has to be carried to sufficiently high G-vectors. A kinetic energy cut-off $E_1 = |\underset{\sim}{G}_{max}|^2 \approx 2.7$ ryd, which is independent of the size of the unit cell was chosen in accordance with earlier bulk calculations[152] on layer crystals. This cutoff which corresponds to a cutoff close to (220) in cubic bulk Si, yields about 160-180 plane waves up to (0,0,12) which allow sufficient variation of the wavefunctions inside the unit cell and at the surface. The variations of the calculated total charge inside the film can be compared to bulk charge densities of Si calculated with much larger cut-off energies. Typical differences are of the order of 20% in the peak values of the charge distribution. To improve the energy convergence another

340 plane waves are included via Lowdin's perturbation scheme[3] which corresponds to a second cut-off at E_2 = 6.0 ryd.

It should be noted that the decay of the wavefunction into the vacuum region does not represent a particular problem in this context. In fact the wavefunctions at the surface decay into the vacuum over about the same length as do wavefunctions in the bulk of very covalent crystals (e.g. bulk Si or layer compounds) decay along certain (no-bond) directions. This can e.g. be inferred from the results of AH which, because they are obtained by real space integration at the surface, should be fully converged.

No group theoretical simplifications were incorporated into the present calculations, since it was desirable to solve Schrödinger's equation for general $\underset{\sim}{k}$-points in the two-dimensional (hexagonal) Brillouin zone. The only remaining symmetry operation which would leave these $\underset{\sim}{k}$-points invariant would be a reflection parallel to the surface plane which however is not present in the D_{3d} group of Si (111) films.

The expansion of the wavefunction leads to a matrix eigenvalue equation of the usual kind

$$\sum_{\underset{\sim}{G}'} (H_{\underset{\sim}{G},\underset{\sim}{G}'} - E\delta_{\underset{\sim}{G},\underset{\sim}{G}'})a_{\underset{\sim}{k}}(\underset{\sim}{G}') = 0 \qquad (42)$$

which is solved by standard methods.[3] The Hamiltonian matrix elements are of the form

$$H_{\underset{\sim}{G},\underset{\sim}{G}'} = |\underset{\sim}{k} + \underset{\sim}{G}|^2 \, \delta_{\underset{\sim}{G},\underset{\sim}{G}'} + V_{PS}(\underset{\sim}{G},\underset{\sim}{G}')$$

where $V_{PS}(\underset{\sim}{G},\underset{\sim}{G}')$ represents a general pseudopotential matrix elements.

The present calculation is restricted to a local pseudopotential. From our earlier results we know such an approach yields satisfactory results for bulk silicon. The self-consistency loop was initiated by an empirical potential as given by (40). The four parameters, a_i, required are given in Table L. These parameters were fixed by fitting (40) to the local form factors given in our discussion of bulk silicon.

Some continuous extrapolation of the kind as (40) is necessary to obtain form factors for the "new" G-vectors of the surface problem. While the shortest $\underset{\sim}{G}$-vector in bulk Si (111) has the length of 1.06 a.u., in the surface problem G-vectors as short as 0.14 a.u. are needed. The empirical potential is very uncertain at these small $\underset{\sim}{G}$-vectors and large changes are expected in the course of corresponding to these small $\underset{\sim}{G}$-vectors are absent in a bulk Si crystal. In the surface case they are important as they form the surfact potential barrier and strongly determine work functions and ionization potentials. The solutions of the secular equation given by (42) are the energies $E_n(\underset{\sim}{k})$ and determine the coefficients $A^n_{\underset{\sim}{k}}(\underset{\sim}{G})$ required for the wavefunction. These quantities were evaluated at k-points in the irreducible part (1/12) of the two-dimensional hexagonal Brillouin zone. This relatively large number of sampling points were chosen rather than one or several "special" $\underset{\sim}{k}$-points to precisely determine the fermi level and the total valence charge. The unreconstructed Si (111) surface is metallic since the fermi level falls within the "dangling bond" surface band. In this surface

band, occupied and unoccupied states differ in their electronic charge distributions which justifies the "fine" sampling of the Brillouin zone. In the case of "true" semiconducting surfaces as unreconstructed (110) zincblende surfaces or (2 x 1) reconstructed (111) Si surfaces, we believe calculations based on a few special $\underset{\sim}{k}$-points will yeild good self-consistent results. To determine the fermi level, the density of states, D(E) was evaluated using the method of Gilat and Dolling[153] with the necessary energy gradients derived by $\underset{\sim}{k}\cdot\underset{\sim}{p}$ techniques. Once the fermi level E_F was known the total valence (pseudo) charge density $\rho(\underset{\sim}{r})$ could be evaluated.

If valence charge density is expressed in terms of its Fourier components $\rho(\underset{\sim}{G})$, the Hartree-Fock type screening potentials V_H and V_X can easily be evaluated. V_H is the repulsive Coulomb potential seen by an electron and generated by all the valence electrons. It is defined by Poisson's equation

$$V_H(\underset{\sim}{r}) = -4\pi e^2 \rho(\underset{\sim}{r})$$

and it can be written as a Fourier series

$$V_H(\underset{\sim}{r}) = \sum_{\underset{\sim}{G}} V_H(\underset{\sim}{G}) e^{i\underset{\sim}{G}\cdot\underset{\sim}{r}}$$

with

$$V_H(\underset{\sim}{G}) = \frac{4\pi e^2 \rho(\underset{\sim}{G})}{|\underset{\sim}{G}|^2}$$

The divergence of $V_H(\underset{\sim}{G})$ for $|\underset{\sim}{G}| \to 0$ is physically irrelevant since it is exactly cancelled by the ionic potential generated by the positive Si^{+4} ion cores (overall charge neutrality). We can therefore arbitrarily set $V_H(\underset{\sim}{G} = 0) = V_{ion}(\underset{\sim}{G} = 0) = 0$. Numerically, however, the divergent character of $V_H(\underset{\sim}{G})$ (and $V_{ion}(\underset{\sim}{G})$) for small $\underset{\sim}{G}$-values poses stability problems as we shall discuss later. The non-local Hartree-Fock exchange potential, $V_X(\underset{\sim}{r},\underset{\sim}{r}')$, which if added to the Hartree potential $V_H(\underset{\sim}{r})$ cancels the electron self energy contained in $V_H(\underset{\sim}{r})$, has been approximated using the statistical exchange model of Slater.[154] It thus has the local form

$$V_X(\underset{\sim}{r}) = -\alpha 3e^2\left(\frac{3}{8\pi}\right)^{1/3}[\rho(\underset{\sim}{r})]^{1/3}$$

In the present calculations the value $\alpha = 0.79$ is used in accordance with AH which brings Slater's exchange in agreement with Wigner's[155] interpolation formula at the average valence charge density of Si. The function $[\rho(\underset{\sim}{r})]^{1/3}$ has been obtained by evaluating $\rho(\underset{\sim}{r}) = \sum_{\underset{\sim}{G}} \rho(\underset{\sim}{G})e^{i\underset{\sim}{G}\cdot\underset{\sim}{r}}$ at a three-dimensional grid of N ~ 10,000 $\underset{\sim}{r}$-points sampling the real space unit cell. The cube root has then been taken at each individual $\underset{\sim}{r}$-point and the resulting function $[\rho(\underset{\sim}{r})]^{1/3}$ has been transformed back into Fourier space according to

$$\rho^{1/3}(\underset{\sim}{G}) = \frac{1}{N}\sum_{\underset{\sim}{r}_i}^{N} [\rho(\underset{\sim}{r}_i)]^{1/3}e^{-i\underset{\sim}{G}\cdot\underset{\sim}{r}_i}.$$

The precision of this procedure can easily be tested by omitting the step at which the cube root of $\rho(\underset{\sim}{r}_i)$ is taken. The final $\rho(\underset{\sim}{G})$ should then be identical to the initial values. The exchange potential then

has the form

$$V_X(\underset{\sim}{r}) = -\alpha(\frac{3}{2\pi})\ e^2(3\pi^2)^{1/3} \sum_{\underset{\sim}{G}} \rho^{1/3}(\underset{\sim}{G})e^{i\underset{\sim}{G}\cdot\underset{\sim}{r}}$$

The exchange potential is an absolute potential which approaches zero in the vacuum as the charge goes to zero. $\rho^{1/3}(\underset{\sim}{G}=0)$ has a finite value and is essential in determining the absolute value of the potential. The sum of the two potentials $V_H(\underset{\sim}{r})$ and $V_X(\underset{\sim}{r})$ yields the electronic screening potential

$$V_{screen}(\underset{\sim}{r}) = \sum_{\underset{\sim}{G}} (V_H(\underset{\sim}{G})+V_X(\underset{\sim}{G}))e^{i\underset{\sim}{G}\cdot\underset{\sim}{r}}$$

and is, at each step in the self-consistent loop, evaluated from the total valence charge.

After initiating the calculations with an empirical potential the self-consistent loop is continued by adding the screening potential V_{screen} to an ionic potential V_{ion} generated by the Si^{+4} ionic cores. This ion pseudopotential contains in addition to the exchange α, the only parameters of the self-consistent calculation. First, there are the atomic positions in the surface which enter V_{ion} via a structure factor. In addition to the structural model, the individual atomic ionic potential is also based on a parametrized model. Assuming that the first order the ion cores do not change in the free ion, in the bulk crystal or in the surface, an atomic model potential which was fit to atomic term values (as done by Heine and Abarenkov[2]) has been used in our calculation. One important (but not sufficient) check on the quality of this potential is to use it to perform a self-consistent Si bulk calculation. This test is not sufficient,

since bulk calculations do not probe the long range Coulomb tail of ionic potentials. In the case of surfaces, however, this tail is of importance. On the other hand, the Coulomb tail is model independent and results in a $1/q^2$ behavior of the Fourier transformed potential for small wavevectors.

The repulsive cores of the ionic model potentials fitted by Heine and Abarenkov to atomic term values are non-local or ℓ-dependent. In the present calculation a local, "on Fermi sphere" approximation was used in deriving the Fourier transform. This Fourier transform was fitted to a four parameter curve of the form given by (41). The values of the parameters, a_i, for the ionic model potential are given in Table L. The ionic potential behaves as $1/q^2$ for small q representing the Coloumb tail and decreases exponentially for large q allowing a definition of a reasonable cutoff $q_c \approx 3$a.u. for Si^{4+}. As mentioned above, self-consistent Si bulk calculations based on this ionic pseudopotential yield a band structure in excellent agreement with the most recent empirical calculations. The most important electronic transition energies are reproduced to within ±0.1 eV. The total bulk valence charge derived from this self-consistent bulk calculation compares very favorably with the empirical charge densities of Walter and Cohen.[21] The values of charge densities in the bonds change from 25.5 to 25.8 electrons per unit cell and at the atomic sites from 7 to 5.5 which results from a more repulsive self-consistent potential at the atoms.

The input potentials for steps n = 1 and 2 of the self-consistent

loop then become

$$V_{in}^{(1)}(\underset{\sim}{r}) = V_{emp}(\underset{\sim}{r})$$

$$V_{in}^{(2)}(\underset{\sim}{r}) = V_{ion}(\underset{\sim}{r}) + V_{screen}^{(1)}(\underset{\sim}{r}) \qquad (43)$$

Note that, while $V_{emp}(\underset{\sim}{r})$ and $V_{ion}(\underset{\sim}{r})$ are linear super-positions of atomic potentials, all other potentials $V_{screen}^{(n)}$ and $V_{in}^{(n+1)}$ $(n \geq 1)$ are of a more general form and can no longer be factorized into strucutre factor times form factor. This fact accounts for the non-linear nature of the dielectric screening and results in the existence of "forbidden" reflections in the self-consistent potential.

Since the potential $V_{emp}(\underset{\sim}{r})$ was determined empirically for Si bulk crystals, it is not expected to yield a very good screening charge for a surface described by the ionic cores $V_{ion}(\underset{\sim}{r})$. In fact $V_{in}^{(2)}(\underset{\sim}{r})$ results in a very different eigenvalue spectrum and charge than does $V_{in}^{(1)}(\underset{\sim}{r})$ and any further steps in the self-consistent loop based on a straightforward extension of (43) would be unreasonable and not converge. This very unstable behavior of the self-consistent potentials in particular for the small $\underset{\sim}{G}$-vectors has already been described by Lang and Kohn[131] and by AK.[127] In agreement with these authors we also find that relaxed, modified versions of (43) which compute the input potential of stage (n+1) from a linear mixture of input and output potentials of stage (n) does not result in a convenient method to attain rapid convergence for the surface problem. In the present calculations these instabilities were dealt with by computing adjusted input potentials $V_{in}^{(n)}(\underset{\sim}{G})$ for $n > 2$ from

preceding input and output potentials individually for each small $\underset{\sim}{G}$-vector. This can best be done by inspecting V_{out} versus V_{in} graphs separately for each small $\underset{\sim}{G}$. Even though the various Fourier components are not independent, this procedure helps to reach convergence fairly rapidly. Mathematically the instabilities are reflected in rather steep curves (with negative slopes) of V_{out} versus V_{in}, i.e. very small changes in V_{in} result in large outshoots in V_{out}. For higher $\underset{\sim}{G}$-vectors, $|\underset{\sim}{G}| \geq$ 1a.u., no instabilities occur and convergence is easily reached. Because of the above mentioned instabilities and difficulties in determining long range potential fluctuations, work functions and ionization potentials are difficult to obtain correctly by our method.

a. Unreconstructed Surface. Clean unreconstructed Si (111) surfaces are known to be thermodynamically unstable below 900°C.[141] Stability can be reached at lower temperatures by adsorption of adatoms.[147] Nevertheless the clean unreconstructed surface presents an excellent model for the theoretical study of surface effects and results obtained for it can be compared to subsequent more elaborate (reconstructed) surface calculations. Our study of the Si (111) surface therefore starts with clean, unrelaxed, unreconstructed surface, in which all surface atoms remain at their exact "bulk" positions. In a second ("relaxed") model the outermost atomic layer was rigidly relaxed inwards by an amount of Δ = 0.33Å as proposed by AH.[150] In Fig. 67 the crystal structure of Si is viewed in perspective along the [110] direction. The [111] direction is vertical. A horizontal

(111) surface is obtained by cutting all vertical bonds in a plane.

An excellent overall impression of the behavior of the electronic states at the Si (111) surface can be obtained by considering the total, self-consistent valence charge distribution, as presented in Fig. 68 for the unrelaxed surface model. The figure shows charge density contours in a (110) plane cutting the (111) surface at right angles (see Fig. 67). The plotting area starts midway between two films and extends about 4 1/2 atomic layers into the bulk. The atomic (unrelaxed) positions are indicated by dots. Moving deeper into the crystal, the charge distribution closely resembles the Si bulk charge densities; near the surface, it decays rapidly into the "vacuum". This rapid decay assures the required "vacuum" and hence the decoupling of the films. No surface states can be recognized on this plot, since only a small number of them exists in a continuum of decaying bulk-like states. It is instructive to compare the charge distribution deeper inside the crystal to the standard, highly convergent Si bulk charge densities of Walter and Cohen.[21] These bulk charge densities which were derived from wavefunctions including about 90 planes waves up to $\underset{\sim}{G} = (331)\ 2\pi/a_c$ have values of 25.5, 7 and 11 electrons per bulk unit cell volume $\Omega = a_c^3/4$ for the bonding site, the atomic site and the antibonding site respectively. Due to the lower degree of convergence in the present surface calculations the charge density reaches values of 20, 9 and 12 at the respective sites. This lack of charge "modulation" which amounts to about 25% at the bonding sites results in an error in the exchange potential ($\sim\rho^{1/3}$) of at most 8% at the bonding sites.

We believe that this range of uncertainty in the potential or charge is acceptable and does not influence the results more than other conceptual uncertainties like the choice of the factor α scaling Slater's exchange potential. The total charge density can also be compared with results obtained by AH for a relaxed Si (111) surface.[150] (The outermost atomic layer has been relaxed inwards by 0.33Å.) Scaling their charge contour plot by the volume Ω the values 20, 3 and 10 (±2) are obtained for the respective sites. Their particularly low value at the atomic site might result from a stronger repulsive core potential.

In Fig. 69 contour plots are presented of the self-consistent pseudopotential giving rise to the valence charge discussed above and of the empirical starting potential. The potentials are displayed in the same plane as the charge in Fig. 68, with values given in rydbergs. Self-consistency was reached (within 0.01 Ry) after 5-7 steps. Normalized to approach zero in the vacuum the potential values for the self-consistent and empirical potentials are -1.8 (-1.8) at the bonding site, +0.8 (+0.1) at the atomic site and -1.6 (-1.0) at the antibonding site respectively. The self-consistent potential at the bonding sites differs slightly for the different bonds, thus causing some asymmetries in the bond charge distributions. Note the more repulsive core of the self-consistent potential resulting from the model ion potential used. As mentioned earlier, both potentials lead to very similar bulk energy spectra and charge densities. The self-consistent potential of AH for a relaxed surface model reaches values of around -2.2, >0.2 and

-1.6 at the bonding site, atomic site and antibonding site respectively. This is in good agreement with our self-consistent potential except possibly at the atomic site where the AH value is not explicitly given in Ref. 150.

To illustrate the various contributions to the total self-consistent potential in Fig. 70b, the potentials $V_{ion}(z)$, $V_H(z)$ and $V_X(z)$ averaged parallel to the surface are plotted as a function of the coordinate z perpendicular to the surface. Due to their strong long-range Coulomb character V_{ion} and V_H show only small short range fluctuations compared to their absolute values. V_{ion} rises about 30 rydbergs over the last six atomic layers and forms a strong surface barrier. It is very delicately balanced by the screening potential V_H leaving a weak attractive net potential with fluctuations on the scale of interatomic distances of the order of 0.5 rydbergs. Strictly specking only the sum of V_H and V_{ion} is physically meaningful; the individual potentials diverge as $|\underset{\sim}{G}|^{-2}_{min}$.

The sum is added to the exchange potential V_X which is of comparable strength and modulation. The resulting total self-consistent potential is indicated in Fig. 70a. In this figure the original empirical starting potential is superimposed to demonstrate the change in the potential occurring because of the self-consistency procedure. While inside the crystal the two potentials $V_{emp}(z)$ and $V_{SC}(z)$ are almost identical (the potential differences visible in Fig. 69 cancel almost exactly after averaging parallel to the surface), the self-consistent potential $V_{SC}(z)$ is somewhat deeper at the outermost atomic layer and exhibits a higher surface barrier

of about 0.2 Ry. These changes localize the charge more in the surface, stabilize the surface states and increase the ionization potential. In fact, using the empirical starting potential, charge originating from states at the top of the valence bands was leaking out into the "vacuum". This charge was confined back to the surface by the stronger potential obtained in course of self-consistency. Though the differences between the empirical and self-consistent surface potentials seem to be relatively small, they are essential to stabilize the surface. An ionization potential of about 4.0 eV has been calculated. As mentioned earlier this quantity is difficult to determine precisely with our method and the calculated value is only approximate (±1 eV).

Figure 71 displays the two-dimensional band structure of a twelve layer Si (111) film based on the self-consistent potential for the relaxed surface model. The band structure is presented for surface $\underset{\sim}{k}$-vector, $\underset{\sim}{k}_{||}$, between $\Gamma(0,0)$, $M(1/2,0)$, $K(1/3,1/3)$ and $\Gamma(0,0)$ in the hexagonal Brillouin zone. The 24 valence bands can be roughly divided into 3 bulk groups, representing the 6 low-lying s-like bands, 6 bands of mixed s- and p-character, 11 p-like bands and one separate p-like dangling-bond band in the fundamental gap. The three groups of bands, would with increasing film thickness approach continua separated by several gaps in which most of the surface states appear. Let us first discuss the dangling bond bands in the fundamental gap. Suppose a Si bulk crystal is cut every 12 layers parallel to the (111) plane and the pieces are gradually separated from each other. With increasing distance one

state each would split away from both the valence-bands and the conduction bands to meet about at half-gap to form the two fold degenerate dangling bond surface band corresponding to the broken bonds on either side of the Si films. In Fig. 71 the two bands are not exactly degenerate corresponding to some weak interaction (~0.2 eV) still present between opposite surfaces of the 12 layer films. If the surfaces are unrelaxed and unreconstructed the two dangling bond bands show almost no dispersion parallel to the surface, i.e. they would appear extremely flat in the band structure plot. If the outermost atomic layer is relaxed inward, the dangling bond band shows an increased dispersion parallel to the surface together with a slight overall shift of the bands (see Fig. 71). This effect shall be discussed later in more detail in relation to charge densities and densities of states. In contrast to the dangling bond surface band which exists throughout the two-dimensional Brillouin zone independent of relaxation, other surface states show up only in parts of the two-dimensional Brillouin zone and some depend on relaxation. They are indicated at the high symmetry points Γ, K and M by dots in Fig. 71. A region of particular interest is around the point K. Strongly localized surface states exist in the gap between -7 eV and -9 eV independent of surface relaxation. These states merge into the continuum at M and become strong surface resonances. A similar behavior is found around K between -2 eV and -4 eV. Even though the existence of these surface states does not depend upon relaxation, their exact energy position is a

function of relaxation. Other surface states appear only after relaxation like the splitting away of the lowest valence band pair between -9.5 eV and -12.5 eV throughout the zone. All these findings have qualitatively also been obtained in a recent analytical model calculation by Yndurain and Falicov.[156]

Comparison with a tight-binding surface band structure calculated by Pandey and Phillips[151] (PP) shows qualitative agreement, though quantitative differences exist in energy and number of surface states. In particular five surface states are found in our calculations at K which agrees with the calculations of Yndurain and Falicov whereas PP only report four surface states. The existence of more than four surface states at a given vector $\underset{\sim}{k}_{||}$ indicates that bonds deeper in the crystal, not connected to the outermost layer are strongly affected by the surface. The character of the various surface states will be discussed later in terms of charge density distributions.

Density of states curves for the self-consistent results for the unrelaxed and relaxed surface models are presented in Fig. 72. Since these curves represent the total density of states for a 12 layer slab, their overall features strongly resemble those of the Si bulk density of states. The results for the (2 x 1) reconstructed surface (insert) are obtained for a 6 layer slab. They shall be discussed in the next section together with 12 layer (2 x 1) reconstructed surface calculations. To locate structures associated with surface states (no distinction is made in the present case

between bona fide surface states and strong surface resonances), we investigated the charge density distributions for small energy intervals scanning the entire width of the valence bands. One problem which arises when simulating surfaces by finite slabs of atoms periodically repeated, is spurious structure in the denisty of states due to the "unreal" periodicity of isolated slabs perpendicular to the surfaces. Spurious two-dimensional singularities occur. Their number increases with the number of atomic layers per slab. For the "true" surface case these singularities become "dense" and disappear. For finite slab calculations all structures in the density of states have to be investigated in this spirit. Similar problems are encountered when simulating an amorphous material by large unit cells periodically repeated.[126] The locations of surface states and strong surface resonances (for the relaxed case) are indicated by arrows in Fig. 72. Their labelling corresponds to the regions around high symmetry $\underset{\sim}{k}$-points in the two-dimensional Brillouin zone, from which they originate (see dots and labelling in Fig. 71). The surface state energies are given in Table LI and compared to experimental data obtained from UPS measurements on (2 x 1) and (7 x 7) reconstructed surfaces. Also indicated in Table LI are the results of the self-consistent pseudo-potential calculation of AH and of the empirical tight-binding calculation of PP on unreconstructed relaxed Si (111) surfaces.

Let us now examine the various surface bands in more detail. When relaxing the outermost atomic layer rigidly inwards by an amount

of $\Delta = 0.33\text{Å}$, a surface band (2-fold quasi-degenerate in our model originating from the two surfaces of the slab) throughout the entire zone splits off between -11 eV and -13 eV. It essentially corresponds to s-like states with some P_z admixture (centered on the two outermost atomic layers) which decay into the crystal. A typical charge density plot of these surface states near Γ ($\Gamma_{\ell b}$) at about -12.7 eV is shown in Fig. 73 (top). As one follows this surface band from Γ to M to K the charge center moves somewhat back into the crystal, e.g. the charge distribution of the state K_b, at about -9.8 eV is mostly s-like on the second atomic layer with charge extending considerably into the "longitudinal" bond between second and third atomic layer. A similar situation is found at M for the state $M_{\ell b}$, at about -10.7 eV. At these two points (K and M) the predominant s-like charge on the outermost layer is transferred to the surface states $K_{\ell b}$ and $M_{\ell b}$ at somewhat higher energies around -8.5 eV. These states (in particular $K_{\ell b}$) are strongly localized on the outermost layer see Fig. 74 (bottom) and decay into the crystal being localized at every other layer (1,3,5 etc.). Roughly it can therefore be said that at K the state $K_{\ell b}$, at -9.8 eV has s-like charge on the second, fourth, etc. atomic layer, decaying into the bulk, whereas the state $K_{\ell b}$ at -8.5 eV has decaying s-like charge at the first, third, etc. atomic layer.

The next surface states or strong surface resonances appear only at considerably higher energy and they correspond to mostly p-like states with some s-admixture. Starting at Γ at -1.5 eV (Γ_{tb}) a

2-fold degenerate (4-fold in our case of two surfaces) surface band appears corresponding to the transverse back bonds between first and second atomic layer; its charge distribution is shown in Fig. 73 (bottom). This band merges into the continuum as one goes from Γ to M where it appears as a strong resonance. Again a region of special interest is at K. A very similar arrangement to the low lying s-states is found for the energies of the p-states. The bulk-like states merge into two narrow groups of bands separated by a ~2 eV gap (see Fig. 71). One surface state ($K_{\ell b'}$) is found inside this gap at about -2 eV. In contrast to the s-like surface state $K_{\ell b}$ at -8.5 eV this state does not appear midgap; a small potential perturbation might have moved this more sensitive p-like state slightly up towards the upper group of bulk-like bands. Another surface state (K_{tb}) splits off below the lower group of bulk-like bands at -4.2 eV. The resemblance between the s-like and p-like band structure at K and an inspection of the corresponding charge densities suggest very strong decoupling of s- and p-states at K. This kind of dehybridization decreases band dispersion, localizes states and favors the formation of surface states. In fact it is the special form of the structure factor at K which allows separation into s-states centered on even or odd numbered layers, longitudinal p-states and transverse p-states.[156] To support this statement further we note that the charge distribution for the state K_{tb} at -4.2 eV is almost identical to the charge of the states Γ_{tb} at -1.5 eV (see Fig. 73 bottom) and therefore has strong transverse character appearing between the first and second, third and

fourth etc. layer. The state $K_{b'}$ at -2.0 eV (see Fig. 74 top) is of longitudinal character, the charge appears in the longitudinal bonds between the second and third, fourth and fifth etc. layer, decaying into the crystal. decaying into the crystal. We would like to note that the behavior of surface states being localized at alternating atomic layers is not an artifact connected with the finite slab approximation; it has analytically been confirmed for semi-infinite surface models.[156]

In contrast to Γ where two transverse back bond states exist, at K only one such surface state appears, the other having merged into the continuum. Again the situation at M is similar to that at K, with smaller gaps, however, and surface states merging into the continuum. The preceding analysis showed clearly that surface states can "penetrate" deeply into the longitudinal bond between second and third layer which puts severe restrictions on the size of model clusters representing the surface and which has to be considered in positioning a matching plane as used by AH separating the surface region from the bulk. It can be inferred from Fig. 72 that inward relaxation strengthens the transverse back bonds and therefore lowers the energies of the states Γ_{tb} and K_{tb}. It weakens the longitudinal back bonds and raises the energy of states like $K_{\ell b'}$. These effects are also reflected in the total charge density. They shall be discussed again in connection with (2 x 1) reconstructed surface.

The most prominent surface states are the dangling bond states in the fundamental gap. In both the unrelaxed and relaxed cases, the surface bands are half occupied leaving the surface metallic with a Fermi level positioned as indicated in Figs. 71 and 72. A charge density plot for the occupied part of this band is presented in Fig. 75. The charge originates from states around M and K and exhibits the very pronounced dangling bond character. The unoccupied states originate from a region around and show some stronger mixing with back bond states. Though the comparative study of the unrelaxed and relaxed surfaces yields very useful information about the existence energy positions and energy shifts of surface states, these two surface models cannot satisfactorily explain a number of experiments. These experiments include various photoemission measurements[149] surface mobility studies,[141] photoconductivity[141] and infrared absorption measurements[144] on freshly cleaved Si (111) surfaces, exhibiting a (2 x 1) reconstruction. The most important experimental facts which cannot be explained involve the surface states in and close to the fundamental gap. To gain some understanding of the behavior of these states after (2 x 1) reconstruction and to find explanations for the various experimental results, we have done fully self-consistent calculations on a (2 x 1) reconstructed surface model. A detailed discussion of this surface model and the results obtained is given in the following section.

b. Reconstructed Surface. Carefully cleaved clean Si (111) surfaces

exhibit a (2 x 1) superstructure as seen from low energy electron diffraction (LEED) patterns. At the present time unfortunately there does not exist a satisfactory analysis of the LEED intensities which would uniquely determine the (2 x 1) surface geometry. Any calculation of the electronic structure of the (2 x 1) surface is therefore necessarily based on empirical structural models. The situation is complicated by the fact that the (2 x 1) reconstructed surface is metastable. It transforms into a more complex (7 x 7) structure upon annealing, which is the thermodynamically stable Si (111) surface geometry, or it transforms into the simple (1 x 1) structure after adsorption of adatoms. Once annealed or contaminated, (2 x 1) structure cannot be recovered. Due to this fact, models for the metastable (2 x 1) surface cannot easily be established on thermodynamical grounds. Various different reconstruction models have thus been suggested.[148] Most recent discussions seem to favor the formation of the (2 x 1) superstructure by periodically raising and lowering rows of surface atoms leaving a buckled surface. This model for reconstructed surfaces was first suggested in 1961 by Haneman[157] and later developed by Taloni and Haneman.[158] In addition to the periodic raising and lowering of rows of surface atoms, in Haneman's nodel, the second layer-atoms are slightly shifted laterally to approximately conserve the individual bond lengths of the transverse back bonds between first and second layer. The situation is schematically indicated in Fig. 76. Without the lateral shift of second layer atoms, transverse back bonds of different lengths would exist. This modified Haneman model has

recently been proposed by AH.[159] In their model calculations done on two differently relaxed (inward and outward) (1 x 1) surfaces, the main emphasis has been put on the existence of stretched and compressed back bonds. The subsequent discussion of our results obtained for a (2 x 1) Haneman model, however, will show that all essential experimental findings can be understood even if the lengths of the transverse back bonds are approximately conserved.

The structural parameters entering our (2 x 1) reconstructed surface model are the following: alternating rows of atoms have been raised by 0.18Å and lowered by 0.11Å , and second layer atoms have been shifted laterally as indicated by the arrows in Fig. 76 such as to approximately preserve the length of the back bonds. This choice of parameters may not represent an optimum choice. In particular, since these parameters represent an overall outward relaxation of the outermost atomic layer, some surface states which depend on inward relaxation like the states $\Gamma_{\ell b}$ at the bottom of the valence bands will become delocalized. Our main interest in this study however is the behavior of the electronic states in the vicinity of the gap and their dependence on the character of the reconstruction (buckling with preserving the length of back bonds). The planar unit cell now contains 4 atoms. First preliminary calculations have been done on six-layer slabs separated by 3 bond lengths of empty space. The corresponding density of states in the vicinity of the valence band edge, obtained from 72 $\underset{\sim}{k}$-points in the two-dimensional Brillouin zone is shown as an insert in Fig. 76.

As expected, qualitative changes compared to the unreconstructed (1 x 1) case occur. Doubling the real space unit cell in one dimension corresponds to folding back the Brillouin zone in certain directions. Thus two surface bands appear separated by a gap resulting from the potential perturbation of the reconstruction. This behavior is reflected by the density of states in Fig. 72 showing two peaks which now correspond to two different bands. In Fig. 72 the density of states does not vanish between the two peaks, thus leaving the surface semi-metallic. In fact the gap between the two surface bands is comparable or smaller than their dispersion. We believe that this behavior is an artifact of only including 6 layers per slab. The sufrace states on opposite surface of the slab show too much interaction, consequently causing the semimetallic behavior. To obtain more quantitative results (2 x 1) calculations with 12 layers per slab have been performed. Because of the large matrix size (about 320 plane waves were included to obtain the same convergence as for the unreconstructed cases), the self-consistent calculations were based on a two-point scheme ((0,0)Γ and (1/2,1/2)K'). For the final self-consistent potential several $\underset{\sim}{k}_{||}$-points along high symmetry directions have also been included. A band structure showing the bands in the vicinity of the fundamental gap is presented in Fig. 77. The two dangling bond surface bands are split by a gap of $\geqslant$ 0.27 eV throughout the zone. They show some dispersion of only about 0.2 eV. The Fermi-level falls between the two bands, thus creating a semi-conducting surface. To obtain a density of states curve for these bands a

four term Fourier expansion for the band energy $E(\underset{\sim}{k}_{||})$ has been fitted to the calculated band structure at the four $\underset{\sim}{k}_{||}$-points Γ, M', $\tilde{M}$ and K', and subsequently evaluated over a fine grid of $\underset{\sim}{k}_{||}$ -points of the two-dimensional Brillouin zone. The results are shown in Fig. 78 (bottom). Two structures are found separated by about 0.4 eV corresponding to the two surface bands. The lower surface band which overlaps with states arising from bulk and other surface bands is centered at about $E = E_V = 0$. Experimental photoemission data[142, 143] show structure at somewhat lower energy ($E \approx -0.5$ eV). Further lowering of the calculate surface band and better agreement with experiment can probably be obtained by using a different choice of atomic displacement parameters. Our results, however, show the definite trend of splitting the dangling bond surface bands combined with an overall lowering because of the buckling structure. Also indicated in Fig. 78 (top) is a joint density of states (JDS) for optical transitions between the lower and the upper surface bands. Matrix-element effects have not been considered in this plot. The JDS curve can be qualitatively compared to infrared absorption measurements[144] (broken line). A quantitative comparison is not reasonable because of the ad hoc choice of atomic displacement parameters and because of probable strong excitonic effects.

It is also instructive to calculate the charge denisty distributions for states inside the two peaks in the density of states of Fig. 78 (bottom). The corresponding charge (or hypothetical charge for the unoccupied upper band) is displayed in Fig. 79 in a (210)

plane intersecting the surface at right angle. This plane corresponds to the (110) plane of the unreconstructed surface. The buckling raises the surface atom on the left hand side and lowers the surface atom on the right hand side. Due to lateral shifts the second layer atoms are slightly moved out of the (210) plane. The states show very interesting real space behavior. Electrons in states originating form the lower peak labelled d_{out} are located predominantly on those atoms which have been raised and avoid those atoms which have been lowered. Conversely the wavefunctions for unoccupied states of the peak labelled d_{in} are concentrated around those atoms which have been lowered. The surface thus exhibits a (2 x 1) pattern of nearly two-fold occupied dangling bond states centered at every second row of atoms. Roughly speaking the unpaired dangling electron of every second surface atom (in) is transferred to its neighboring atom (out) where it paris up with another electron, thus creating an ionic semi-conducting surface. In view of this picture infrared transitions are expected to have a very weak oscillator strength because of the small wavefunction overlap. In fact, the calculated dipole matrix elements are of the order of $0.05\ 2\pi/a_c$ and about one order of magnitude smaller than average bulk matrix elements. However, the net charge transfer obtained in our calculation is presumably too large and would be decreased by correlation effects. These effects can be considerable for bands of 0.3 eV width; since they are not included in our calculations, the results are of a more qualitative nature. It can be seen from Fig. 79 that the charge distribution of the lower peak (d_{out}) extends somewhat into the back

bonds. This mixing of states happens around the Γ-point where the lower dangling bond band actually overlaps with lower lying back bond states. In fact some of the transverse back bond states (Γ_{tb}) found at -1.5 eV for the unreconstructed surface rise in energy upon reconstruction and fall between 0 and -0.8 eV. At $\underset{\sim}{k}_{||}$-points further away from the Γ-point (K',M',M) the dangling bond surface bands have very pure dangling bond character and do not show any noticable mixing with the back bonds which decrease in energy to about -3.5 eV. The existence of transverse back bonding surface states (or strong surface resonances) close to the valence band maximum may explain angular photoemission results[149] involving states between 0 and -1.4 eV. These results show a threefold rotational pattern as do the transverse back bonding states but the pure longitudinal dangling bond states do not. The results we obtained for the (2 x 1) reconstructed surface can be understood on the basis of simple chemical arguments. Since our calculations were based on Haneman's model which excludes bond length variations (such as AH propose in their model) the various changes in the electronic structure must in first order are caused by bond angle variations. This concept is not new, in fact Haneman's original model was designed on this basis.

The following discussion includes three different bonds and their respective energies i.e. the energies of a state whose charge are primarily concentrated in one of these bonds: the (longitudinal) dangling bonds d with energy ε_d, the transverse back bonds b_t (ε_t) between first and second atomic layer and the longitudinal back bonds $b_\ell(\varepsilon_\ell)$ between second and third atomic layer.

Let us consider the case of the raised outermost atom. In this case the bond angles between the longitudinal orbitals are the transverse orbitals are increased whereas the bond angles among the transverse orbitals are decreased. The ideal sp^3 hybridization is consequently changed in such a way as to increase the amount of s-like character in the longitudinal orbitals and of p-like character in the transverse orbitals. As a consequence the energy ε_d of the dangling bonds d is lowered due to an increased s-admixture. The transverse back bonds b_t now contain more p-character which raises their energy ε_t and weakens the bonds. The longitudinal back bonds like the dangling bonds contain more s-character which lowers their energy ε_ℓ and strengthens them. The inclusion of bond-length variations (AH model) would result in an additional stretching of the transverse back bonds b_t and a further weakening. In the case of the lowered outermost atom the bond angles change the opposite way causing a decrease of s-character in the longitudinal orbitals. The energy ε_d of the dangling bonds d is raised, the energy ε_t of the transverse back bonds b_t is lowered combined with a strengthening of the bonds (an additional bond length contraction would increase this effect) and the energy ε_ℓ of the longitudinal back bonds b is increased combined with a weakening of the bonds. Raising and lowering of alternating rows of atoms leads in first order to a combination of the above effects. The net effect on the longitudinal back bonds cannot be anticipated in this simple picture. The simple picture apparently underlies our self-consistent

pseudopotential results. It accounts for the following facts:

(a) the strengthening of the transverse back bonds and the weakening of the longitudinal back bonds in the relaxed (1 x 1) geometry. (Here the transverse back bonds have also been contracted.)

(b) the raising of the dangling bond energy ε_b at Γ in the relaxed (1 x 1) geometry.

(c) the more s-like character of the lower dangling bond band in the (2 x 1) geometry as compared to the upper more p_z-like dangling bond band. This can be recognized from the dangling bond charge having a different asymmetry around the outermost atoms in Fig. 79 (top and bottom).

(d) the localization of the lower occupied dangling bond orbitals on the raised atoms and of the higher unoccupied dangling bond orbitals on the raised atoms and of the higher unoccupied dangling bond orbitals on the lowered atoms in the (2 x 1) geometry.

(e) the raising of the transverse back bond energies ε_t up to about -0.5 eV at Γ and -3.5 at K' for back bonds connected to raised outermost atoms in the (2 x 1) geometry.

To summarize our silicon surface calculations, we have investigated three different surface models: and ideal, or unrelaxed surface, a relaxed surface and a reconstructed surface. The unrelaxed and relaxed surfaces have also been investigated by Appelbaum and Hamann[150] in the only previously existing self-consistent calculation. Their results are basically consistent with our calculations. In addition new types of surface states corresponding

to the longitudinal back bonds between the second and third atomic layer and found and complete density of states curces are presented. A buckled (2 x 1) surface model such as proposed by Haneman (with perserved back bond lengths) has been used to study the (2 x 1) reconstructed surface. The salient experimental results on (2 x 1) Si (111) surfaces can be understood on the basis of this model. Upon reconstruction the dangling bond band is split and lowered considerably in energy. The surface is found to be semiconducting producing a infrared absorption peak at low energies. Transverse back bonding surface states are found to be raised in energy and appear between 0 and -0.5 eV below the valence band edge at and above -3.5 eV at K'. These states may be the origin of the angular dependent photoemission results . The various effects are discussed on chemical grounds in terms of bond angle variations occurring with reconstruction. Changes in back bond lengths such as claimed by AH in a recent paper[159] to be <u>essential</u> are thus <u>not necessary</u> for a satisfactory explanation of spectroscopic data. The existence of bond length changes, however, cannot be ruled out on the basis of the existing results since both bond angle- and bond length variations seem to alter the electronic structure at the surface in a similar manner.

2. <u>GaAs (110) Surface</u>

In this section we continue our discussion of semiconductor surfaces by considering the electronic structure of the (110) GaAs surface. To our knowledge, this is the first self-consistent surface calculation for a zincblende material. Although our

structural model is for an unrelaxed surface, a comparison with recent experimental data exhibits excellent agreement for the energy spectrum of the dangling bond surface states. In addition to displaying the valence change density for these states, and the total charge density, we present a local density of states calculation. This latter function, which displays the density of states layer by layer, illustrates the relative decay into the bulk of the surface states.

The (110) surface is of natural interest in GaAs as this is the surface formed upon cleaving. The "surface" unit cell for GaAs (110) surface is displayed in Fig. 80. Low energy electron diffraction studies[160] have indicated that this surface does not reconstruct, but retains its primitive configuration. This, unfortunately, does not rule out a non-ideal surface such as a relaxed or "buckled" (1 x 1) surface which would yield a similar diffraction patterns. Experimentally, photoemission,[142, 161] partial yield photoemission,[162] energy loss spectroscopy,[163-165] band bending,[166] and ellipsometry[167] measurements have verified the existence of two surface states of an apparently dangling bond nature: one occupied surface state lying approximately 0.5 eV below the valence band maximum, the other, an empty surface state, 0.8 to 1.0 eV above the valence band maximum. Although the photoemission measurement[142] responsible for the positioning of the occupied surface state has been the subject of controversy[161, 164] the existence of an occupied state in this general region seems to be well accepted. The empty surface state, on the other hand,

has been measured by several different methods[162, 163, 166] with agreement between the various techniques. In fact, not only is the energy placement well established for this state, but its localization and angular momentum charcter have also been investigated.[163] Becuase energy loss experiments involving excitations from the d-core levels of As show no evidence of a loss peak corresponding to the empty surface state, it is felt that these states are localized primarily on the Ga atoms[163] (the occupied surface states then being associated primarily with As). Further, such experiments have yielded apparent selection rule effects indicating a primarily s-character for the Ga dangling-bond states.[163] The separation in energy of the Ga and As dangling bond states by an energy of the order of the bulk band gap has also been ascertained by ellipsometry measurements.[167]

The theoretical picture has lagged, regretably, behind these experimental advances. While self-consistent calculations on Si[150, 168] exist in good accord with the prominent experimental features, thus far only tight binding[169, 170] and "abrupt-potential" matching scheme[171] calculations have been performed on this surface. While the tight binding appraoch has provided quite useful,[151, 169, 170] it is deficient in several respects. The method is, of course, not self-consistent and thus the parameters which characterize the surface are usually obtained from bulk calculations via simplified assumptions which may not accurately reflect the actual situation at the surface. Also since the tight binding method parameterizes the surface problem by interaction parameters, wave functions are

not obtained. With regard to the abrupt potential model, while such a potential is quite unphysical, useful qualitative trends can be obtained with this appraoch.

In any event, while such calculations have yielded dangling bond surface states in approximate agreement with experiment, they do not agree among themselves with respect to the dispersion at the surface bands, or a precise placement for these bands.

The calculation was performed in a manner similar to the silicon surface. Our slab thickness was chosen to be eleven layers; the separation between neighboring slabs was taken to be eight layers.

The empirical and ionic potentials for GaAs are given in Table LII. Our final potential was self-consistent to within 0.01 Ry. In order to assume accurately converged wavefunctions to determine the screening potential, the basis set consisted of approximately 450 planes waves. Symmetrized waves were used to decompose the secular equation into two matrices approximately 225 x 225. An additional 500 waves were treated in an approximate fashion by a second order perturbation technique.[3] Becuase of the semiconducting nature of this surface we need only consider a few representative points to obtain a sufficiently accurate charge density. Twenty points in the two dimensional Brillouin zone were used for this purpose.

In Fig. 81 the total valence charge density for the (110) surface is displayed for the two types of surface atoms. We note in both figures, as was true for the case of Si,[150, 168]

the presence of a channel with essentially zero charge extending from vacuum to bulk. It has been suggested[150] that impurities or interstitials could migrate along such a channel. With respect to the bonding charge we note the surface perturbation is essentially healed to its bulk configuration by the third layer. An interesting, but not surprising, result is the localization of the dangling bond charge on the As rather than Ga atom. The stronger As potential is dominant in determining the bond shape and position, therefore, the removal of the Ga atom by the creation of a surface has relatively little effect on the bonding charge.

Although the charge is localized relatively more on the As as a whole, the surface appears not to be more ionic than the bulk. By examining the bonding charge as a function of distance from delocalization or weakening of the bond; however, the relative ratio of charge localized on the As with respect to Ga remains roughly the same.

In Fig. 82 the charge densities are displayed for the dangling bond surface states. The occupied surface state is localized on the As with the empty state localized on the Ga in agreement with experiment.[163] The As state is located in energy below the valence band maximum for the most part, but at the zone center it becomes quasi-degenerate with the valence band maximum. This type of energy dispersion is in agreement with the tight binding calculation of Ref. 170, but not that of Ref. 169 where the surface band minimum was found to occur at the zone center. That this band does not extend into the optical gap is of some interest, because while

the precise position of this state has been questioned, it appears to be well established[161] that it does not contribute significantly to the density of states in the bulk band gap region.

The charge density of the occupied state is of predominently p-character as can be observed from the two lobe configuration displayed in Fig. 82. This is to be contrasted with the Ga dangling bond states. Here the character is more s-like but retains some p-character as indicated by the small lobe-like feature opposite to the charge maximum. In fact, it has been suggested, as mentioned previously, that such a trend should be observed.[163]

In Fig. 83 we present the results of a local density of states (LDOS) calculation. Previously one of the advantages of the tight binding methods relative to the pseudopotential methods was the ease in which LDOS calculations can be performed. In the tight binding case[170] we may define the local density by

$$N_i(E) = \sum_{\substack{k_{||},n \\ j}} |\langle \psi_{\underset{\sim}{k}_{||},n} | \phi^i_{\underset{\sim}{k}_{||},j} \rangle|^2 \delta[E - E_n(\underset{\sim}{k}_{||})]$$

where $\underset{\sim}{k}_{||}$ is the wavevector parallel to the surface, n is the band index, $\psi_{\underset{\sim}{k}_{||},n}$ is the wavefunction of the total Hamiltonian and $\phi^i_{\underset{\sim}{k}_{||},j}$ is the jth Bloch function orbital centered on an atom i. Physically this can be interpreted as the probability an electron will be at the ith site with energy, E. Such a definition can easily be modified using pseudo wavefunctions to

$$N(E) = \sum_{\underset{\sim}{k}_{||},n} \int_{\Omega} |\psi_{\underset{\sim}{k}_{||},n}(\underset{\sim}{r})|^2 d^3\underset{\sim}{r}\,\delta[E-E_n(\underset{\sim}{k}_{||})] \tag{44}$$

The integral extends over the volume of interest, Ω. Thus $N_\Omega(E)$ can be interpreted as the probability an electron with energy, E, is in the region Ω.

In order to ascertain the LDOS defined by (44) as a function of distance from vacuum to bulk, we have chosen to be bound by planes parallel to the surface and passing through the mid-point between layers. Thus "Layer 1" of Fig. 83 corresponds to integrating all charge within one-half an interlayer distance on both sides of the surface atoms. Five points in the irreducible zone went into the make-up of the histograms. Accordingly 220 eigenvalues went into the valence band portion of the figure.

The positions of four prominent surface states are indicated by the shaded areas in Fig. 83. These surface features have been observed previously in tight binding LDOS calculations[170] with the energy positions in approximate agreement with our results. However, there are some weak surface features near -2 eV which are observed in our calculation via a charge density analysis, but are not observed in the tight binding calculation.

The approximate energy positions of the surface features with respect to the top of the valence band are listed in Table LIII. These features may be classified by the character of their charge density. The deepest lying surface state is localized on the As and has s-like character. The next surface feature, on the high energy side of the antisymmetric gap, is localized on the Ga and also has s-character. Near the top of the valence band are three distinct types of surface states which are p-like and localized mostly on the As. These surface features are "back" bonds with charge localized between the first and second surface layers, "parallel" bonds with charge localized along the bonding direction between neighboring surface atoms, and "dangling" bonds localized on the cut bond formed by the creation of the surface (as in Fig. 82). The "parallel" and "dangling" bond surface states are nearly degenerate in energy, although the dangling band feature is must stronger in the LDOS figure. In the next section on ZnSe illustrations of the parallel and back bond surface states will be presented. The states in the gap, as mentioned, are predominantly localized along

the dangling bond, and centered on the Ga.

Finally, with regards to Fig. 82 we note the finite width of the histogram means both bulk and surface contributions can be included in the same energy interval. Nevertheless, the major features are quite clear, and the decay of the surface features can be easily discerned. In no case has the surface perturbation not decayed to less than a quarter of its value from the first to third layer in the LDOS plot. We note by the fifth layer the general features of the LDOS curve are in good agreement with the known bulk spectrum.[12] This confirms our use of only eleven layers in the repeated slab.

3. ZnSe (110) Surface

Although the ZnSe (110) surface has not been studied experimentally to the extent GaAs has been, it allows us to describe trends with ionicity and to examine the surface states present in II-VI compounds.

The details of the ZnSe surface calculation are identical to the GaAs surface calculation with the exception, of course, of the ionic potentials. The empirical and ion core potentials used for ZnSe are listed in Table LIV.

A total charge denisty for the ZnSe surface is presented in Fig. 84. The planes displayed are as in the GaAs calculation. The obvious difference from GaAs is the greater charge transfer present in ZnSe. This is to be expected by a comparison with the bulk charge densities. There are some noticeable differences due to surface properties in ZnSe. The surface perturbation appears to heal more rapidly in ZnSe than GaAs. The only difference

between the Se ions on the surface and deep in the bulk is a slight decrease of charge on the Se surface ions. A similar effect is found for the Zn ions. A comparison of the charge density for local pseudopotential[21] calculations for ZnSe with the charge away from the surface is quite satisfactory. Although our convergence criteria is slightly less than ZnSe bulk calculations, the difference between the "bulk" charges is typically less than 20%. Such a discrepancy existed in the Si surface calculation.

In Fig. 85 a LDOS curve is presented for the ZnSe surface. Away from the surface layers the density of states appears quite similar to bulk ZnSe calculations. While the local pseudopotential apporach yields valence band widths too narrow compared to experiment (see the ZnSe bulk section), we should be able to determine accurate trends for the ZnSe surface. Figure 85 also shows the much more rapid decay of surface states in the "antisymmetric" and fundamental gaps of ZnSe compared to the GaAs surface. Similar surface features occur for the ZnSe surface as compared with GaAs. In Table LV we list the surface states for ZnSe and their approximate positions with respect to the bulk valence band maximum.

The lowest lying surface state is localized on Se and is displayed in Fig. 86. The charge density is localized completely on the Se and is obviously s-like. The state, unlike the corresponding GaAs state, has split away form the bottom valence band (creating nearly 2 eV gap between the surface state and valence band). Unfortunately, the Zn 3d core states lie in this energy region and,

therefore, experimental election of the Se s-like surface state would be difficult.

In Fig. 87 the a Zn-Se "mixed" surface state is displayed. It is less well defined than the Se state and is localized somewhat on the Zn ion. Unlike GaAs, it lies almost 1.5 eV above the second valence band edge (well into the bulk valence density of state). Such a trend can be understood by considering the weakening of the Zn potential compared to Ga. Not only has the weakened Zn potential led to a higher energy placement for this state, but also the Zn dangling bond state.

In Figs. 88, 89 and 90 we display the charge densities for the "back", "parallel" and "dangling" bonds localized on Se. In constrast to GaAs, these states are very strong in the LDOS curve. Specifically, the Se back bonds are well defined. The parallel and dangling bonds show more dispersion then the corresponding states in GaAs and are more extended into the fundamental gap than in GaAs. As the potential strengthens it is to be expected that differences between the parallel and dangling bond states should be larger and consequently the splitting between become larger.

Finally in Fig. 91 we have displayed the charge density for the dangling bond surface states localized on the Zn. The splitting of Zn and Se dangling bond states has increased considerably compared to GaAs. This is to be expected; with increasing ionicity the surface states become more disimilar and the energy gap between them increases.

Table I. Parameters used in the calculations.

Si	Form Factors (Ryd)			A_0	$\partial A_0/\partial E$	a
	$V(\sqrt{3})$	$V(\sqrt{8})$	$V(\sqrt{11})$	(Ryd)		(A^o)
Local	-0.2241	0.0551	0.0724	--	--	5.43
Energy Dependent Non-local	-0.257	-0.040	0.033	0.55	0.32	5.43

Table II. Eigenvalues (in eV) at Γ, X, L symmetry points for local and energy dependent non-local pseudopotential calculations for silicon.

Point	Level	Local	Energy Dependent Non-local
Γ	Γ_1	-12.53	-12.36
	$\Gamma_{25'}$	0.00	0.00
	Γ_{15}	3.43	3.42
	$\Gamma_{2'}$	4.17	4.10
	Γ_1	8.60	7.69
	$\Gamma_{12'}$	7.82	8.19
X	X_1	-8.27	-7.69
	X_4	-2.99	-2.86
	X_1	1.22	1.17
L	L_2	-10.17	-9.55
	L_1	-7.24	-6.96
	$L_{3'}$	-1.22	-1.23
	L_1	2.15	2.23
	L_3	4.00	4.34

Table III. Sum rules from Eq. (37) for $\varepsilon_{0,G}$ and $\varepsilon_{G,G'}$ in units of $(eV)^2$ in the limit $q \to 0$ along the $\hat{x}$-direction.

$(\frac{a}{2\pi})G$	$(\frac{a}{2\pi})G'$	$\int \omega \mathrm{Im}\, \varepsilon_{G,G'} d\omega$	$\frac{\pi}{2}\omega_p^2 \left[\frac{\rho(G-G')}{\rho(0)}\right] \hat{e}(q+G)\cdot\hat{e}(q+G')$
(000)	(000)	415.6	433.5
(111)	(111)	431.6	433.5
(200)	(200)	430.1	433.5
(220)	(220)	403.2	433.5
(311)	(311)	311.8	433.5
(222)	(222)	278.4	433.5
(000)	(111)	-50.9	-54.7
(000)	(200)	0.0	0.0
(000)	(220)	11.5	10.3
(000)	(311)	21.6	20.2
(000)	(131)	7.2	6.7
(000)	(222)	15.5	15.0

Table IV. Theoretical and experimental reflectivity structure and their identifications including location in the Brillouin zone, energy (in eV) and symmetry of the calculated critical points for Si.

Reflectivity Structure				Associated Critical Points		Symmetry		Critical Point Energy	
Theory		Experiment		Location in the Brillouin Zone		of CP			
Local	Non-local	5°K[a]	80°K[b]	Local	Non-local	Local	Non-local	Local	Non-local
3.48	3.49	3.40	3.36	$L_3'-L_1$	$L_3'-L$	M_0	M_0	3.37	3.46
		3.45	3.41	$\Gamma_{25}'-\Gamma_{15}$	$\Gamma_{25}'-\Gamma_{15}$	M_0	M_0	3.43	3.42
				Near (0.1,0.02,0.02)	Near (0.1,0.05,0.05)	M_0	M_0	3.46	3.42
3.75	3.70	3.66	(3.88)[c]	Vol. along Δ	Vol. along Δ	--	--	--	--
4.26	4.15	4.30	4.38	Vol. near (.9,.1,.1)	Vol. near (.9,.1,.1)	--	--	--	--
4.53	5.47	4.57	4.57	Large region near (.5,.25,.25) and $\Sigma_4-\Sigma_1$	Large region near (.6,.3,.3) and $\Sigma_4-\Sigma_1$	M_2	M_2	4.53	4.47
						M_2	M_2	4.49	4.60
				L_3-L_3'	L_3-L_3'	M_0	M_2	5.22	5.56
5.32	5.58	5.48	--	$\Lambda_3-\Lambda_3'$,(.4,.4,.4)	$\Lambda_3-\Lambda_3'$,(.45,.45,.45)	M_1	M_3	5.25	5.57

a) From Ref. 47.

b) From Ref. 48.

c) Inferred from $\varepsilon_2(\omega)$ data of Ref. 48.

Table V. Comparison of critical point energies (in eV) for Ge as calculated by local and energy dependent non-local pseudopotentials and as measured by photoemission experiments.

Energy Level	Theory		Experiment
	Local	Non-local	
$\Gamma_{12'}$	8.60↓	8.19	8.3 ± 0.1[a]
Γ_1	7.82↑	7.69	7.6[a]
$\Gamma_{2'}$	4.17	4.10	4.15 ± 0.05[a]
Γ_1	-12.53	-12.36	-12.4 ± 0.6,[b] -12.5 ± 0.6[c]
X_4	-2.99	-2.86	-2.9,[a] -2.5 ± 0.3[c]
Σ_1^{min}	-4.48	-4.47	-4.4,[a] -4.7 ± 0.3[b,c]
L_3	4.00	4.34	3.9 ± 0.1[a]
$L_{3'}$	-1.22	-1.23	-1.2 ± 0.2[a]
L_1	-7.24	-6.96	-6.4 ± 0.4,[b] -6.8 ± 0.2[c]
$L_{2'}$	-10.17	-9.55	-9.3 ± 0.4[c]

a. From Ref. 63.

b. From Ref. 6.

c. From Ref. 4.

Table VI. Cyclotron mass parameters (see text) and conduction band minimum masses compared to the theoretical values from a local and energy dependent non-local pseudopotential. The magnitude and position of the indirect gap along the Δ direction is also given.

Ge	Experiment	Theory	
		Local	Non-local
F'	-5.04[a]	-5.11	-5.07
H'	-4.53[a]	-4.49	-4.23
G'	-0.87[a]	-0.88	-0.89
$m_0/m_{c\perp}$	5.25[b]	5.15	5.31
$m_0/m_{c\parallel}$	1.09[b]	1.21	1.18
$ak_{min}/2\pi$	0.86[c]	~0.85	~0.85
E_{ind}	1.15[d]	1.13	1.05

a) From J.C. Hensel as listed in Ref. 69.

b) See Ref. 70.

c) See Ref. 71.

d) See Ref. 72.

Table VII. Fourier coefficients of the valence pseudocharge density (units of e/Ω_c) as calculated by local and energy dependent non-local pseudopotentials for Si.

$\underset{\sim}{G}(a/2\pi)$	Local	Non-local
000	8.00	8.00
111	-1.748	-1.924
220	0.270	0.035
311	0.412	0.345
222	0.481	0.467
400	0.206	0.273
331	0.018	0.015
422	-0.006	-0.033
333	-0.001	-0.032
511	-0.004	-0.022
440	0.007	0.002

Table.VIII. Parameters used for Ge. A gaussian non-local d-well was employed.

Form Factors (Ry)			A_2	a
V(√3)	V(√8)	V(√11)	(Ry)	(Å)
-.221	.019	.056	0.275	5.65

Spin-orbit parameter: $\mu = 0.00097$

Table IX. Ge eigenvalues in eV at Γ, X and L symmetry points. The symmetry labels are from Ref. 23.

Γ_6^v	-12.66	X_5^v	-8.65	L_6^v	-10.39
Γ_7^v	-0.29	X_5^v	-3.29	L_6^v	-7.61
Γ_8^v	0.00	X_5^c	1.16	L_6^v	-1.63
Γ_7^c	0.90			$L_4^v+L_5^v$	-1.43
Γ_6^c	3.01			L_6^c	0.76
Γ_8^c	3.22			L_6^c	4.16
				$L_4^c+L_5^c$	4.25

Table X. Theoretical and experimental reflectivity structure at 5°K for Ge (from Ref. 90), and their identifications, including the location in the Brillouin zone, energy and symmetry of the calculated critical points.

Reflectivity Structure (eV)		Associated Critical Points Location in Zone	Symmetry	Critical Point Energy (eV)
Theory	Experiment			
2.20	2.22	$L_6^v - L_6^c$ (0.5,0.5,0.5)	M_1	2.19
2.40	2.42	$L_{4,5}^v - L_6^v$	M_1	2.39
3.3	3.20	$\Gamma_{25}^v - \Gamma_{15}^c$ complex (0.0,0.0,0.0)	M_o	3.25
4.51	4.5	Region near (0.75,0.25,0.25)	--	--
5.40	5.65	$\Delta_6^v - \Delta_6^c$ (0.5,0.,0.)	M_1	5.40
		$\Delta_7^v - \Delta_6^c$		5.35
5.88	5.88	$L_{4,5}^v - L_{4,5}^c$ (0.5,0.5,0.5)	M_1	5.88
		$L_6^v - L_6^c$	M_1	5.60

Table XI. Comparison of theoretical and experimental transitions for Ge.

Transition	Experiment (eV)	Theory (eV)
$\Gamma_1 - \Gamma_{25'}$	12.6 ± 0.3[a], 12.8 ± 0.4[b]	12.56
$L_2 - \Gamma_{25'}$	10.6 ± 0.4[a], 10.5 ± 0.4[b]	10.30
$L_1 - \Gamma_{25'}$	7.7 ± 0.2[a], 7.4 ± 0.2[b]	7.52
$\Sigma_1^{min} - \Gamma_{25'}$	4.5 ± 0.2[a], 4.5 ± 0.3[b]	4.55
$L_{3'} - \Gamma_{25'}$	1.4 ± 0.2[c]	1.44
$\Gamma_{25'} - \Gamma_2$,	0.98[d]	0.99
$\Gamma_{25'} - \Gamma_{15}$	3.24[e]	3.25
$\Gamma_{25'} - L_1$	0.87[f]	0.85
$25' - X_1$	1.2[g]	1.25
$25' - L_3$	4.3[c]	4.30

a. See Ref. 6.

b. See Ref. 5 and Ref. 12.

c. See Ref. 63.

d. See Ref. 92.

e. See Ref. 84.

f. See Ref. 93.

g. See Ref. 88.

Table XII. Comparison of the theoretically determined interband mass, m_{ij}, from (39) and the experimental results of Ref. 84. Absolute values of the masses are tabulated; the notation is from Ref. 84.

Ge Transition	Interband Masses: Mass Component (field [110])	Expt. Value[a] (in m_e)	Theor. Value[b] (m_{ij})
E_o	μ_{hh}, $\hat{e}[1\bar{1}0]$	0.0366 ± 0.013	0.022
$E_o+\Delta_o$	μ_{so}	0.0269	
E_1	μ_T	0.045 ± 0.004	0.050
$E_1+\Delta_1$	μ_T	0.042 ± 0.005	
E_o'	μ, $\hat{e}[001]$	0.034 ± 0.005	0.047[c]
$E_o'+\Delta_o'$	μ,$\hat{e}[1\bar{1}0]$	0.048 ± 0.009	
$E_o'+\Delta_o'+\Delta_o$	μ,$\hat{e}[001]$	0.062 ± 0.006	
E_2	μ_T(?)	0.139 0.015	0.11

a. See Ref. 84.

b. Spin-orbit interactions have not been included.

c. The E_o' interband mass is from $\Gamma_{25}'-\Gamma_{15}$.

Table XIII. Parameters used for GaAs. A gaussian non-local d-well was employed.

	Local Form Factors (Ry)			
	$V(\sqrt{3})$	$V(\sqrt{4})$	$V(\sqrt{8})$	$V(\sqrt{11})$
V^S	-.214	--	0.014	0.067
V^A	0.055	0.038	--	0.001

Lattice Constant: 5.65Å

Spin-orbit parameters: $\mu = 0.0078$

$\alpha = 1.377$

Non-local Well Depths: A_2 (Ga) = 0.125 Ry

A_2 (As) = 0.625 Ry

Table XIV. GaAs eigenvalues in eV at Γ, X, and L symmetry points.

Γ_6^v	-12.55	X_6^v	-9.83	L_6^v	-10.60
Γ_7^v	-0.35	X_6^v	-6.88	L_6^v	-6.83
Γ_8^v	0.00	X_6^v	-2.99	L_6^v	-1.42
Γ_6^c	1.51	X_7^v	-2.89	$L_{4,5}^v$	-1.20
Γ_7^c	4.55	X_6^c	2.03	L_6^c	1.82
Γ_8^c	4.71	X_7^c	2.38	$L_{4,5}^c$	5.52

Table XV. Theoretical and experimental reflectivity structure for GaAs at 5°K (from Ref. 90), and their identifications, including the location in the Brillouin zone, energy and symmetry of the calculated critical points.

Reflectivity Structure (eV)		Associated Critical points, Location in The Zone	Symmetry	Critical Point Energy (eV)
Theory	Experiment			
3.03	3.02	$L_{4,5}^{v}-L_{6}^{c}$ (0.5,0.5,0.5)	M_1	3.03
3.25	3.25	$L_{6}^{v}-L_{6}^{c}$	M_1	3.25
4.55	4.44	$\Delta_{5}^{v}-\Delta_{5}^{c}$ (0.1,0.0,0.0)	M_1	4.54
4.70	4.64	$\Delta_{5}^{v}-\Delta_{5}^{c}$		4.70
5.13	5.11	Plateau near (0.75,0.25,0.25)	--	5.07
5.59	5.64	$X_{7}^{v}-X_{7}^{c}$ (1.0,0.0,0.0)	M_o	5.28
		$X_{6}^{v}-X_{7}^{c}$		
5.84	5.91	$\Delta_{5}^{v}-\Delta_{5}^{c}$ (0.55,0.0,0.0)	M_1	5.76
6.7	6.6[a]	$L_{4,5}^{v}-L_{4,5}^{c}$	M_1	6.67
		$L_{4,5}^{v}-L_{4,5}^{c}$		6.74

a. From Ref. 45.

Table XVI. Comparison of theoretical and experimental critical point energies for GaAs. Energies in eV.

Transition	Experiment		Theory		
	Reflectivity Structure	Critical[d] Point	Non-local EPM	Local[c] EPM	OPW[e]
E_o $\Gamma_8^v-\Gamma_6^c$	1.52[a]	1.52	1.51	1.52	1.34
$E_o+\Delta_o$ $\Gamma_7^v-\Gamma_6^c$	1.86[b]	1.86	1.86	1.87	1.66
E_1 $L_{4,5}^v-L_6^c$	3.02[c]	3.04	3.03	2.82	2.62
$E_1+\Delta_1$ $L_6^v-L_6^c$	3.25[c]	3.25	3.25	3.05	2.82
$E_o'(\Gamma)$ $\Gamma_8^v-\Gamma_7^c$	--	4.49	4.54	4.80	4.12
$E_o'+\Delta_o'$ $\Gamma_8^v-\Gamma_8^v$	--	4.66	4.71	4.93	4.30
$E_o'+\Delta_o+\Delta_o'$ $\Gamma_7^v-\Gamma_8^c$	--	5.01	5.05	5.28	4.62
$E_o'(\Delta)$ $\Delta_5^v-\Delta_5^c$	4.44[c]	4.53	4.54	4.38	--
$E_o'+\Delta_o'(\Delta)$ $\Delta_5^v-\Delta_5^c$	4.64[c]	4.71	4.70	4.55	--
Σ	5.11[c]	5.14	5.07	4.88	--
$X_7^v-X_6^c$	--	4.94	4.92	4.40	4.33
$X_6^v-X_6^c$	--	5.01	5.01	4.49	4.52
$X_7^v-X_7^c$	5.64[c]	5.34	5.28	4.67	4.58
$X_6^v-X_7^c$		5.42	5.38	4.76	4.67

a. From Ref. 97.
b. From Ref. 98.
c. From Ref. 47.
d. From Ref. 94.
e. From Ref. 99.

Table XVII. Transitions in GaAs: experimental and theoretical results. (Energies in eV).

Transition	Photoemission		Theory		
	UPS[a]	XPS[b]	Non-local EPM	local[c] EPM	OPW[d]
$L_3^v - \Gamma_{15}^v$	0.8±0.2	1.4±0.3	1.31	0.85	1.06
$\Sigma_1^{min} - \Gamma_{15}^v$	4.1±0.2	4.4±0.2	4.23	3.35	--
$X_1^v - \Gamma_{15}^v$	6.9±0.2	7.1±0.2	6.88	6.23	6.43
$X_3^v - \Gamma_{15}^v$	10.0±0.2	10.7±0.3	9.87	10.00	10.24
$\Gamma_1^v - \Gamma_{15}^v$	12.9±0.5	13.8±0.4	12.10	12.10	12.44

Transition	Experiment[e]	Non-local EPM
$\Gamma_1^c - X_1^c$	0.38	0.52
$\Gamma_{15}^v - X_1^c$	1.7	2.16
$L_1^c - X_1^c$	0.09±0.02	0.20
$\Gamma_{15}^v - X_3^c$	2.3	2.51

a. See Ref. 101.

b. See Ref. 102.

c. See Ref. 47.

d. See Ref. 99.

e. See Ref. 100.

Table XVIII. Parameters used for ZnSe. A Gaussian non-local d-well was employed.

	Local Form Factors (Ry)			
	$V(\sqrt{3})$	$V(\sqrt{4})$	$V(\sqrt{8})$	$V(\sqrt{11})$
V^S	-.218	--	0.0287	0.0642
V^A	0.139	.0621	--	0.0157

Lattic Constant: 5.65Å

Spin-orbit Parameters: $\mu = 0.0061$

$\alpha = 1.90$

Non-local Well Depths: $A_2(Zn) = {}^{-}0.125$ Ry

$A_2(Se) = {}^{+}0.925$ Ry

Table XIX. ZnSe eigenvalues in eV at Γ, X and L symmetry points.

Γ_6^v	-12.25	X_6^v	-10.72	L_6^v	-11.08
Γ_7^v	-0.45	X_6^v	-4.96	L_6^v	-5.08
Γ_8^v	0.00	X_6^v	-2.17	L_6^v	-1.04
Γ_6^c	2.76	X_7^v	-1.96	$L_{4,5}^v$	-0.76
Γ_7^c	7.33	X_6^c	4.54	L_6^c	3.96
Γ_8^c	7.42	X_7^c	5.17	L_6^c	7.68
				$L_{4,5}^c$	7.72

Table XX. Theoretical and experimental reflectivity structure at 300°K and their identifications, including the location in the Brillouin zone, energy and symmetry of the calculated critical points for ZnSe. The experimental results are from Ref. 26.

Reflectivity Structure (eV)		Associated Transitions Located in the Zone	Symmetry	Critical Point Energy (eV)
4.79	4.75	$L_{4,5}^{v}-L_{6}^{c}$ (0.5,0.5,0.5)	M_1	4.72
5.06	5.05	$L_{6}^{v}-L_{6}^{c}$	M_1	5.00
--	6.00	--	--	--
(6.6)[a]	6.50	$\Delta_{5}^{v}-\Delta_{5}^{c}$ (0.5,0.0,0.0)	M_0	6.55
6.71	6.63	Plateau near (0.8,0.2,0.2)	--	6.69
7.22	7.15	$\Delta_{5}^{v}-\Delta_{5}^{c}$ (0.6,0.0,0.0)	M_1	7.08
7.47	7.60	$\Gamma_{8}^{v}-\Gamma_{8}^{c}$ (0.0,0.0,0.0)	M_0	7.42
7.76	7.80	$\Gamma_{7}^{v}-\Gamma_{8}^{c}$	M_0	7.87
8.39	8.45	$L_{4,5}^{v}-L_{4,5}^{c},L_{6}^{c}$ (0.5,0.5,0.5)	M_0	8.46
		$\Lambda_{4,5}-\Lambda_{4,5},\Lambda_{6}^{c}$ (0.35,0.35,0.35)	M_1	8.48
8.86	8.97	$L_{6}^{v}-L_{4,5},L_{6}^{c}$ (0.5,0.5,0.5)	M_0	8.74
		$\Lambda_{6}^{v}-\Lambda_{4,5},\Lambda_{6}^{c}$ (0.35,0.35,0.35)	M_1	8.76

a. See text.

Table XXI. Comparison of theoretical and experimental features in the electronic density of states. The energies are measured in eV and are with respect to the valence band maximum.

Feature	Experiment		Theory
ZnSe	XPS[a]	UPS[b]	
L_3^v	1.3 ± 0.3	0.7 ± 0.2	1.0
X_5^v	2.1 ± 0.3	---	2.2
Σ_1^{min}	3.4 ± 0.2	3.4 ± 0.3	3.4
L_2^v	5.6 ± 0.3	5.3 ± 0.3	5.1
X_1^v	12.5 ± 0.4	---	10.7
Γ_1^v	15.2 ± 0.6	---	12.3

a. See Ref. 102.

b. See Ref. 101.

Table XXII. Parameters used for α-Sn. Square-well non-local potentials were used.

Local Form Factors (Ry)		
$V(\sqrt{3})$	$V(\sqrt{8})$	$V(\sqrt{11})$
-0.190	-0.008	+.040

Lattice Constant: 6.49Å

Spin-orbit parameter: $\mu = 0.00225$

Non-local Well Depthes: $\partial A_o/\partial E = +0.40$

$A_2 = 0.70$ Ry

Table XXIII. α-Sn eigenvalues at Γ, X, and L symmetry points. Energies in eV.

Γ_6^c	-11.34	X_5^v	-7.88	L_6^v	-9.44
Γ_{7v}	-0.80	X_5^v	-2.75	L_6^v	-6.60
Γ_7^v	-0.42	X_5^c	0.90	L_6^v	-1.68
Γ_8^{v-c}	0.00			$L_{4,5}^v$	-1.20
Γ_6^c	2.08			L_6^c	0.14
Γ_8^c	2.66			L_6^c	3.48
				$L_{4,5}^c$	3.77

Table XXIV. Theoretical and experimental reflectivity structure for α-Sn and their identifications, including the location in the Brillouin zone, energy and symmetry of the calculated critical points.

Reflectivity Structure (eV)			Associated Critical Points Location in Zone	Symmetry	Critical Point Energy (eV)
Theory	Experiment (a)	(b)			
1.34	1.365	1.365	L_6^v-$L_{4,5}^c$(0.5,0.5,0.5)	M_1	1.34
1.83	1.832	1.845	L_6^v-L_6^c	M_1	1.83
2.31	--	2.28	Γ_8^v-Γ_6^c (0.0,0.0,0.0)	M_0	2.08
2.67	2.62	2.63	Γ_8^v-Γ_8^c	M_0	2.66
2.95	2.85	--	Δ_7^v-Δ_6^c (0.2,0.0,0.0)	M_1	2.91
3.40	3.3	3.3	Γ_7^v-Γ_8^c	M_0	3.46
3.78	3.75	3.718	Plateau near (0.75,0.25,0.25)	--	--
4.2	4.0	4.12	Δ_6^v-Δ_7^c (0.6,0.0,0.0)	M_1	4.13
4.31	4.43	4.43	Δ_7^v-Δ_7^c	M_1	4.25
4.91	4.89	4.89	$L_{4,5}^v$-L_6^c	M_1	4.68

a. Reflectivity measurement from Ref. 107

b. Electroreflectence measurement from Ref. 108 and 109.

Table XXV. Transitions in α-Sn: Experimental and theoretical results. (Energies in eV)

Transition	Non-local EPM	OPW[a]	Experiment
Γ_7^v-$\Gamma_8^{c,v}$	0.42	0.14	0.4[b]
L_6^c-$\Gamma_8^{c,v}$	0.14	0.32	0.1[c]
$L_{4,5}^v$-$\Gamma_8^{c,v}$	1.20	1.43	(1.5)[d]
Σ_1^{min}-$\Gamma_8^{c,v}$	3.32	--	(3.5)[d]
$L_6^v(L_1)$-$\Gamma_8^{c,v}$	6.60	6.17	(6.5)[d]
$L_6^v(L_{2'})$-$\Gamma_8^{c,v}$	9.44	8.92	(9.0)[d]
Γ_6^v-Γ_8^c	11.34	10.49	(11.5)[d]

a. See Ref. 109.

b. See Ref. 107.

c. See Ref. 106.

d. See Text

Table XXVI. Parameters used for InSb. Square-well non-local potentials were employed in the calculation.

	Local Form Factors (Ry)			
	$V(\sqrt{3})$	$V(\sqrt{4})$	$V(\sqrt{8})$	$V(\sqrt{11})$
V^S	-0.200	--	-0.010	0.044
V^A	0.044	0.030	--	0.015

Lattice Constant: 6.47Å

Spin-orbit parameters: μ = 0.00175Å

α = 1.206

Non-local well Depths

	A_2(Ry)	$\partial A_o/2E$
In	0.55	0.45
Sb	0.70	0.48

Table XXVII. InSb eigenvalues in eV at Γ, X and L symmetry points.

Γ_6^v	-11.71	X_6^v	-9.20	L_6^v	-9.95
Γ_7^v	-0.82	X_6^v	-6.43	L_6^v	-5.92
Γ_8^v	0.00	X_6^v	-2.45	L_6^v	-1.44
Γ_6^c	0.25	X_7^v	-2.24	$L_{4,5}^v$	-0.96
Γ_7^c	3.16	X_6^c	1.71	L_6^v	1.03
Γ_8^c	3.59	X_7^c	1.83	L_6^c	4.30
				$L_{4,5}^c$	4.53

Table XXVIII. Theoretical and experimental reflectivity structure for InSb and their identifications, including the location in the Brillouin zone, energy and symmetry of the calculated critical points.

Reflectivity Structure (eV)		Associated Critical Points Location in Zone		Symmetry	Critical Points Energy (eV)
Theory	Experiment[a]				
1.99	1.98	$L_{4,5}^{v}-L_{6}^{c}$	(0.5,0.5,0.5)	M_1	1.99
2.47	2.48	$L_{6}^{v}-L_{6}^{c}$		M_1	2.47
3.53	3.39	$\Gamma_{8}^{v}-\Gamma_{7}^{c}$	(0.0,0.0,0.0)	M_0	3.16
3.80	3.78	$\Gamma_{8}^{v}-\Gamma_{8}^{c}$		M_0	3.59
		$\Delta_{5}^{v}-\Delta_{5}^{c}$	(0.3,0.0,0.0)	M_1	3.3
				M_o	3.7
4.18	4.23	Plateu near	(0.7,0.2,0.2)	--	4.05
4.54	4.56	$\Delta_{5}^{v}-\Delta_{5}^{c}$	(0.5,0.0,0.0)	M_1	4.44
4.74	4.75			M_1	4.69
5.44	5.33	$L_{4}^{v}-L_{6}^{c}$	(0.5,0.5,0.5)	M_1	5.26
6.16	5.96	$L_{6}^{v}-L_{4,5}^{c}$	(0.5,0.5,0.5)	M_1	5.97

A. See Ref. 90.

Table XXIX. Comparison of theoretical and experimental features in the electronic density of states. The energies are in eV and are with respect to the valence band maximum.

Feature	Experiment		Theory
InSb	XPS[a]	UPS[b]	
L_3^v	1.4 ± 0.3	1.05 ± 0.3	1.0
X_5^v	2.4 ± 0.4	---	2.3
Σ_1^{min}	3.4 ± 0.2	3.65 ± 0.3	3.4
X_3^v	6.4 ± 0.2	6.5 ± 0.3	6.4
X_1^v	9.5 ± 0.2	9.0 ± 0.3	9.2
Γ_1^v	11.7 ± 0.3	11.2 ± 0.5	11.7

a. See Ref. 102.

b. See Ref. 101

Table XXX. Parameters used for CdTe. A square-well correction term involving non-local s and d angular momentum components was employed.

	Local Form Factors (Ry)			
	$V(\sqrt{3})$	$V(\sqrt{4})$	$V(\sqrt{8})$	$V(\sqrt{11})$
V^S	-0.220	--	0.000	0.062
V^A	0.060	0.050	--	0.025

Lattice Constant: 6.48Å

Spin-orbit parameters: $\mu = 0.00137$

$\alpha = 1.6418$

Non-local Well Depths

	A_2(Ry)	$\partial A_0/\partial E$
Cd	0.00	0.40
Te	2.00	0.40

Table XXXI. CdTe eigenvalues in eV at Γ, X and L symmetry points.

Γ_6^v	-11.07	X_6^v	-9.12	L_6^v	-9.64
Γ_7^v	-0.89	X_6^v	-5.05	L_6^v	-4.73
Γ_8^v	0.00	X_6^v	-1.98	L_6^v	-1.18
Γ_6^c	1.59	X_7^v	-1.60	$L_{4,5}^v$	-0.65
Γ_7^c	5.36	X_6^c	3.48	L_6^c	2.82
Γ_8^c	5.61	X_7^c	3.95	L_6^c	6.18
				$L_{4,5}^c$	6.35

Table XXXII. Theoretical and experimental reflectivity structure for CdTe and their identifications, including the location in the Brillouin zone, energy and symmetry of the calculated critical points. The experiment is from Ref. 118.

Reflectivity Structure (eV)		Associated Critical Points Location in zone		Critical Point Energy (eV)
Theory	Experiment			
1.65	1.59	$\Gamma_8^v - \Gamma_7^c$ (0.0,0.0,0.0)	M_0	1.59
3.49	3.46	$L_{4,5}^v - L_6^c$ (0.5,0.5,0.5)	M_1	3.47
4.04	4.03	$L_6^v - L_6^c$	M_1	4.00
5.16	5.18	$\Delta_5^v - \Delta_5^c$ (0.5,0.0,0.0)	M_0	5.14
5.50	5.53	Plateau near (0.75,0.25,0.25)	--	5.45
5.68	5.68	$\Delta_5^v - \Delta_5^c$ (0.75,0.0,0.0)	M_1	5.58
5.00	5.95	$\Delta_5^v - \Delta_5^c$	M_1	5.96
6.91	6.82	$L_{4,5}^v - L_6^c$ (0.5,0.5,0.5)	M_1	6.83
--	7.44			
7.79	7.6	$L_6^v - L_{4,5}^c$ (0.5,0.5,0.5)	M_1	7.53

Table XXXIII. Comparison of theoretical and experimental features in The electronic density of states. The energies are measured in eV and are with respect to the valence band maximum.

Feature	Experiment		Theory
CdTe	XPS[a]	UPS[b]	
L_3^v	0.9 ± 0.3	0.7 ± 0.2	0.9
X_5^v	1.8 ± 0.2	---	1.7
Σ_1^{min}	2.7 ± 0.3	2.8 ± 0.2	2.7
X_3^v	5.1 ± 0.2	4.7 ± 0.2	5.2
X_1^v	---	8.8 ± 0.3	9.1
Γ_1^v	---	---	11.1

a. See Ref. 102.

b. See Ref. 101.

Table XXXIV. Parameters used for GaP. Non-local square well correction terms were employed.

Local Form Factors (Ry)

	$V(\sqrt{3})$	$V(\sqrt{4})$	$V(\sqrt{8})$	$V(\sqrt{11})$
V^S	-0.230	--	0.020	0.057
V^A	0.100	0.070	--	0.025

Lattice Constant: 5.45Å

Non-local Well Depths

	$A_2(R_y)$	$A_0(R_y)$	$\partial A_0/\partial E$
Ga	0.40	--	0.30
P	0.45	0.32	0.05

Table XXXV. Eigenvalues in eV for GaP at the symmetry points Γ, X and L.

Γ_1^v	-12.99	X_1^v	-9.46	L_1^v	-10.60
Γ_{15}^v	0.00	X_3^v	-7.07	L_2^v	-6.84
Γ_1^c	2.88	X_5^v	-2.73	L_3^v	-1.10
Γ_{15}^c	5.24	X_1^c	2.16	L_1^c	2.79
		X_3^c	2.71	L_3^c	5.74

Table XXXVI. Identification of transitions responsible for the prominent theoretical and experimental reflectivity structure in GaP, including location in the Brillouin zone, energy and symmetry for calculated critical points. The experimental results are from Ref. 119 for 5°K.

Reflectivity Structure (eV)		Location in Brillouin zone	Symmetry	Critical Energy (eV)
Theory	Experimental			
2.95	2.89[a]	$\Gamma_{15}^{v}-\Gamma_{1}^{c}$ (0.0,0.0,0.0)	M_0	2.88
	2.97			
3.89	3.79	$L_{3}^{v}-L_{1}^{c}$ (0.5,0.5,0.5)	M_1	3.89
4.95	4.80	$\Delta_{5}^{v}-\Delta_{1}^{c}$ (0.7,0.0,0)	M_1	4.91
5.24	5.19	$\Gamma_{15}^{v}-\Gamma_{15}^{c}$ (0.0,0.0,0.0)	--	5.24
5.45	5.42	Plateau near (0.6,0.2,0.2)	--	5.41
6.8	6.7[b]	$L_{3}^{v}-L_{3}^{c}$(0.5,0.5,0.5)	M_1	6.84

a. Spin-orbit splitting (not included in the calculation).

b. From Ref. 100.

Table XXXVII. Transitions in GaP. Energies are in eV.

Transition	Experiment				Theory
	UPS[a]		XPS[b]		
$L_3^v-\Gamma_{15}^v$	0.8	0.2	1.2	0.3	1.1
$X_5^v-\Gamma_{15}^v$	--		2.7	0.2	2.7
$\Sigma_1^{min}-\Gamma_{15}^v$	4.1	0.2	4.0	0.3	4.2
$X_3^v-\Gamma_{15}^v$	6.9	0.2	6.9	0.3	7.1
$X_1^v-\Gamma_{15}^v$	9.7	0.3	9.6	0.3	9.5
$\Gamma_1^v-\Gamma_{15}^v$	11.8	0.5	13.2	0.4	13.0
$\Gamma_{15}^v-X_1^c$		2.34[c]			2.16
$X_1^c-X_3^c$		0.3[c]			0.5
$\Gamma_{15}^c-\Gamma_{12}^c$		10[c]			10.5
$\Gamma_{15}^v-\Gamma_1^c$		2.8[d]			2.8
$\Gamma_{15}^v-\Gamma_{15}^c$		5.0[d]			5.2

a. See Ref. 101.

b. See Ref. 102.

c. See Ref. 100.

d. See Ref. 63.

Table XXXVIII. Parameters used for GaSb. Non-local square well correction terms were used.

	Local Form Factors (Ry)			
	$V(\sqrt{3})$	$V(\sqrt{4})$	$V(\sqrt{8})$	$V(\sqrt{11})$
V^S	-0.220	--	0.005	0.045
V^A	0.040	0.030	--	0.000

Lattice Constant: 6.10Å

Spin-orbit Parameters: $\mu = 0.00113$

$\alpha = 2.217$

	Non-local Well Depths	
	A_2(Ry)	$\partial A_0/\partial E$
Ga	0.20	0.20
Sb	0.60	0.30

Table XXXIX. Eigenvalues for GaSb in eV at the symmetry points Γ, X and L

Γ_6^v	-12.00	X_6^v	-9.33	L_6^v	-10.17
Γ_7^v	-0.76	X_6^v	-6.76	L_6^v	-6.25
Γ_8^v	0.00	X_6^v	-2.61	L_6^v	-1.45
Γ_6^c	0.86	X_7^v	-2.37	$L_{4,5}^v$	-1.00
Γ_7^c	3.44	X_6^c	1.72	L_6^c	1.22
Γ_8^c	3.77	X_7^c	1.79	L_6^c	4.43
				$L_{4,5}^c$	4.59

Table XL. Identification of transitions responsible for the prominent theoretical and experimental reflectivity structure in Ga Sb, including local in the Brillouin zone, energy and symmetry of calculated critical points. The experimental results are from Ref. 90.

Reflectivity Structure (eV)		Location in the Brillouin zone	Symmetry	Critical Points Energy (eV)
Theory	Experiment			
2.22	2.15	$L^v_{4,5}$-L^c_6 (0.5,0.5,0.5)	M_1	2.22
2.86	2.60	L^v_6-L^c_6	M_1	2.67
3.3	3.35	Γ^v_8-Γ^c_7 (0.0,0.0,0.0)	M_0	3.44
3.76	3.69	Γ^v_8-Γ^c_8 (0.0,0.0,0.0)	M_0	3.77
4.37	4.35	Plateau near (0.7,0.2,0.2)	--	
4.84	4.75	Δ^v_5-Δ^c_5 (0.6,0.0,0.0)	M_1	4.84
5.13	5.07	Δ^v_5-Δ^c_5	M_1	5.12
5.65	5.65	$L^v_{4,5}$-L^c_6 (0.5,0.5,0.5)	M_1	5.43

Table XLI. Theoretical and experimental valence and conduction band features. Energies are in eV and measured from the valence band maximum.

Feature	Experiment	Theory
GaSb		
L_3^v	1.3 ± 0.2[a]	1.2
X_5^v	2.7 ± 0.2[a]	2.5
Σ_1^{min}	3.8 ± 0.2[a]	3.6
X_3^v	6.9 ± 0.3[a]	6.8
X_1^v	9.4 ± 0.2[a]	9.3
Γ_1^v	11.6 ± 0.3[a]	12.0
Γ_{15}^c	3.4[b]	3.6
X_1^c	~1.7[b]	1.7

a. See Ref. 102.

b. See Ref. 63.

Table XLII. Parameters used for InP. Non-local square well correction terms were employed.

Local Form Factors (R_y)

	$V(\sqrt{3})$	$V(\sqrt{4})$	$V(\sqrt{8})$	$V(\sqrt{11})$
V^S	-0.235	--	0.000	0.053
V^A	0.080	0.060	--	0.030

Lattice Constant: 5.86Å

Spin-orbit parameter: $\mu = 0.002$

$\alpha = 0.160$

Non-local Well Depths

	$A_0(R_y)$	$\frac{\partial A_0}{\partial E}$	$A_2(R_y)$
In	--	0.25	0.55
P	0.30	0.05	0.35

Table XLIII. Calculated eigenvalues for InP for the symmetry point Γ, X and L. Energies in eV.

Γ_6^v -11.42	X_6^v -8.91	L_6^6 -9.67
Γ_7^v -0.21	X_6^v -6.01	L_6^v -5.84
Γ_8^v -0.00	X_6^v -2.09	L_6^v -1.09
Γ_6^c 1.50	X_7^v -2.06	$L_{4,5}^v$ -0.94
Γ_8^c 4.64	X_6^c 2.44	L_6^v 2.19
Γ_8^c 4.92	X_7^c 2.97	L_6^c 5.58
		$L_{4,5}^v$ 5.70

Table XLIV. Identification of transitions responsible for the prominent theoretical and experimental reflectiveity structure in InP, including location in the Brillouin zone, energy and symmetry of calculated critical points. The experimental results are from Ref. 119 (except as noted).

Reflectivity Structure (eV)		Location in the Brillouin zone	Symmetry	Critical Point Energy (eV)
Theory	Experiment			
1.50	1.42	Γ_8^v-Γ_6^c (0.0,0.0,0.0)	M_0	1.50
3.13	3.24	$L_{4,5}^v$-L_6^c (0.5,0.5,0.5)	M_1	3.13
3.28	3.38	L_6^v-L_6^c		3.28
4.76	4.78	Γ_8^v-Γ_7^c (0.0,0.0,0.0.)	M_0	4.64
		Δ_5^v-Δ_5^c (0.2,0.0,0.0)	M_1	4.80
5.05	5.10	Plateau near (0.75,0.25,0.25)	--	5.00
5.44	5.25[a]	Γ_7^v-Γ_8^c (0.0,0.0,0.0)	M_0	5.13
5.73	5.77	Δ_5^v-Δ_5^c (0.7,0.0,0.0)	M_1	5.62
6.55	6.57[a]	$L_{4,5}^v$-L_6^c (0.5,0.5,0.5)	M_1	6.52

a. From Ref. 111.

Table XLV. Theoretical and experimental valence band features. Energies are in eV and measured from the valence band maximum.

Feature	Experiment	Theory
InP	XPS[a]	
L_3^v	1.0 ± 0.3	1.0
X_5^v	2.0 ± 0.2	2.1
Σ_1^{min}	3.2 ± 0.2	3.3
X_3^v	5.9 ± 0.2	6.0
X_1^v	8.9 ± 0.3	8.9
Γ_1^v	11.0 ± 0.4	11.4

a. See Ref. 102.

Table XLVI. Parameters used for InAs. Non-local square well corretion terms were employed.

Local From Factors (Ry)

	V(√3)	V(√4)	V(√8)	V(√11)
V^S	-.230	--	0.000	0.045
V^A	0.055	0.045	--	0.010

Lattice Constant: 6.05Å

Spin-orbit parameters: $\mu = 0.00117$

$\alpha = 0.795$

Non-local Well Depths

	A_2(Ry)	$\partial A_0/\partial E$
In	0.50	0.35
As	1.00	0.25

Table XLVII. Calculated eigenvalues for InAs for the symmetry points Γ, X and L. Energies in eV.

Γ_6^v	-12.69	X_6^v	-10.20	L_6^v	-10.92
Γ_7^v	-0.43	X_6^v	-6.64	L_6^v	-6.23
Γ_8^v	0.00	X_6^v	-2.47	L_6^v	-1.26
Γ_6^c	0.37	X_7^v	-2.37	$L_{4,5}^v$	-1.00
Γ_7^c	4.39	X_6^c	2.28	L_6^c	1.53
Γ_8^c	4.63	X_7^c	2.66	L_6^c	5.42
				$L_{4,5}^c$	5.55

Table XLVIII. Identification of transitors responsible for the prominent theoretical and experimental reflectivity structure in InAs, including location in the Brillouin zone, energy and symmetry of calculated critical points. The experimental results are from Ref. 90 (except as noted).

Reflectivity Structure (eV)		Location in the Brillouin Zone		Symmetry	Critical Point Energy (eV)
Theory	Experiment				
2.54	2.61	$L^v_{4,5}$-L^c_6	(0.5,0.5,0.5)	M_1	2.53
2.81	2.88	L^v_6-L^c_6		M_1	2.79
4.3	4.39	Γ^v_8-Γ^c_7	(0.0,0.0,0.0)	M_0	4.39
4.52	4.58	Γ^v_8-Γ^c_8		M_0	4.63
4.85	4.74	Plateau near (0.75,0.25,0,25)		--	
5.36	5.31	Δ^v_5-Δ^c_5	(0.7,0.0,0.0)	M_1	5.24
5.45	5.5	Δ^v_5-Δ^c_5		M_1	5.34
6.49	6.5	$L^v_{4,5}$-L^c_6	(0.5,0.5,0.5)	M_1	6.42
6.92	6.8[a]	L^v_6-$L^c_{4,5}$	(0.5,0.5,0.5)	M_1	6.81

a. See Ref. 123.

Table XLIX. Theoretical and experimental valence band features. Energies are in eV and measured from the valence band maximum.

Feature	Experiment	Theory
InAs	XPS[a]	
L_3^v	0.9 ± 0.3	1.1
X_5^v	2.4 ± 0.3	2.4
Σ_1^{min}	3.3 ± 0.2	3.4
X_3^v	6.3 ± 0.2	6.2
X_1^v	9.8 ± 0.3	10.2
Γ_1^v	12.3 ± 0.4	12.7

a. See Ref. 102.

Table L. The ionic and empirical parameters, a_i, for the Si potential. The potentials are normalized to an atomic volume of 169 $(a.u.)^3$ and the units are Ry if q is entered in a.u. The forms of the potential are given by (40) for the empirical and (41) for the ionic.

	V^{at}_{emp}	V^{at}_{ion}
a_1	0.279	-0.992
a_2	2.214	0.791
a_3	0.863	-0.352
a_4	1.535	-0.018

Table LI. Calculated energies of surface states and strong surface resonances of the relaxed Si (111) surface at Γ (center), K (corner) and M (edge midpoint) of the two-dimensional Brillouin zone. Also indicated are experimental (UPS) results are (2 x 1) and (7 x 7) reconstructed surfaces. The energy zero is taken at the bulk valence band edge E_V.

	SCLC		AH[e]	PP[f]	experiment	
	(1 x 1) relaxed surface				(2 x 1)	(7 x 7)
Γ	1.2	Γ_d	0.88	1.04		
	-1.5(2x)	Γ_{tb}	-1.95(2x)	-1.71(2x)	~-1.0[d]	-1.5[a]
	-12.7	Γ_{Lb}	-12.87	-12.9	-11.7[a]	-12.3[a]
K	0.5	K_d		0.11	-0.5[a] -0.45[b] -0.6[c]	0.1[a]
	-2.0	$K_{Lb'}$				
	-4.2	K_{tb}		-5.65		
	-8.5	K_{Lb}		-8.35		-7.5[a]
	-9.8	$K_{Lb'}$		-9.6		
M	0.5	M_d	0.04	0.17		
	-2.6	$M_{\ell b'}$				
	-3.1	M_{tb}	-3.55	-3.78		-3.6[a]
	-8.1 -8.7	M_{Lb}				
	-10.7	$M_{Lb'}$				

a. See Ref. 146.

b. See Ref. 142.

c. See Ref. 143

d. See Ref. 149.

e. See Ref. 150.

f. See Ref. 151.

Table LII. The ionic and empirical parameters for the Ga and As potentials. The potentials are normalized to an atomic volume of 152 $(a.u.)^3$. The form and units of the potentials are as in Table L. The Ga ion potenital is valid only for $q \leq 3$ (a.u.).

	Ga		As	
	V_{emp}^{at}	V_{ion}^{at}	V_{emp}^{at}	V_{ion}^{at}
a_1	1.22	-.34	0.35	-0.71
a_2	2.45	1.33	2.62	1.07
a_3	0.54	0.45	0.93	0.17
a_4	-2.71	0.0071	1.57	-0.015

Table LIII. Surface features for the GaAs (110) surface and their approximate position with respect to the top of the valence band.

Feature		Energy (eV)
As	s-like	-9.0
Ga	s-like	-5.8
As	back bond	-2.0
As	parallel bond	-0.5
As	dangling bond	-0.25
Ga	dangling bond	+1.0

Table LIV. The ionic and empirical parameters for the Zn and Se potentials. Units and normalization as in Table LII.

	Zn		Se	
	V^{at}_{emp}	V^{at}_{ion}	V^{at}_{emp}	V^{at}_{ion}
a_1	6.70	- .31	0.23	-2.32
a_2	1.50	1.34	3.39	0.53
a_3	0.67	0.082	0.73	- .57
a_4	-4.71	- .0086	2.20	0.32

Table LV. Surface features for the ZnSe (110) surface and their approximate position with respect to the top of the bulk valence band.

Feature	Energy (eV)
Se s-like	-10.0
Zn-Se mixed	- 2.5
Se back bond	- 0.5
Se parallel bond	+ 0.25
Se dangling bond	+ 0.5
Zn dangling bond	+ 5.25

FIGURE CAPTIONS

Fig. 1. Behavior of the Heine-Abarenkov well depth, $A_\ell(E)$, as determined by Animalu (Technical Report No. 4, Solid State Theory Group, Cavendish Laboratory, Cambridge, England).

Fig. 2. Band structure for Si as determined from a local pseudopotential calculation (dotted line) and an energy dependent non-local pseudopotential calculation (solid line).

Fig. 3a. Calculated $\varepsilon_2(\omega)$ for Si, with (dashed curve) and without (dotted curve) local-field effects, compared with experiment (solid curve) from Ref. 45.

Fig. 3b. Calculated $\varepsilon_1(\omega)$ for Si compared to the experimental results of Ref. 45.

Fig. 3c. Calculated reflectivity for Si compared to the experimental results of Ref. 45.

Fig. 4. Experimental and theoretical reflectivity derivative spectrum for Si. The experimental results (a) are from Ref. 47. The Dotted theoretical curve (b) was calculated from a local pseudopotential and the solid curve from an energy dependent non-local potential.

Fig. 5. Experimentally (a) and theoretically (b) determined electronic density of states for Si. The experimental results are from Ref. 4. The dotted theoretical curve is from a local pseudopotential calculation; the solid curve is from an energy dependent non-local pseudopotential calculation.

Fig. 6. The valence charge density as determined by Yang and Coppens (Ref. 72) using the X-ray results of Ref. 74. The contours are in units of e/Ω_c.

Fig. 7. The valence pseudocharge density for Si as calculated by a local pseudopotential (a) and by an energy dependent non-local pseudopotential (b). The contours are in units of e/Ω_c.

Fig. 8. The pseudocharge density band by band for Si as calculated by a local pseudopotential. The contours are in units of e/Ω_c.

Fig. 9. The pesudocharge density band by band for Si calculated by an energy dependent non-local pseudopotential. The contours are in units of e/Ω_c.

Fig. 10. The temperature dependence of the F^b_{222} structure factor for silicon. The experimental data points are from Roberto, Batterman and Keating.[77] The solid line shows the temperature dependence as calculated by a non-local pseudopotential and the dotted line indicates the temperature dependence of the Debye-Waller factor for the ion core.

Fig. 11. Band structure for Ge.

Fig. 12. Calculated reflectivity spectrum for Ge compared to the experimental results of Ref. 45.

Fig. 13. Modulated reflectivity spectrum for Ge. The experimental curve is from Ref. 90.

Fig. 14. Energy contours for the 4-5 transitions for the region of the Brillouin zone which contributes to the E_2 peak. The part of the Γ-X-U-L plane displayed is indicated by the shaded

region. The contours are drawn in 0.01 eV steps. (Contours below 4.30 eV and above 4.43 eV are not included.)

Fig. 15. Experimentally are theoretically determined electronic density of states for Ge. The experimental results are from Ref. 6.

Fig. 16. Calculated valence charge density for Ge. The contours are in units of e/Ω_c.

Fig. 17. The temperature dependence of the F^b_{222} structure factor germanium. The experimental data points are from Roberto, Batterman and Keating.[77] The solid line shows the temperature behavior as calculated by a non-local pseudopotential, and the dotted line indicates the temperature dependence of the Debye-Waller factor for the ion core.

Fig. 18. Band structure for GaAs.

Fig. 19. Calculated imaginary (a) and real (b) parts of the dielectric function and the reflectivity (c) for GaAs compared to the experimental results of Ref. 45.

Fig. 20. Comparison of theoretical (solid line) and experimental (dashed line) modulated reflectivity for GaAs. The experimental results are from Ref. 90. For A, B, C, see text.

Fig. 21. Calculated band structure for GaAs near Γ showing the critical point location for the E_o' structure. Also indicated (dashed line) is an M_o critical point resulting from the pseudocrossing of the Δ_5 conduction bands.

Fig. 22. Experimentally and theoretically determined density of states for GaAs. The experimental results are from Ref. 102.

Fig. 23. Calculated valence charge density for GaAs band by band. The contours are in units of e/Ω_c.

Fig. 24. Calculated valence charge density for GaAs summed over the valence bands. The contours are in units of e/Ω_c.

Fig. 25. Calculated band structure for ZnSe.

Fig. 26. Measured reflectivity spectra from Ref. 26 (dashed line) and Ref. 105 (dotted line) compared to the calculated reflectivity spectrum for ZnSe.

Fig. 27. X-ray photoemission spectra for ZnSe from Ref. 102 (dotted line) and ultraviolet photoemission spectra from Ref. 101 (dashed line) in arbitrary units compared to the calculated density of states (solid line). There appears to be a uniform shift between XPS and UPS data of approximately 0.5 eV. The UPS results appear to be in better agreement with the calculated results. The Zn 3d core states, which occur at approximately 9 eV below the top of the valence band, have been subtracted out of the experimental spectra.

Fig. 28. The valence charge density for ZnSe. The contours are in units of e/Ω_c.

Fig. 29. Band structure of grey tin.

Fig. 30. Calculated reflectivity for α-Sn compared to the experimental results of Ref. 108.

Fig. 31. Calculated electronic density of states for α-Sn.

Fig. 32. Charge density for grey tin. Contours are in units of e/Ω_c.

Fig. 33. Band structure of InSb.

Fig. 34. Calculated reflectivity for InSb compared to the experimental results of Ref. 45 (dashed line) and Ref. 111 (dotted line).

Fig. 35. Calculated modulated reflectivity for InSb compared to the experimental results of Ref. 90.

Fig. 36. Calculated electronic density of states for InSb compared to the experimental results of Ref. 102.

Fig. 37. Charge density of InSb. Contours are in units of e/Ω_c.

Fig. 38. Band structure of CdTe.

Fig. 39. Calculated reflectivity spectrum for CdTe compared to the experimental results of Ref. 118.

Fig. 40. Calculated electronic density of states for CdTe compared to the experimental results of Ref. 101. The contribution from the Cd 4d core states has been removed from the experimental data.

Fig. 41. Charge density for CdTe. The contours are in units of e/Ω_c.

Fig. 42. Band structure of GaP.

Fig. 43. Calculated reflectivity spectrum for GaP compared to the experiment results of Ref. 45.

Fig. 44. Calculated modulated reflectivity spectrum for GaP compared to the experimental results of Ref. 119.

Fig. 45. Calculated electronic density of states for GaP compared to the experimental results of Ref. 102.

Fig. 46. Calculated valence charge density for GaP. The contours are in units of e/Ω_c.

Fig. 47. Band structure of GaSb.

Fig. 48. Calculated reflectivity spectrum for GaSb compared to the experimental results of Ref. 111 (dashed line) and of Ref. 120 (dotted line).

Fig. 49. Calculated modulated reflectivity spectrum for GaSb compared to the experimental results of Ref. 90.

Fig. 50. Calculated electronic density of states for GaSb compared to the experimental results of Ref. 102.

Fig. 51. Calculated valence charge density for GaSb. The contours are in units of e/Ω_c.

Fig. 52. Band structure of InP.

Fig. 53. Calculated reflectivity spectrum for InP compared to the experimental results of Ref. 119 (dotted line) and Ref. 122 (dashed line).

Fig. 54. Calculated modulated reflectivity spectrum for InP compared to the experimental results of Ref. 119.

Fig. 55. Calculated electronic density of states for InP compared to the experimental results of Ref. 102.

Fig. 56. Calculated valence charge density for InP. The contours are in units of e/Ω_c.

Fig. 57. Band structure of InAs.

Fig. 58. Calculated reflectivity spectrum for InAs compared to the experimental results of Ref. 123.

Fig. 58. Calculated modulated reflectivity for InAs compared to the experimental results of Ref. 90.

Fig. 60. Calculated electronic density of states for InAs compared to the experimental results of Ref. 102.

Fig. 61. Calculated valence charge density for InAs. The contours are in units of e/Ω_c.

Fig. 62. Molecular potentials plotted along a line connecting the two Si atoms. Also indicated are the molecular orbital energies.

Fig. 63. Charge density contours for the four occupied molecular orbitals. The values are given in $2e/\Omega_c$ where $\Omega_c = 400\text{Å}^3$ is unit cell volume.

Fig. 64. Total charge density of the Si_2 molecule in the ground state.

Fig. 65. The top figure indicates the self-consistent potential averaged parallel to the surface and plotted as a function of distance into the bulk. The middle figure shows a similarly averaged total charge density (normalized to one electron per unit cell, Ω cell = 300Å^3). The bottom figure shows the total charge density in the (110) plane, with the same normalization; the contour spacing is in units 0.15. Only the minima of the charge density are labelled. The ionic positions are indicated by the black dots.

Fig. 66. The top figure shows the averaged charge as in Fig. 65 for the surface state at K. The bottom figure shows the charge density for this state in the (110) plane. The contours are spaced by units of 0.75.

Fig. 67. Perspective view of the Si crystal structure projected on a (110) plane. The [111] direction is vertical. The (111) surface is obtained by cutting the vertical bonds in a horizontal plane.

Fig. 68. Total valence charge distribution for an unrelaxed Si (111) surface. The charge is plotted as contours in a (110) plane intersecting the (111) surface a right angles. The plotting area starts in the vacuum and extends about 4 1/2 atomic layers into the crystal. The atomic positions and bond directions are indicated by dots and heavy lines respectively. The contours are normalized to electrons per Si bulk unit cell volume $\Omega_0 = \frac{a_c^3}{4}$.

Fig. 69. Contour plots of the empirical starting potential V_{emp} (top) and the final self-consistent potential V_{SC} (bottom). The plotting areas are identical to Fig. 68. The potential values are given in rydbergs normalized to zero in the vacuum.

Fig. 70. a. Empirical (V_{emp}) and self-consistent (V_{SC}) potentials averaged parallel to the (111) surface plotted as a function of the coordinate z perpendicular to the surface.
b. Individual potential contributions adding up to the self-consistent potential V_{SC} of Fig. 70a.

Fig. 71. Two-dimensional band structure of a twelve layer Si (111) film (relaxed surface model). The energy is plotted as a function of $\underset{\sim}{k}_{||}$ in the two-dimensional hexagonal Brillouin zone. The various surface states or strong surface resonances at high symmetry points are indicated by dots

and labelled according to the description in the text.

Fig. 72. Density of states curves for the self-consistent results on twelve layer films for the relaxed (broken line) and unrelaxed (solid line) surface geometry. Surface states are indicated by arrows and labelled according to Fig. 71. Inserted is the density of states in the vicinity of the fundamental gap for a six layer (2 x 1) reconstructed surface model.

Fig. 73. Charge density contour plots for two surface states at The states (Γ_{1b}) at -12.7 eV form the bottom of the valence bands (top figure), the transverse back bonds Γ_{tb} (bottom figure) are located -1.5 eV below the valence band maximum. The indicated charge values are only for comparison.

Fig. 74. Charge density contour plots for two surface states at K. The longitudinal p-like back bond orbitals $K_{\ell b}$, (top figure) are located at -2 eV while the s-like charge $K_{\ell b}$ localized on the outermost, third, etc. atomic layers (bottom figure) has an energy of -8.5 eV.

Fig. 75. Charge density contour plot of the dangling bond state K_d at 0.5 eV around the points M and K in the Brillouin zone.

Fig. 76. Schematic representation of the ideal and (2 x 1) reconstructed Si (111) surface. The reconstruction is done according to Haneman's model[157] and leaves the surface buckled as indicated by arrows. The slight lateral shifts

of second layer atoms are also indicated by arrows.

Fig. 77. Two-dimensional band structure around the fundamental gap for a (2 x 1) reconstructed Si (111) twelve layer film. The folded back Brillouin zone is indicated in the insert.

Fig. 78. Calculated joint density of states curve for low energy transitions between dangling bond bands of (2 x 1) Si (111) (top). Also indicated is the experimental absorption $\varepsilon_2(\omega)$ as obtained in Ref. 144. The bottom figure shows the regular density of states for the two dangling bond bands (d_{in} and d_{out}) of (2 x 1) Si (111).

Fig. 79. Charge density contour plots for the dangling bond states d_{out}(top) and d_{in} (bottom) of (2 x 1) Si (111). The charge is plotted in a (210) plane of (2 x 1) Si which corresponds to the (110) plane of (1 x 1) Si. The raised and lowered atoms are marked by arrows.

Fig. 80. The unit "surface" cell for zincblende (110) surfaces. The surface is defined by the plane ABCD. Dangling bond from ions A, E and D are shown schematically.

Fig. 81. Total valence charge density plotted in the $(1\bar{1}0)$ plane terminated on the (a) Ga atom and (b) As atom. The charge density has been normalized to one electron per unit cell volume, $\Omega_{cell} = 812\text{Å}^3$. The contour spacing is in units of 0.35.

Fig. 82. Charge density of the (a) Ga dangling bond and (b) As dangling bond surface states in the same place and normalization as in Fig. 81. The contour spacing is in

units of 2.0.

Fig. 83. Local density of states in arbitrary units as defined by Eq. (44). The total density of states was obtained by summing over all layers.

Fig. 84. Total valence charge density plotted in the (110) plane terminated on the a) Zn atom and b) se atom. The charge density has been normalized to one electron per unit cell, $\Omega_{cell} = 812\text{Å}^3$. The contour spacing is in units of 0.5.

Fig. 85. Local density of states for ZnSe (110) surface (as in Fig. 83).

Fig. 86. Charge density for the deepest lying surface state for the (110) ZnSe surface. The normalization is as in Fig. 84 with the contour spacing in units of 5.0. The $(1\bar{1}0)$ plane is displayed terminating in the Se.

Fig. 87. Charge density for next lowest lying ZnSe (110) surface states (see Fig. 85). The normalization is as in Fig. 84 with the contour spacing in units of 2.0. The $(1\bar{1}0)$ plane is displayed terminating on the Zn.

Fig. 88. Back bonding surface states for the ZnSe $(1\bar{1}0)$ plane is displayed terminating on the Se. Normalization and contour spacing as in Fig. 87.

Fig. 89. Parallel bonding surface states for the ZnSe (110) surface. The plane displayed contains atoms A and E in Fig. 80 and is perpendicular to the (110) surface. The contour spacing is in units of 3.0.

Fig. 90. Dangling bond surface states localized on Se for the ZnSe (110) surface. The plane, normalization and contour spacing is as in Fig. 88.

Fig. 91. Dangling bond surface state localized on Zn for the ZnSe (110) surface. The plane, normalization and contour spacing is as in Fig. 87.

REFERENCES

1. J. C. Phillips and L. Kleinman, Phys. Rev. 116, 287 (1959).
2. I. V. Abarenkov and V. Heine, Phil. Mag. 12, 529 (1965).
3. M. L. Cohen and V. Heine, Solid State Physics 24, 37 (1970).
4. L. Ley, S. Kowalczyk, R. Pollak and D. A. Shirley, Phys. Rev. Lett. 29, 1088 (1972).
5. R. Pollak, L. Ley, S. Kowalczyk, D. A. Shirley, J. D. Joannopoulos, D. J. Chadi and M. L. Cohen, Phys. Rev. Lett. 29, 1103 (1972).
6. W. D. Grobman and D. E. Eastman, Phys. Rev. Lett. 29, 1508 (1972).
7. L. Ley, R. A. Pollak, F. R. McFeely, S. P. Kowalczyk and D. A. Shirley, Phys. Rev. B9, 600 (1974).
8. J. R. Chelikowsky and M. L. Cohen, Phys. Rev. Lett. 31, 1582 (1973).
9. K. C. Pandey and J. C. Phillips, Phys. Rev. B9, 1552 (1974).
10. J. R. Chelikowsky and M. L. Cohen, Phys. Rev. B10, 5095 (1974).
11. V. Heine, Solid State Physics 24, 1 (1970).
12. J. R. Chelikowsky, D. J. Chadi and M. L. Cohen, Phys. Rev. B8, 2786 (1973).
13. J. C. Phillips and K. C. Pandey, Phys. Rev. Lett. 30, 787 (1973).
14. I. V. Abarenkow and V. Heine, Phil. Mag. 12, 1249 (1965).
15. R.M. Shaw, Phys. Rev. 174 769 (1968).
16. J. R. Chelikowsky and M. L. Cohen, Phys. Rev. B10, 5095 (1974).
17. A. O. E. Animalu and V. Heine, Phil. Mag. 12 1249 (1965).
18. G. Gilat and L. J. Raubenheiner, Phys. Rev. 144, 390 (1966).
19. D. H. Chadi and M. L. Cohen, Phys. Rev. B8, 5747 (1973).

20. A. Baldereschi, Phys. Rev. B7, 5212 (1973).

21. J. P. Walter and M. L. Cohen, Phys. Rev. B4, 1877.

22. D. J. Chadi, private communication.

23. L. R. Saravia dnd B. Burst, Phys. Rev. 176, 915 (1968).

24. G. Weisz, Phys. Rev. 149, 504 (1966).

25. S. Bloom and T. K. Bergstresser, Solid State Commun. 6, 465 (1960).

26. J. P. Walter, M. L. Cohen, Y. Petroff and M. Balkanski, Phys. Rev. B1, 2661 (1970).

27. F. Herman and S. Skillman, Atomic Structure Calculations (Prentice Hall, Englewood Cliffs, N. J., 1963).

28. M. L. Cohen and T. K. Bergstresser, Phys. Rev. 141, 789 (1966).

29. E. O. Kane, Phys. Rev. B4, 1910 (1971).

30. S. L. Adler, Phys. Rev. 126, 413 (1962); N. Wiser, Phys. Rev. 129, 62 (1963).

31. J. A. Van Vechten and R. M. Martin, Phys. Rev. Lett. 28, 446 (1972).

32. W. R. Hanke and L. J. Sham, Phys. Rev. Lett. 33, 582 (1974).

33. T. K. Bergstresser and G. W. Rubloff, Phys. Rev. Lett. 30, 794 (1973).

34. N. H. March and M. P. Tosi, Proc. R. Soc. A330, 373 (1972).

35. K. C. Pandey, P. M. Platzman, P. Eisenberger and E. N. Foo, Phys. Rev. B9, 5046 (1974).

36. E. Tosatti, C. Calandra, V. Bortolani and C. M. Bertoni, J. Phys. C5, L299 (1972).

37. L. H. Sham, Phys. Rev. 188, 1431 (1969).

38. R. M. Pick, M. H. Cohen and R. M. Martin, Phys. Rev. B1, 910 (1970).

39. R. M. Martin, Phys, Rev. 186, 871 (1969).

40. W. R. Hanke, Phys. Rev. B8, 4585, 4591 (1973).

41. C. M. Bertoni, V. Bortolani, C. Calandra and E. Tosatti, Phys. Rev. Lett. 28, 1578 (1972) and Phys. Rev. B9, 1710 (1974).

42. Equation (35) differs from the definition of $\varepsilon_{\underset{\sim}{G},\underset{\sim}{G}'}$ in Ref. 30 by a factor $|q+G|/|q+G'|$. This definition arises if electric fields are used in Eq. (34) instead of potentials. Both approaches lead to the same macroscopic dielectric function.

43. H. Ehrenreich and M. H. Cohen, Phys. Rev. 115, 786 (1959).

44. D. L. Johnson, Phys. Rev. B9, 4475 (1974).

45. H. R. Philipp and H. Ehrenreich, Phys. Rev. 129, 1550 (1963).

46. L. R. Savarin and D. Brust, Phys. Rev. 171, 916 (1968).

47. R. R. L. Zucca, J. P. Walter, Y. R. Shen and M. L. Cohen, Solid State Comm. 8, 627 (1970).

48. M. Welkowsky and R. Braunstein, Phys. Rev. B5, 497 (1972).

49. E. O. Kane and G. O Gobeli, Phys. Rev. Lett. 15, 142 (1965).

50. U. Gerhardt, Phys. Rev. Lett. 15, 401 (1965), Phys. Status Solidi 11, 301 (1965).

51. J. Tauc and A. Abraham, Proc. Int. Conf. on Semiconductor Physics, Prague 1960 (Czechoslovakian Academy of Science, Prague 1961) p. 375; J. Phys. Che. Sol. 20, 190 (1961).

52. F. H. Pollak and M. Cardona, Phys. Rev. 172, 816 (1968).

53. J. Koo, Y. R. Shen and R. R. L. Zucca, Solid State Comm. 9, 2229 (1971).

54. F. H. Pollak and G. W. Rubloff, Bull. Amer. Phys. Soc. 17, 258 (1972).

55. J. W. Grover and P. Handler, Phys. Rev. B9, 2600 (1974).

56. J. R. Chelikowsky and M. L. Cohen, Phys. Rev. Lett. 31, 1582 (1973).

57. J. R. Chelikowsky and M. L. Cohen, Phys. Rev. Lett. 32, 674 (1974).

58. D. E. Aspnes ana A. A. Studna, Solid State Comm. 11, 1375 (1972).

59. A. B. Kunz, Phys. Rev. Lett. 27, 567 (1971).

60. S. T. Pantelides and F. C. Brown (to be published).

61. See Fig. 2 of Ref. 59.

62. J. S. Kline, F. H. Pollak and M. Cardona, Helv. Phys. Acta 41, 968 (1968).

63. W. E. spicer and R. C. Eden in Proceedings of the Ninth International Conference of the Physics of Semiconductors, Moscow, 1968 (Nauka, Leningrad, USSR, 1968), vol. 1. p. 61.

64. G. Dresselhaus, A. F. Kip and C. Kittel, Phys. Rev. 98, 368 (1955).

65. E. O. Kane, Phys. Rev. B4, 1910 (1971).

66. D. J. Stukel and R. N. Euwema, Phys. Rev. B4, 1635 (1970).

67. D. Stukel, T. Collins and R. Euwema in Proceedings of the Third International Materials Research Symposium, Gaithersburg, Maryland, 1969, ed. by L. Bennet, Nat. Bur. Stand. Special Pub.

No. 323, (U. S. GPO, Washington, D. C. 1971).

68. J. P. Van Dyke, Phys. Rev. B5, 1489 (1972).

69. E. O. Kane, Phys. Rev. 146, 558 (1966).

70. J. C. Hensel, H. Hasegawa and M. Nakagama, Phys. Rev. 138, A225 (1965).

71. E. B. Hale and T. G. Castner, Phys. Rev. B1, 4763 (1970).

72. A. Frova and P. Handler, Phys. Rev. Lett. 14, 178 (1965).

73. Y. W. Yang and P. Coppens, to be published.

74. In particular see H. Hattori, H. Kuriyama, T. Katayawa and M. Kato, J. Phys. Soc. Japan 20, 988 (1965); M. Kato and S. Tanemura, Acta Cryst. A28, 69 (1972); P. J. E. Aldred and M. Jart, Proc. Roy. Soc. London A332, 223 and 239 (1973); J. B. Roberto and B. W. Batterman, Phys. Rev. B2, 3220 (1970); and P. Trucano and B. W. Batterman, Phys. Rev. B6, 3659 (1972).

75. E. Clementi, IBM J. Res. Devel. Suppl. 9, 2 (1965).

75a. W. Brinkman and B. Goodman, Phys. Rev. 149, 597 (1966).

76. P. M. Raccah, R. N. Euwema, D. J. Stukel and T. C. Collins, Phys. Rev. B1, 756 (1970).

77. J. B. Roberto, B. W. Batterman and D. T. Keating, Phys. Rev. B9, 2590 (1974).

78. See the second ref. in 74.

79. J. C. Phillips, Phys. Lett. 37A, 434 (1971).

80. B. Dawson and B. T. M. Willis, Proc. Roy. Soc. London A298, 307 (1966).

81. J. P. Walter, R. R. L. Zucca, M. L. Cohen and Y. R. Shen, Phys. Rev. Lett. 24, 102 (1970).

82. American Institute of Physics Handbook, ed. D. E. Gray, (McGraw Hill, New York 1970, p. 4-119.

83. B. W. Batterman and D. R. Chipman, Phys. Rev. 127, 690 (1967).

84. D. E. Aspnes, Phys. Rev. Lett. 31, 230 (1973).

85. G. Dresselhaus and M. S. Dresselhaus, Phys. Rev. 160, 649 (1967).

86. M. Cardona and Fred H. Pollak, Phys. Rev. 142, 530 (1966).

87. L. R. Saravia and D. Brust, Phys. Rev. 176, 915 (1968) and D. Brust, Phys. Rev. 134, A1137 (1964).

88. F. Herman, R. L. Kortum, D. C. Kuglin and R. A. Short in Quantum Theory of Atoms, Molecules and the Solid State, edited by P. O. Löwdin (Adacemic Press, New York, 1966).

89. For the E_2 peak in GaSb, R. Cahn and M. L. Cohen, Phys. Rev. B1, 2569 (1970).

90. R. R. L. Zucca and Y. R. Shen, Phys. Rev. B1, 2668 (1970).

91. M. Welkowsky and R. Braunstein, Phys. Rev. B5, 497 (1972).

92. J. E. Fischer, in Proceedings of the Tenth International Conference on the Physics of Semiconductors, Cambridge, Massachusetts, 1970 edited by S. P. Keller, J. C. Hensel and F. Stern, Cont. - 700901 (U. S. AEC Division of Technical Information, Springfield, Va., 1970) p. 427.

93. J. Halpern and B. Lax, J. Phys. Chem. Sol. 26, 911 (1965).

94. D. E. Aspnes and A. A. Studna, Phys. Rev. B7, 4605 (1973).

95. J. R. Chelikowsky and M. L. Cohen, Phys. Rev. Lett. 32, 674 (1974).

96. V. Rehn and D. S. Kyser, Phys. Rev. Lett. 28, 494 (1972).

97. D. D. Sell, R. Dingle, S. E. Stokowski and J. V. Lorenzo, Phys. Rev. Lett. 27, 1644 (1971).

98. See Dee. Sell and S. E. Stokowski in Proceedings of the Tenth International Conference on the Physics of Semiconductors, edited by S. P. Keller, J. C. Hensel and F. Stern (U. S. AEC Oak Ridge, Tenn. 1970) p. 417.

99. I. B. Ortenburger and W. E. Rudge, (IBM Research Report RJ-0141).

100. A. M. Gray, Phys. Stat. Sol. 37, 11 (1970).

101. D. E. Eastman, W. D. Grobman, J. L. Freeouf and M. Erbudak, Phys. Rev. B9, 3473 (1974).

102. L. Ley, R. A. Pollak, F. R. McFeely, S. P. Kowalczyck and Shirley, Phys. Rev. B9, 600 (1974).

103. J. R. Chelikowsky and M. L. Cohen, to be published.

104. A similar calculation with different radii was published by the author with M. L. Cohen, Phys. Lett. 47A, 7 (1974). The results of this calculation are essentially identical to the results tabulated here.

105. J. L. Freeouf, Phys. Rev. B7, 3810 (1973).

106. S. Groves and W. Paul in Proceedings of the International Conference on the Physics of Semiconductors, Paris, 1964 (Dunod, Paris, 1964), p. 41

107. M. Cardona, P. Elroy, F. H. Pollak and K. L. Shaklee, Solid State Comm. 4, 319 (1966).

108. P. T. McElroy, Technical Report No. HP-21 (ARPA-34), Division of Engineering and Applied Physics, Harvard University.

109. F. H. Pollak, M. Cardona, C. W. Higginbotham, F. Herman and J. P. Van Dyke, Phys. Rev. B2, 352 (1970).

110. H. Ehrenreich, H. R. Philipp, J. C. Phillips, Phys. Rev. Lett. 8, 58 (1962).

111. S. S. Vishnubhatla and J. C. Woolley, Cand. J. Phys. 46, 1769 (168).

112. H. Ehrenreich, J. Appl. Phys. Suppl. 32, 2155 (1961).

113. C. Varea de Alvarez, J. P. Walter, R. W. Boyd and M. L. Cohen, J. Phys. Chem. Solids 34, 337 (1973).

114. R. Glosser, J. E. Fischer and B. O. Seraphin, Phys. Rev. B1, 1607 (1970).

115. J. C. Phillips, Rev. Mod. Phys. 42, 317 (1970).

116. D. J. Chadi, M. L. Cohen, W. D. Grobman Phys. Rev. B8, 5578 (1973).

117. M. Cardona, K. L. Shaklee and F. H. Pollak, Phys. Rev. 154, 696 (1967).

118. D. J. Chadi, J. P. Walter, M. L. Cohen, Y. Petroff and M. Balkanski, Phys. Rev. B5, 3058 (1972).

119. C. Varea de Alvarez, J. P. Walter, M. L. Cohen, J. Stokes and Y. R. Shen, Phys. Rev. B6, 1412 (1972).

120. M. Cardona, J. Appl. Phys. Suppl. 32 2151 (1961).

121. B. B. Kosicki, Technical Report No. HP-19, Harvard University, 1967 (unpublished).

122. M. Cardona in Semiconductors and Semimetals, Vol. 3 ed. R. Willardson and A. Beer (academic Press, N.Y. 1967) p. 138.

123. E. Ehrenreich, H. R. Philipp and J. C. Phillips, Phys. Rev. Lett. 8, 59 (1962).

124. J. R. Dixon and J. M. Ellis, Phys. Rev. 123, 1560, (1961).

125. F. Matossi and F. Stein, Phys. Rev. 111, 472 (1958).

126. J. D. Joannopoulos and M. L. Cohen, Phys. Rev. B7, 2644 (1973).

127. G. P. Alldredge and L. Kleinman, Phys. Rev. Lett. 28, 1264 (1972), and G. P. Alldredge and L. Kleinmen, Phys. Rev. B10 559 (1974).

128. J. A. Appelbaum and D. R. Hamann, Phys. Rev. B8, 1777 (1973); J. P. Walter and M. L. Cohen, Phys. Rev. B2, 1821 (1970).

129. R. D. Verma and P. A. Warsop, Can. J. Phys. 41, 152 (1963).

130. P. Bagus, private communication.

131. N. D. Lang and W. Kohn, Phys. Rev. B1, 4555 (1970), B3, 1215 (1971) and N. D. Lang, Solid State Physics 28, 225 (1973).

132. J. Appelbaum and D. Hamann, Phys. Rev. B6, 2166 (1972).

133. The requirement for a bona fide surface state is the occurrence of a gap in the projected bulk band structure on the two dimensional zone. See V. Heine, Proc. Phys. Soc. 81, 300 (1963).

134. D. S. Boudreaux, Surf. Sci. 28, 344 (1971).

135. E. Caruthers, L. Kleinman and G. P. Alldredge (referred to as CKA in the text), Phys. Rev. B10, 1252 (1974), B9, 3325, 3330 (1974), and B8, 4570 (1973).

136. In order to obtain accurate wavefunctions we employ the same convergence requirements of Ref. 135.

137. J. C. Riviere, Solid State Surface Science, ed. M. Green (Marcel Dekker, New York) 1, 1969.

138. While anisotropy for ϕ in metals is small it can typically amount to 0.05 Ry (see Ref. 137) from the loosely packed faces to the more densely packed faces.

139. J. P. Walter, C. Y. Fong and M. L. Cohen, Solid State Comm. 12, 303 (1973).

140. The surface states occurring at M in the CKA calculation and above E_F.

141. Experimental literature through 1973 is compiled by W. Mönch in Festkörperprobleme XIII, 241, (1973).

142. D. E. Eastman and W. D. Grobman, Phys. Rev. Lett. 28, 1378 (1972).

143. L. F. Wagner and W. E. Spicer, Phys. Rev. Lett. 28, 1381 (1972).

144. G. Chiarotti, S. Nannarone, R. Pastore and P. Chiaradia, Phys. Rev. B4, 3398 (1971).

145. J. E. Rowe and H. Ibach, Phys. Rev. Lett. 31, 102 (1973).

146. J. E. Rowe and H. Ibach, Phys. Rev. Lett. 32, 421 (1974).

147. H. Ibach and J. E. Rowe, Surf. Science 43, 481 (1974).

148. J. E. Rowe and J. C. Phillips, Phys. Rev. Lett. 32, 1315 (1974).

149. J. E. Rowe, M. M.Traum and N. V. Smith, Phys. Rev. Lett. 33, 1333 (1974).

150. J. A. Appelbaum and D. R. Hamann, Phys. Rev. Lett. 31, 106 (1973), Phys. Rev. Lett. 32, 225 (1974) and Phys. Rev. B8, 1777 (1973).

151. K. C. Pandey and J. C. Phillips, Phys. Rev. Lett. 32, 1433 (1974).

152. E. Mosser, M. Schlüter, I. Ch. Schlüter, J. Phys. Chem. Solids 35, 1269 (1974).

153. G. Gilat and G. Dolling, Phys. Lett. 8, 304 (1974).

154. J. C. Slater, Phys. Rev. 81, 385 (1951), W. Kohn and L. J. Sham, Phys. Rev. 140, A1133 (1965).

155. E. P. Wigner, Phys. Rev. 46, 1002 (1934).

156. L. Falicov and F. Yndurain, J. Phys. C. 8, 147 (1975).

157. D. Haneman, Phys. Rev. 121, 1093 (1961).

158. A. Toloni and D. Haneman, Surf. Sci. 10, 215 (1968).

159. J. Appelbaum and D. Hamann, to be published.

160. H. Lüth and G. J. Russel, Surf. Sic. 45, 329 (1974).

161. P. E. Gregory, W. E. Spicer, S. Ciraci and W. A. Harrison, Appl. Phys. Lett. 25, 511 (1974).

162. D. E. Eastman and J. L. Freeouf, Phys. Rev. Lett. 33, 1601 (1974).

163. R. Ludcke and A. Koma, Phys. Rev. Lett. 34, 817 (1975).

164. H. Froithzheim and H. Ibach, Surf. Sci 47 713 (1975).

165. J. E. Rowe, to be published.

166. J. M. Dinan, L. K. Galbraith and T. E. Fischer, Surf. Sci. 26, 587 (1971).

167. R. Dorn and H. Luth, Phys. Rev. Lett. 33 1024 (1974).

168. M. Schlüter, J. R. Chelikowsky, S. G. Louie and M. L. Cohen, Phys. Rev. Lett. 34, 1385 (1975).

169. C. Calandra and G. Santoro, J. Phys. C. 8, L86 (1975).

170. J. D. Joannopoulos and M. L. Cohen, Phys. Rev. B10, 5075 (1974).

171. N. Garcia, J. Solana and N. Cabrera, Solid State Comm. (in press).

ACKNOWLEDGEMENTS

I wish to express my deep appreciation to my thesis adviser, Prof. Marvin L. Cohen. Without his excellent guidence, encouragement and advice, this work would not have been possible.

I would like to acknowledge helpful discussions and advice from Profs. Leo Falicov, Charles Kittel, Ron Shen and Ching Fong.

Conversations with Prof. Hanemann and Dr. Felix Yndurain on silicon surfaces and Dr. N. Garcia on aluminum surfaces are gratefully acknowledged.

I would also like to thank Prof. D. A. Shirley, Dr. R. Pollak, Dr. L. Ley, S. Kowalczyk, R. McFeely, Dr. W. D. Grobman and Dr. D. E. Eastman for helpful discussions on photoemission spectroscopy and data before publication.

Special thanks, indeed, are reserved for Dr. Michael Schluter and Steven G. Louie for their collaborations on the Si molecule and surface, and the aluminum surface. Further, I acknowledge Steven's collaboration on the local fields section. In addition to which, I acknowledge numerous invaluable discussions with Michael and Steve on related topics.

I am also pleased to mention numerous other helpful conversations during the early stages of this work with Drs. Jim Chadi, John Joannopoulos, Carmen Varea de Alvarez and Yvonne Tsang. And in the latter stages, as it were, with Kai-Ming Ho, Belita Koiller, William Hsu, David Denley and V. T. Rajan.

Financial support by a National Science Foundation Fellowship for my first three years of study and research is gratefully acknowledged. This work was also partially supported by the U. S. Energy Research and Development Administration.

Finally, for their patience in deciphering my inscrutable handwriting and their excellent typewriting of this and other manuscripts I wish to thank Carol Tung, Madeline Moore and Lorine Hesleph.

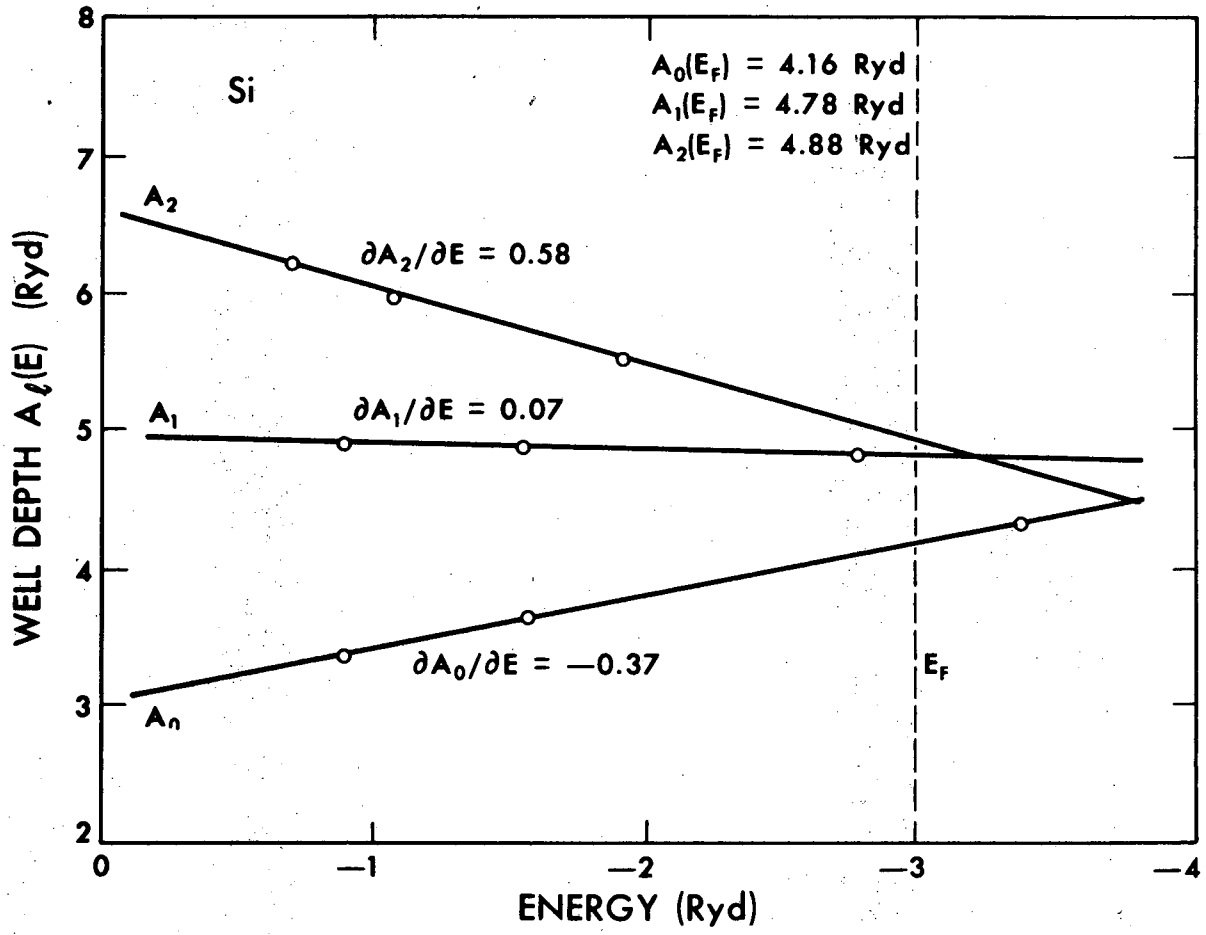

XBL 758-6955

Fig. 1.

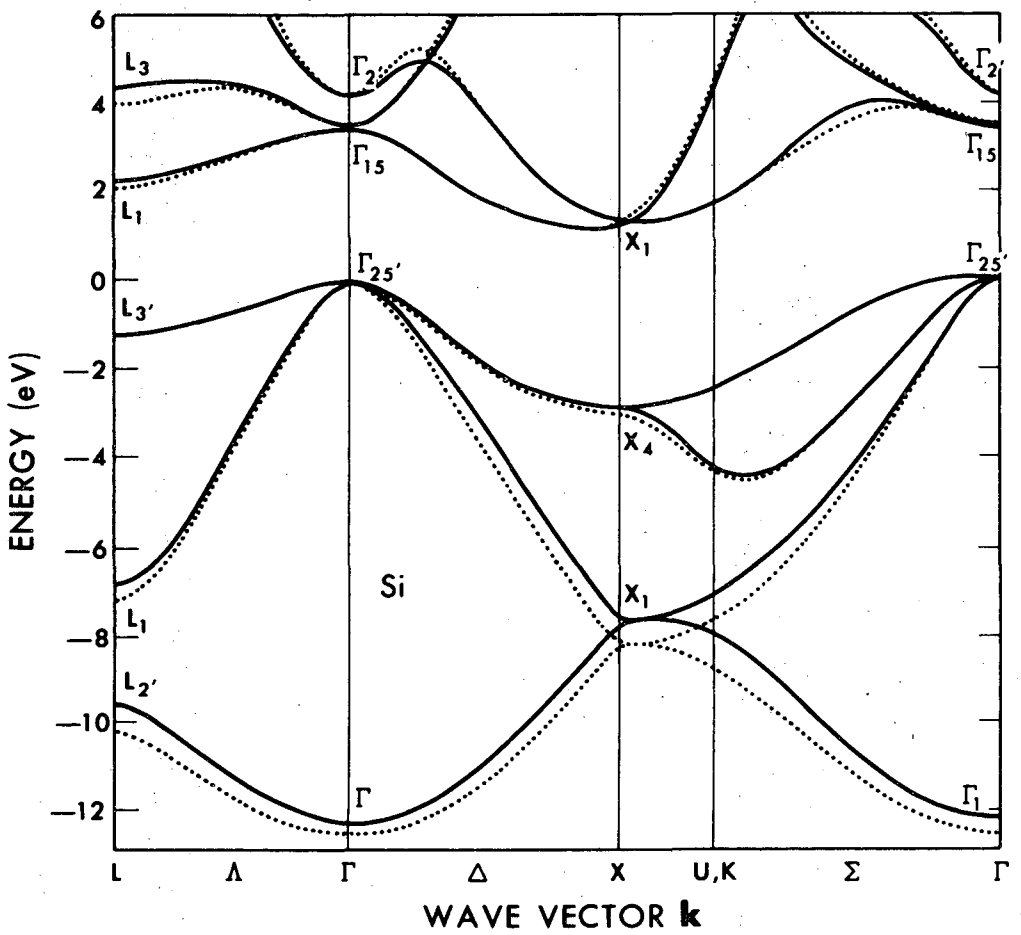

XBL-758-6943

Fig. 2.

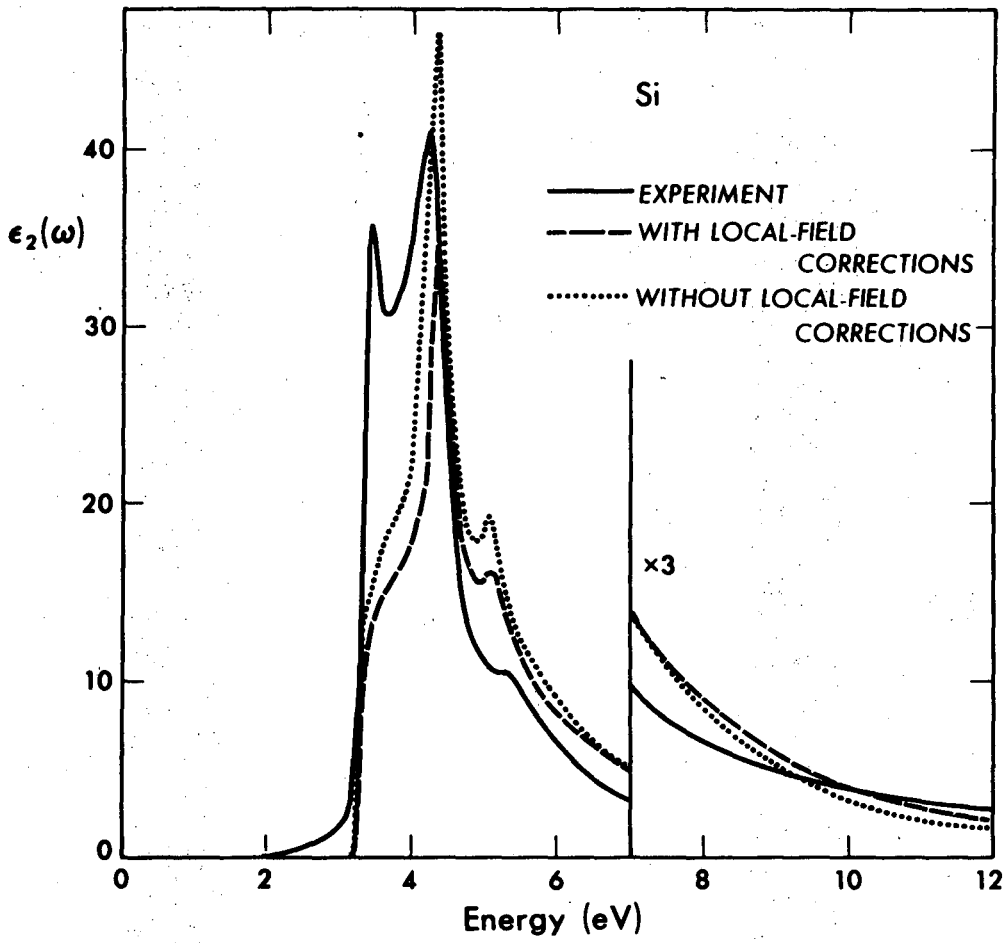

XBL 758-6957

Fig. 3a.

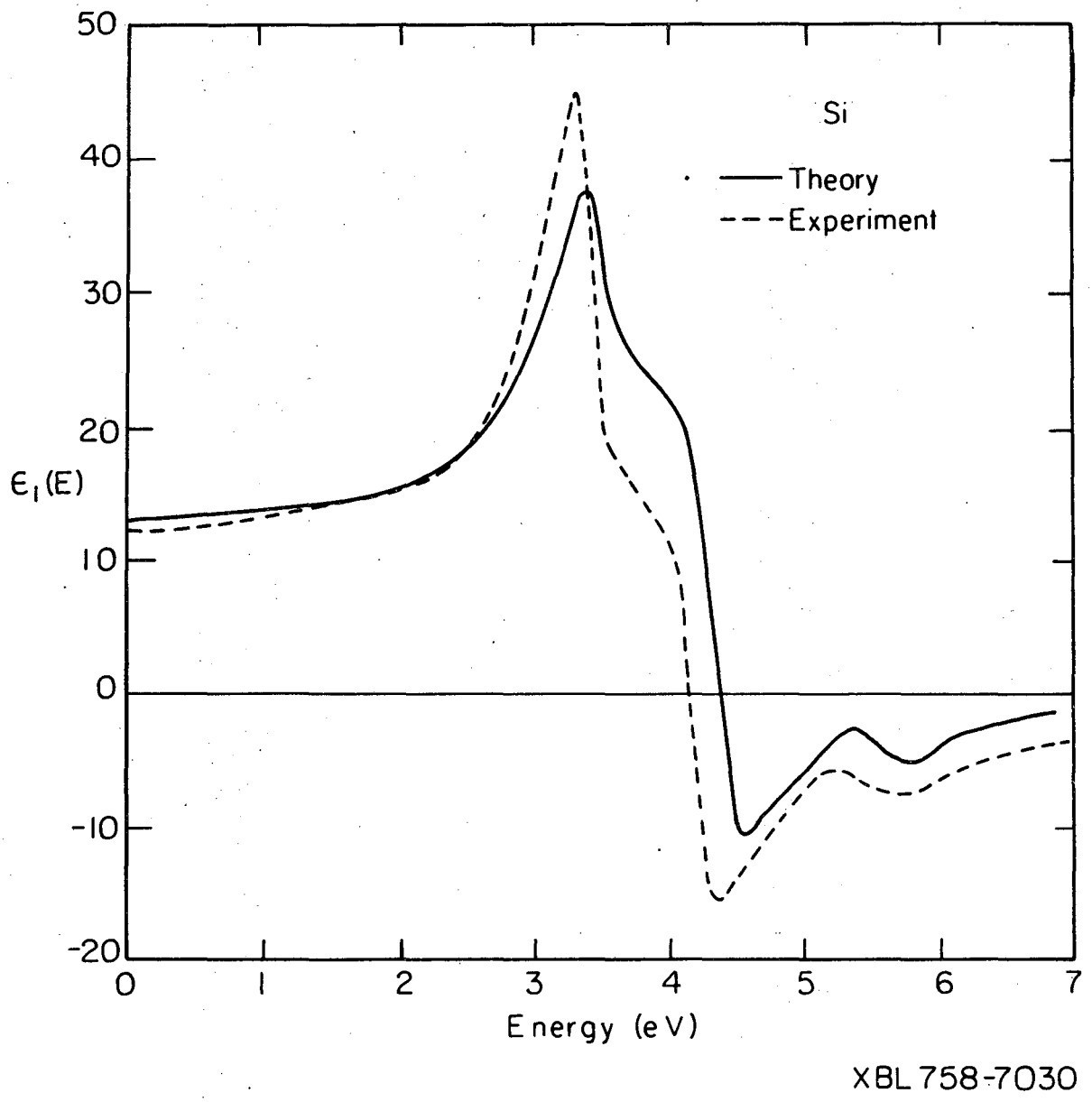
Si
Theory
Experiment
$\epsilon_1(E)$
Energy (eV)
50
40
30
20
10
0
-10
-20
0
1
2
3
4
5
6
7
XBL 758-7030

Fig. 3b.

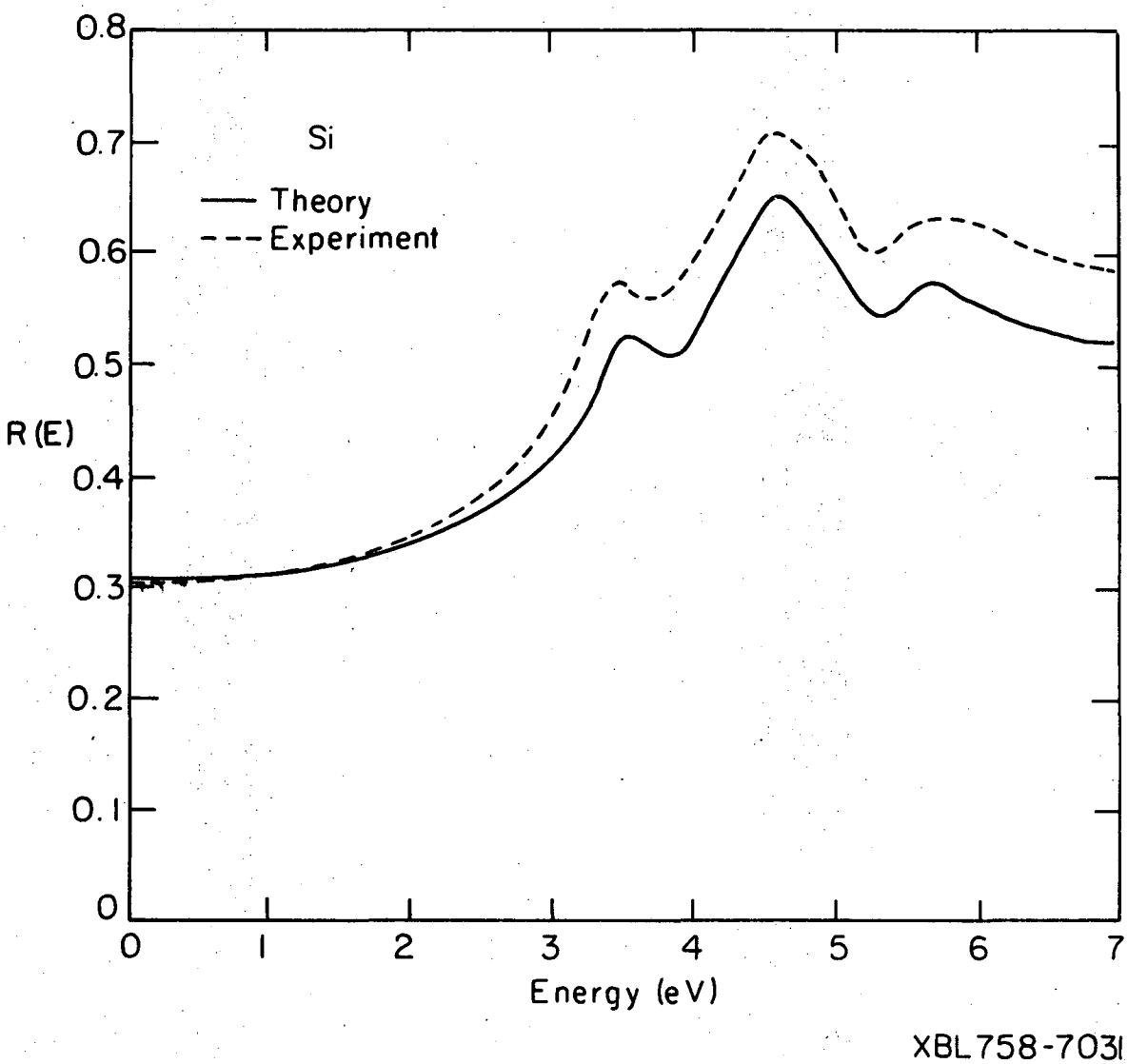

Fig. 3c.

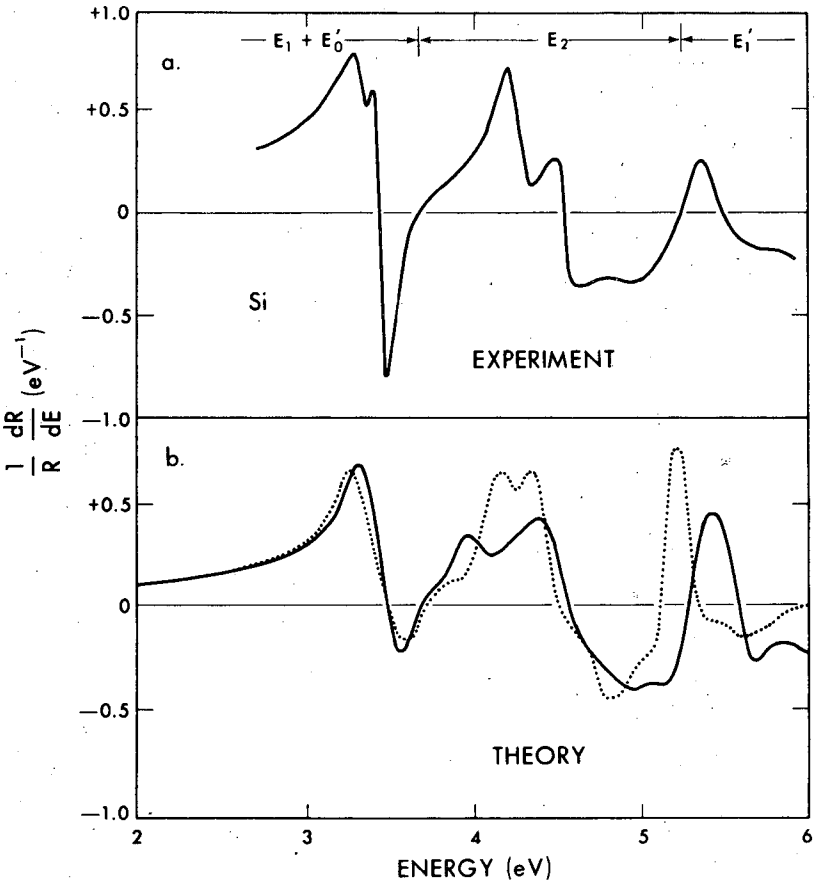

XBL 758-6972

Fig. 4.

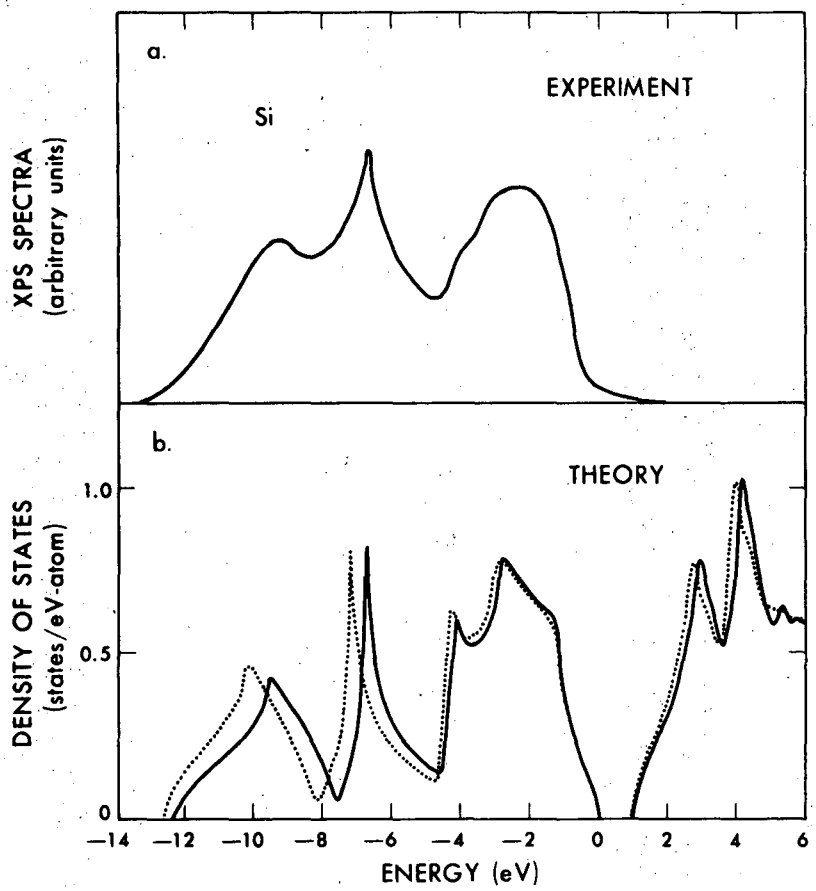

XBL 758-6966

Fig. 5.

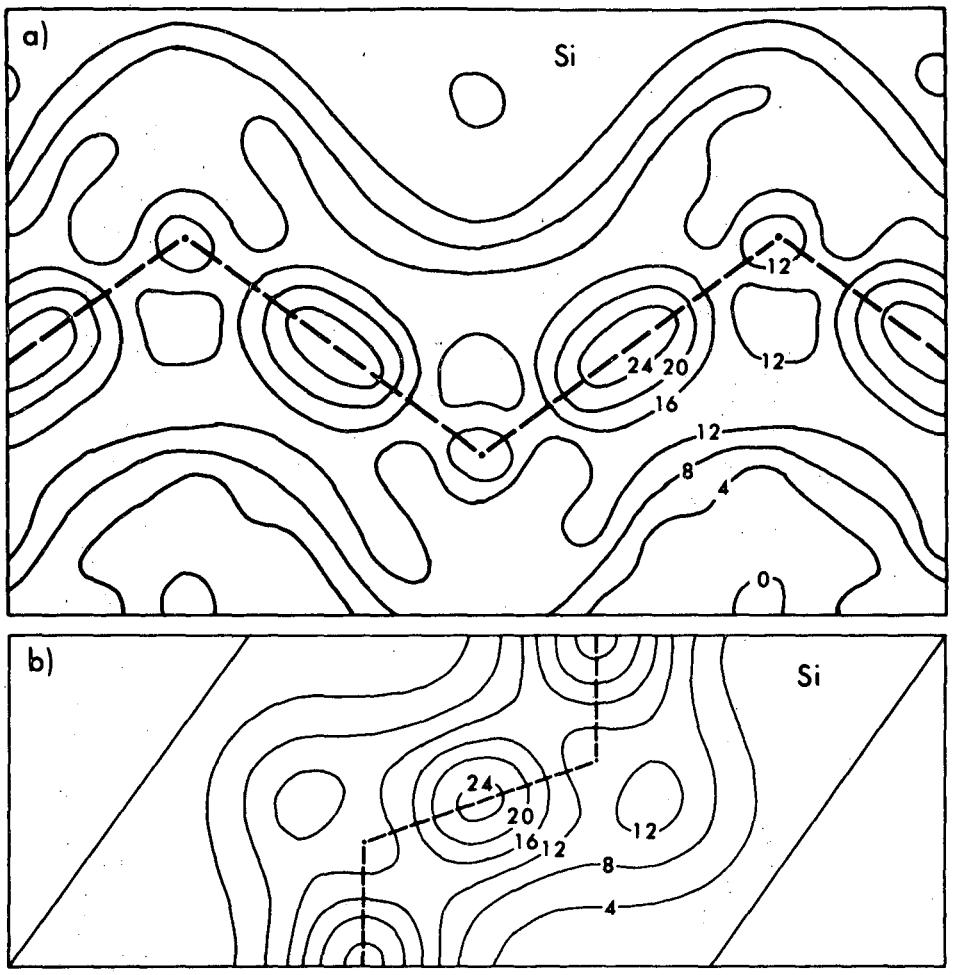

XBL 758-6958

Fig. 6.

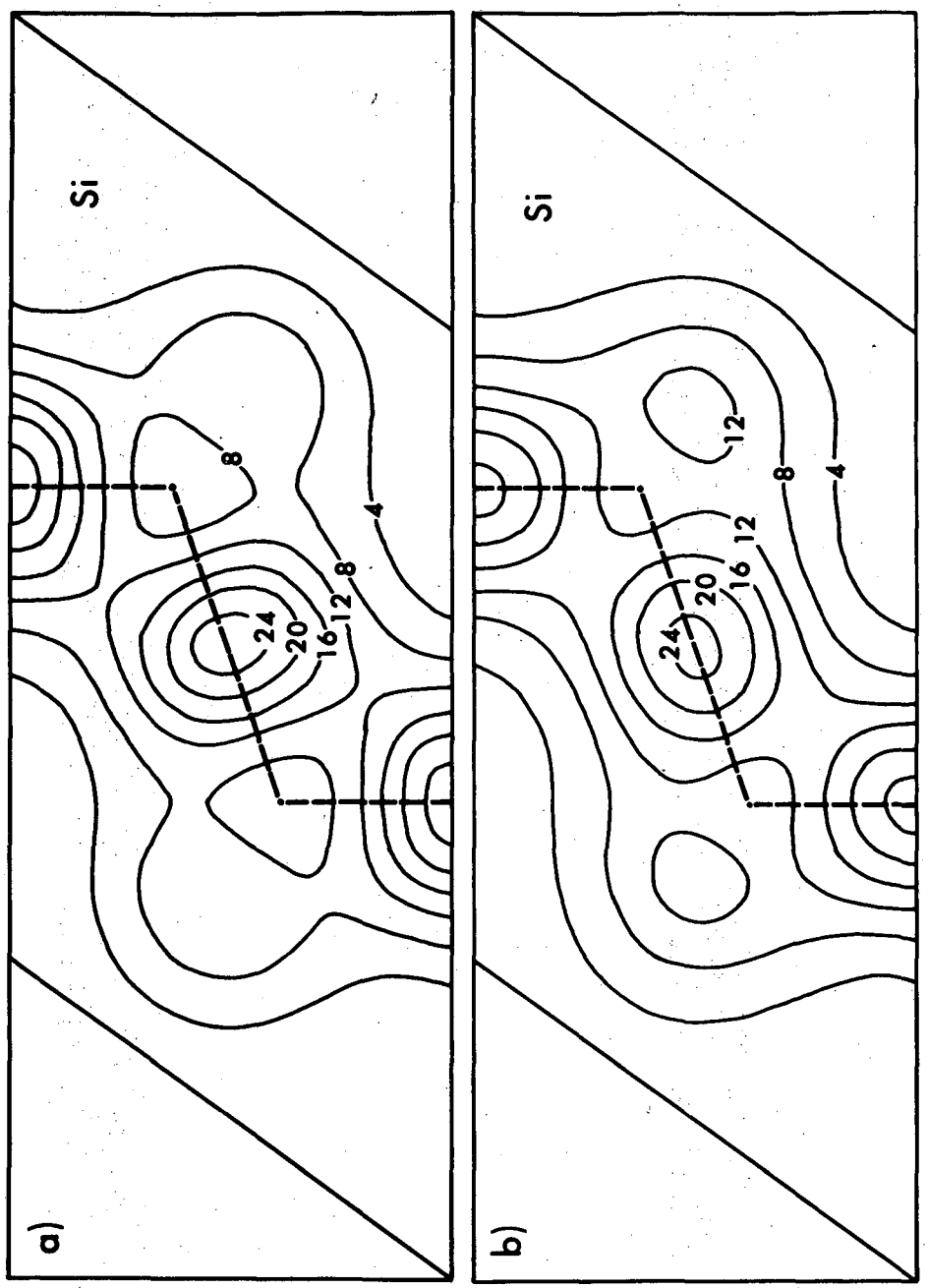

XBL-758-6942

Fig. 7.

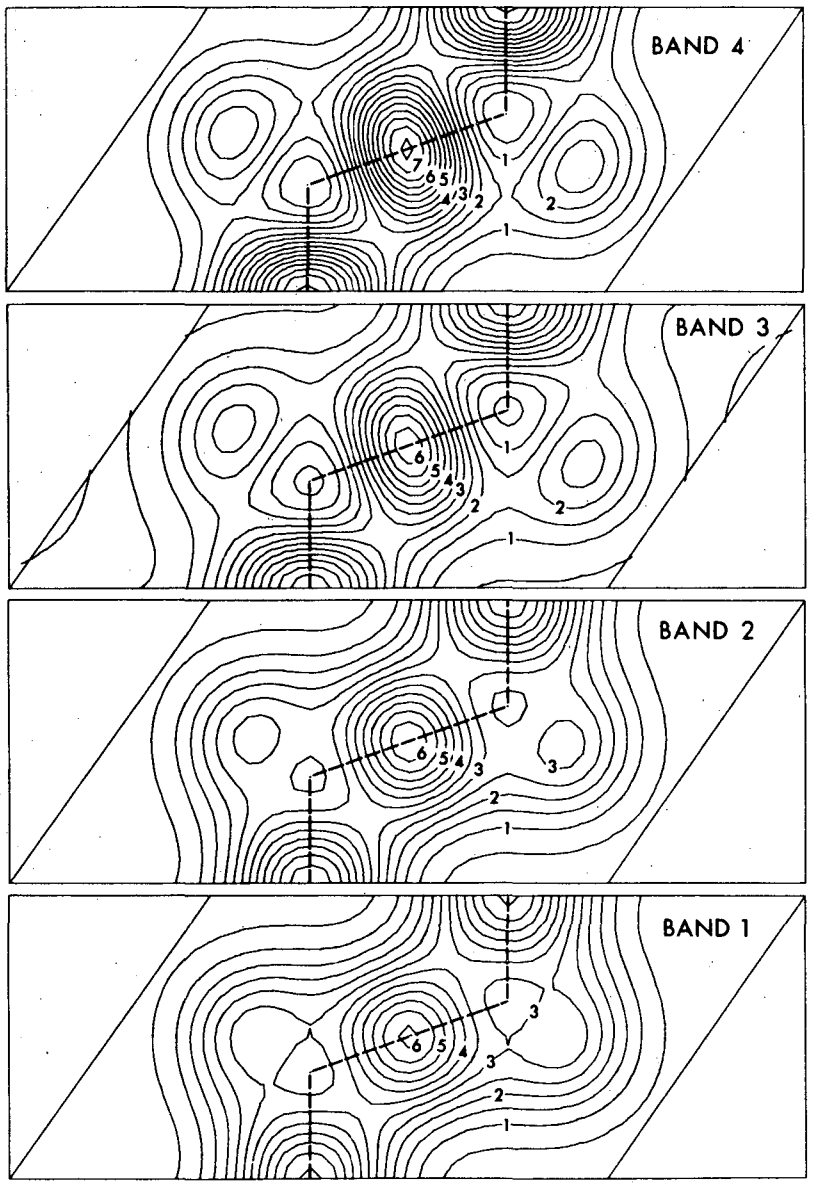

XBL 758-7914

Fig. 8.

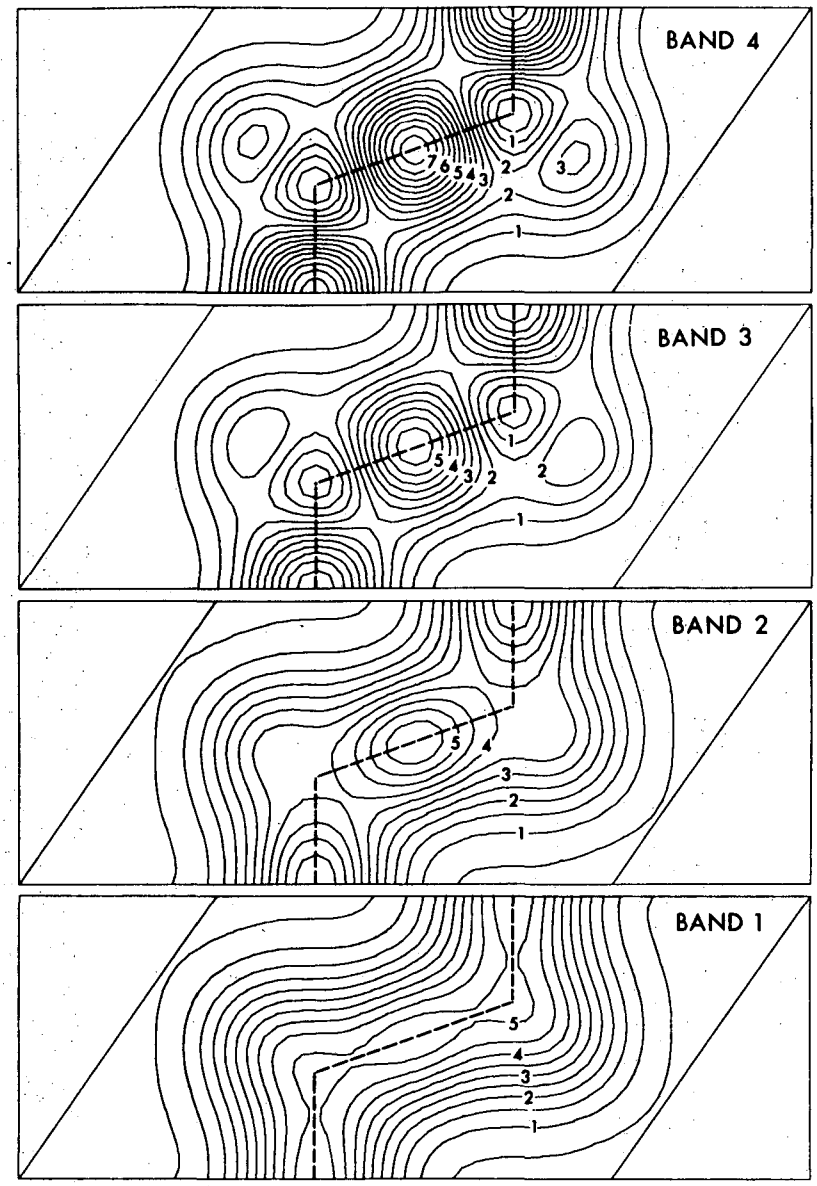

XBL 758-6963

Fig. 9.

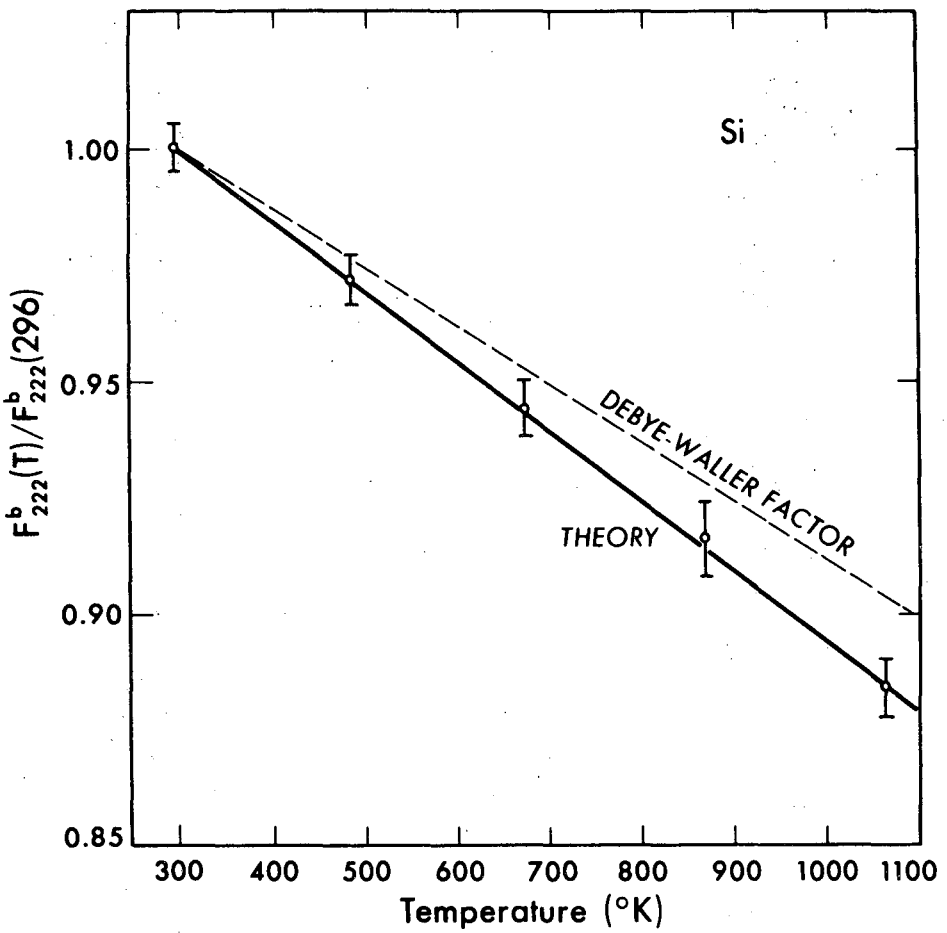

XBL 758-6949

Fig. 10.

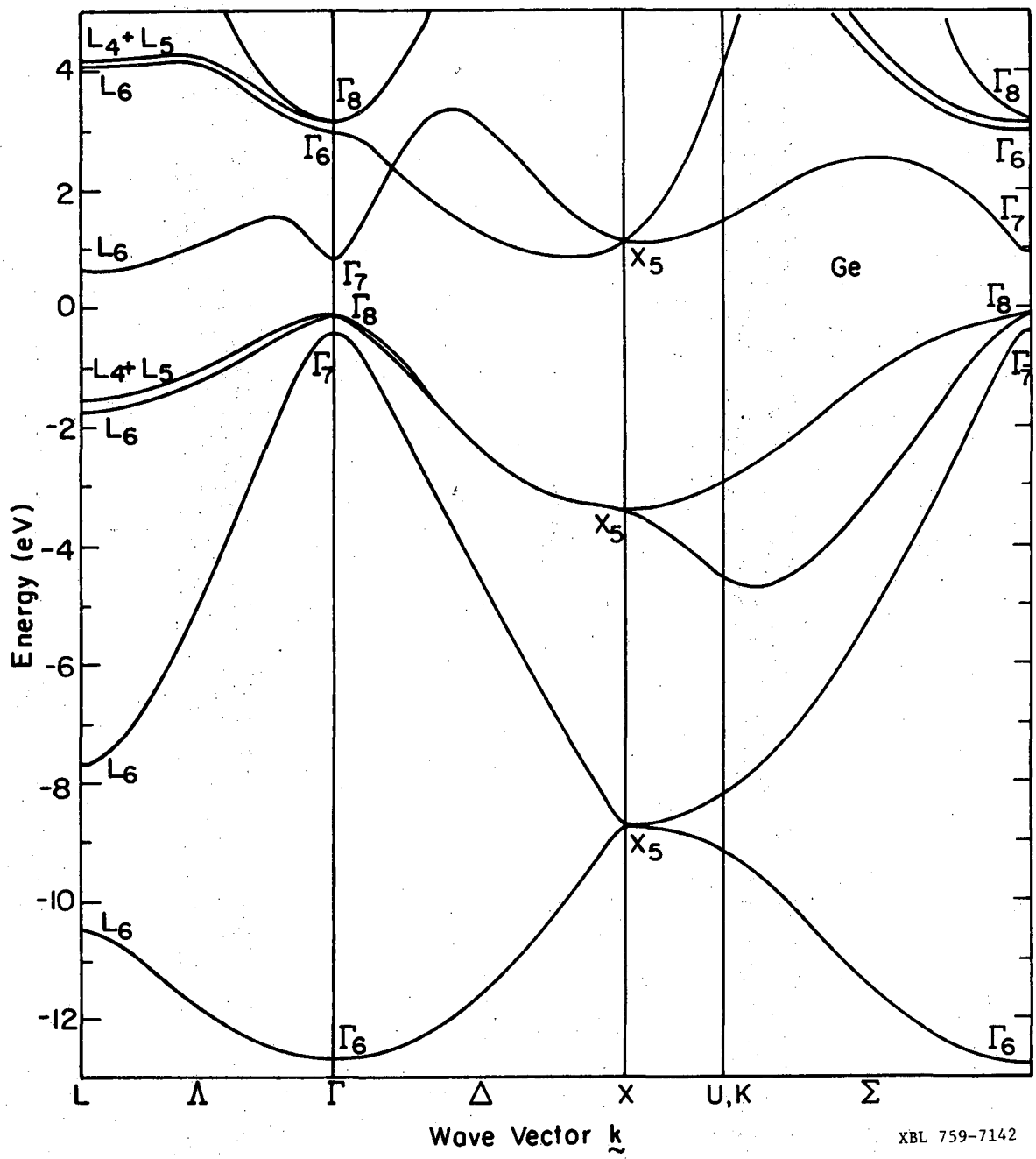

Fig. 11.

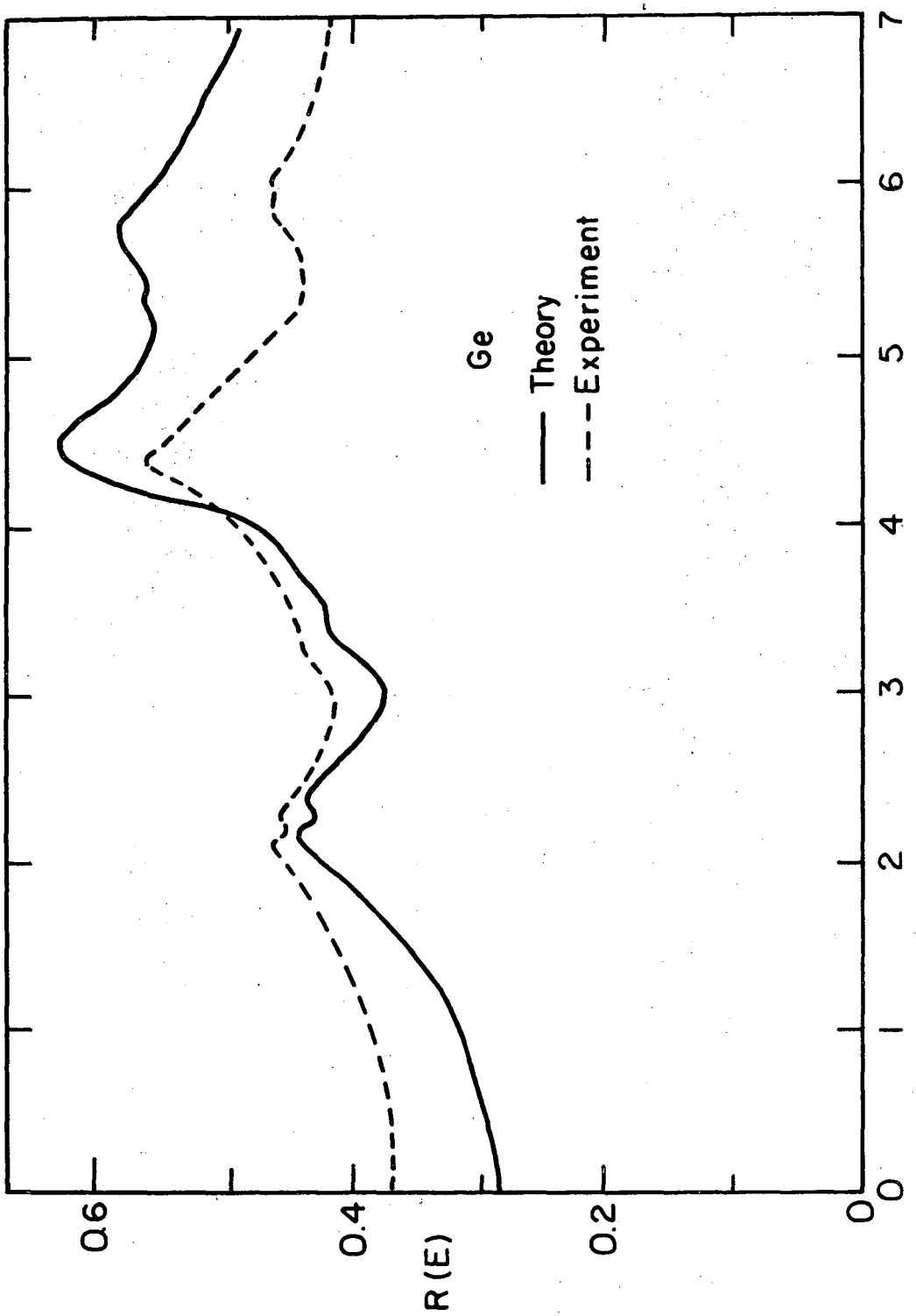
Ge
Theory
Experiment
R(E)
0.6
0.4
0.2
0
0
1
2
3
4
5
6
7
Energy (eV)
XBL758-7033

Fig. 12.

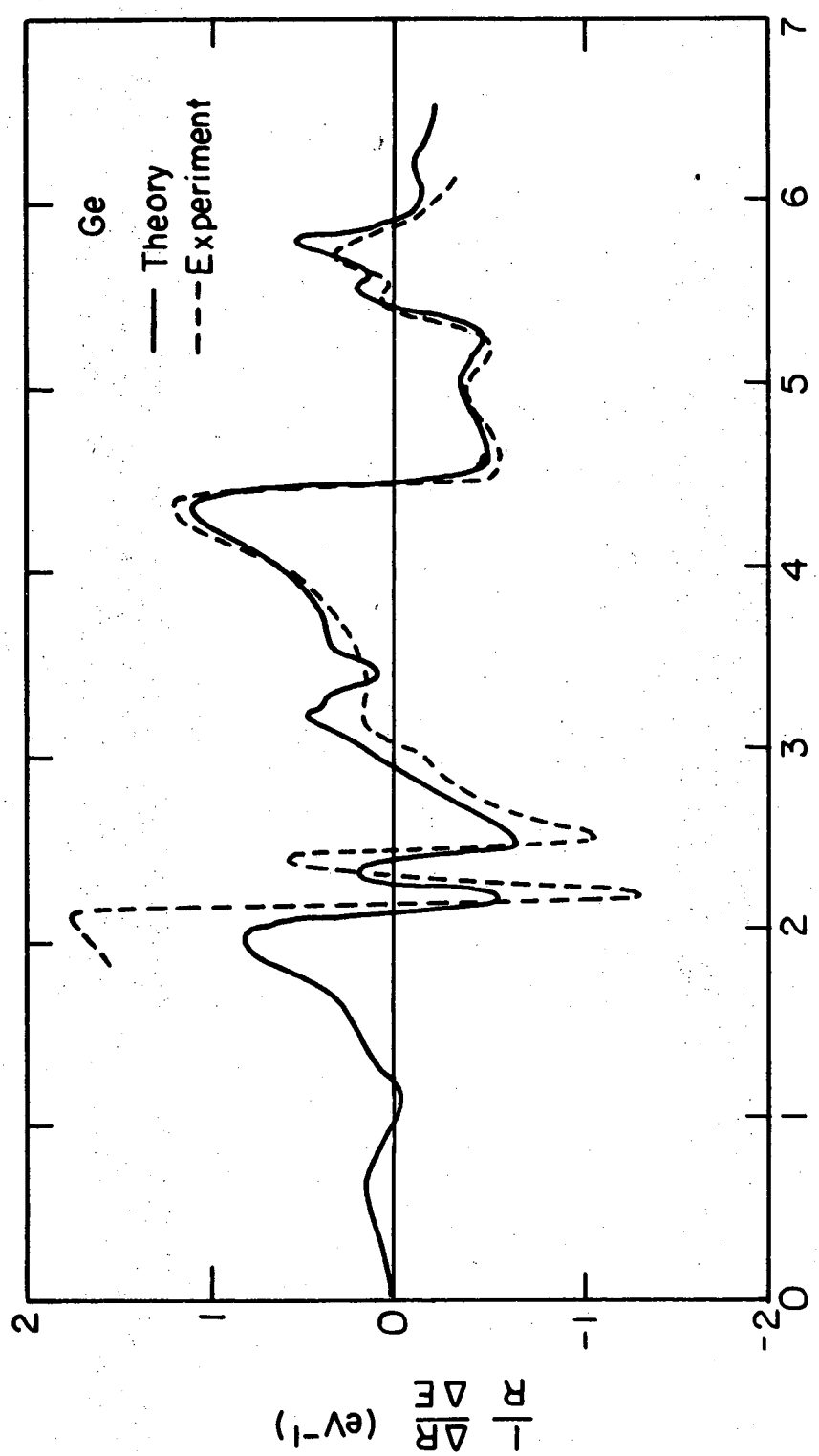

Fig. 13.

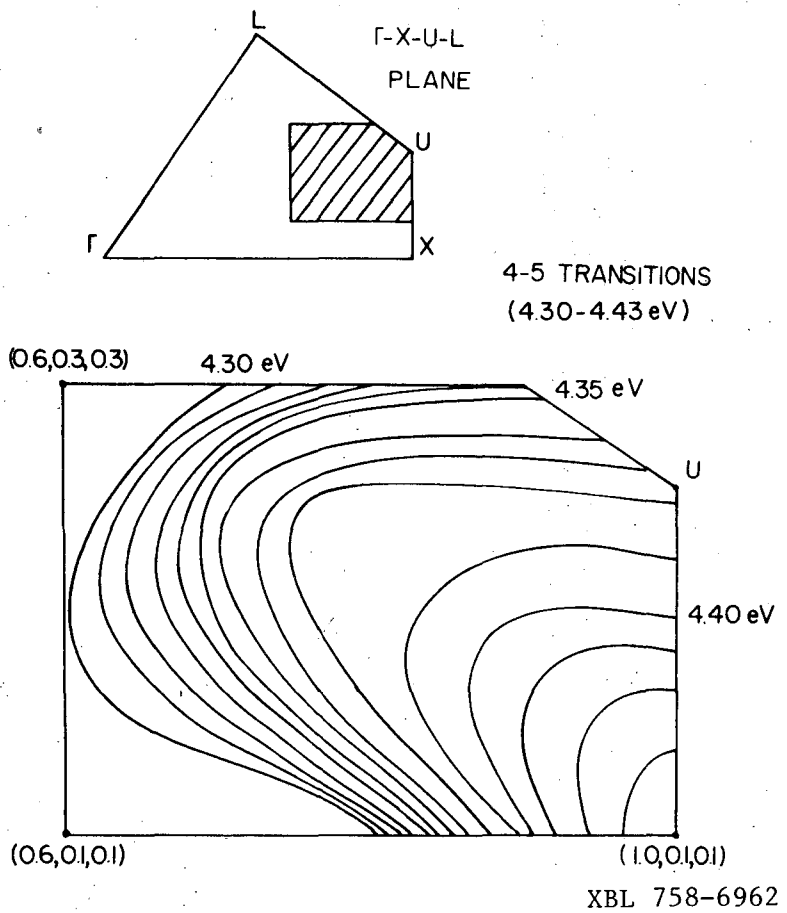
L
Γ-X-U-L
PLANE
U
Γ
X
4-5 TRANSITIONS
(4.30-4.43 eV)
(0.6,0.3,0.3)
4.30 eV
4.35 eV
U
4.40 eV
(0.6,0.1,0.1)
(1.0,0.1,0.1)
XBL 758-6962

Fig. 14.

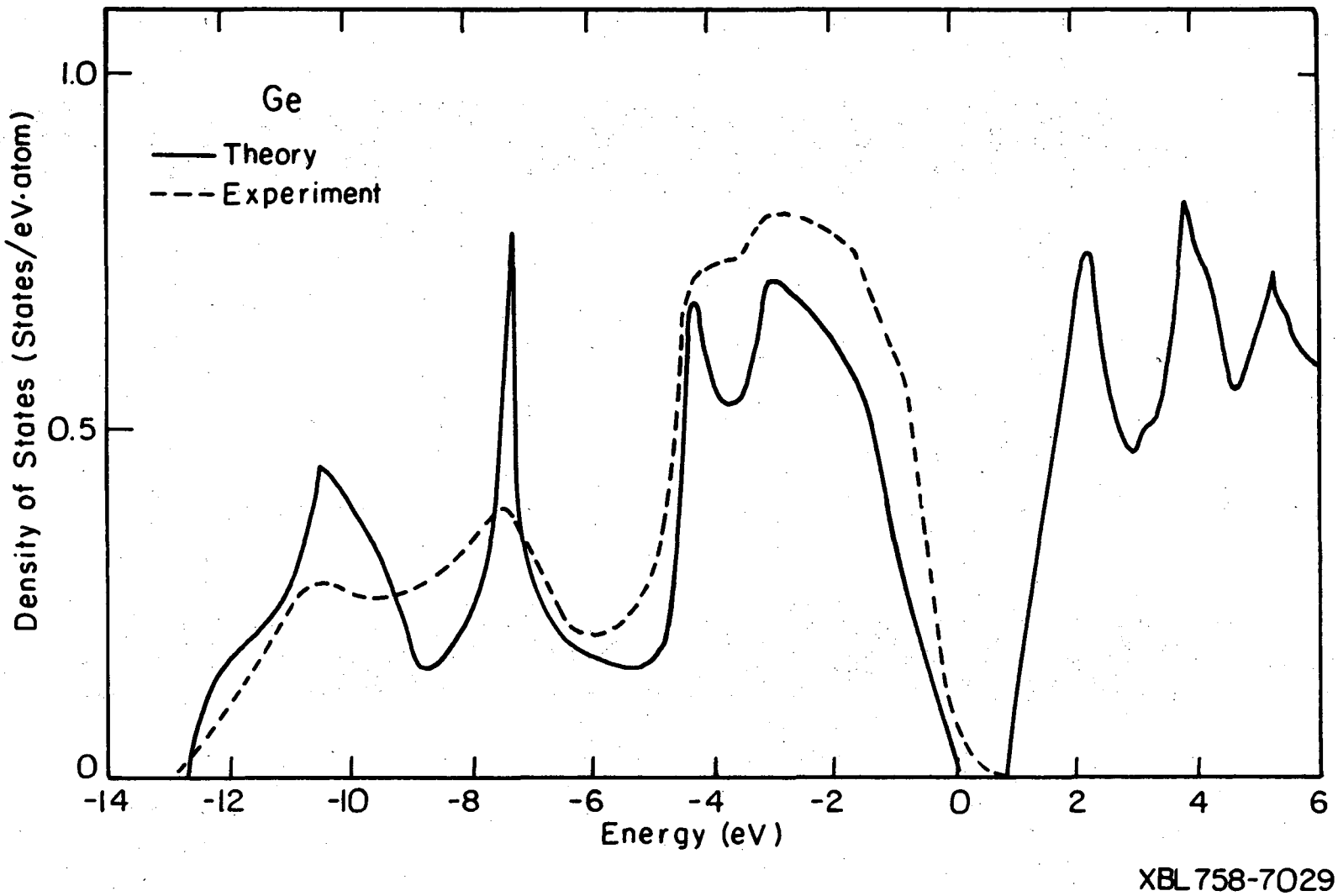

Fig. 15.

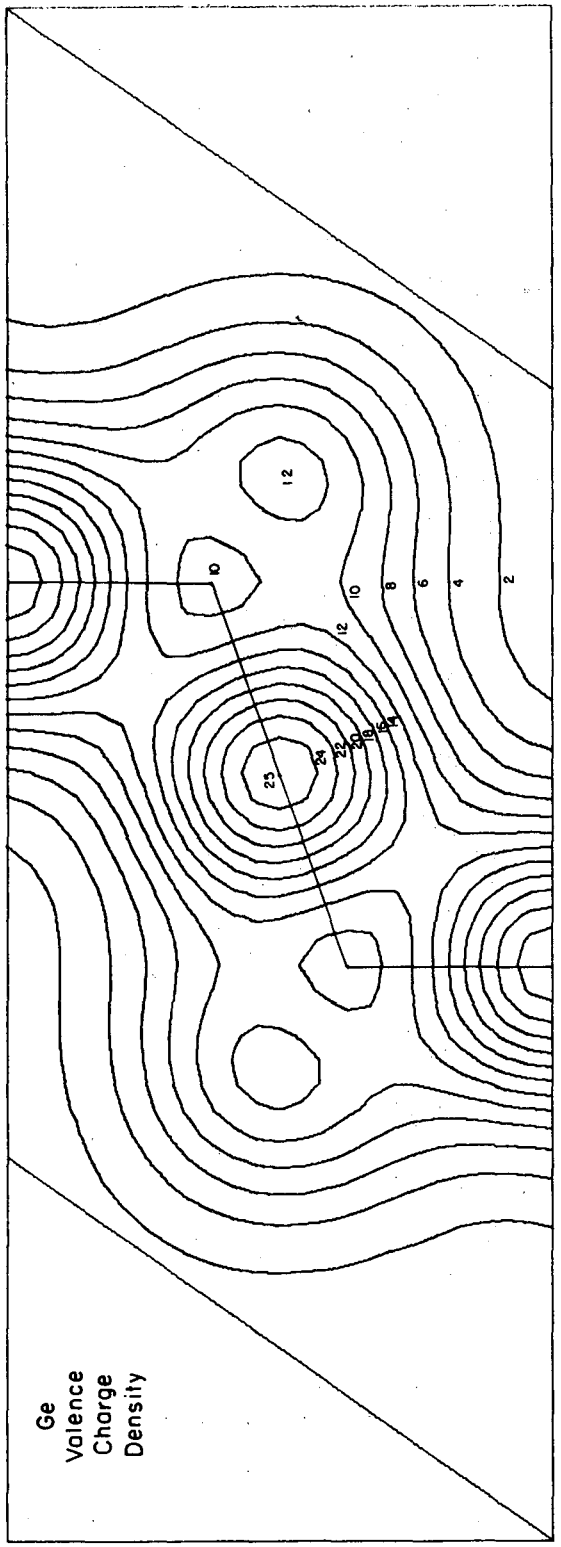

XBL 758-7059

Fig. 16.

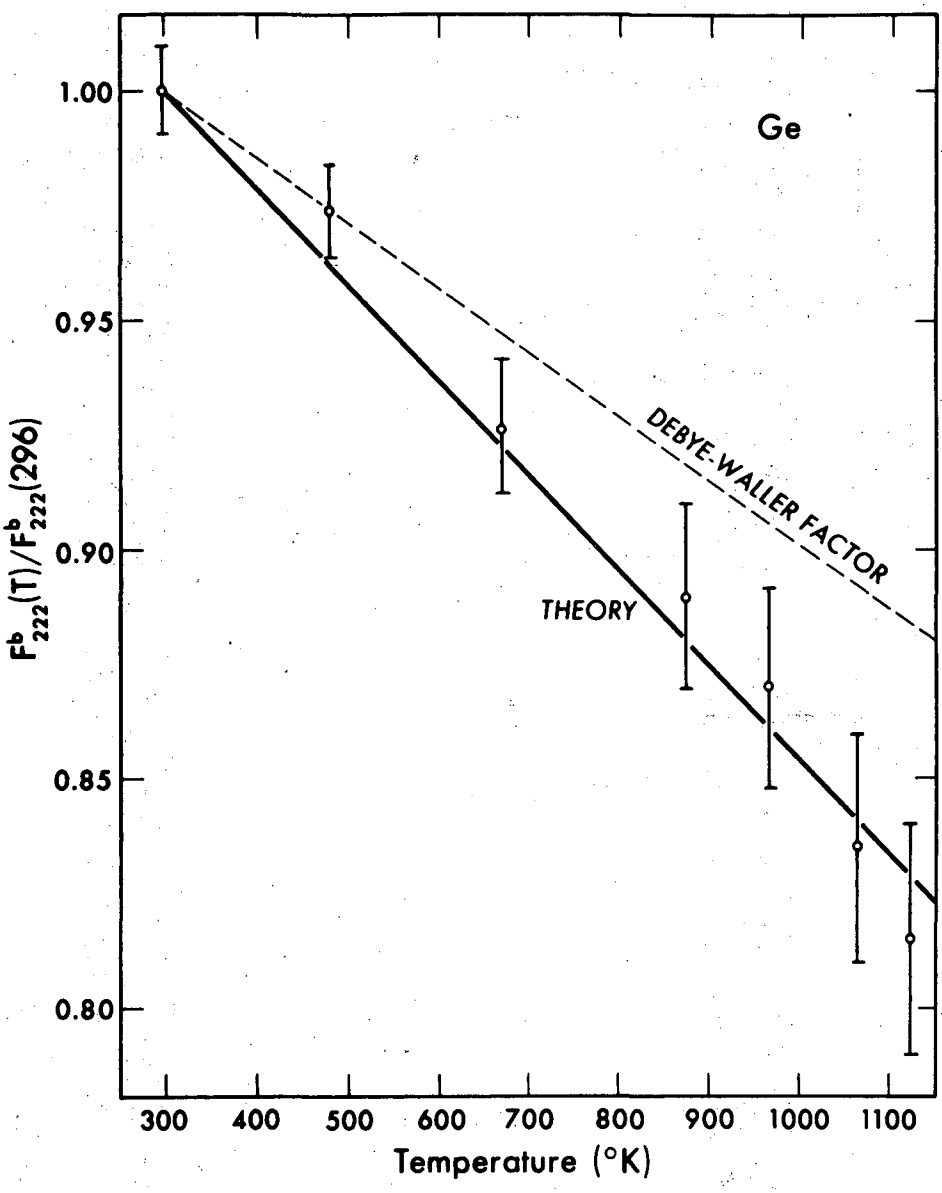

XBL 758-6954

Fig. 17.

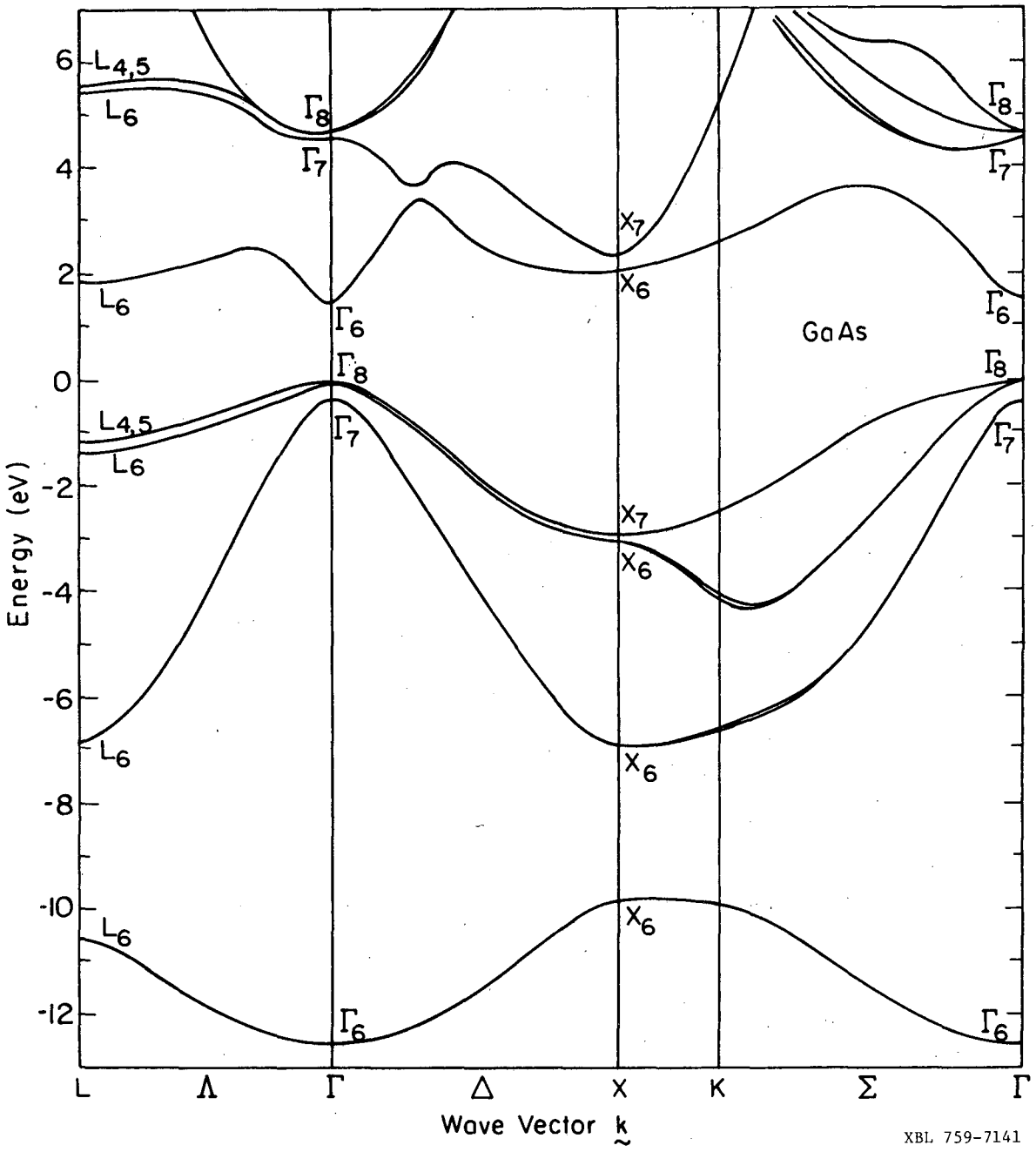
6
4
2
0
-2
-4
-6
-8
-10
-12
Energy (eV)
L4,5
L6
Γ8
Γ7
Γ6
X7
X6
GaAs
L
Λ
Γ
Δ
X
K
Σ
Γ
Wave Vector k
XBL 759-7141

Fig. 18.

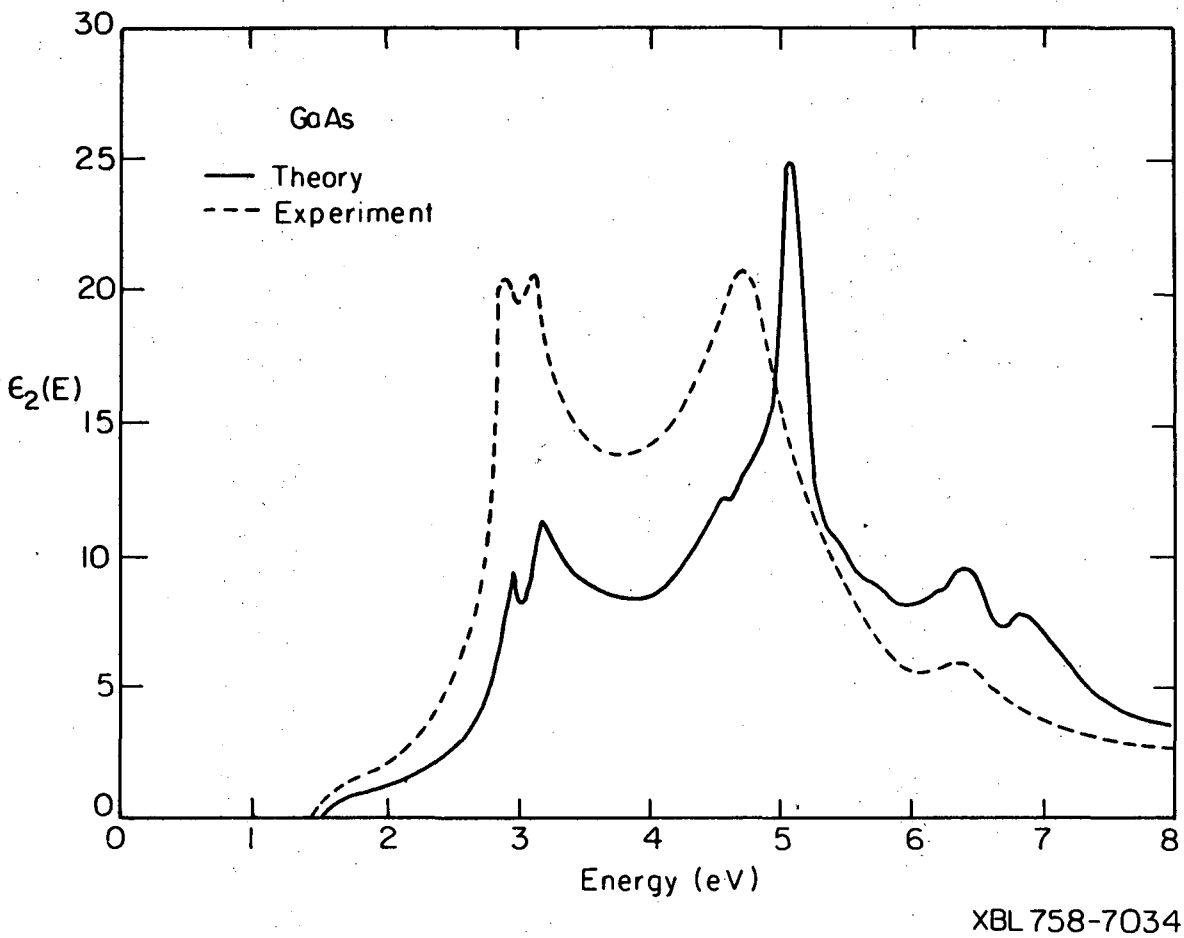

Fig 19a.

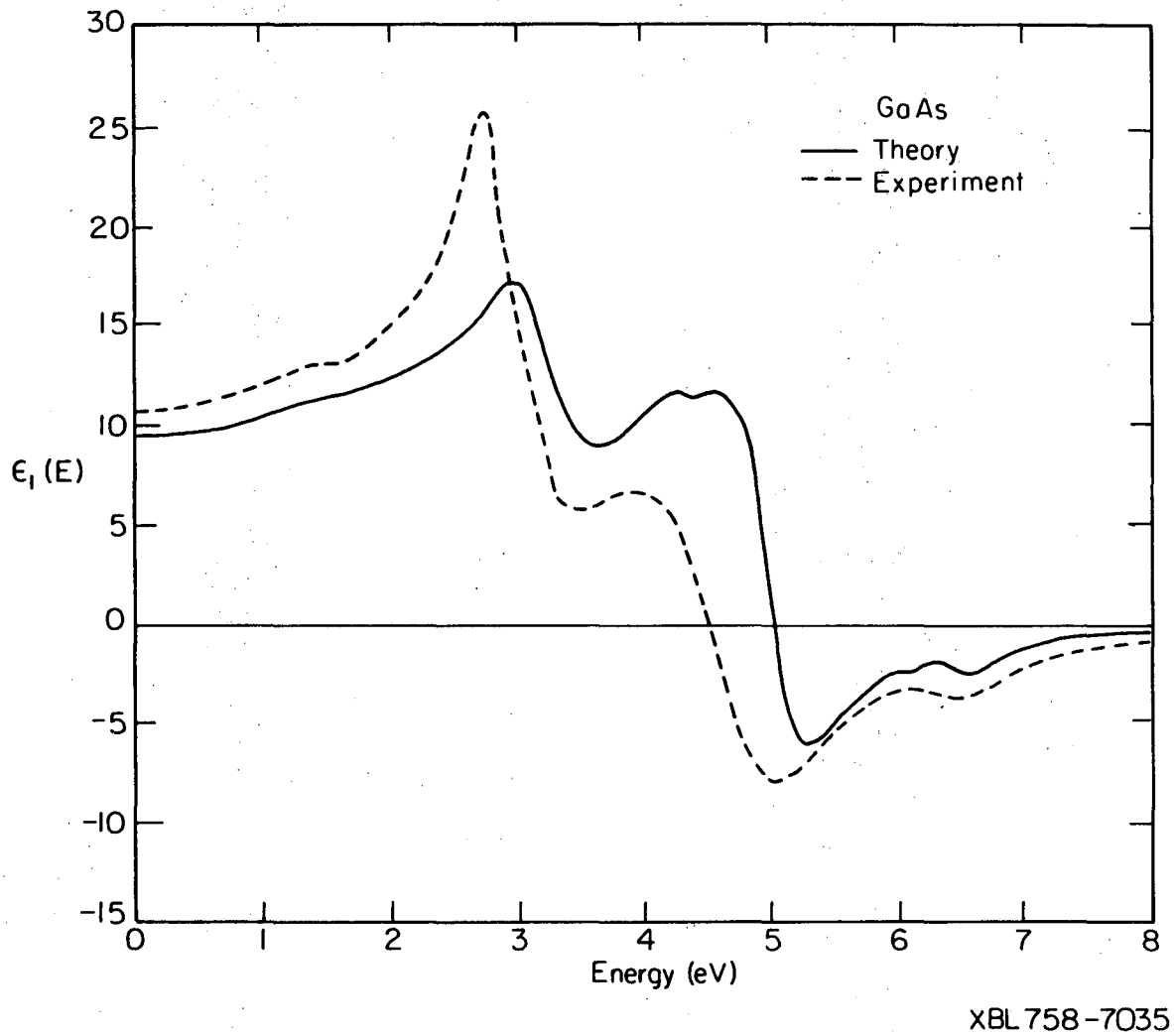
GaAs
Theory
Experiment
$\epsilon_1(E)$
Energy (eV)
30
25
20
15
10
5
0
-5
-10
-15
0
1
2
3
4
5
6
7
8
XBL758-7035

Fig. 19b.

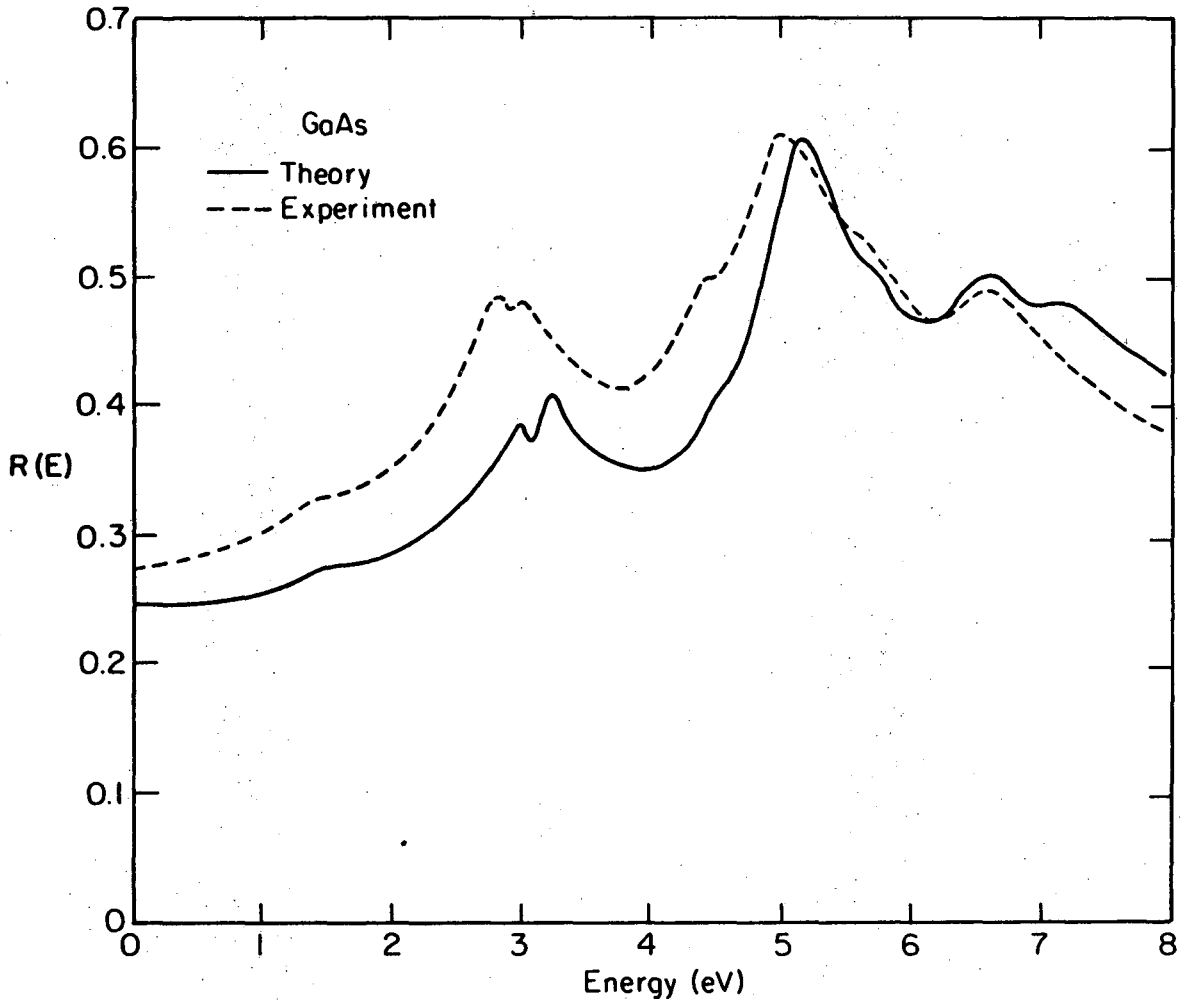

Fig. 19c.

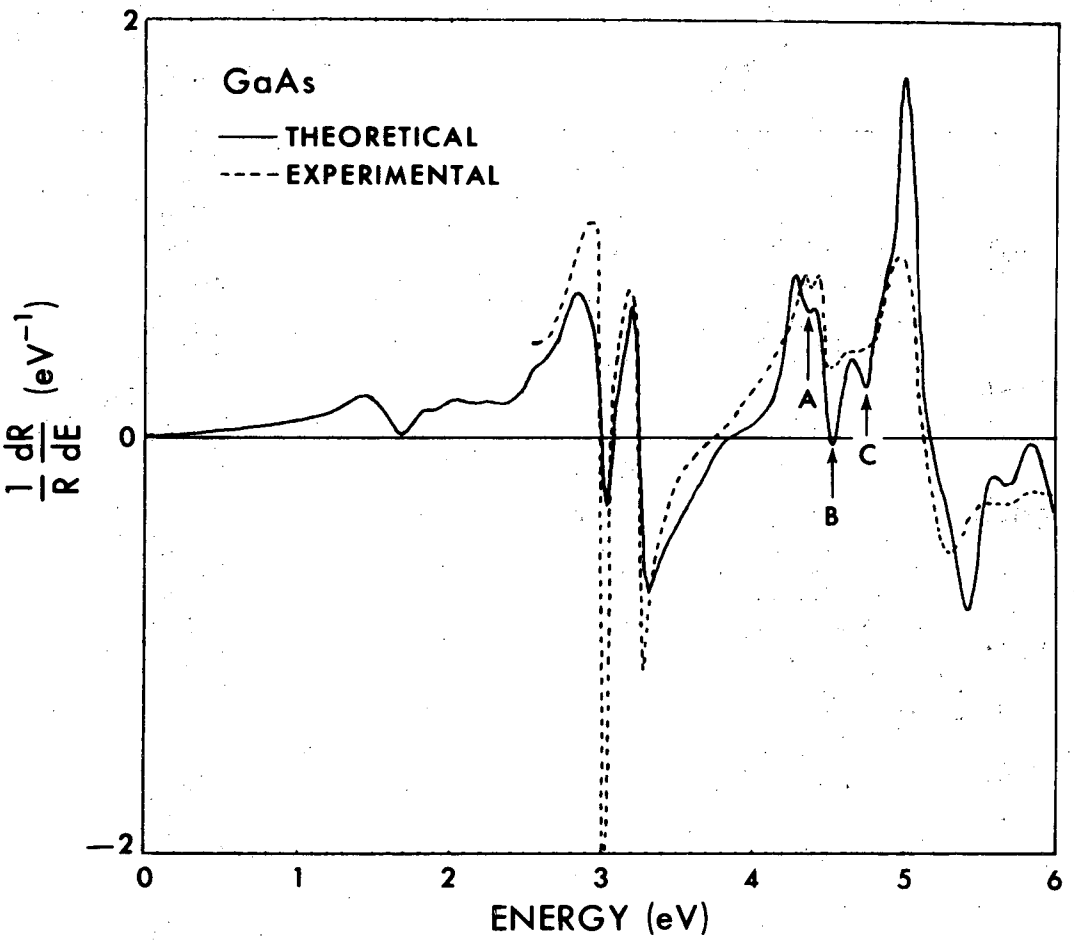

XBL 758-6947

Fig. 20.

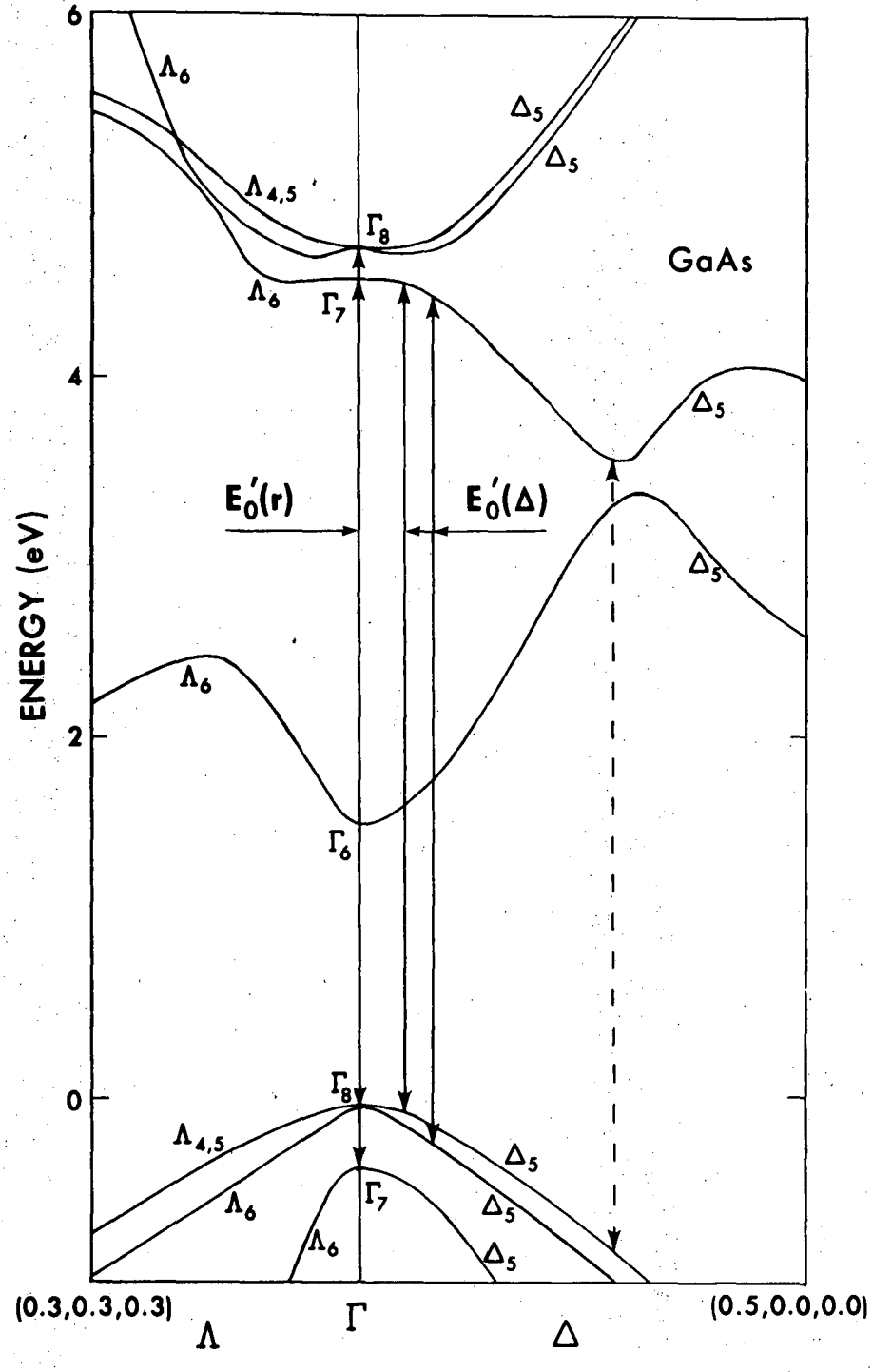

XBL 758-6951

Fig. 21.

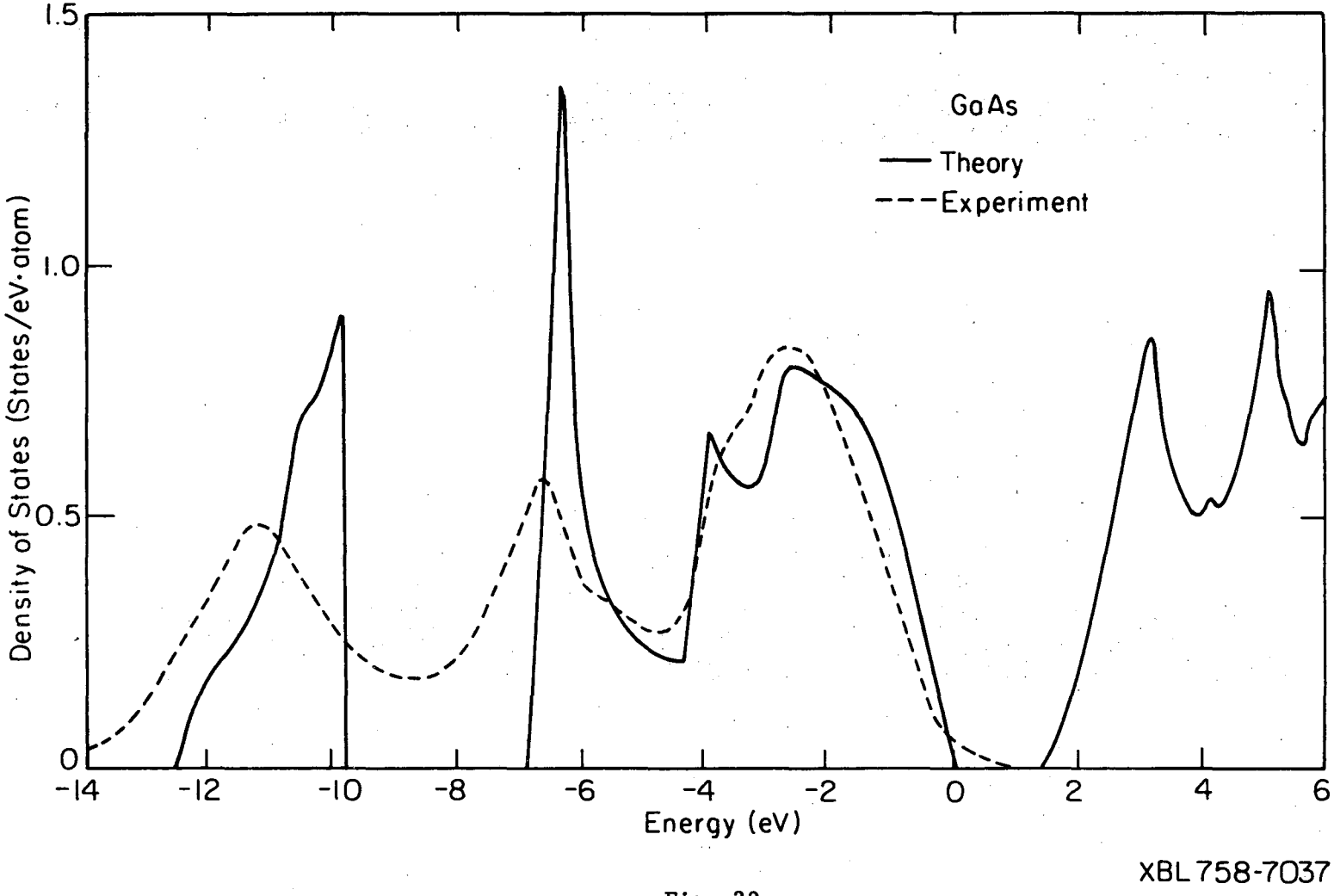
GaAs
Theory
Experiment
Density of States (States/eV·atom)
Energy (eV)
1.5
1.0
0.5
0
-14
-12
-10
-8
-6
-4
-2
0
2
4
6
XBL 758-7037

Fig. 22.

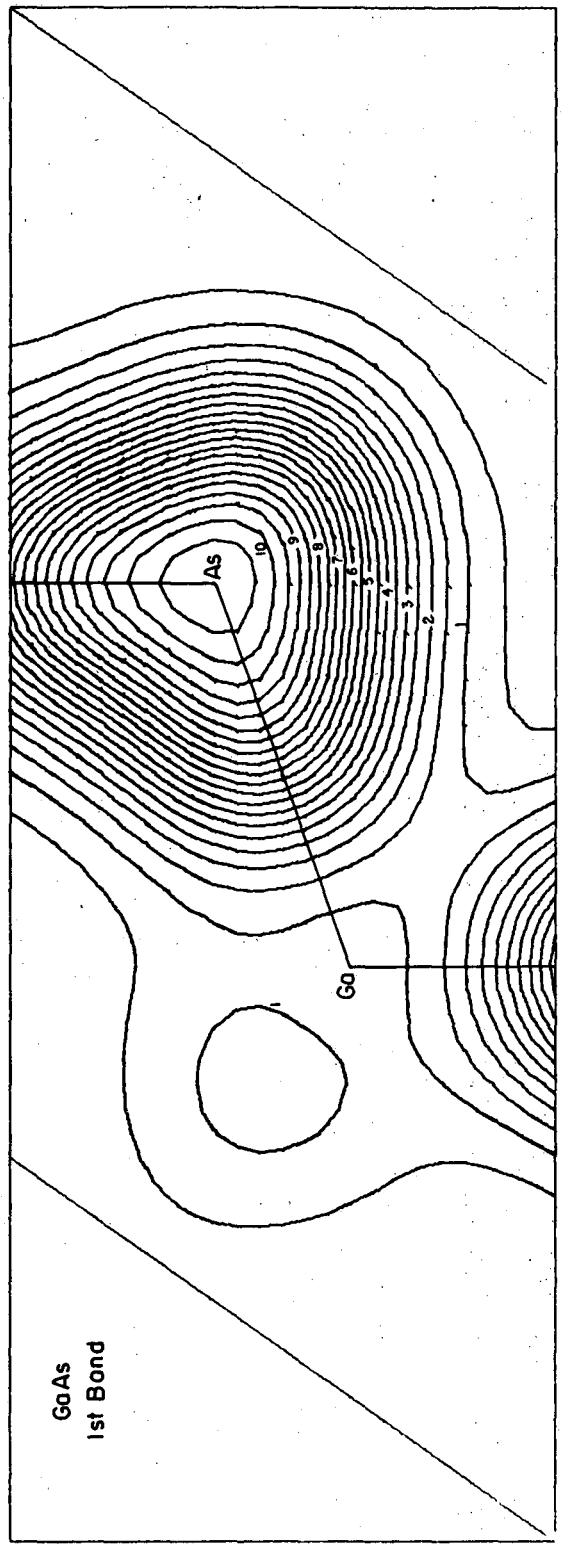

XBL 758-7057

Fig. 23.

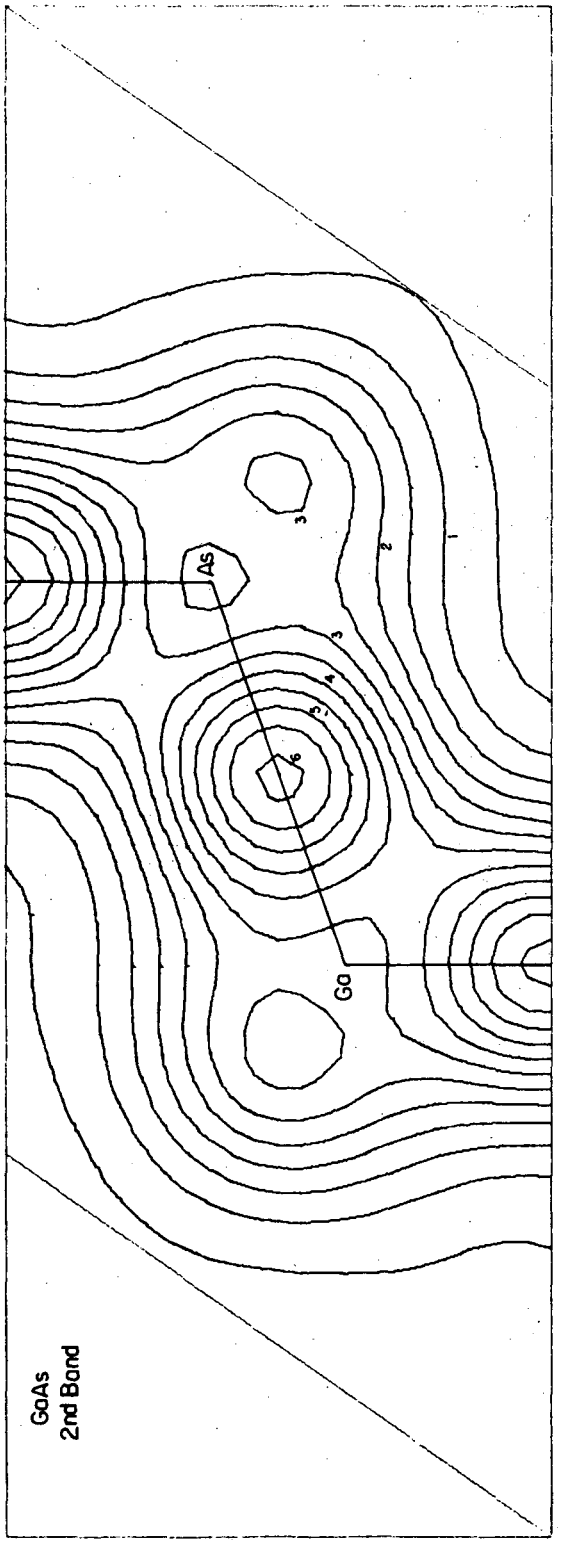

Fig. 23.

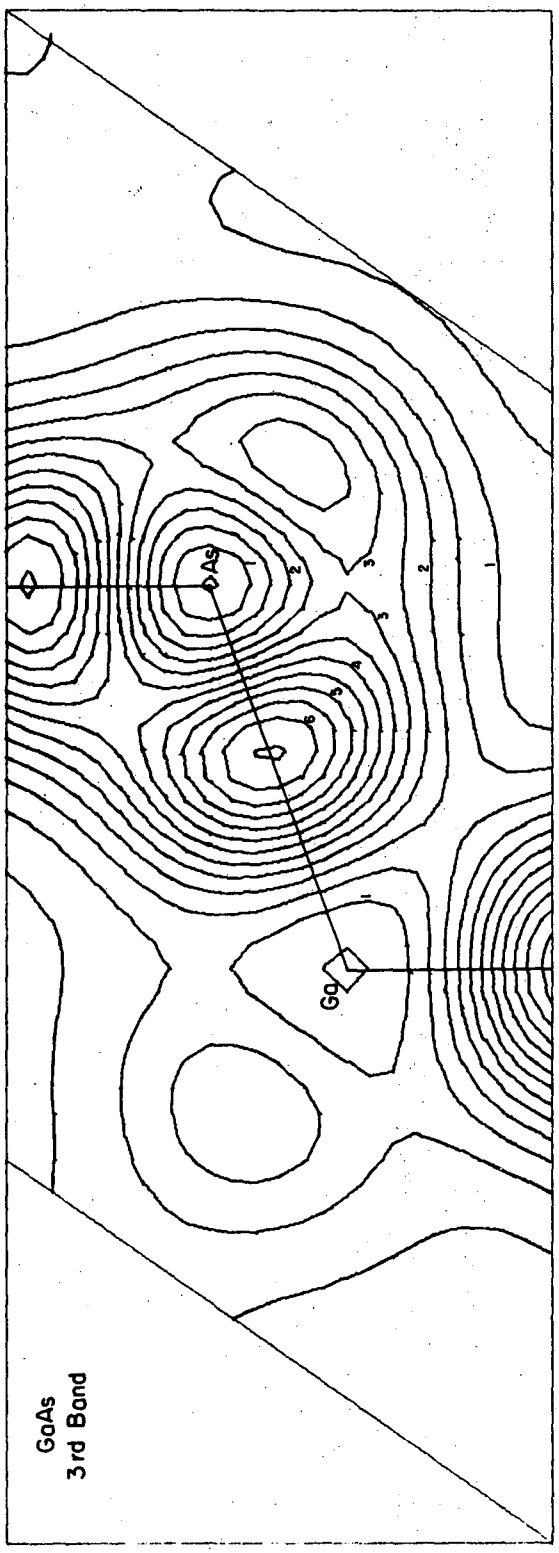

Fig. 23.

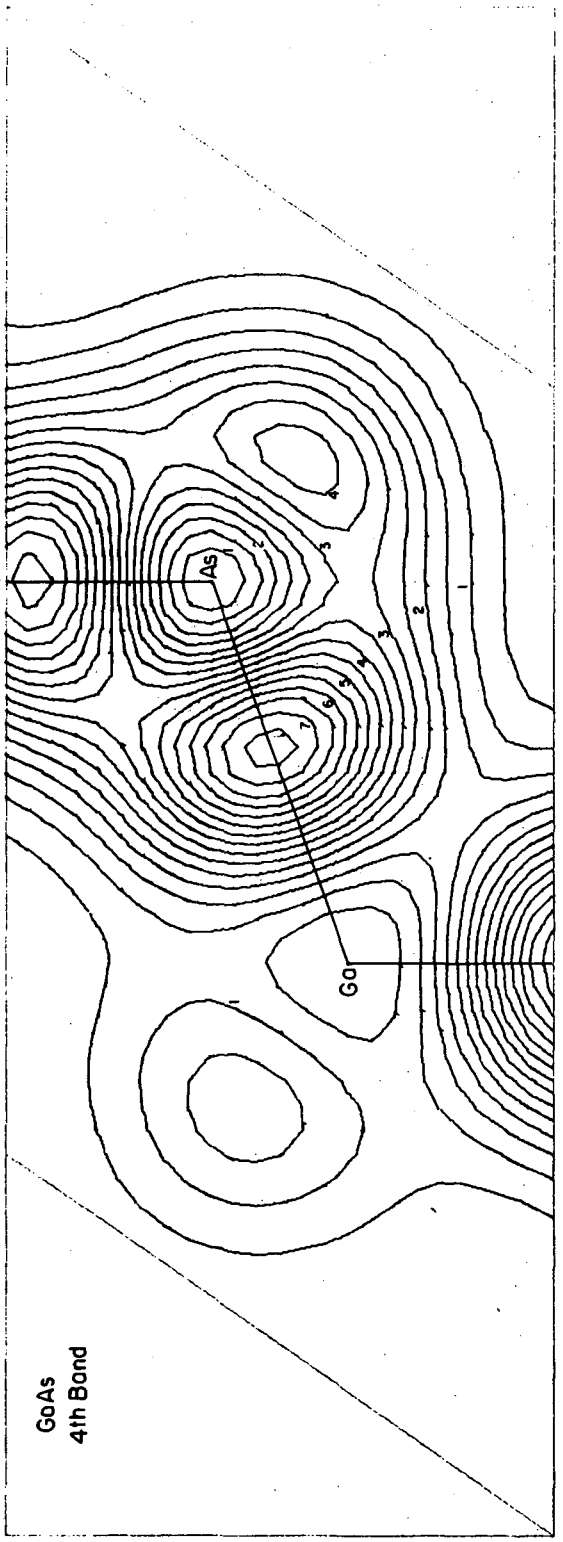

XBL758-7054

Fig. 23.

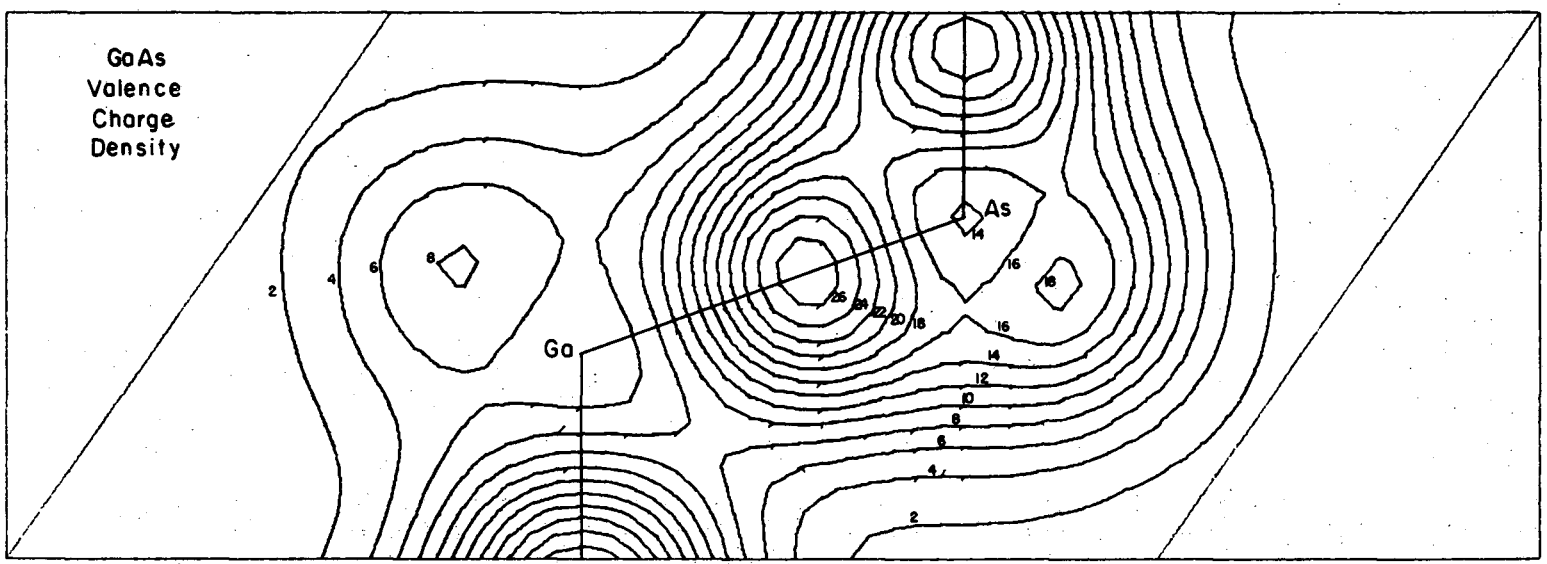

XBL758-7053

Fig. 24.

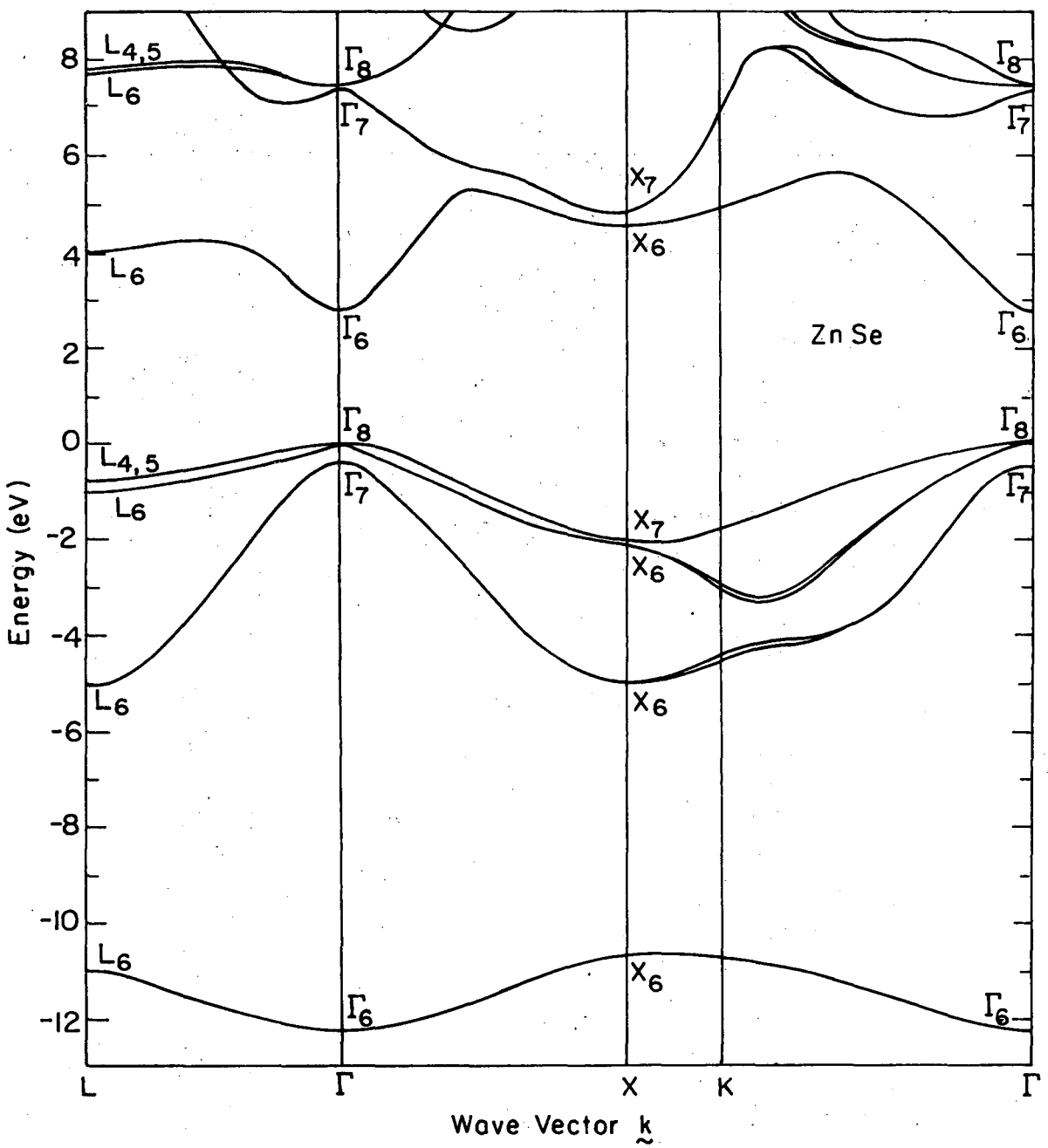

XBL 759-7144

Fig. 25.

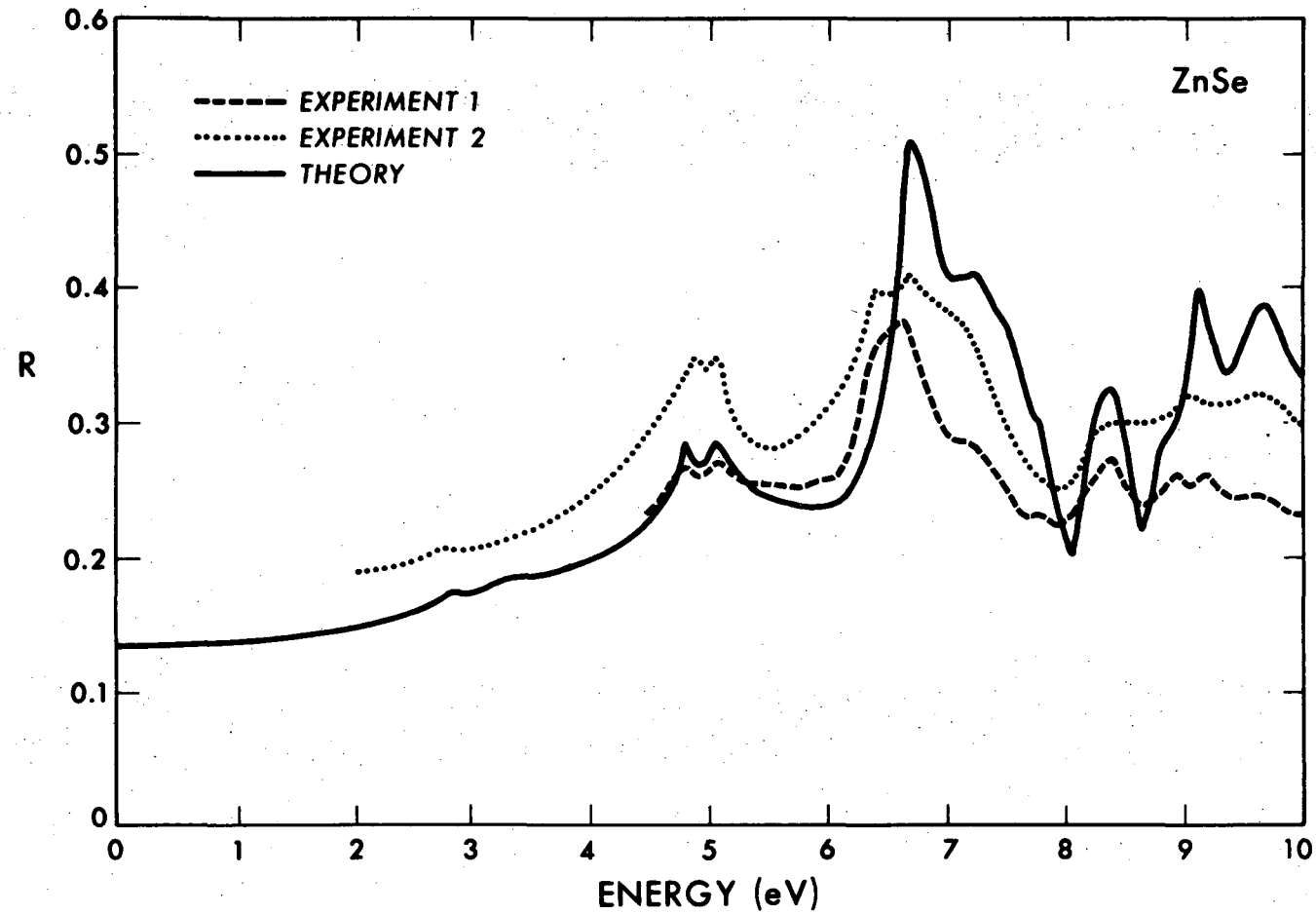

XBL-758-6945

Fig. 26.

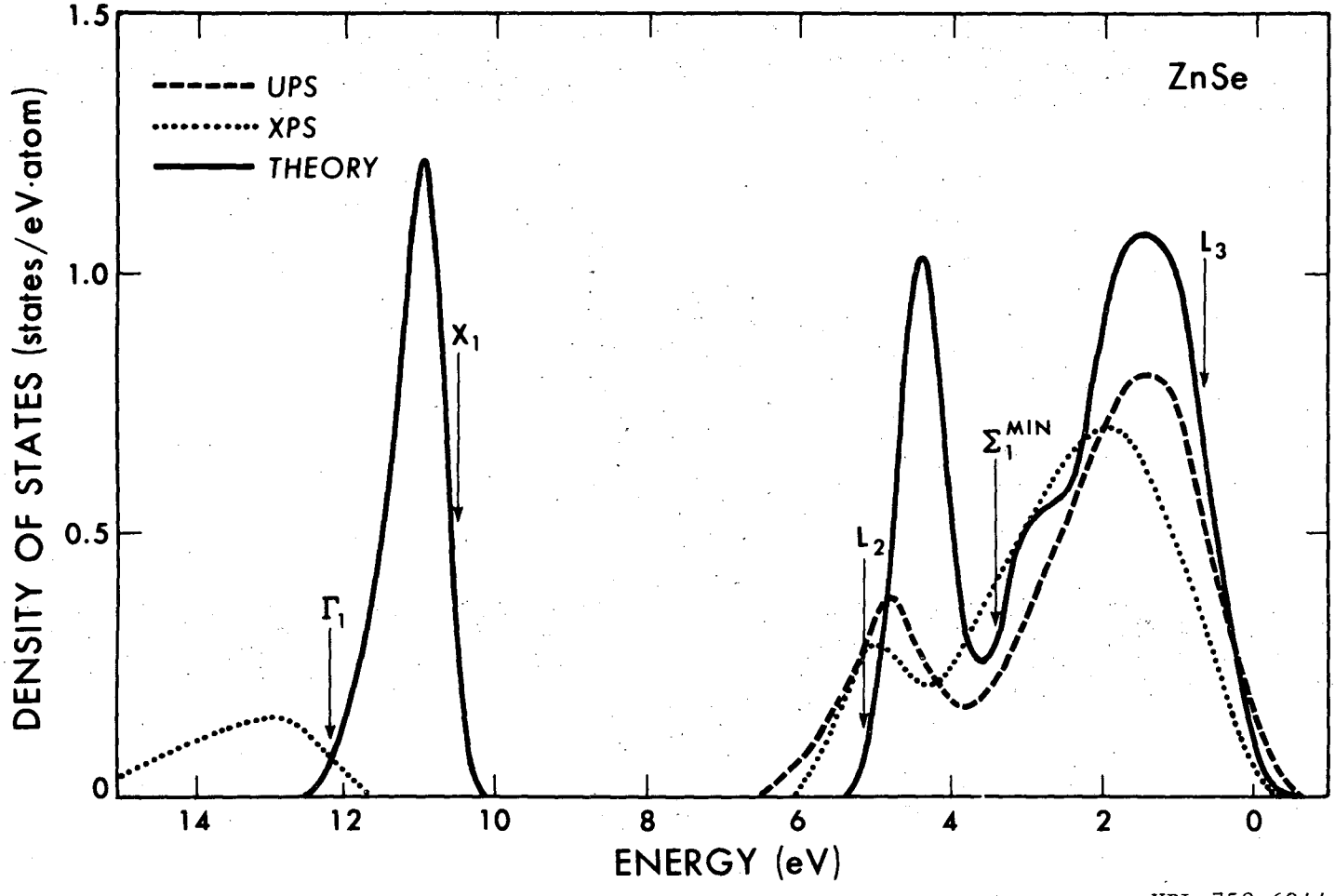

XBL-758-6944

Fig. 27.

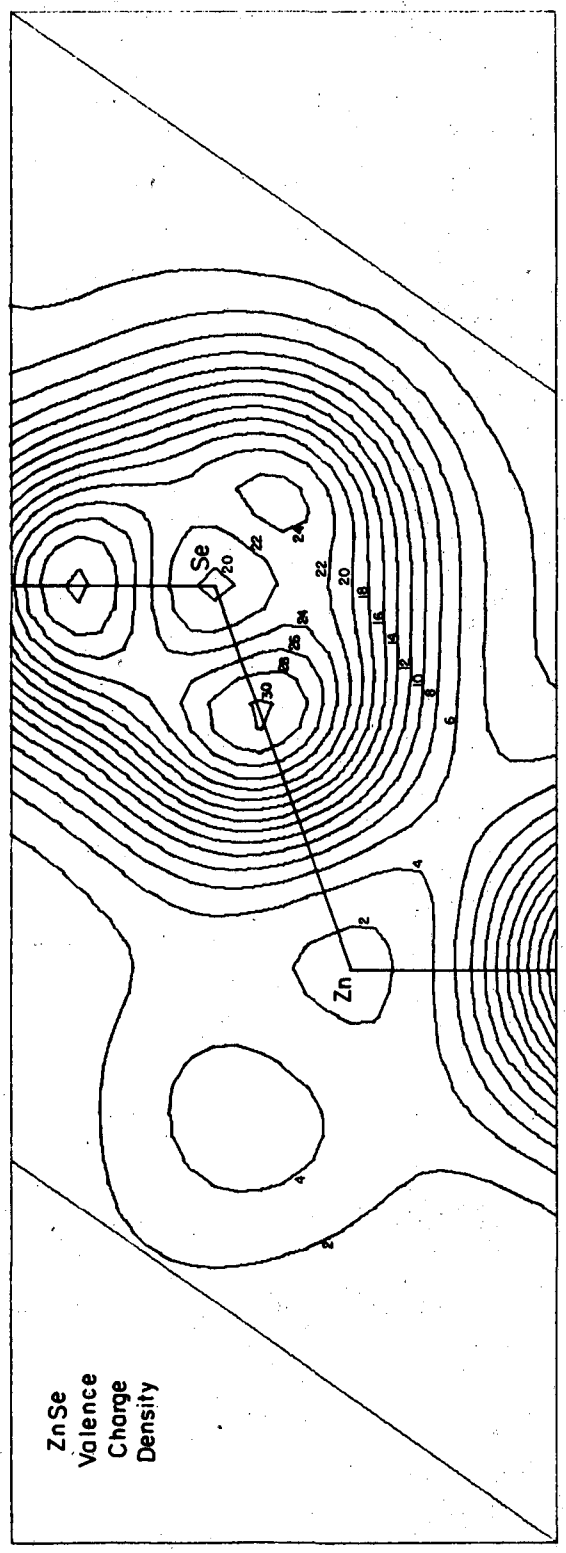

XBL758-7058

Fig. 28.

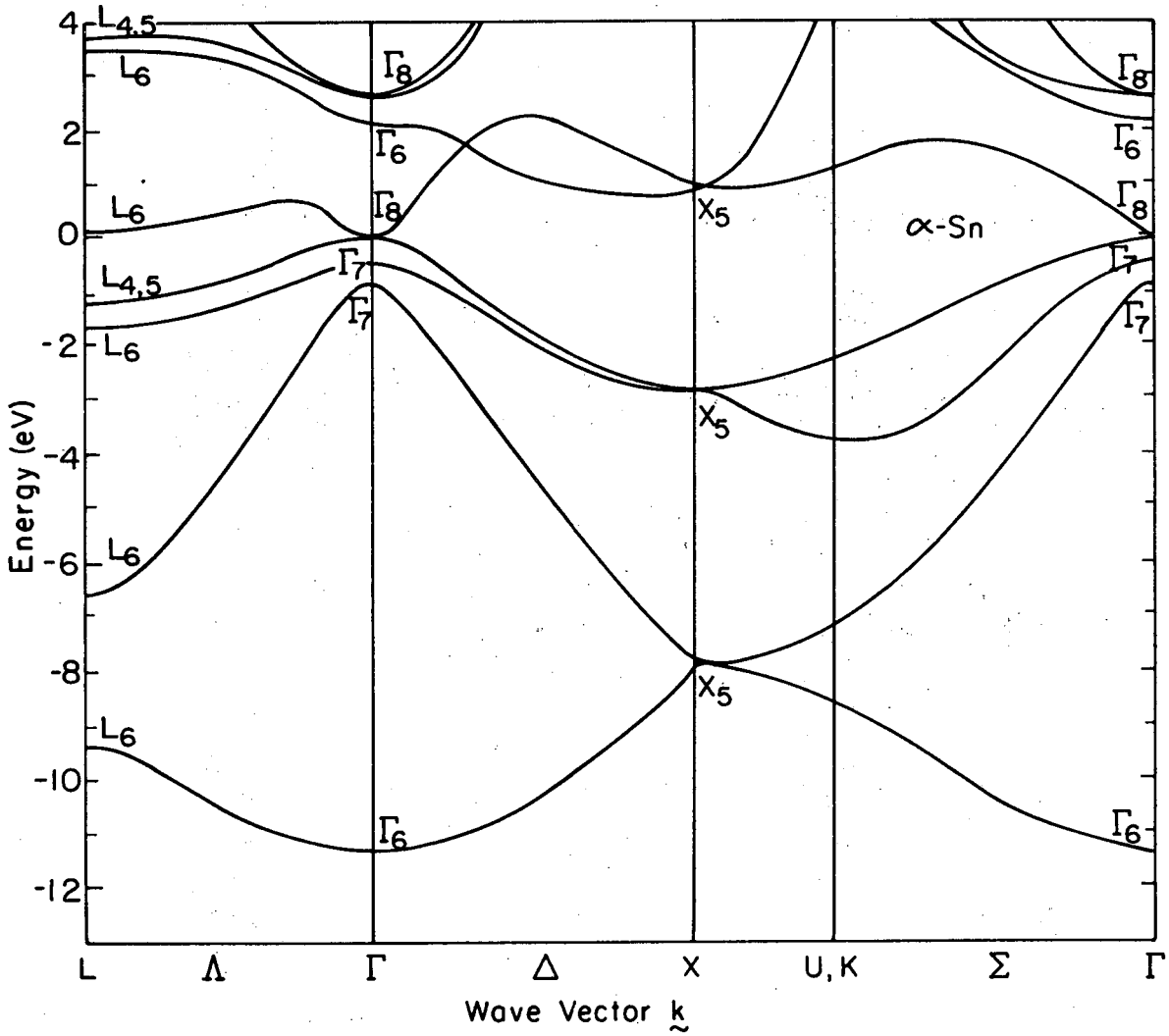
Energy (eV)
4
2
0
-2
-4
-6
-8
-10
-12
L
Λ
Γ
Δ
X
U, K
Σ
Γ
Wave Vector k
L4,5
L6
Γ8
Γ6
Γ7
X5
α-Sn
XBL 759-7140

Fig. 29.

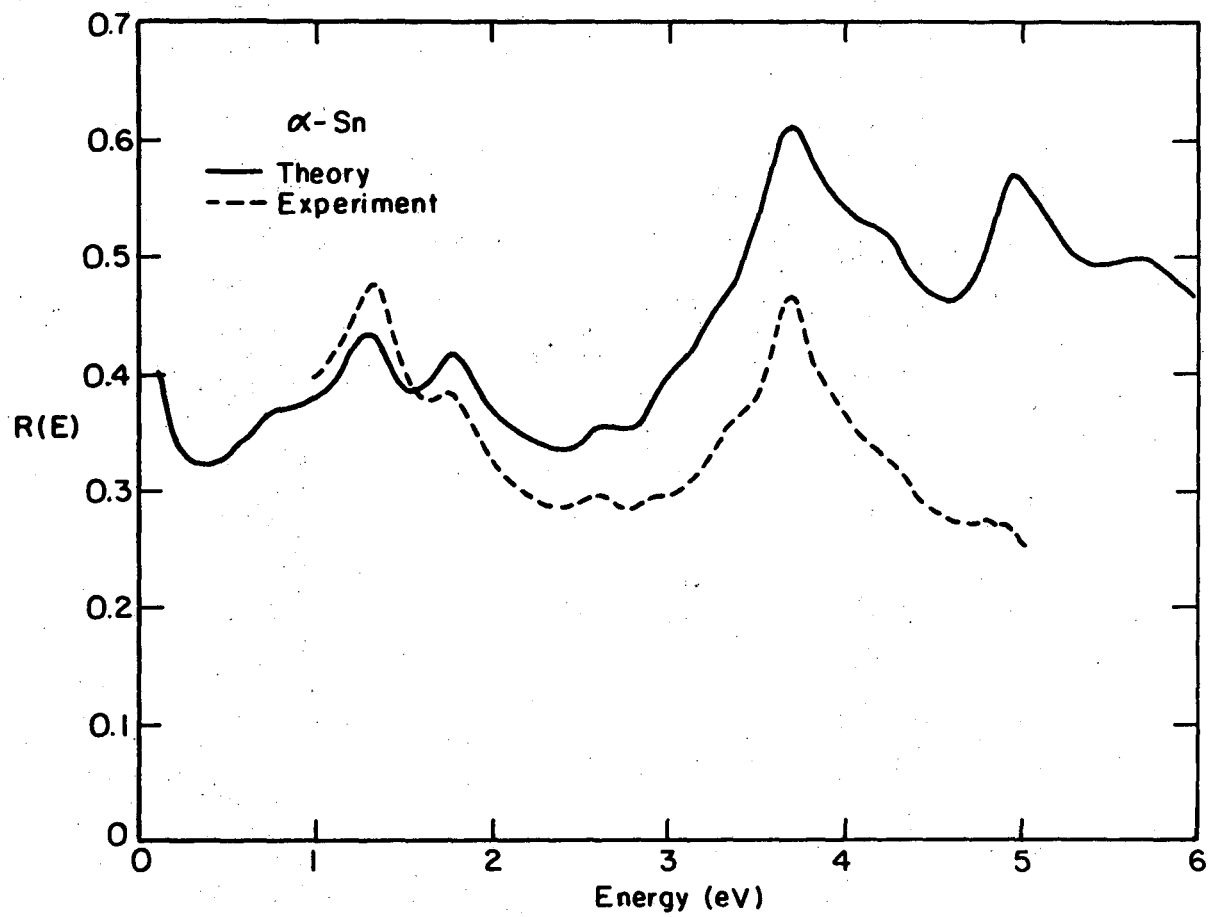

XBL 758-7040

Fig. 30.

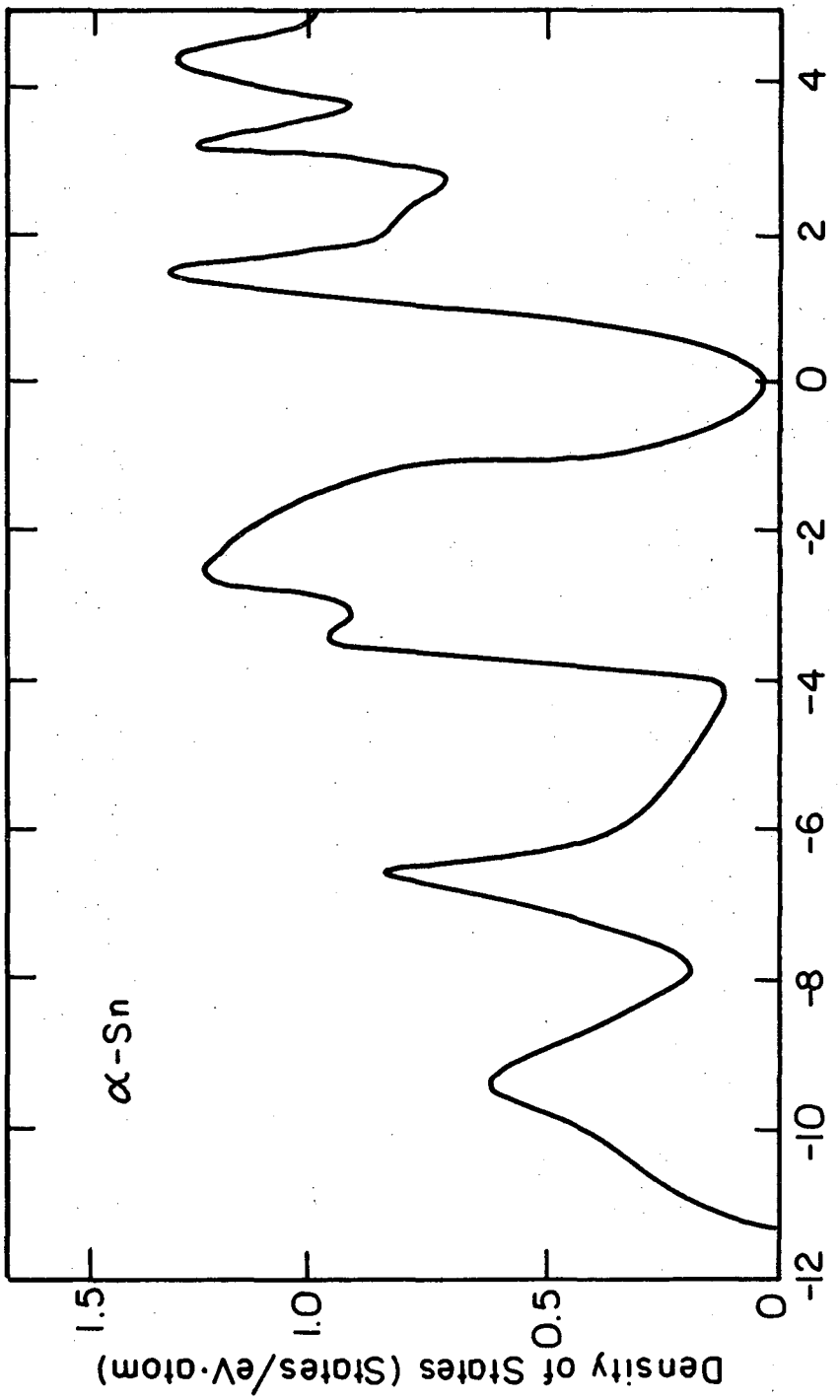
α-Sn
Density of States (States/eV·atom)
0
0.5
1.0
1.5
-12
-10
-8
-6
-4
-2
0
2
4
Energy (eV)
XBL758-7039

Fig. 31.

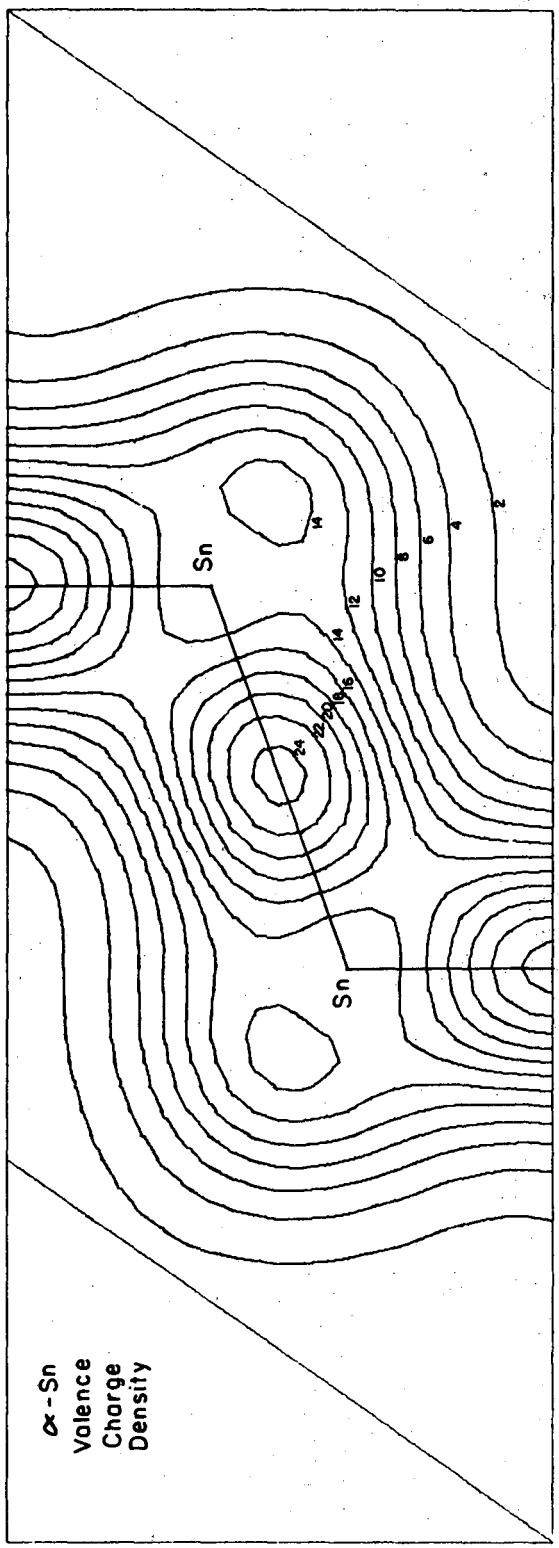

XBL758-7063

Fig. 32.

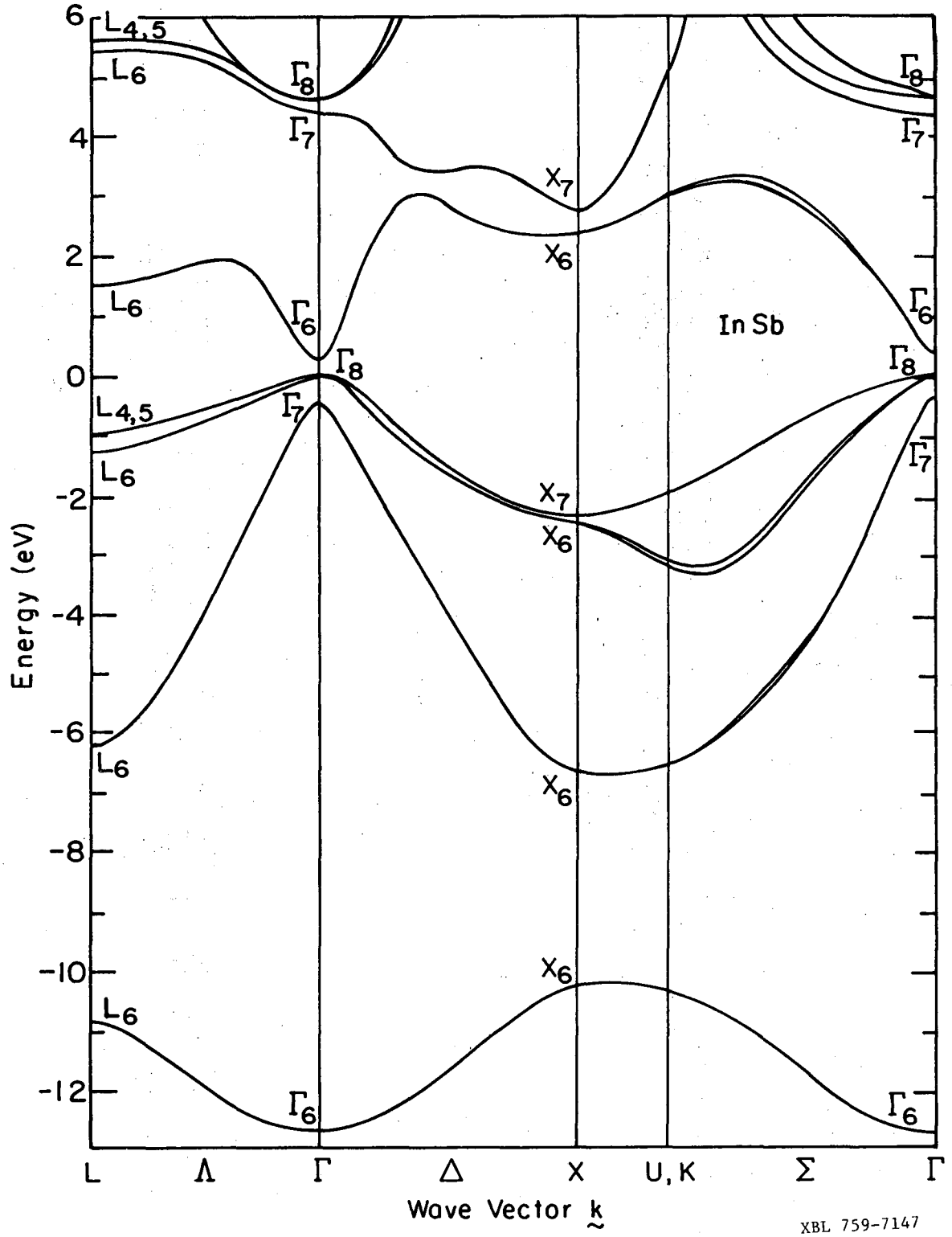
6
4
2
0
-2
-4
-6
-8
-10
-12
Energy (eV)
L4,5
L6
Γ8
Γ7
X7
X6
Γ6
In Sb
L
Λ
Γ
Δ
X
U, K
Σ
Γ
Wave Vector k
XBL 759-7147

Fig. 33.

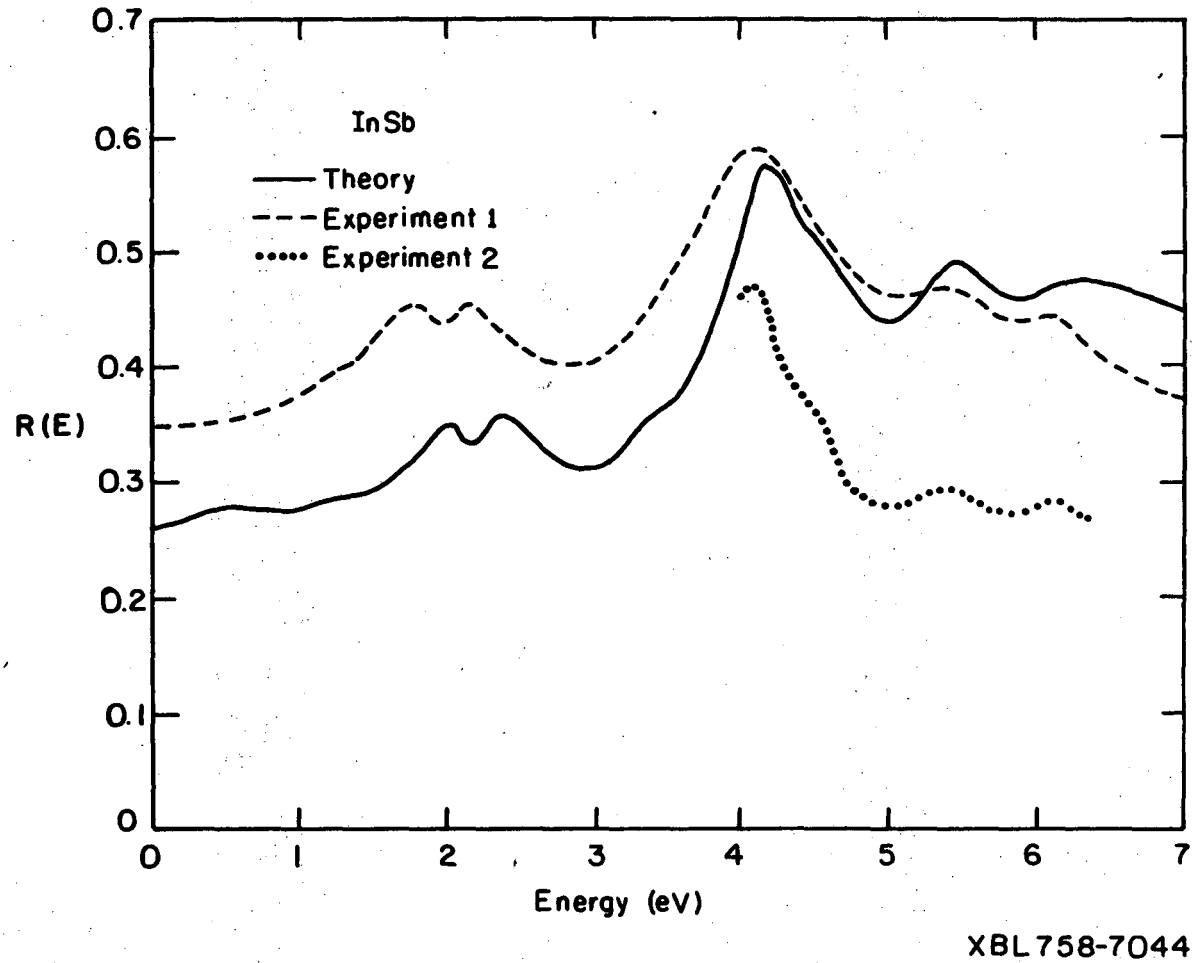

Fig. 34.

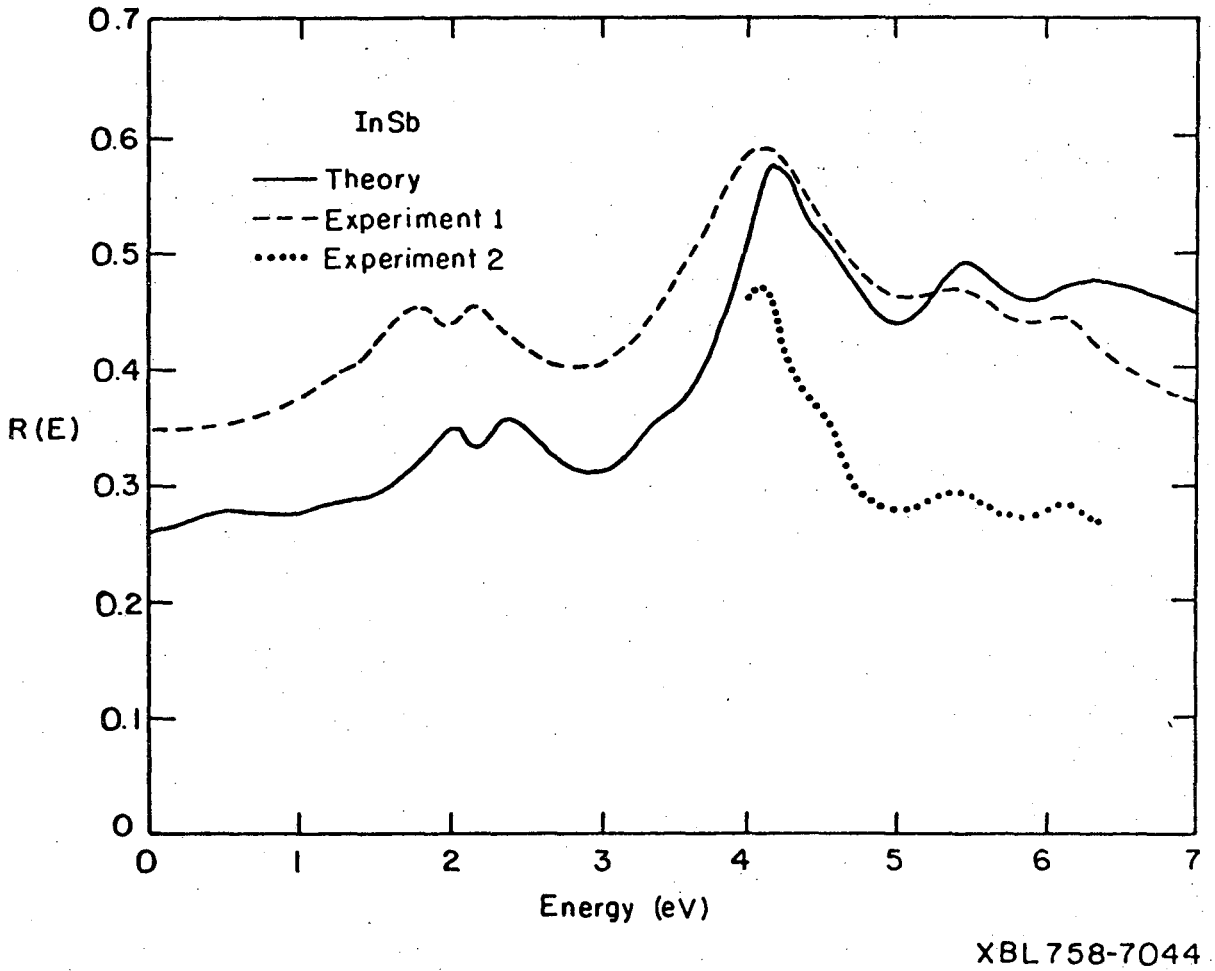
InSb
Theory
Experiment 1
Experiment 2
R(E)
Energy (eV)
0.7
0.6
0.5
0.4
0.3
0.2
0.1
0
0
1
2
3
4
5
6
7
XBL758-7044

Fig. 34.

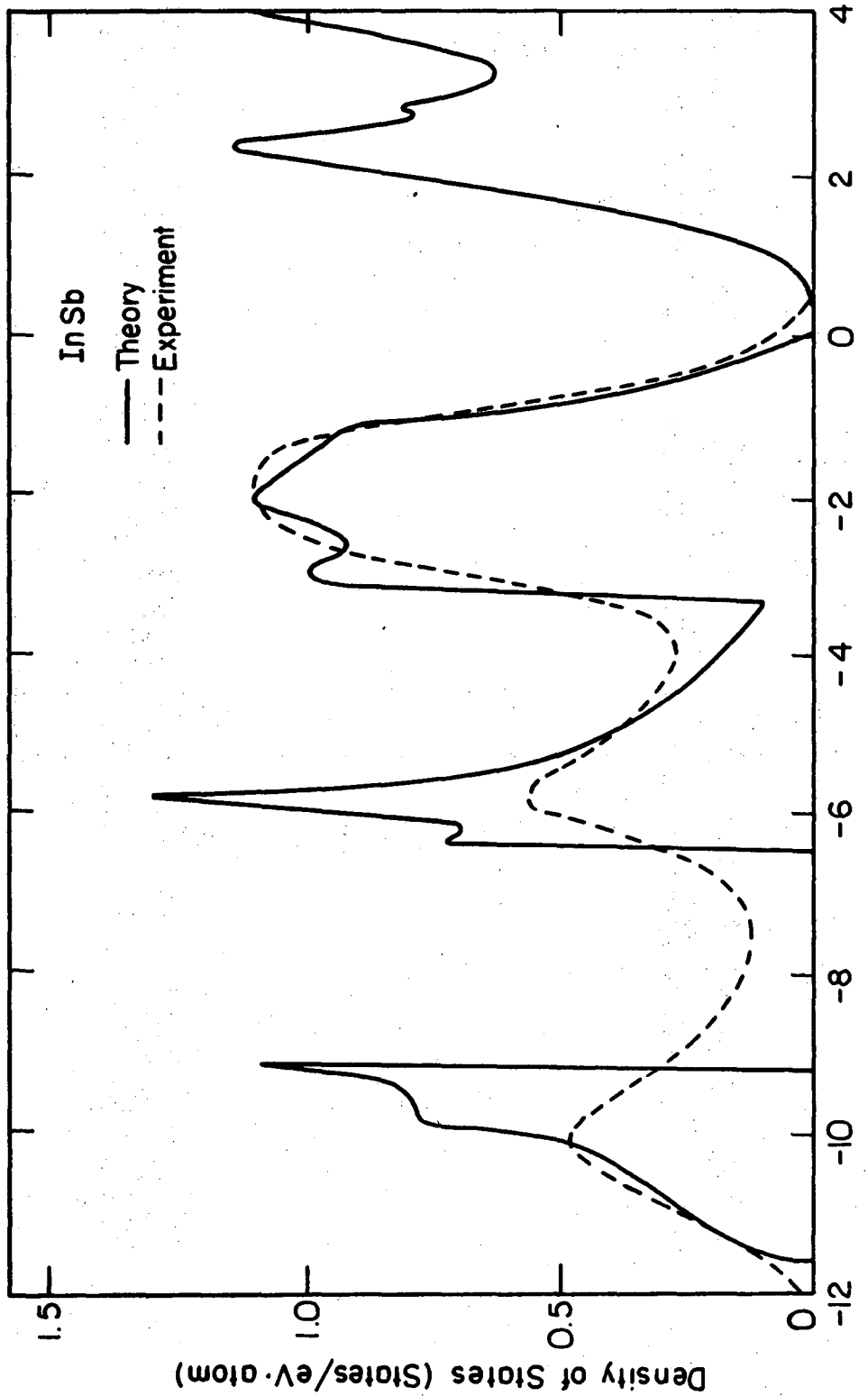

XBL 758-7027

Fig. 36.

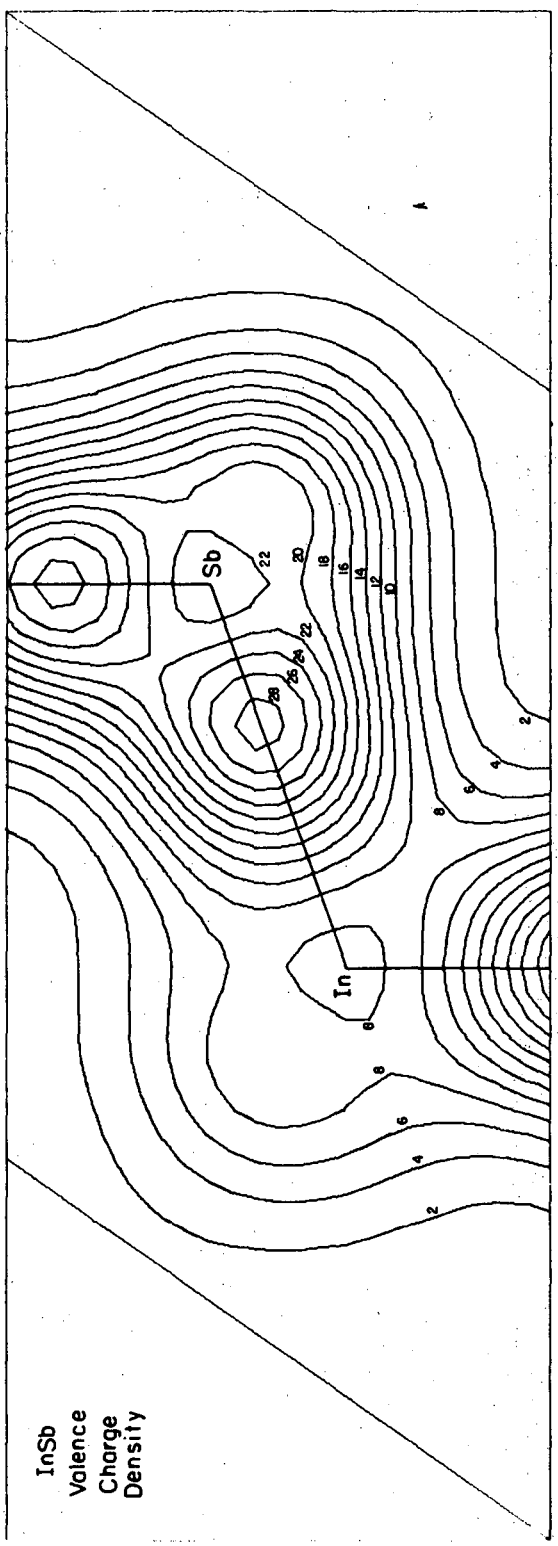

Fig. 37.

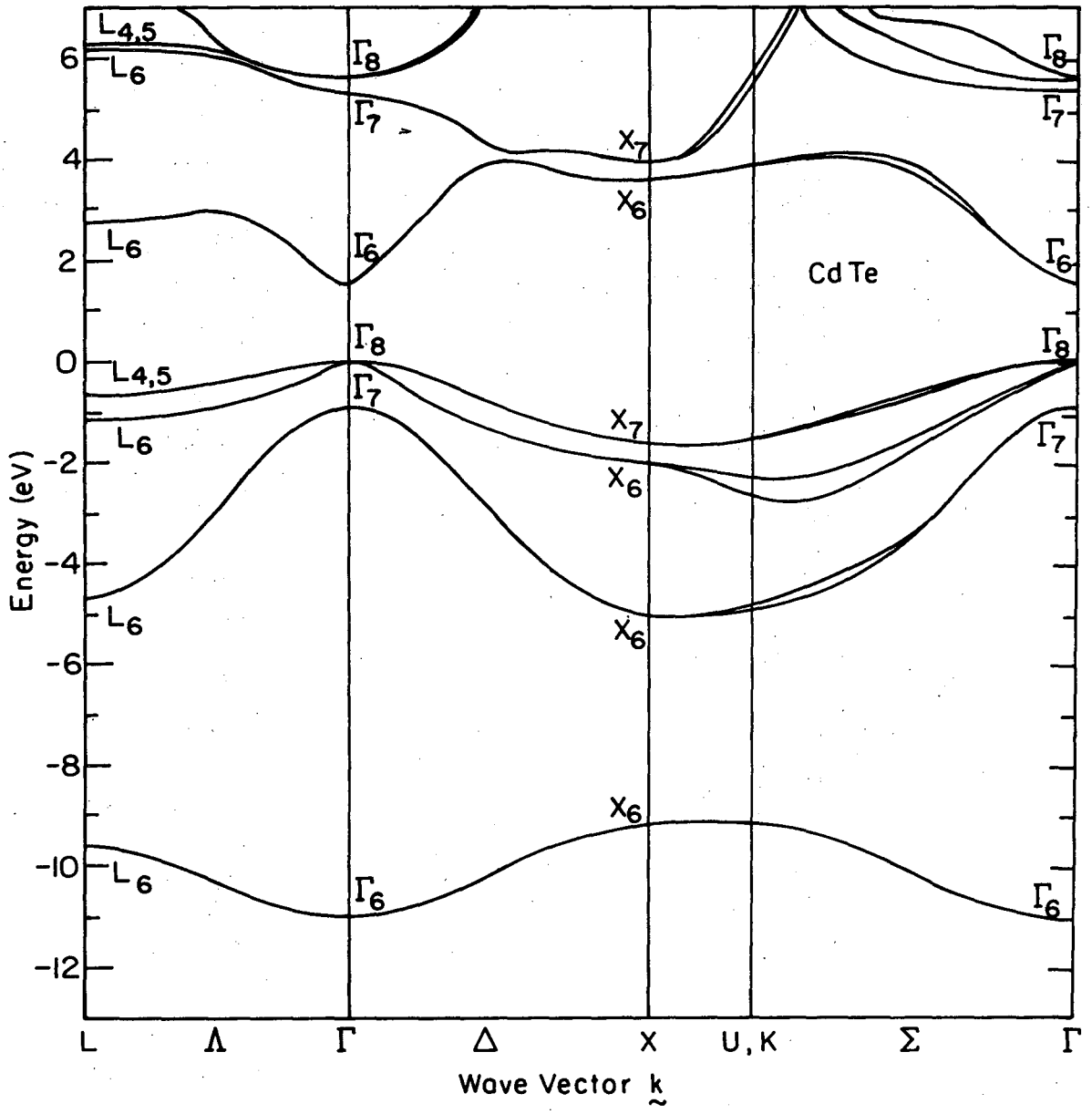

XBL 759-7146

Fig. 38.

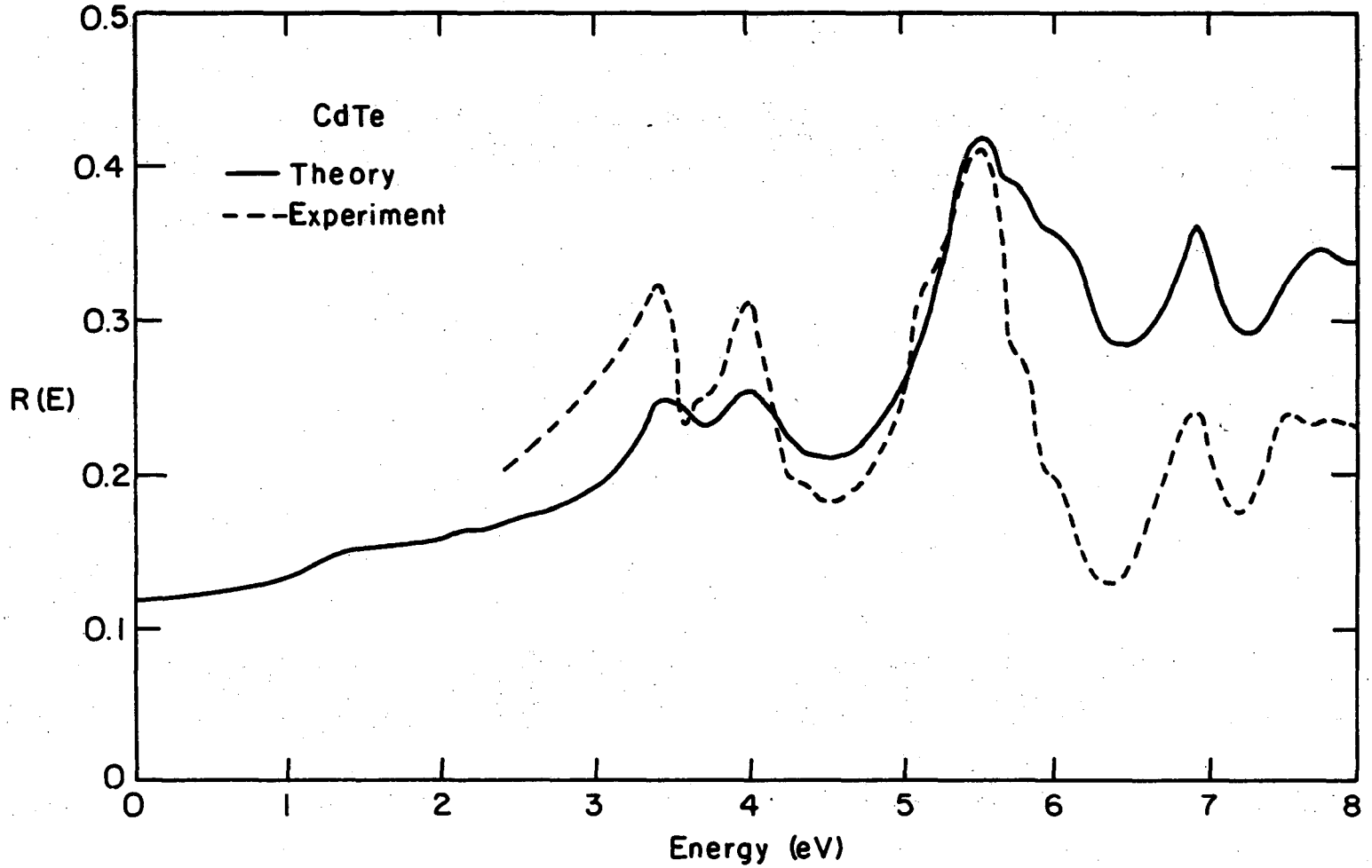

XBL 758-7043

Fig. 39.

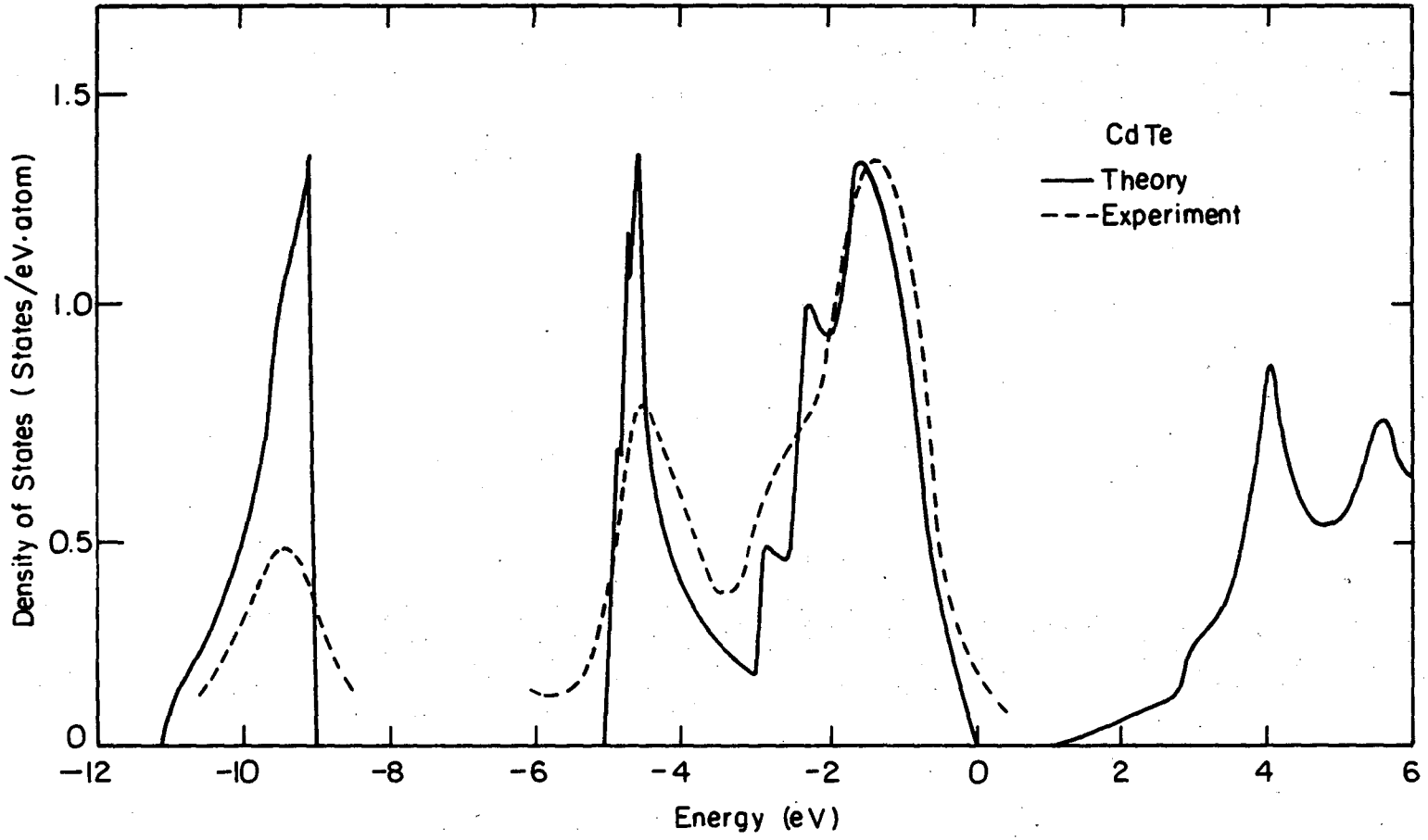

Fig. 40.

XBL758-7026

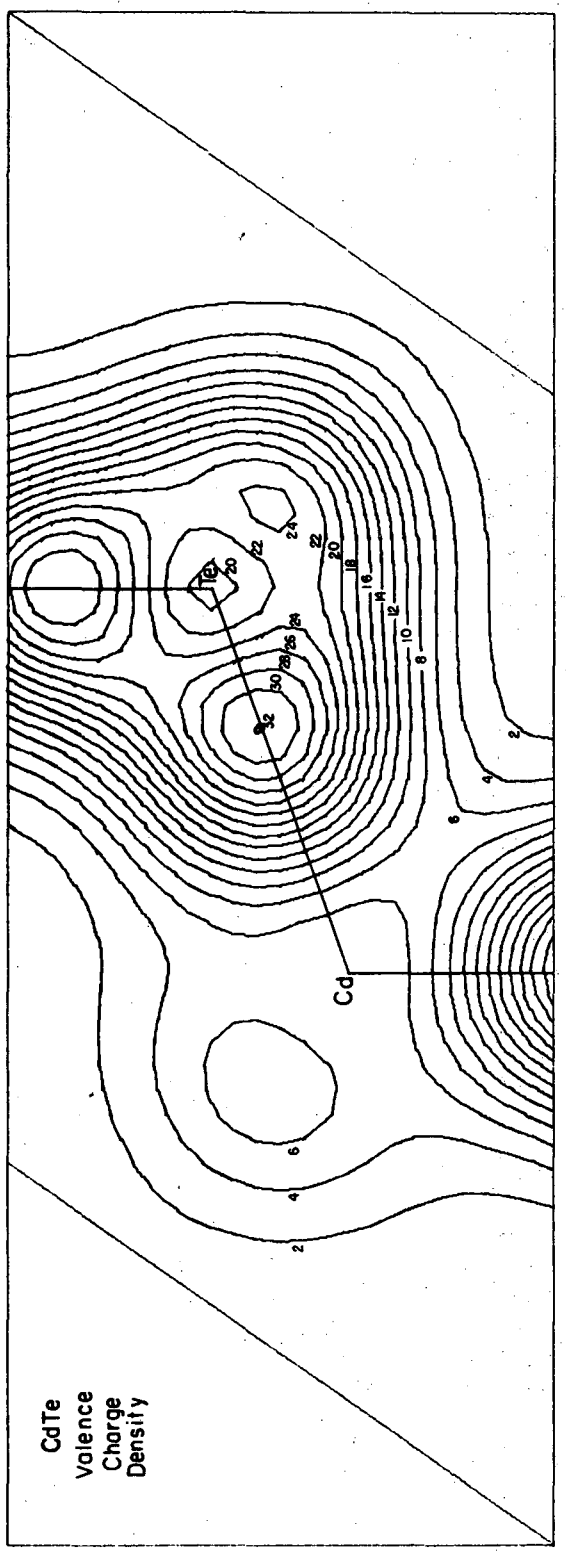

XBL 758-7060

Fig. 41.

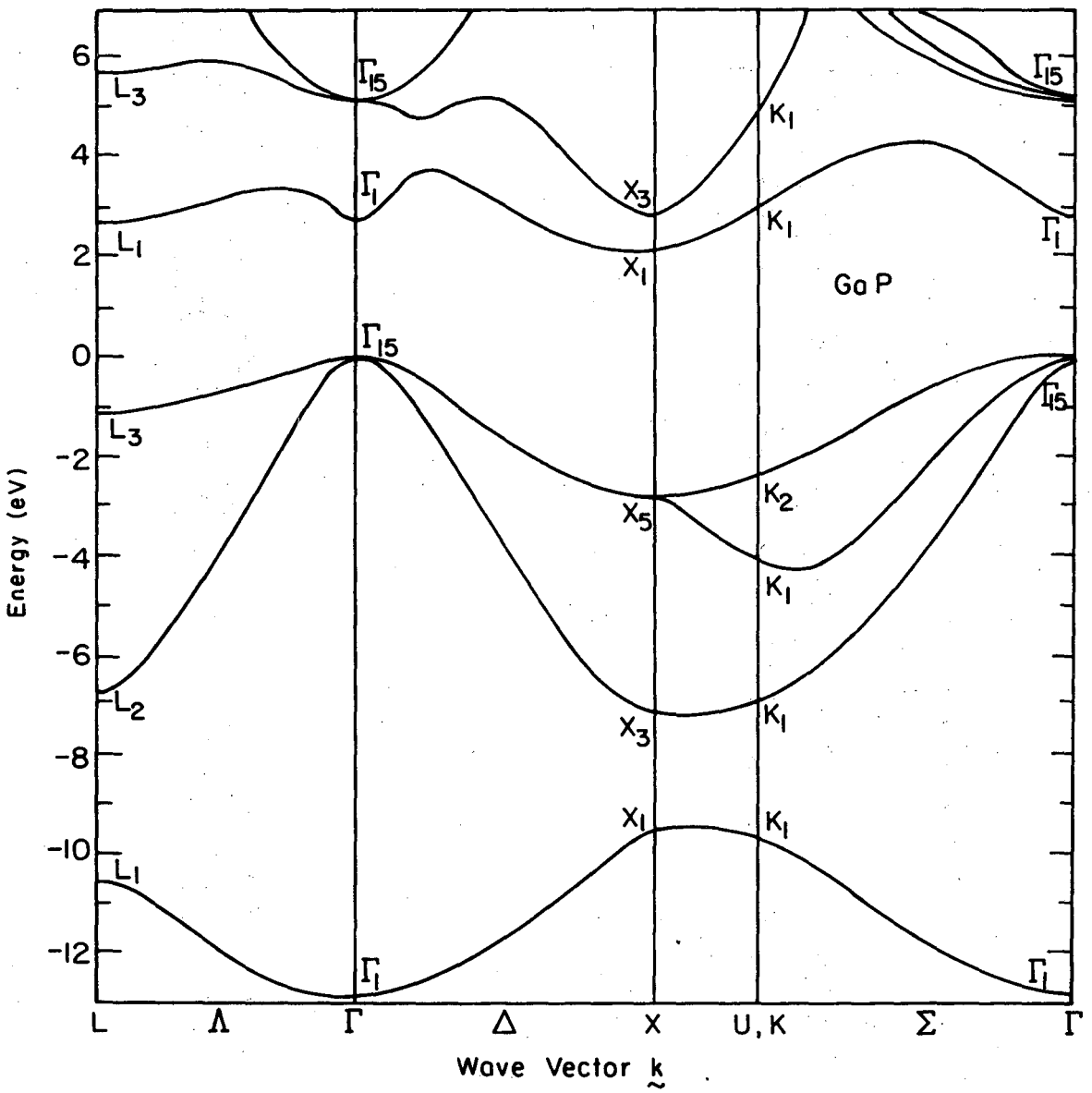

XBL 758-7068

Fig. 42.

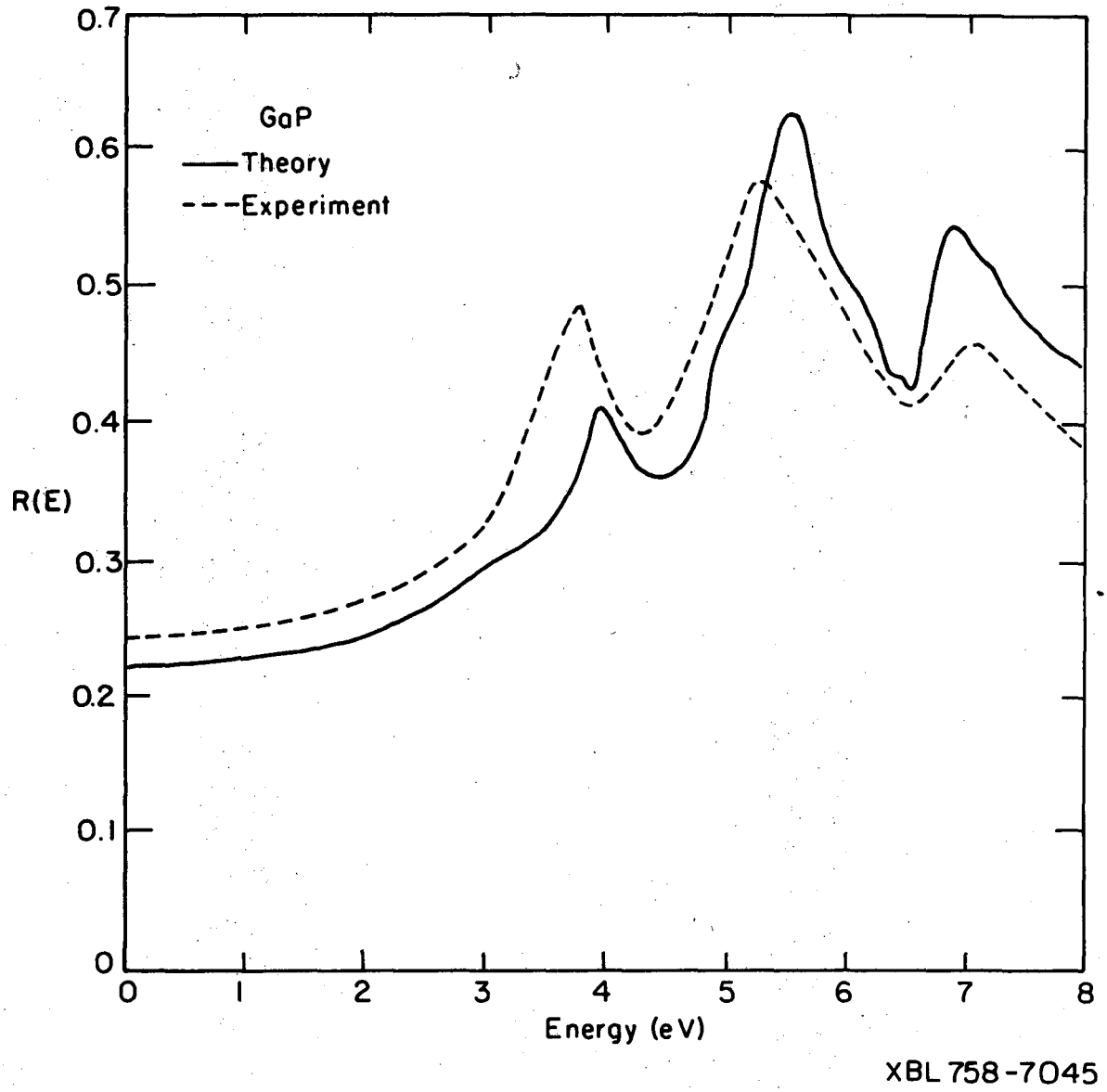

Fig. 43.

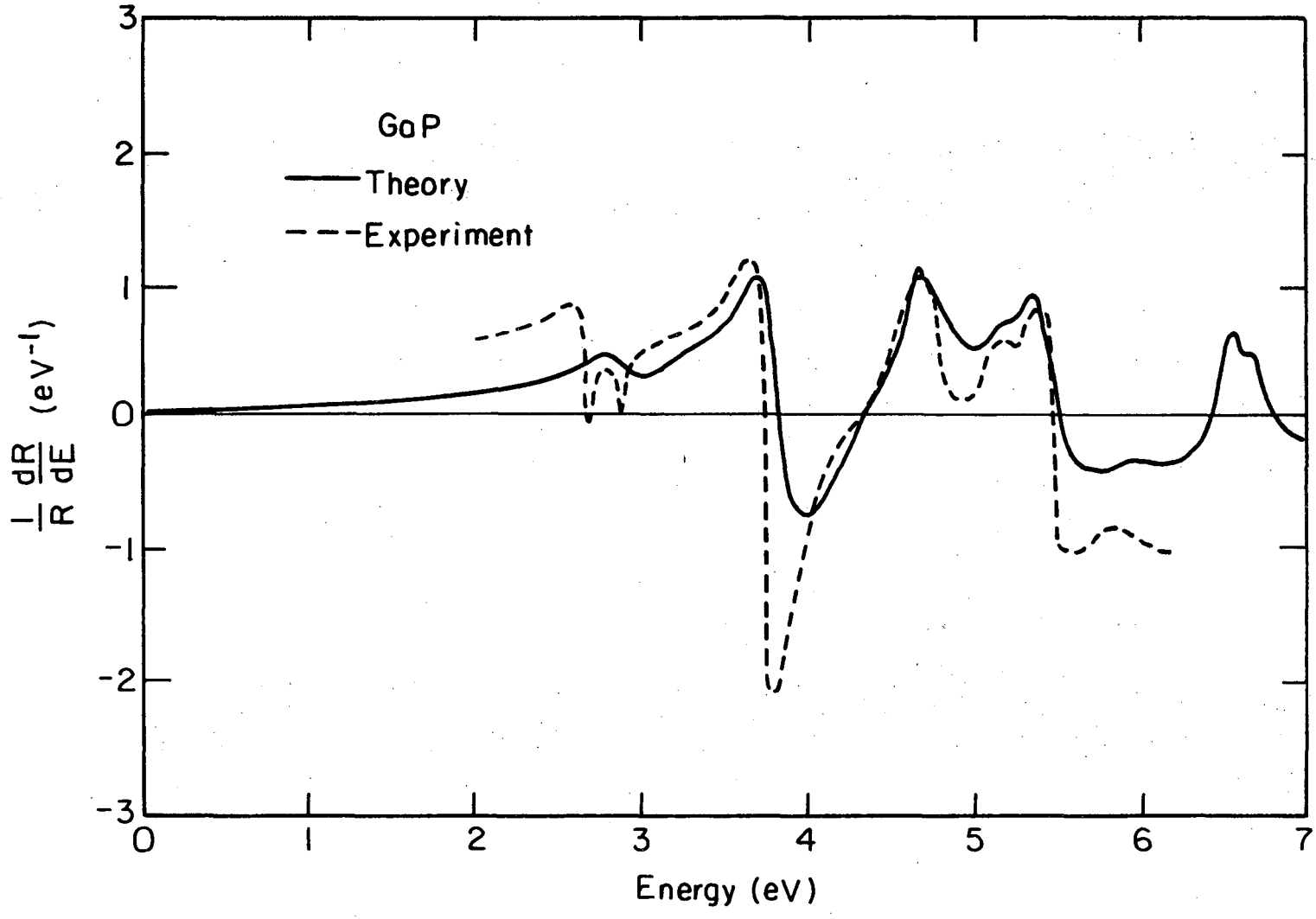

XBL758-7036

Fig. 44.

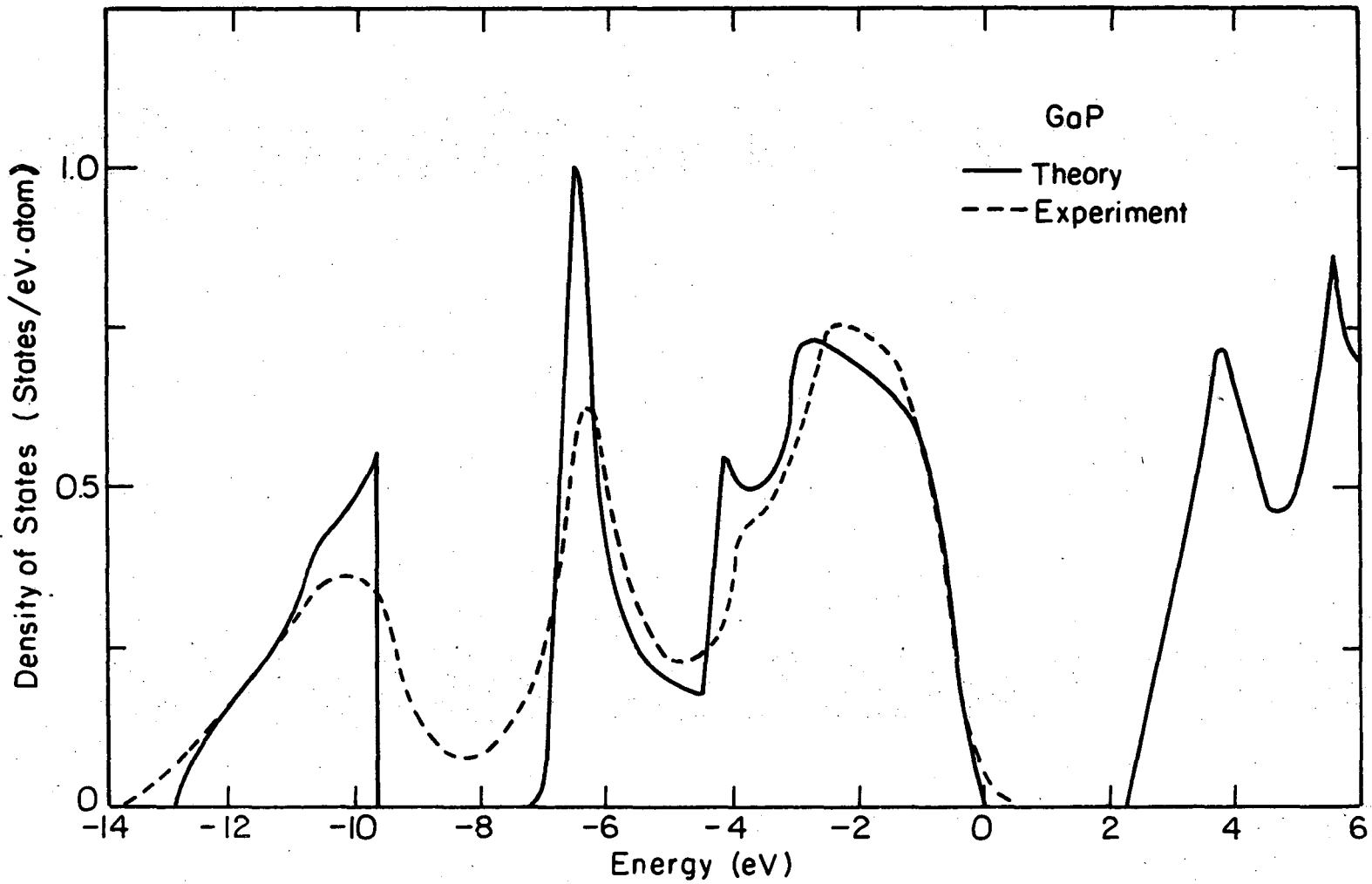

XBL 758-7025

Fig. 45.

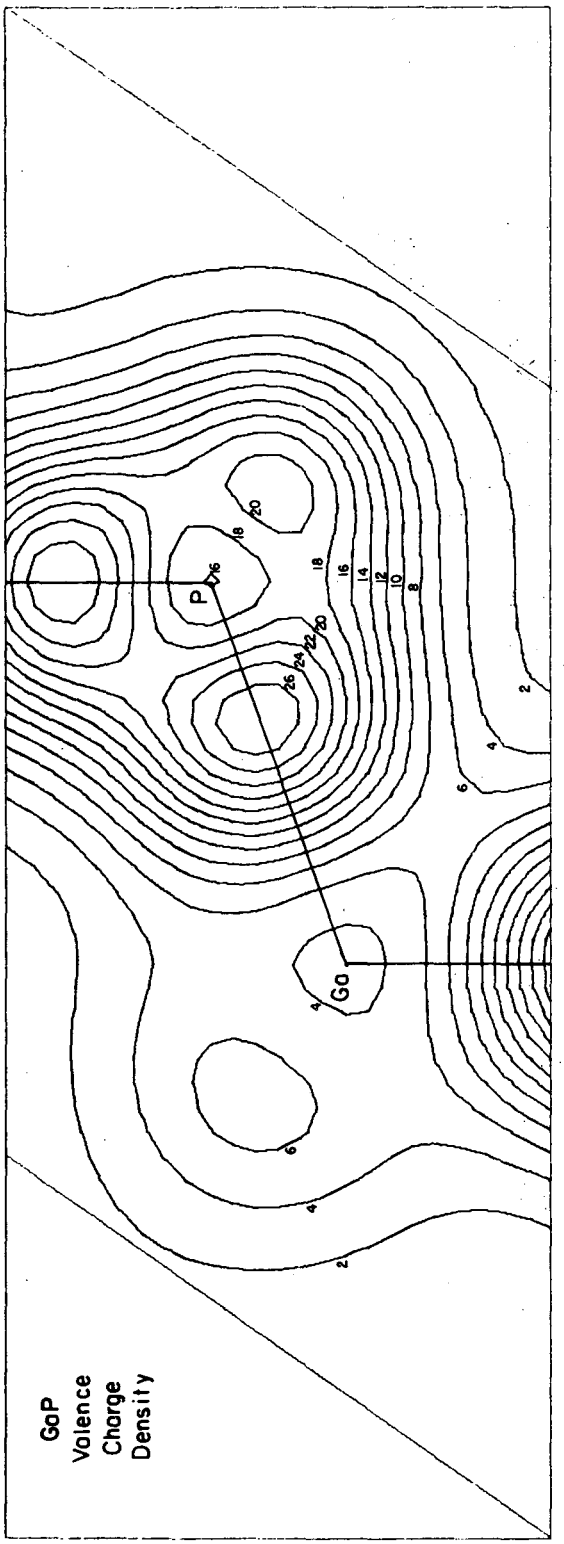

Fig. 46.

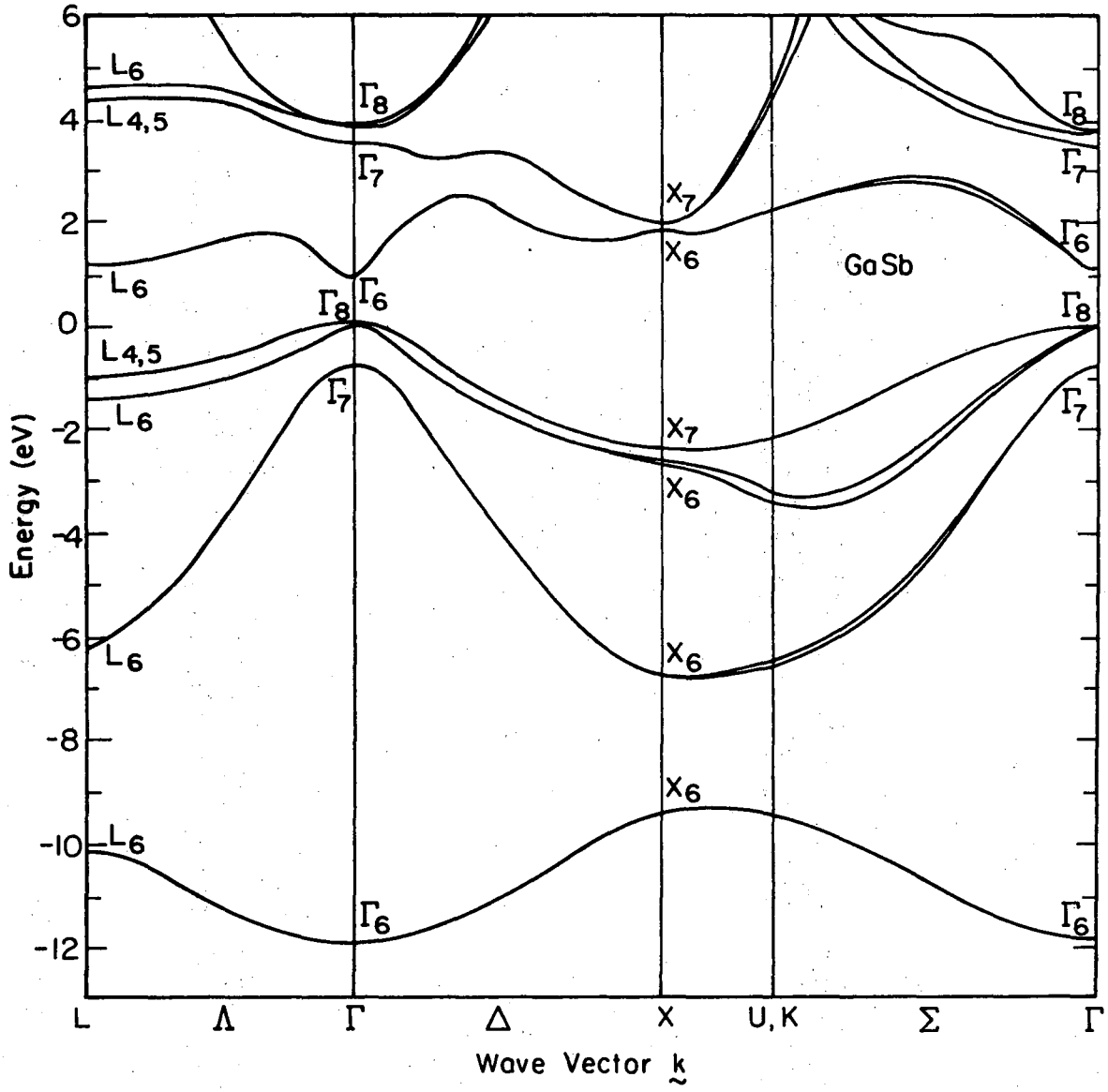

XBL 759-7145

Fig. 47.

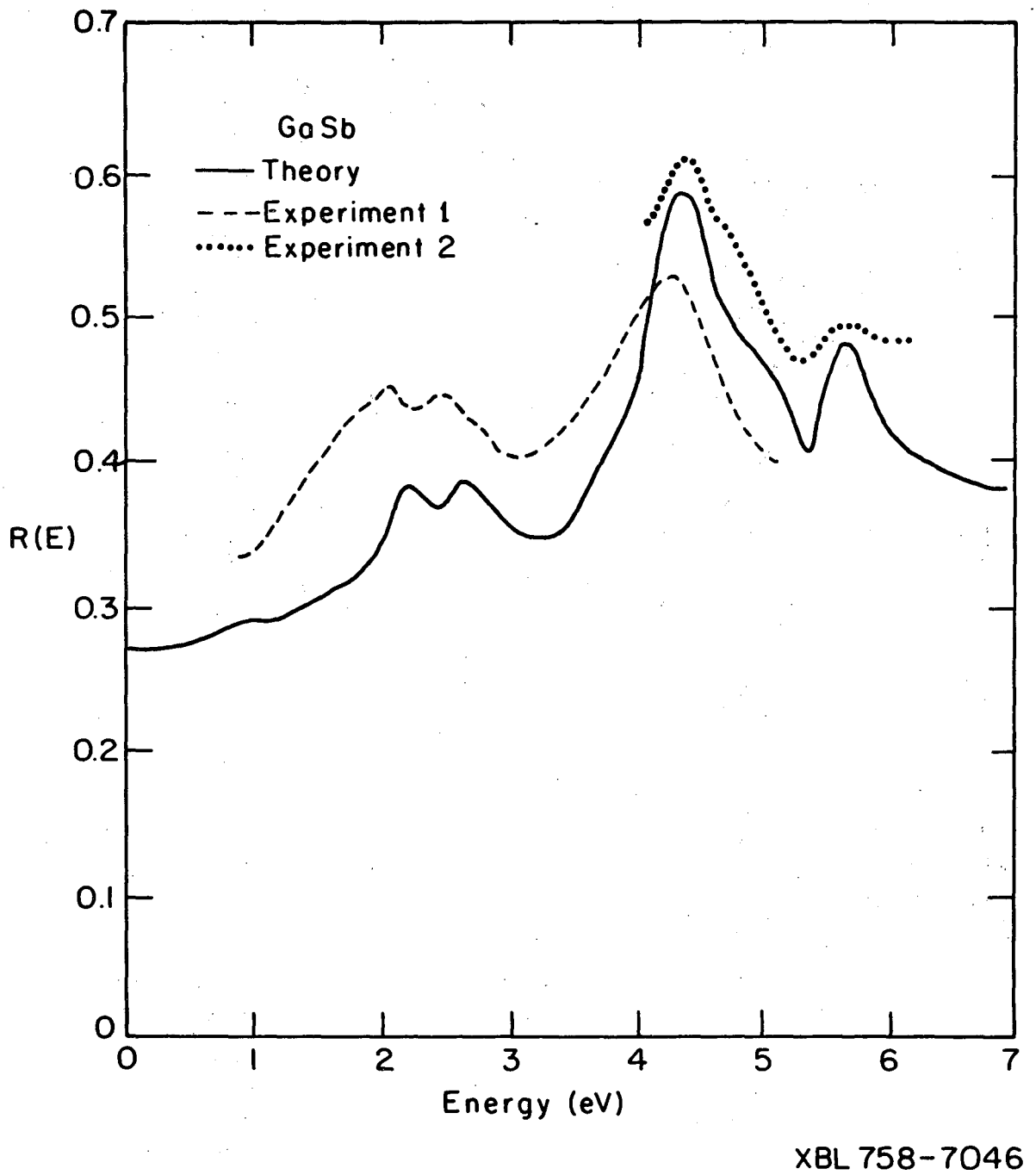
GaSb
Theory
Experiment 1
Experiment 2
R(E)
Energy (eV)
0.7
0.6
0.5
0.4
0.3
0.2
0.1
0
0
1
2
3
4
5
6
7
XBL 758-7046

Fig. 48.

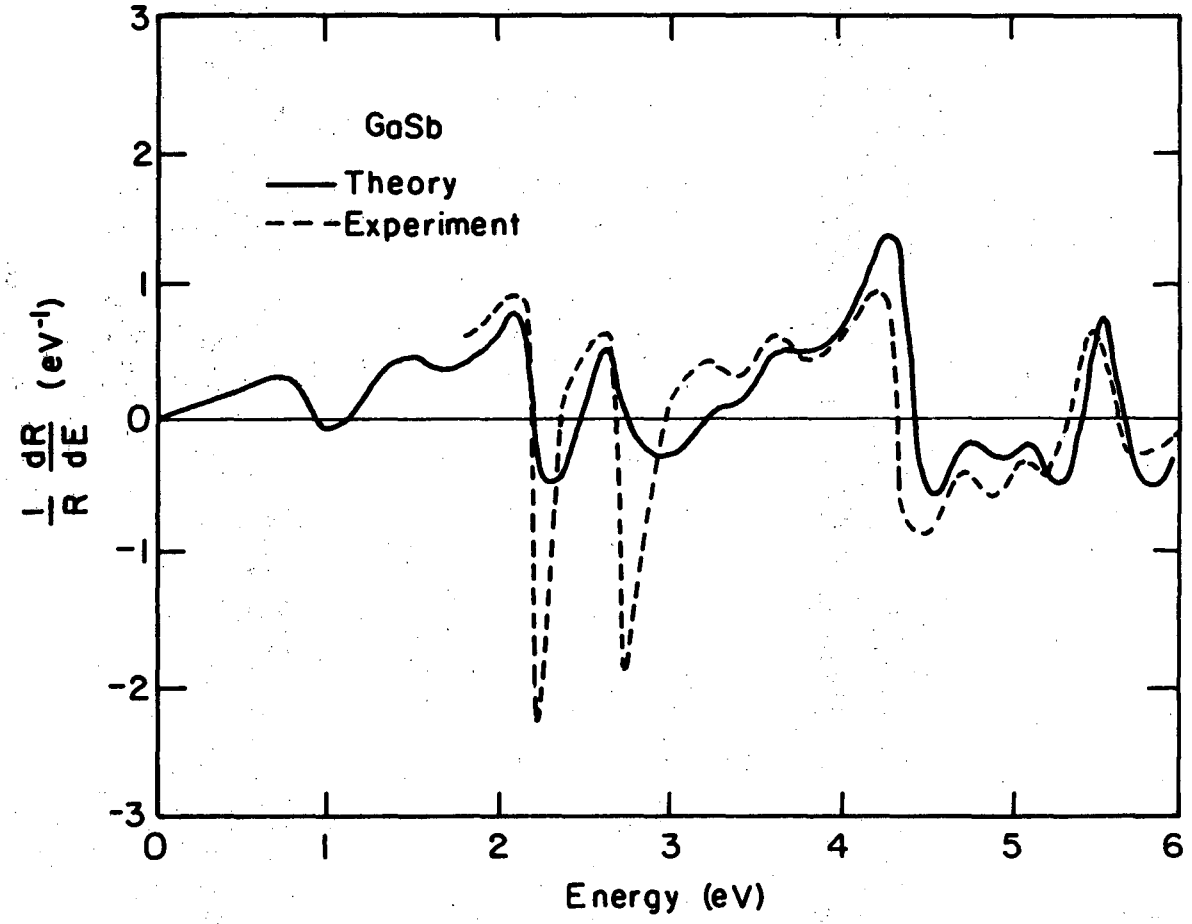

XBL 758-7041

Fig. 49.

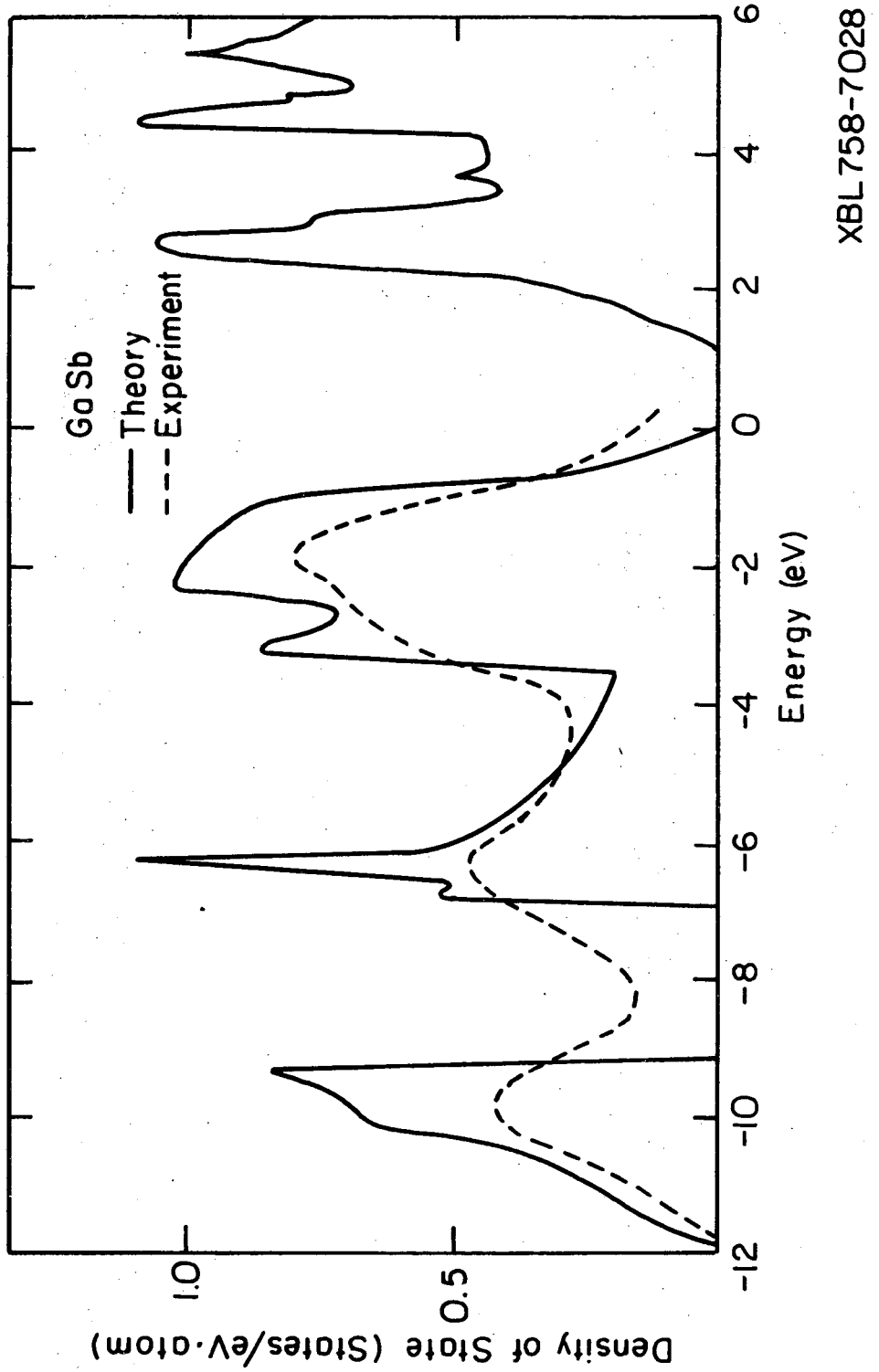
GaSb
Theory
Experiment
Density of State (States/eV·atom)
0.5
1.0
-12
-10
-8
-6
-4
-2
0
2
4
6
Energy (eV)
XBL758-7028

Fig. 50.

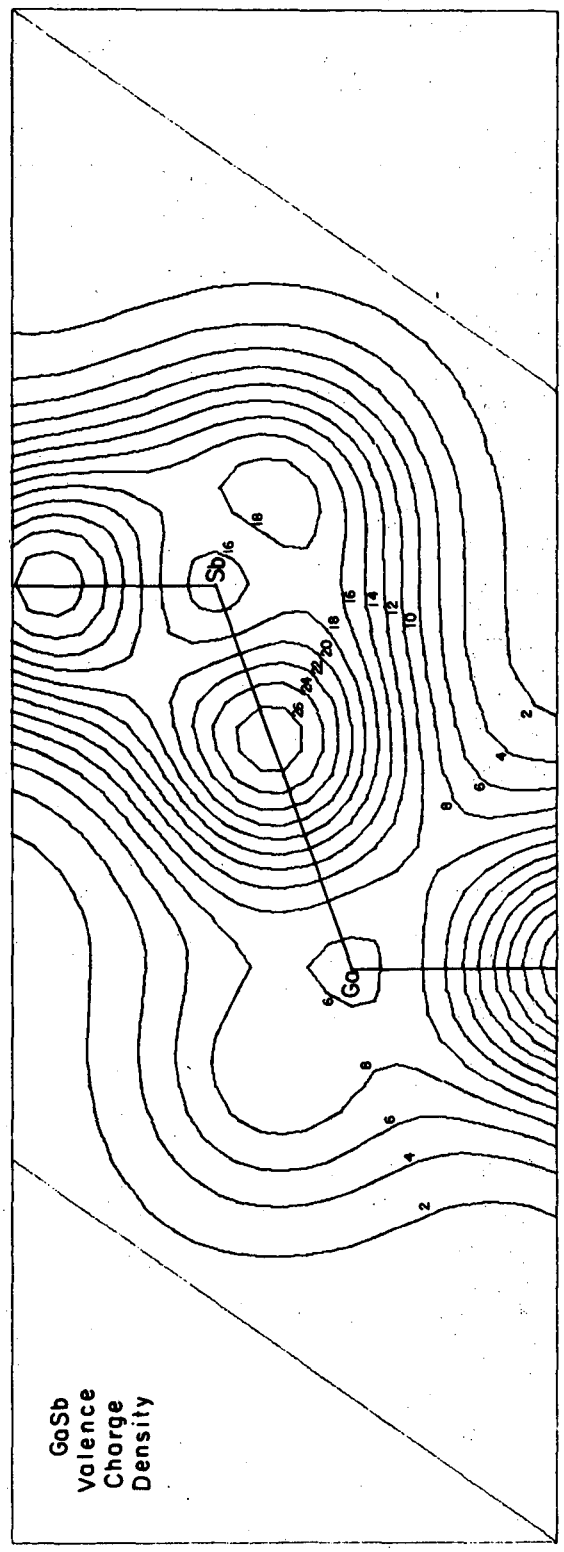

XBL758-7062

Fig. 51.

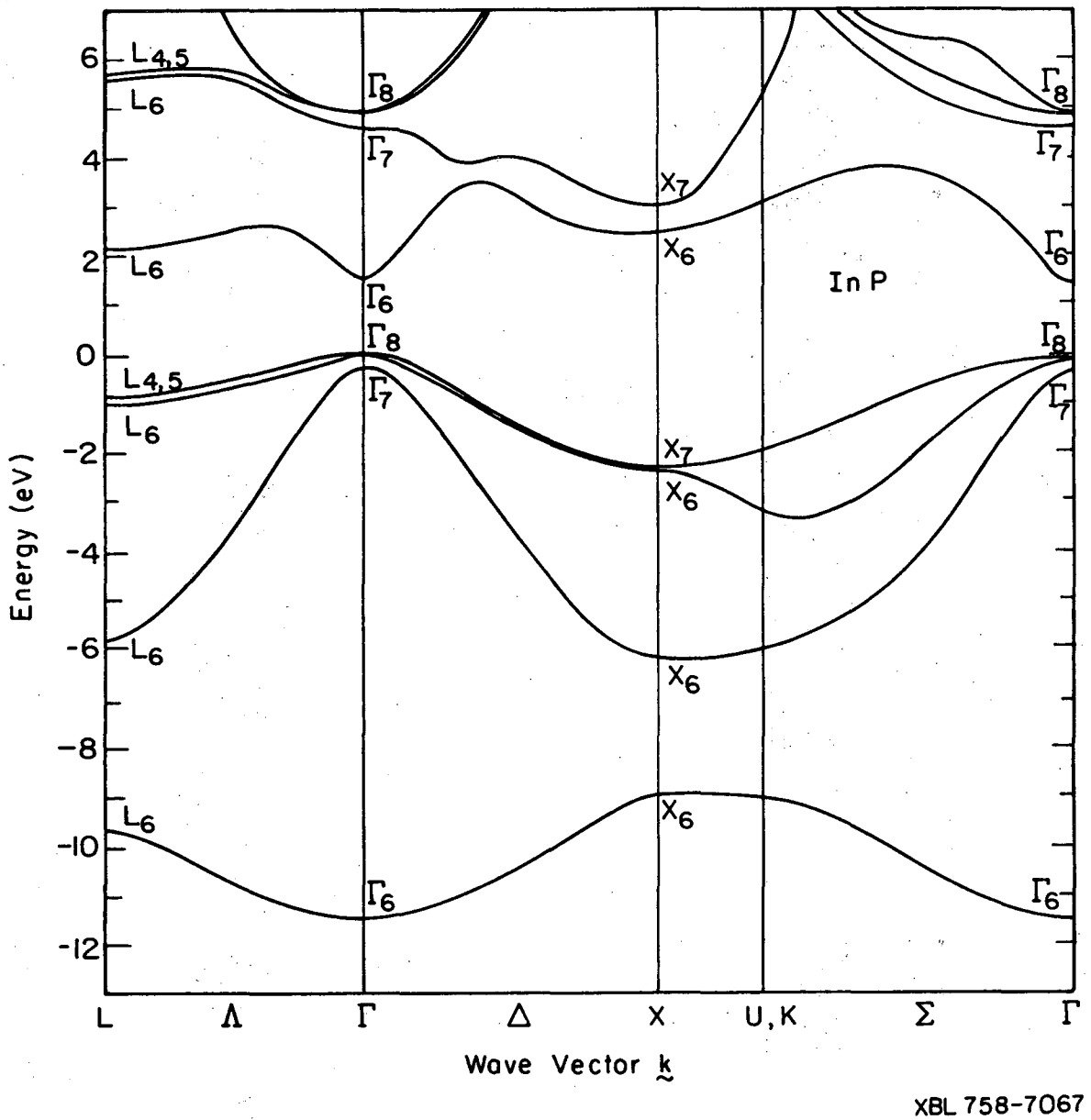
6
4
2
0
-2
-4
-6
-8
-10
-12
Energy (eV)
L4,5
L6
Γ8
Γ7
X7
X6
Γ6
In P
L
Λ
Γ
Δ
X
U,K
Σ
Γ
Wave Vector k
XBL 758-7067

Fig. 52.

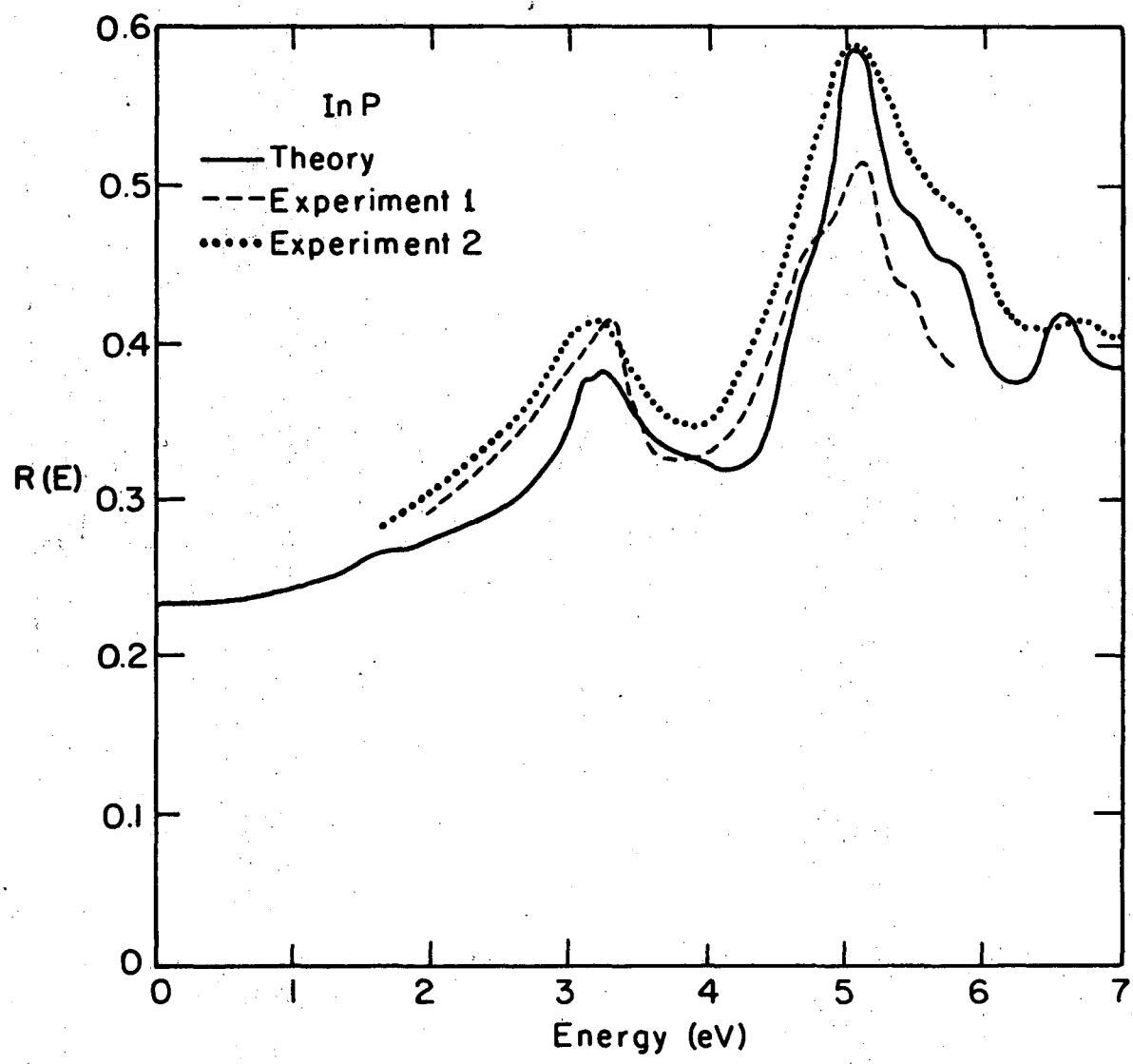

Fig. 53.

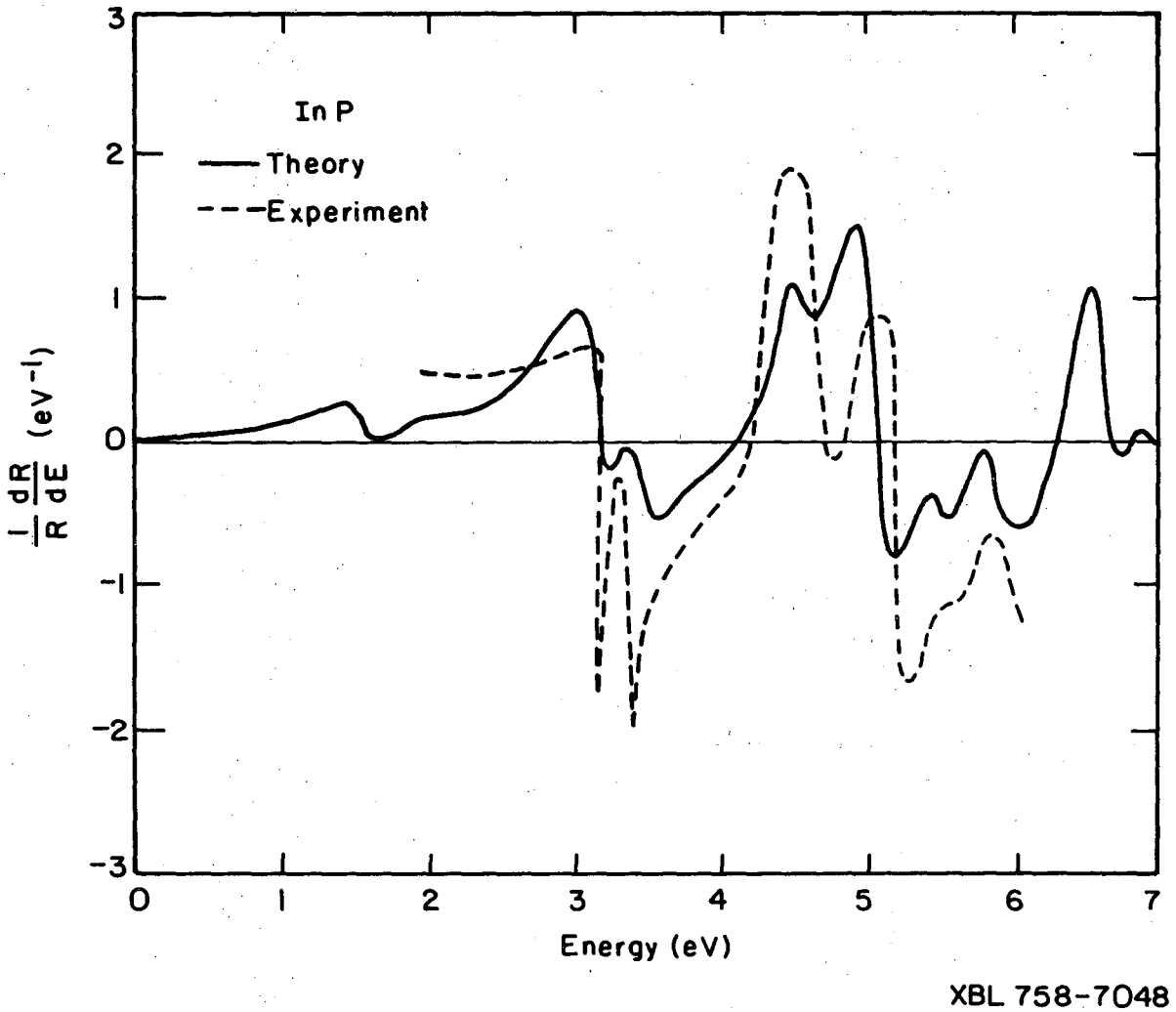
In P
Theory
Experiment
$\frac{1}{R}\frac{dR}{dE}$ (eV^{-1})
Energy (eV)
3
2
1
0
-1
-2
-3
0
1
2
3
4
5
6
7
XBL 758-7048

Fig. 54.

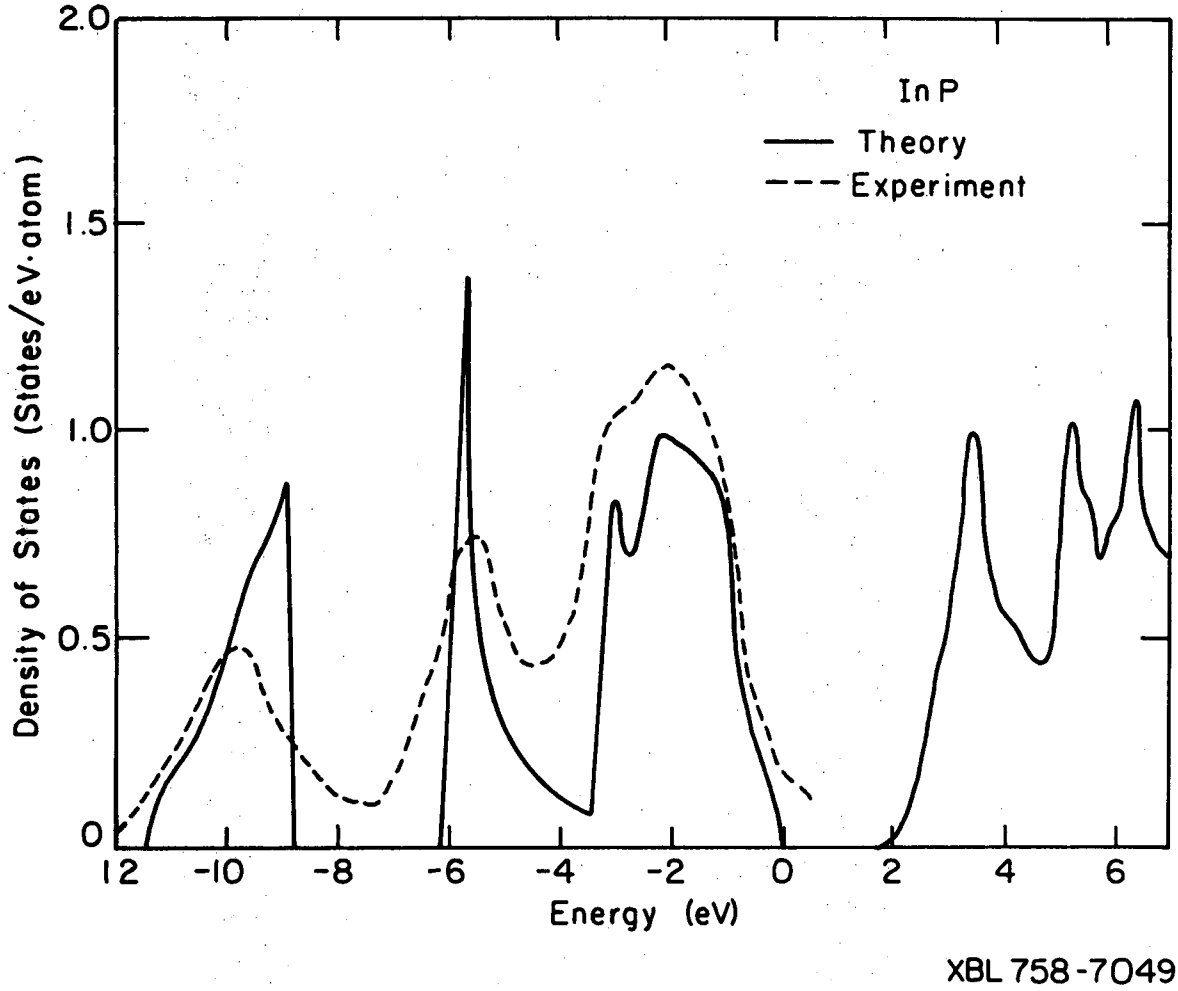

Fig. 55.

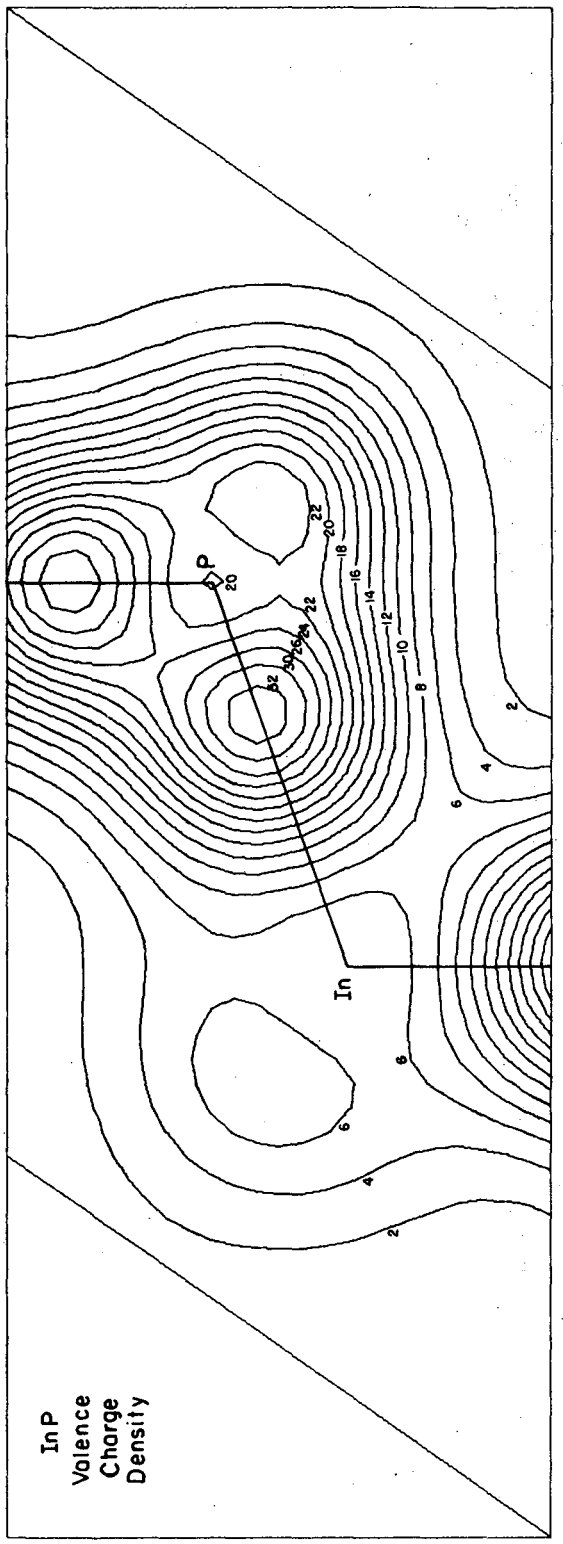

Fig. 56.

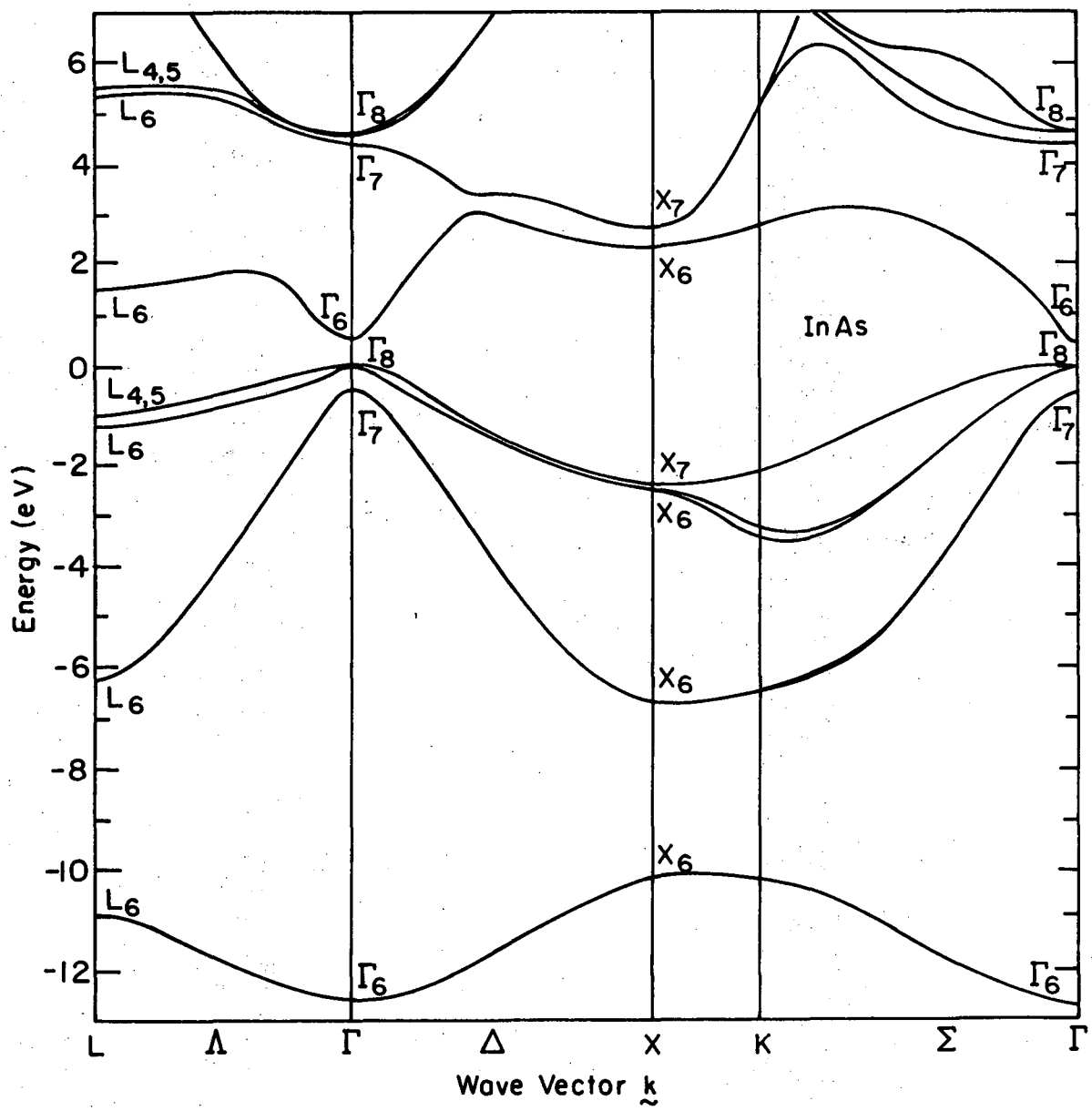

XBL 759-7148

Fig. 57.

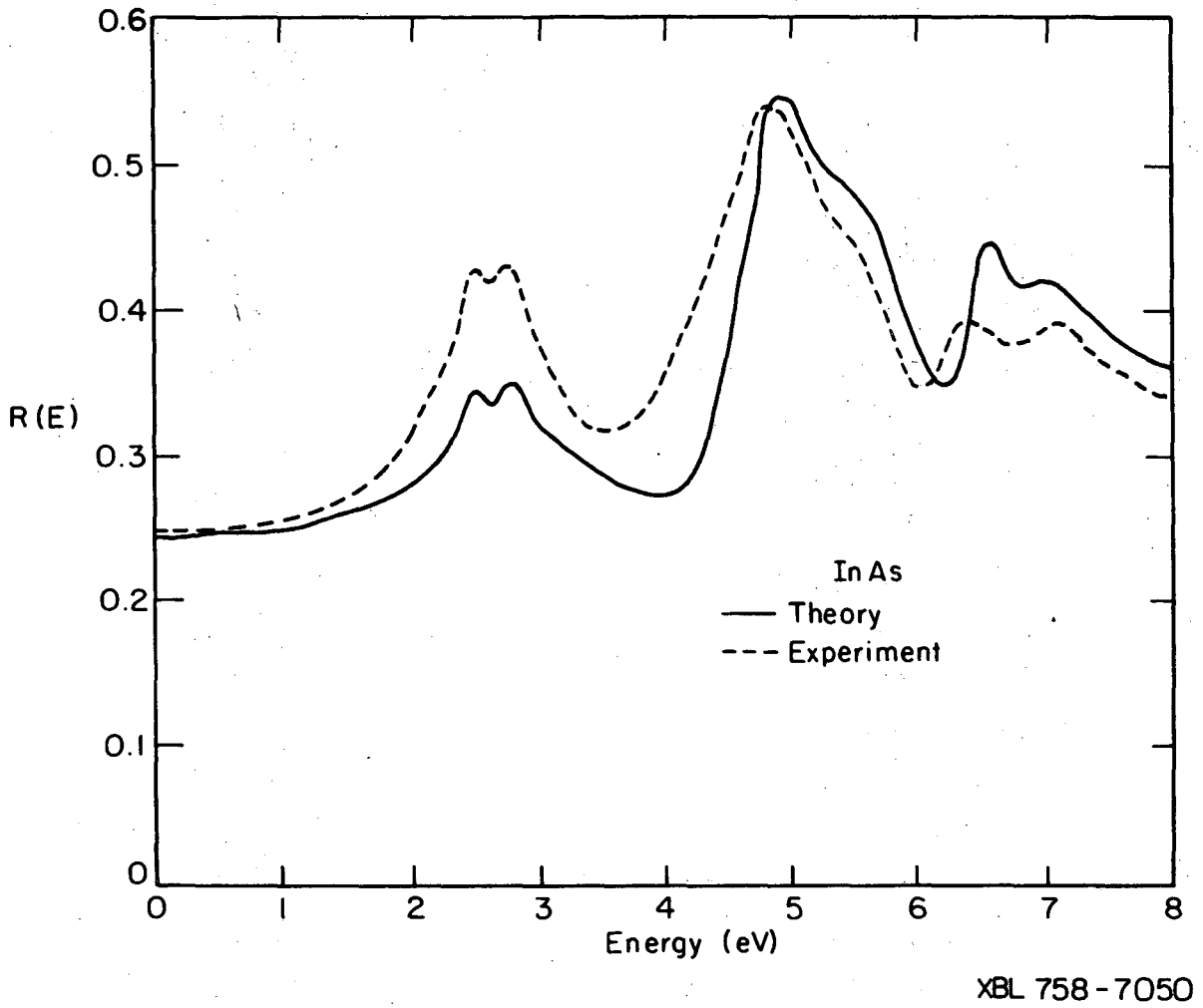
0.6
0.5
0.4
0.3
0.2
0.1
0
R(E)
0
1
2
3
4
5
6
7
8
Energy (eV)
In As
Theory
Experiment
XBL 758-7050

Fig. 58.

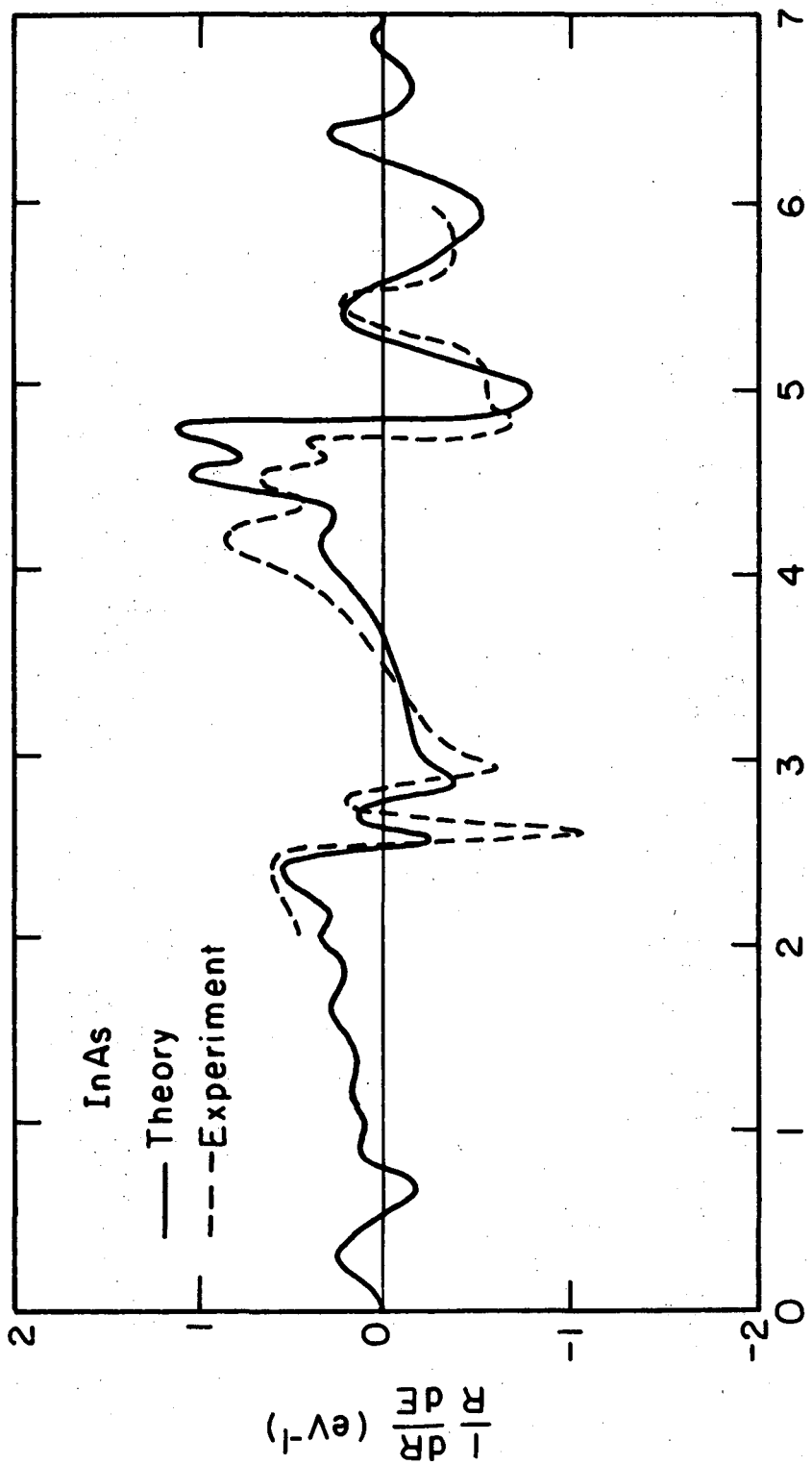

Fig. 59.

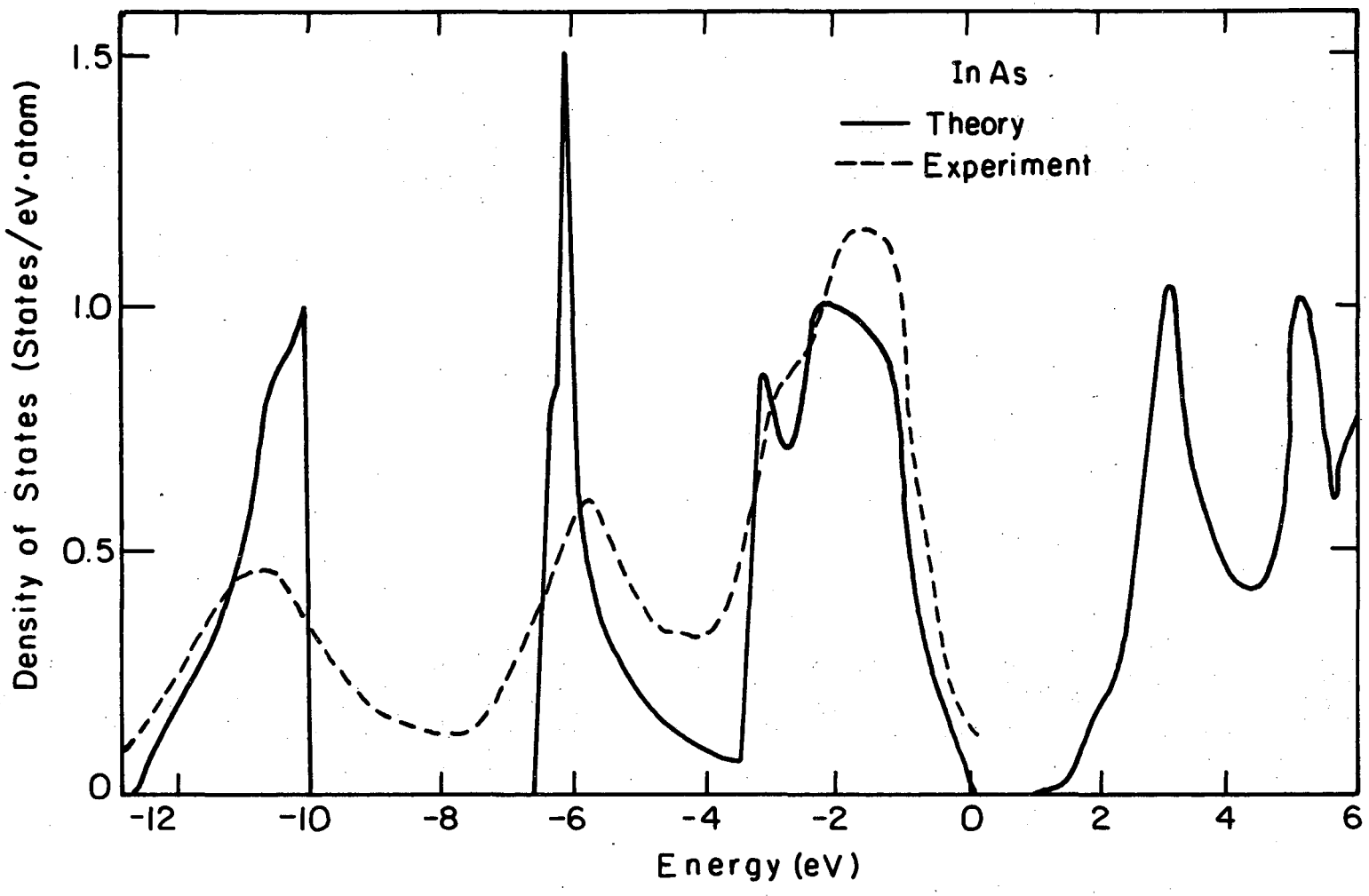
In As
Theory
Experiment
Density of States (States/eV·atom)
1.5
1.0
0.5
0
-12
-10
-8
-6
-4
-2
0
2
4
6
Energy (eV)
XBL 758-7052

Fig. 60.

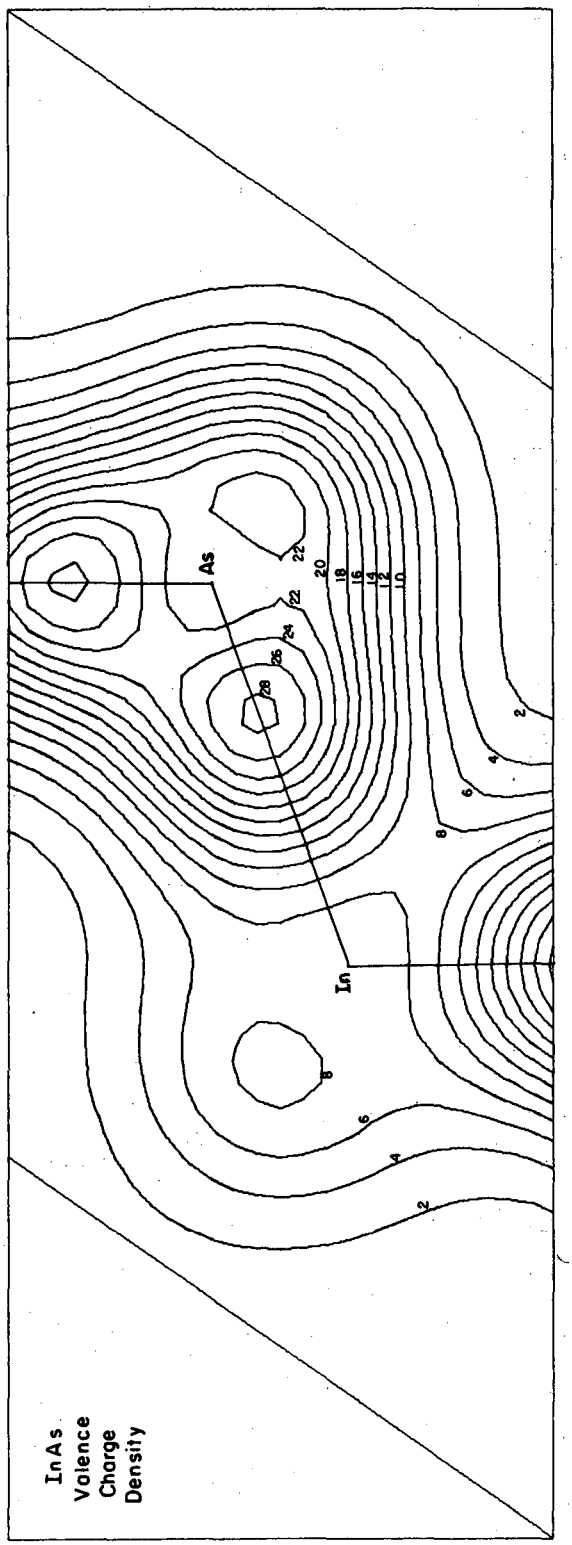

XBL758-7066

Fig. 61.

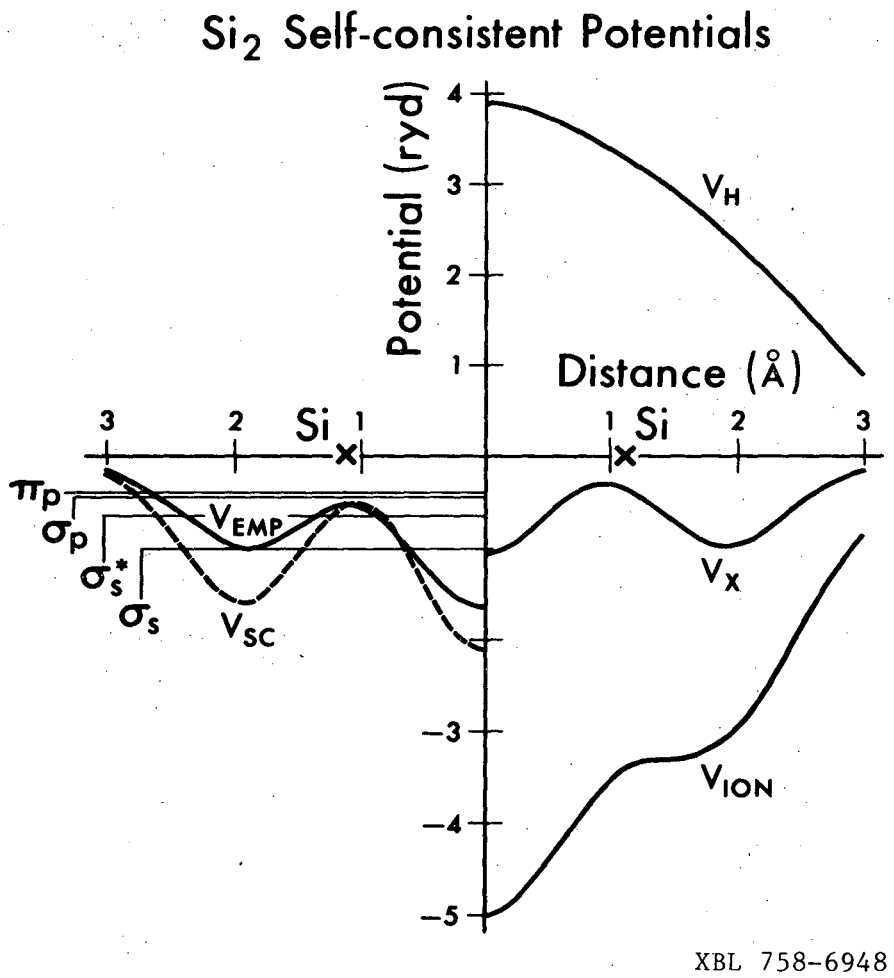
Si2 Self-consistent Potentials
Potential (ryd)
4
3
2
1
−3
−4
−5
Distance (Å)
3
2
Si
1
1
Si
2
3
VH
VEMP
VSC
VX
VION
πp
σp
σs*
σs
XBL 758-6948

Fig. 62.

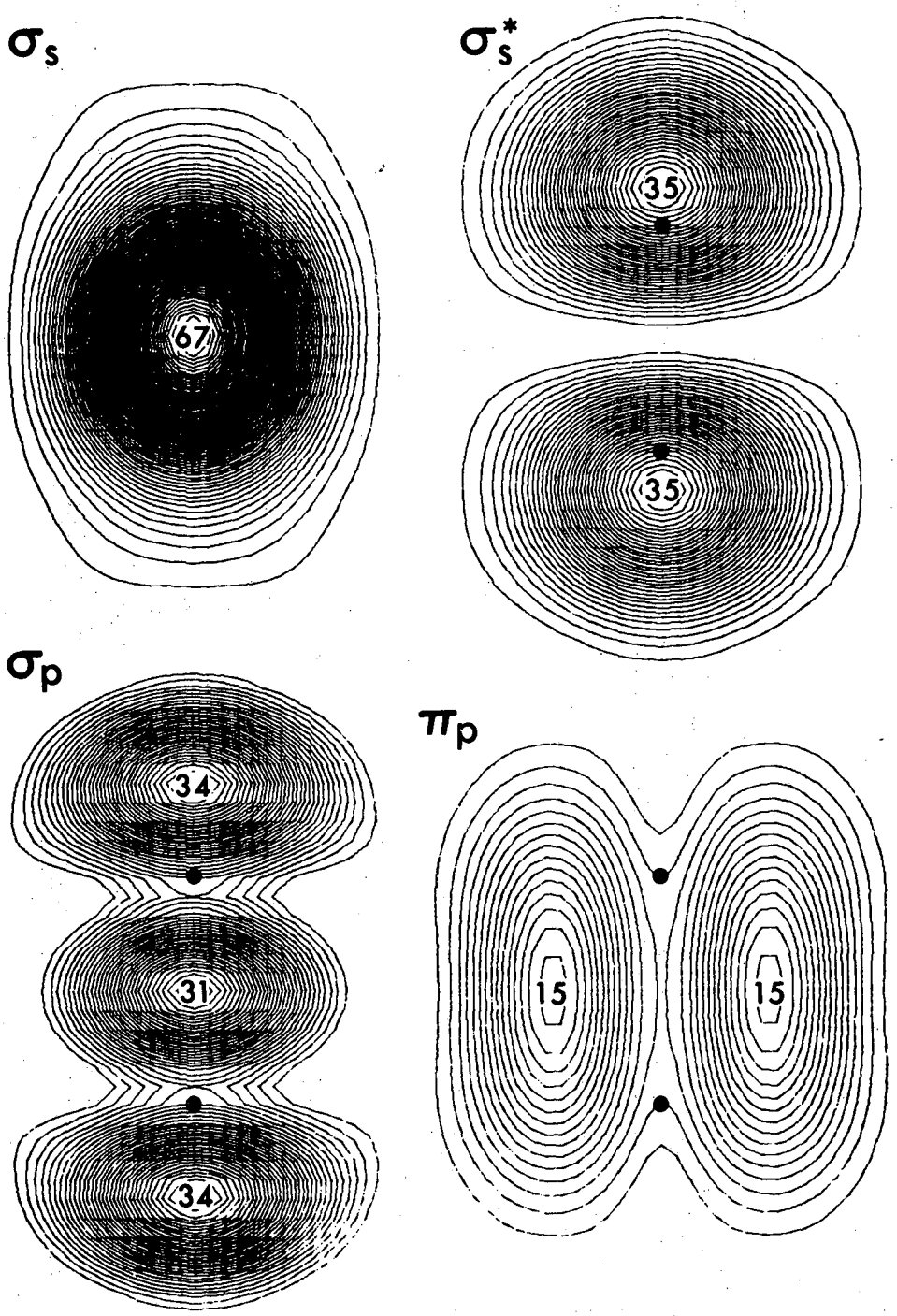

XBL-758-6946

Fig. 63.

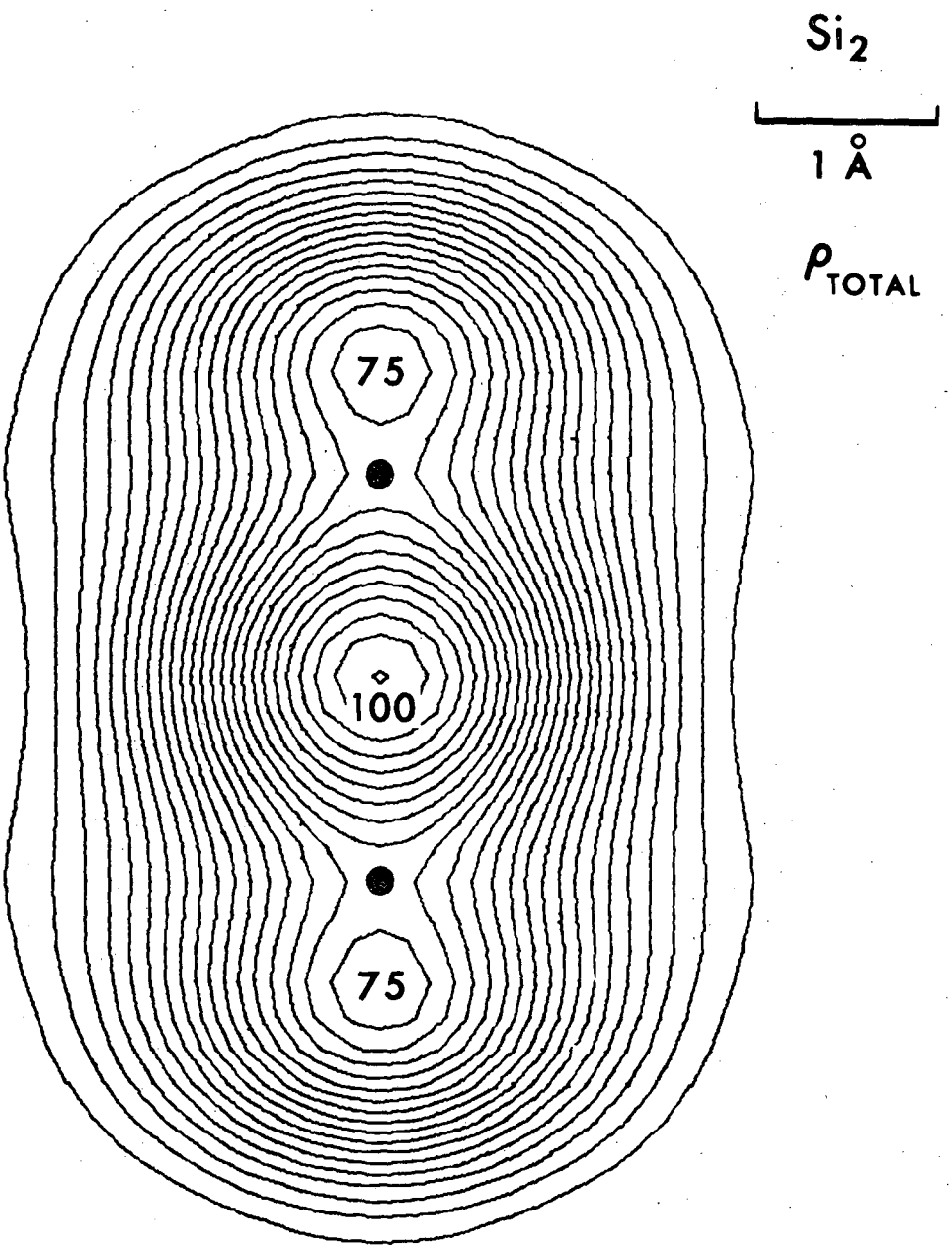

XBL 758-6952

Fig. 64.

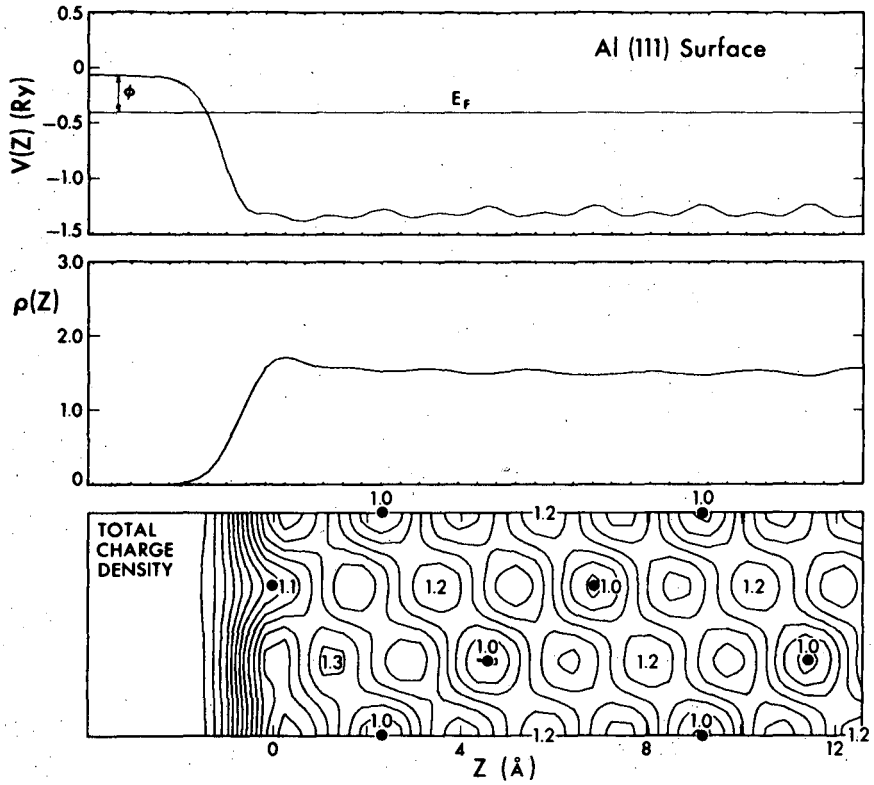

XBL 758-6969

Fig. 65.

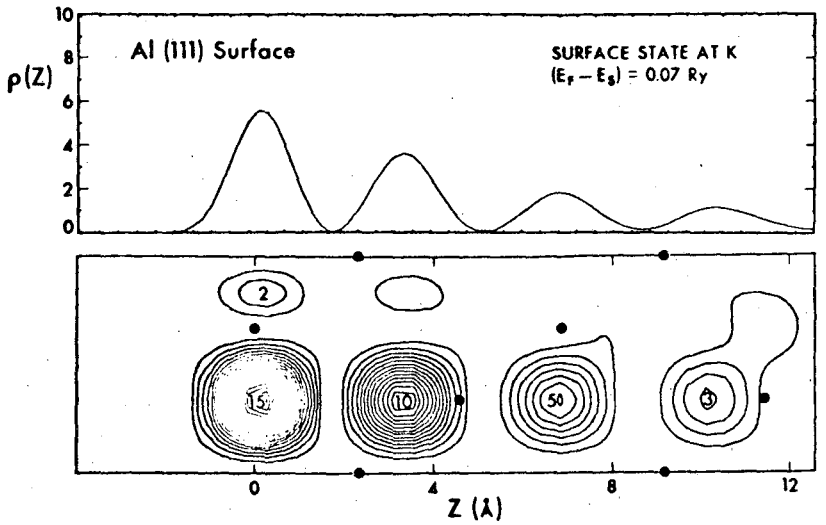

XBL 759-7131

Fig. 66.

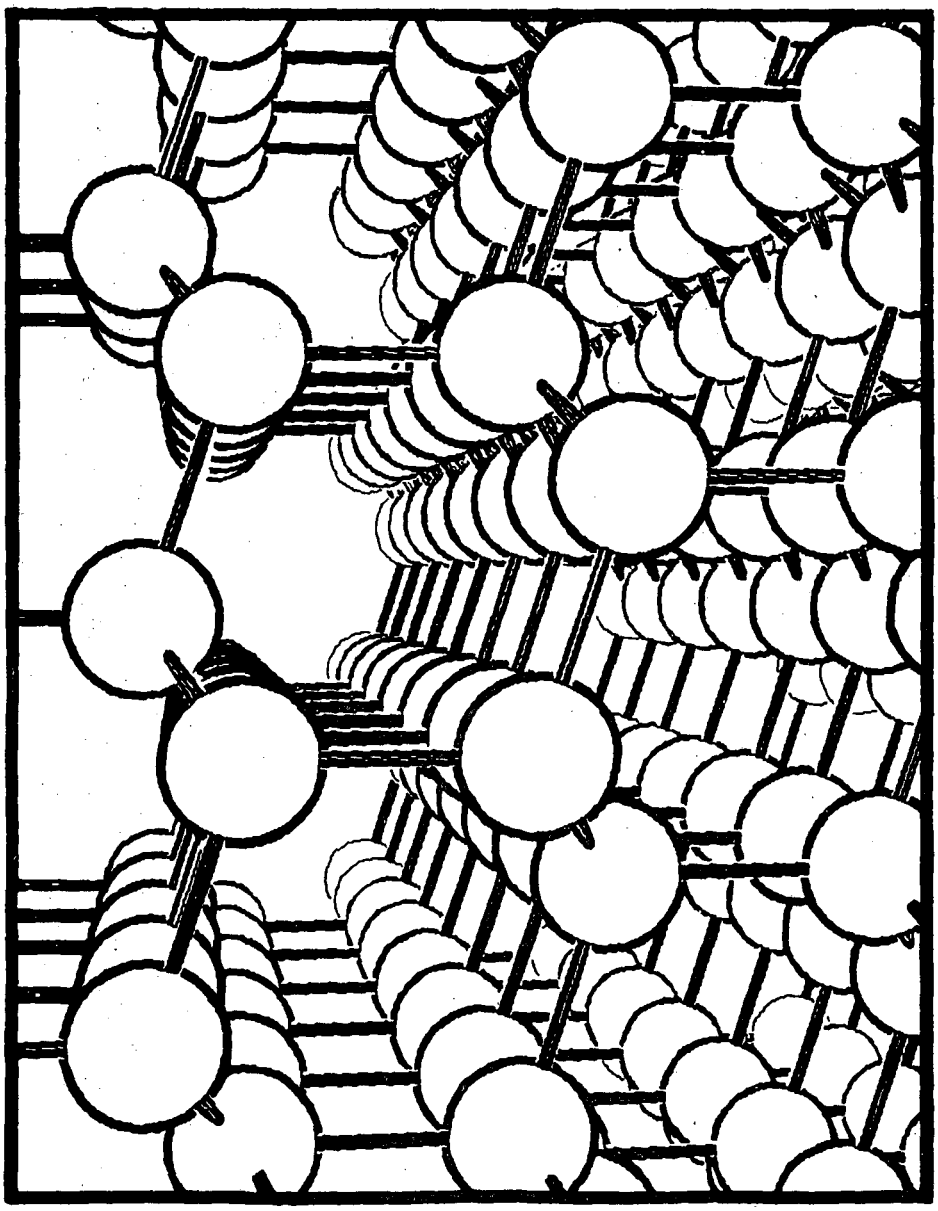

XBL-758-6940

Fig. 67.

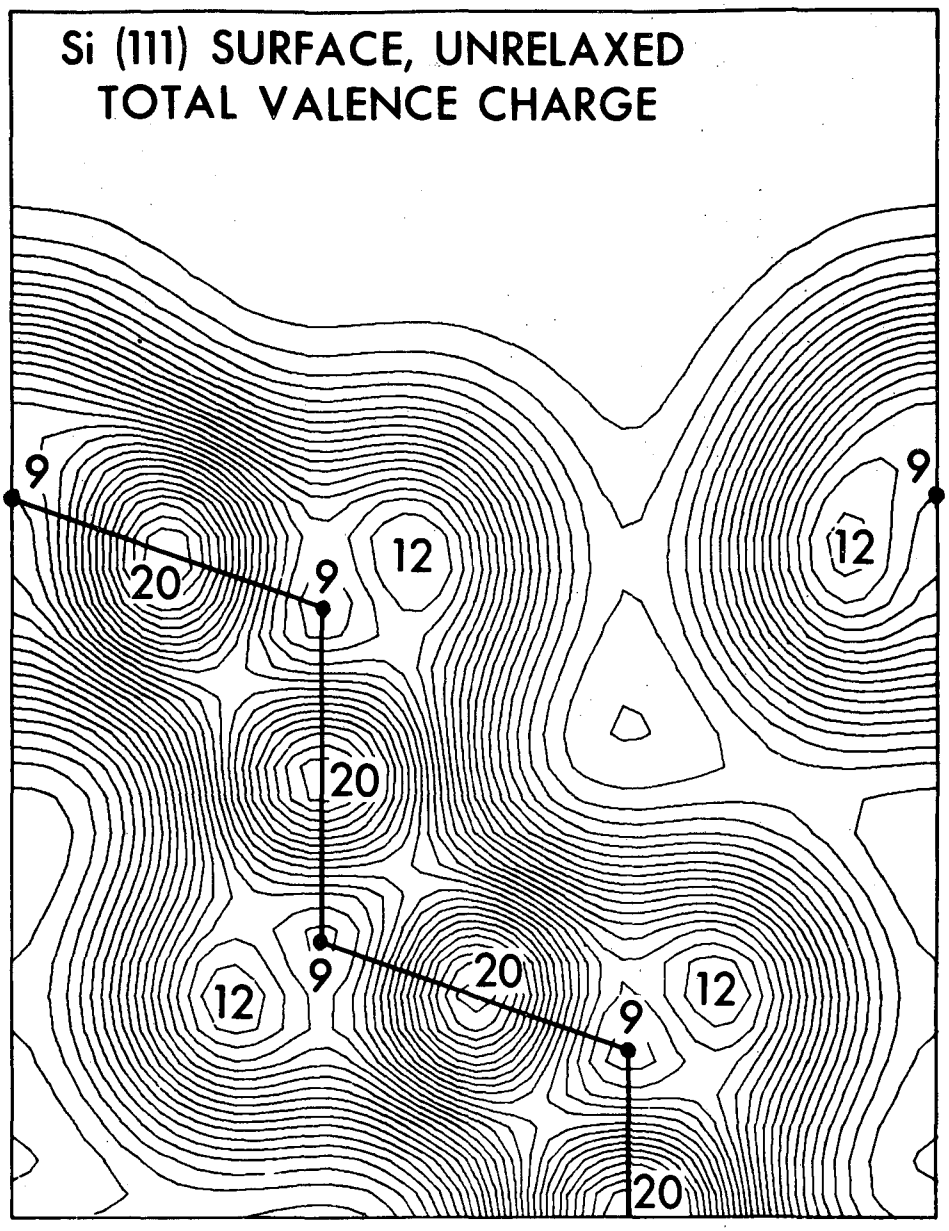

XBL 758-6950

Fig. 68.

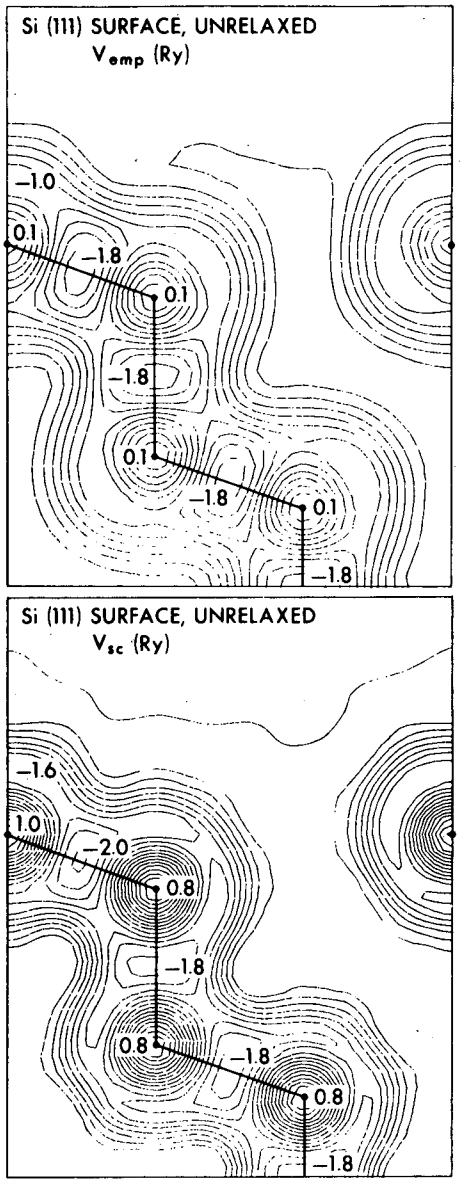

XBL 758-6971

Fig. 69.

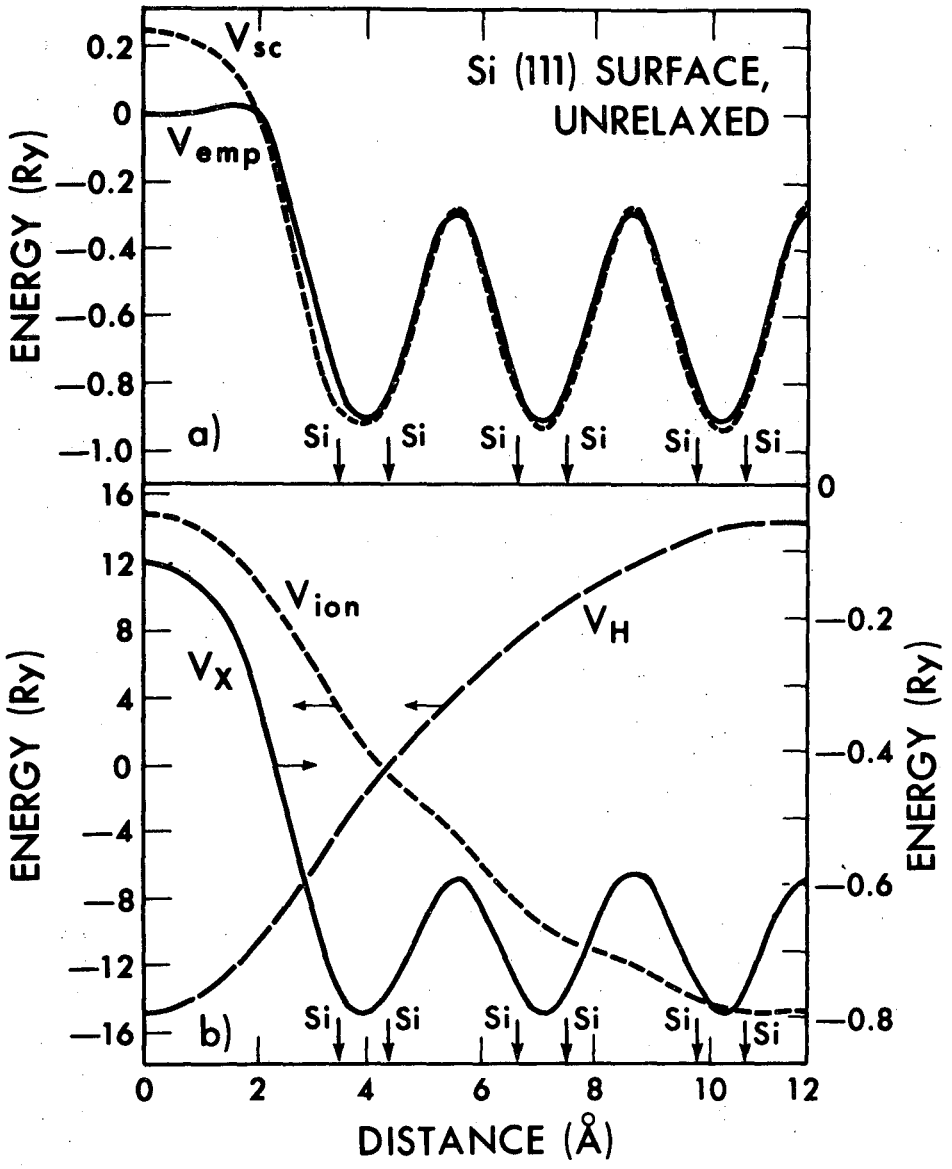
Si (111) SURFACE,
UNRELAXED
V_{sc}
V_{emp}
a)
Si
ENERGY (Ry)
0.2
0
−0.2
−0.4
−0.6
−0.8
−1.0
V_{ion}
V_H
V_X
b)
16
12
8
4
0
−4
−8
−12
−16
−0.2
−0.4
−0.6
−0.8
0
2
4
6
8
10
12
DISTANCE (Å)
XBL-758-6941

Fig. 70.

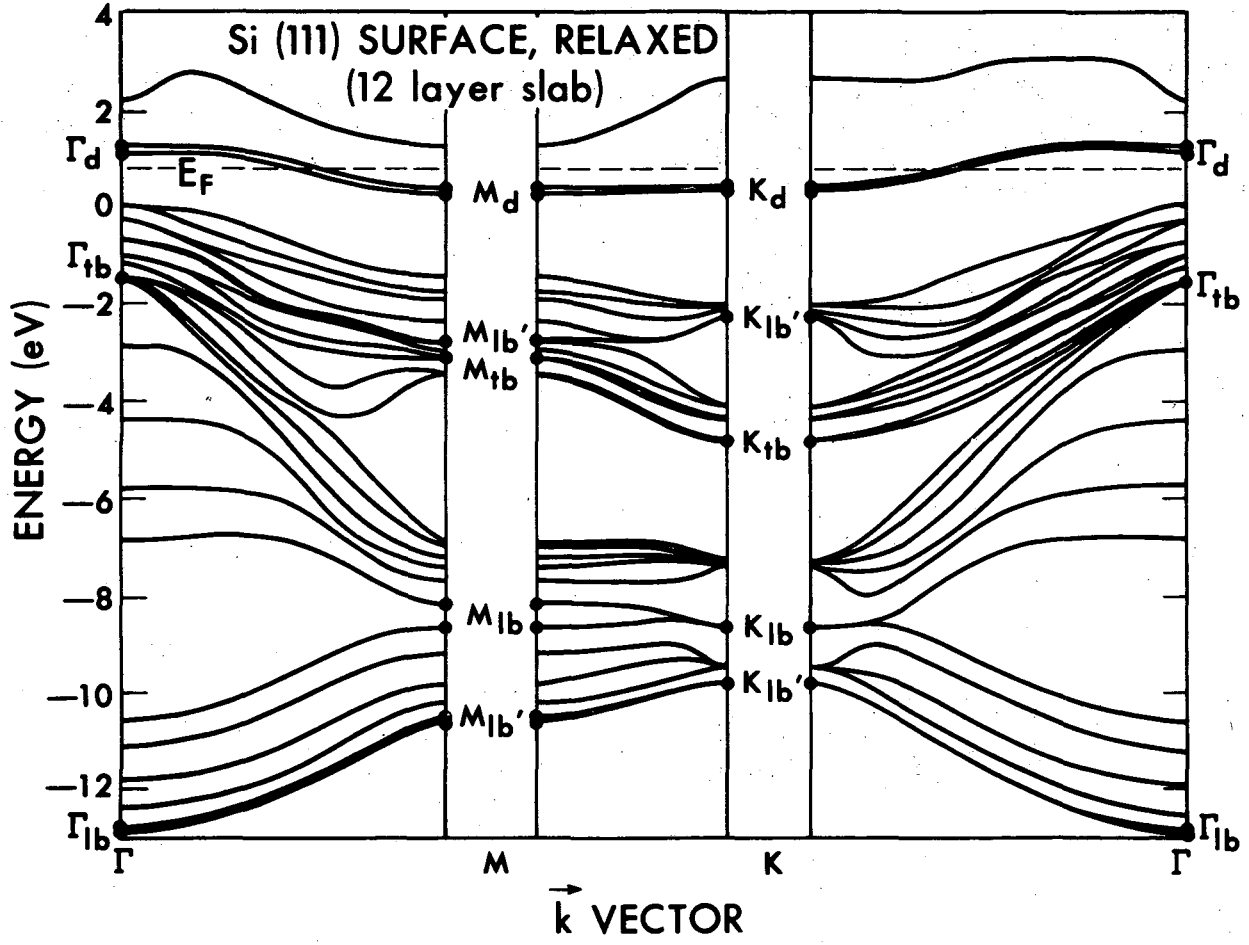

XBL 758-6959

Fig. 71.

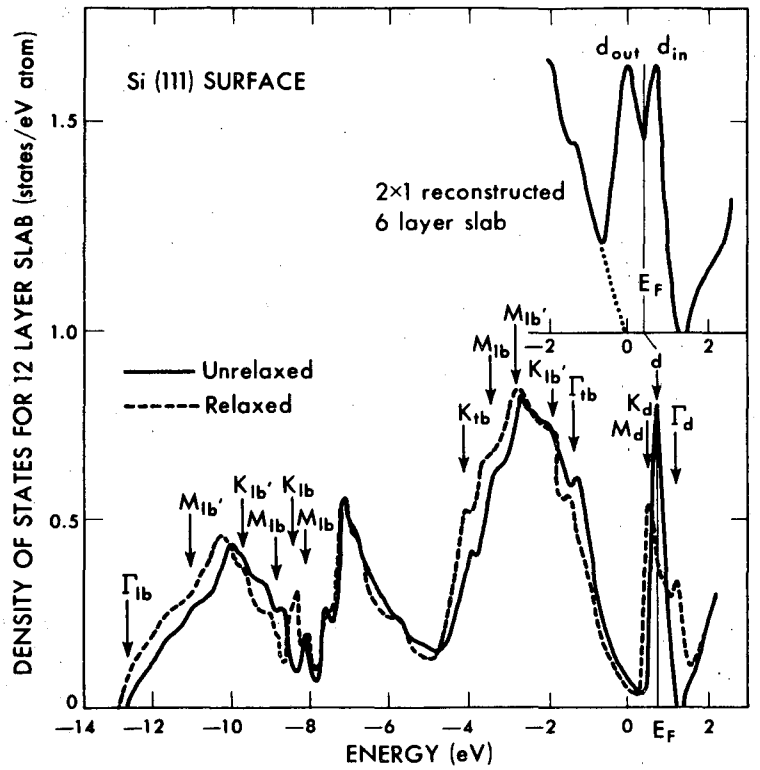
Si (111) SURFACE
2×1 reconstructed
6 layer slab
d_{out} d_{in}
E_F
d
Unrelaxed
Relaxed
Γ_{1b}
$M_{1b'}$
$K_{1b'}$ K_{1b}
M_{1b}
M_{1b}
K_{1b}
$M_{1b'}$
$K_{1b'}$
Γ_{1b}
K_d
M_d
Γ_d
DENSITY OF STATES FOR 12 LAYER SLAB (states/eV atom)
ENERGY (eV)
XBL 758-6965

Fig. 72.

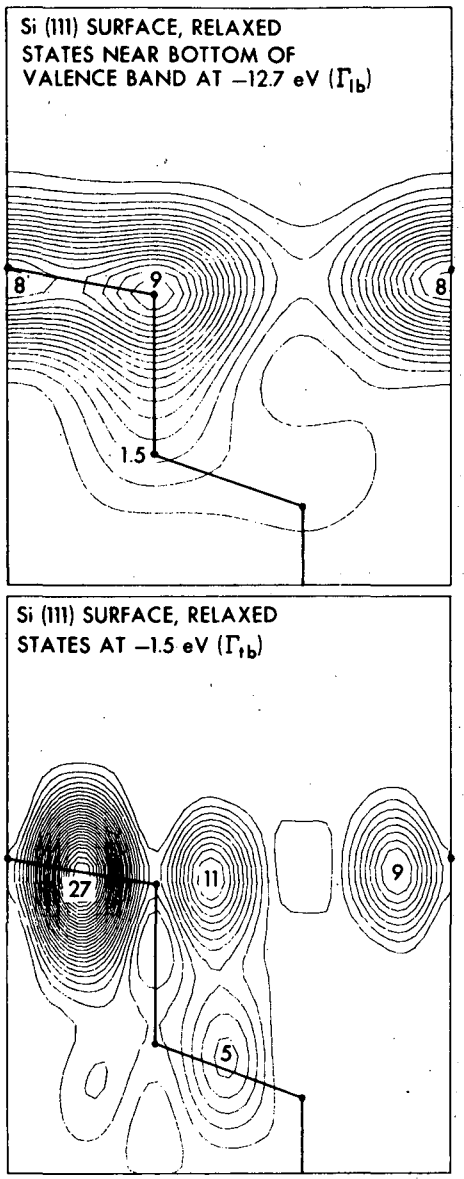

XBL 758-6964

Fig. 73.

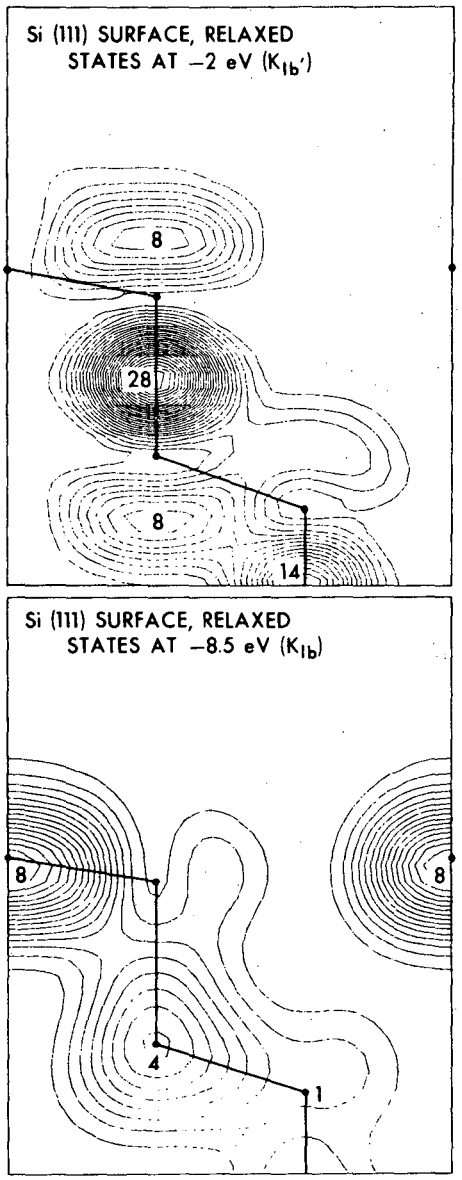

XBL 758-6970

Fig. 74.

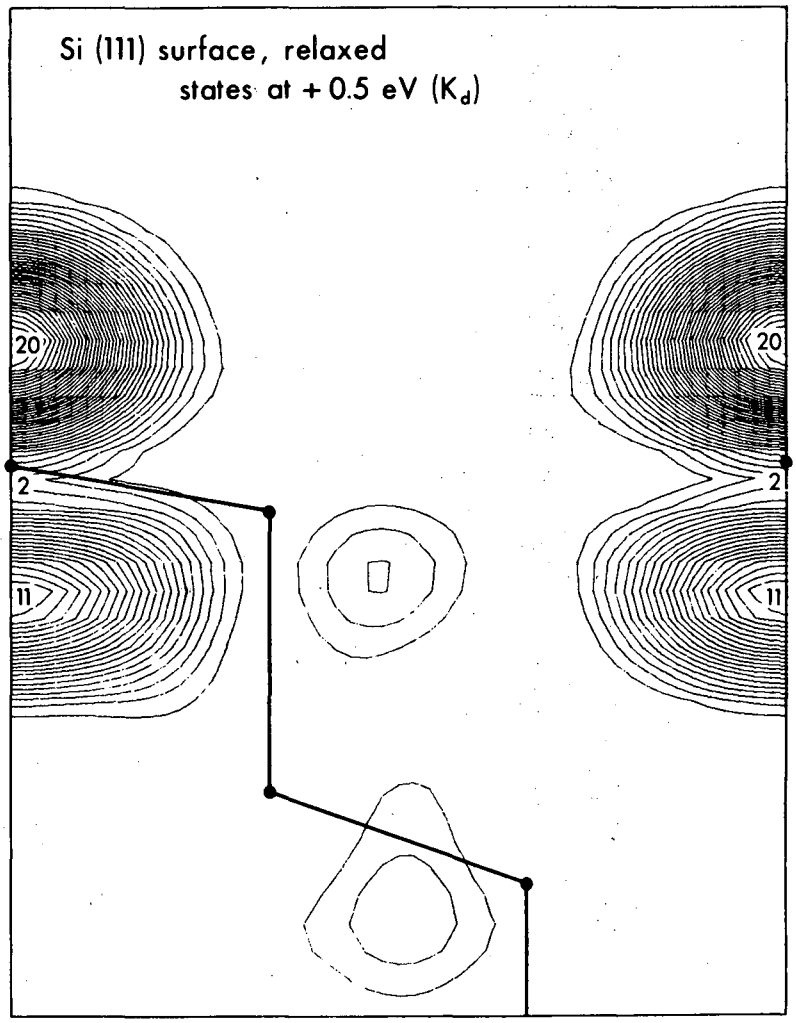

XBL 758-6968

Fig. 75.

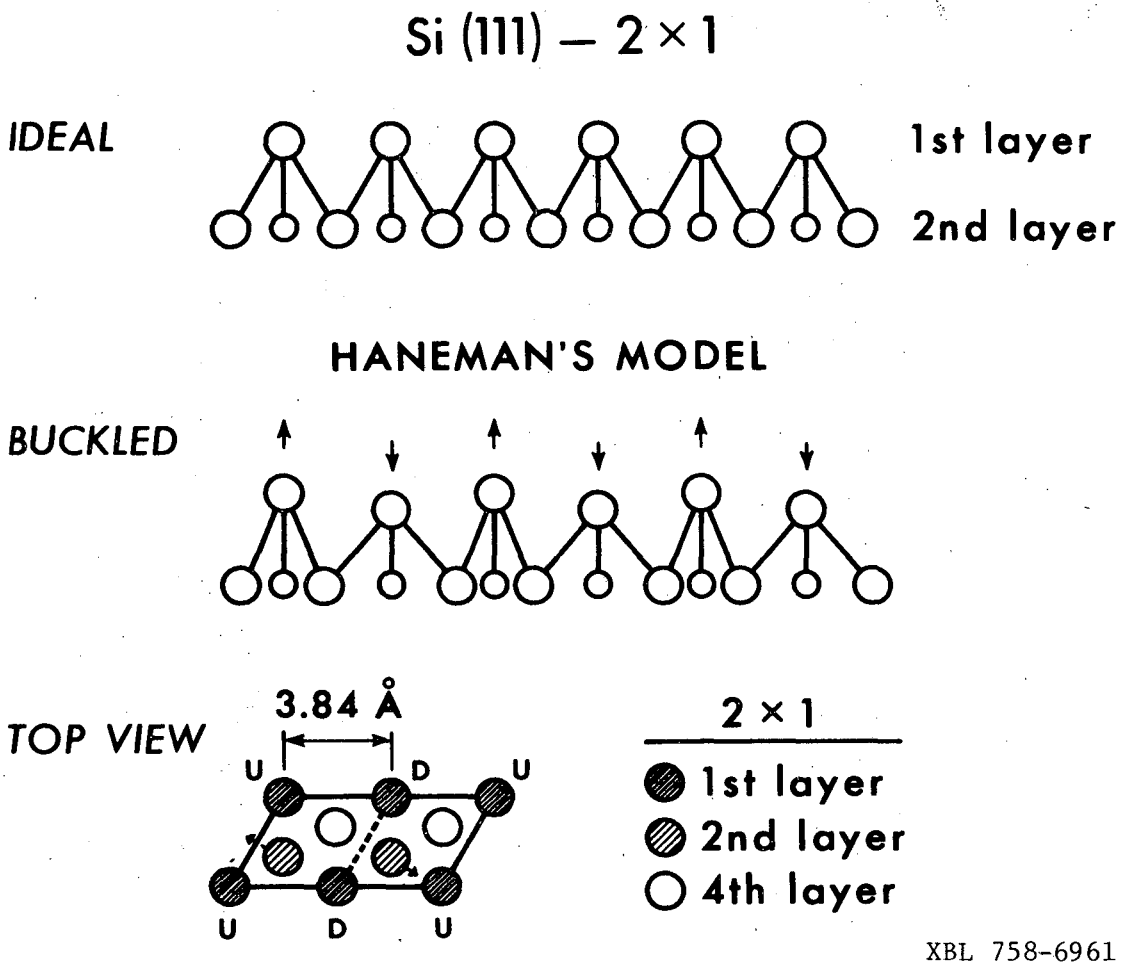
Si (111) — 2 × 1
IDEAL
1st layer
2nd layer
HANEMAN'S MODEL
BUCKLED
TOP VIEW
3.84 Å
U
D
U
U
D
U
2 × 1
1st layer
2nd layer
4th layer
XBL 758-6961

Fig. 76.

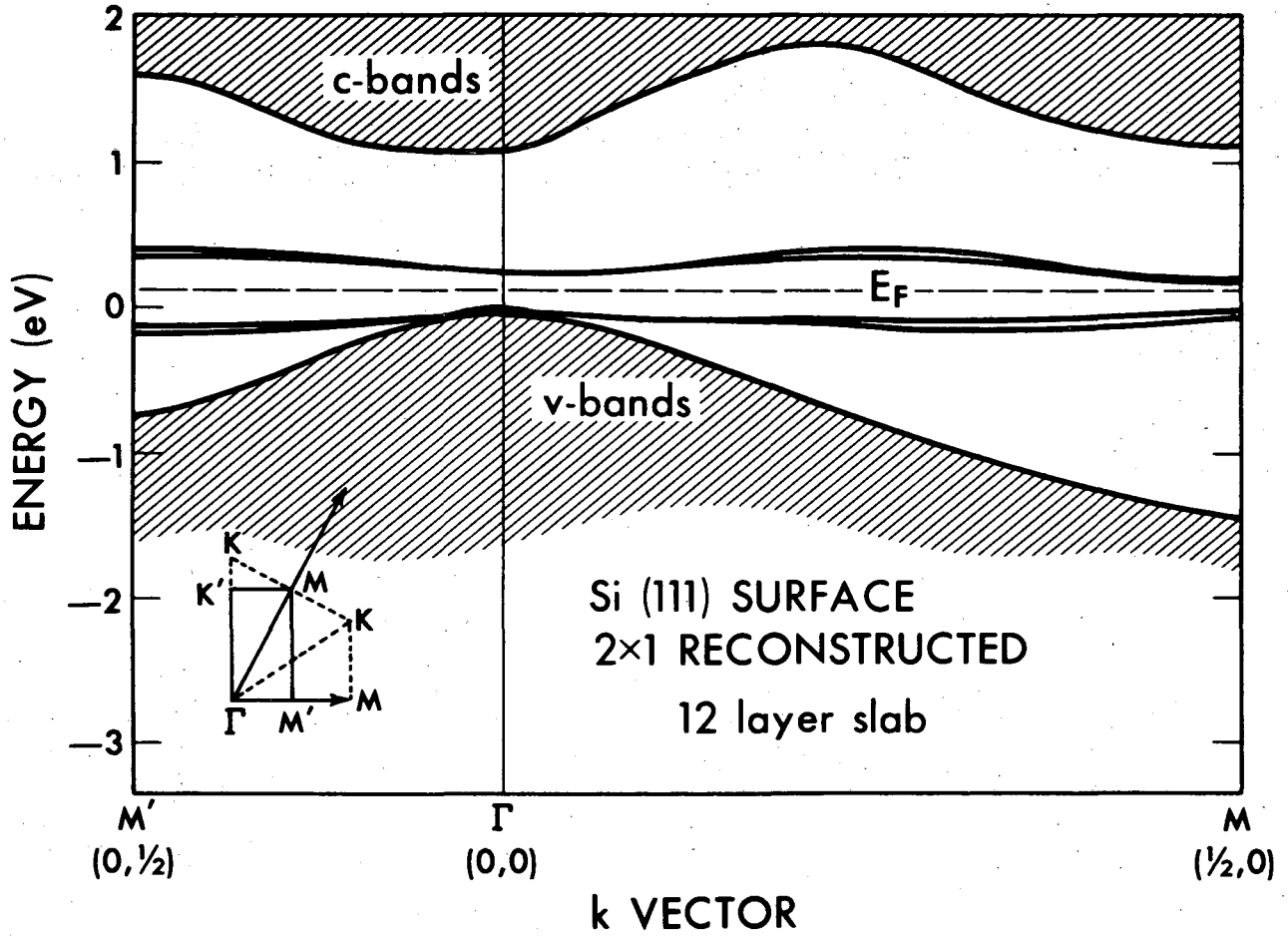

XBL 758-6960

Fig. 77.

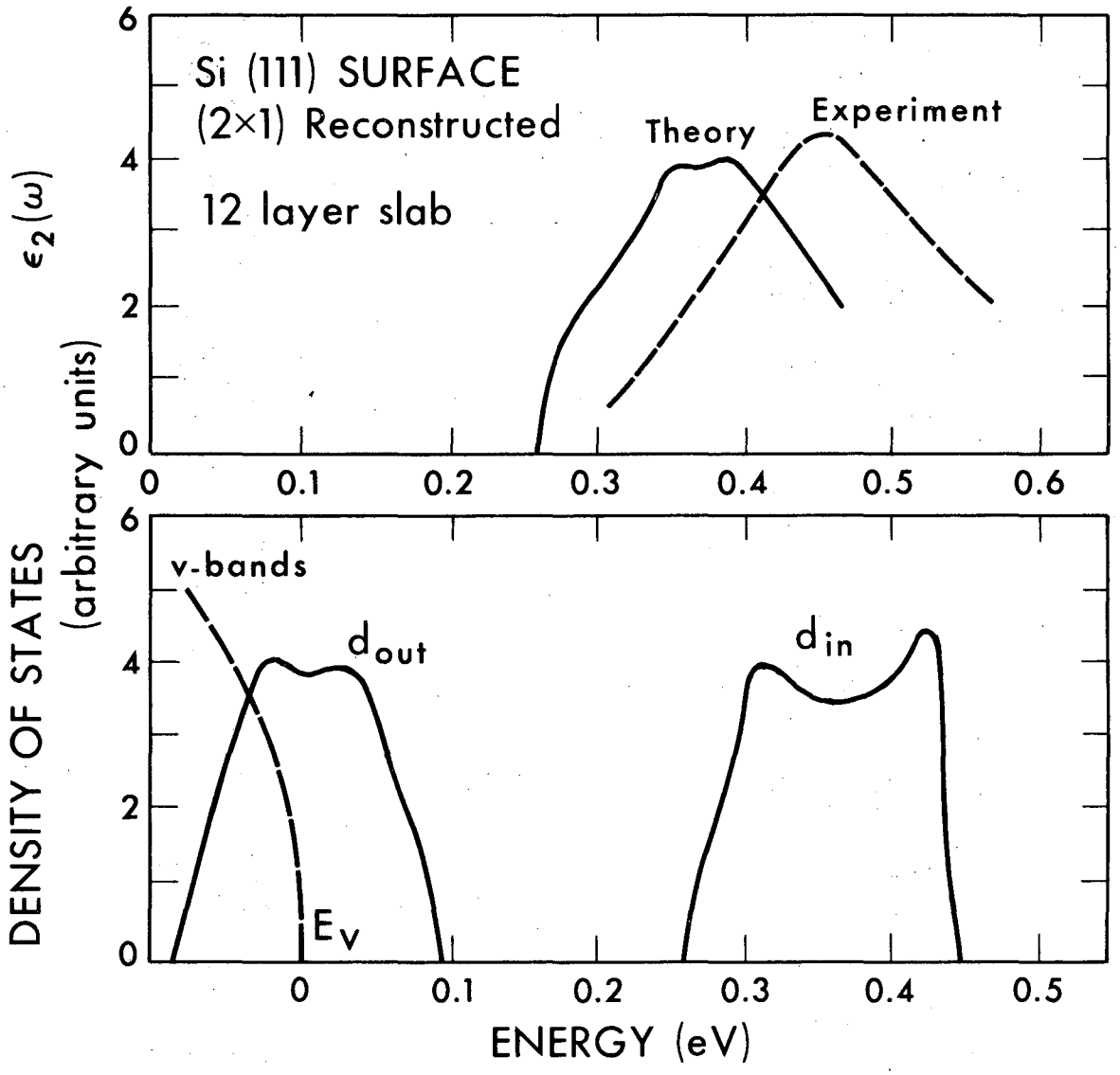

XBL 759-7234

Fig. 78.

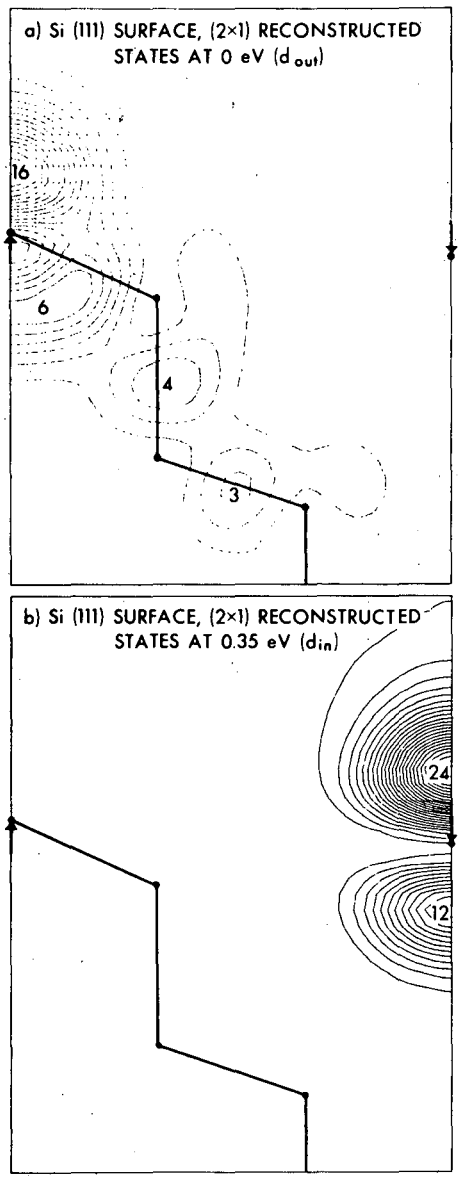

XBL 758-6973

Fig. 79.

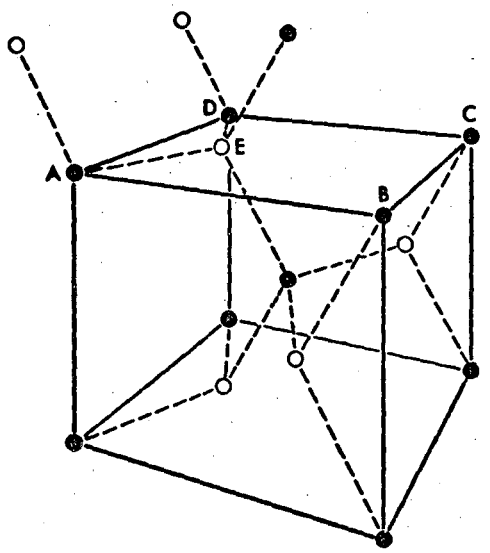

XBL 759-7127

Fig. 80.

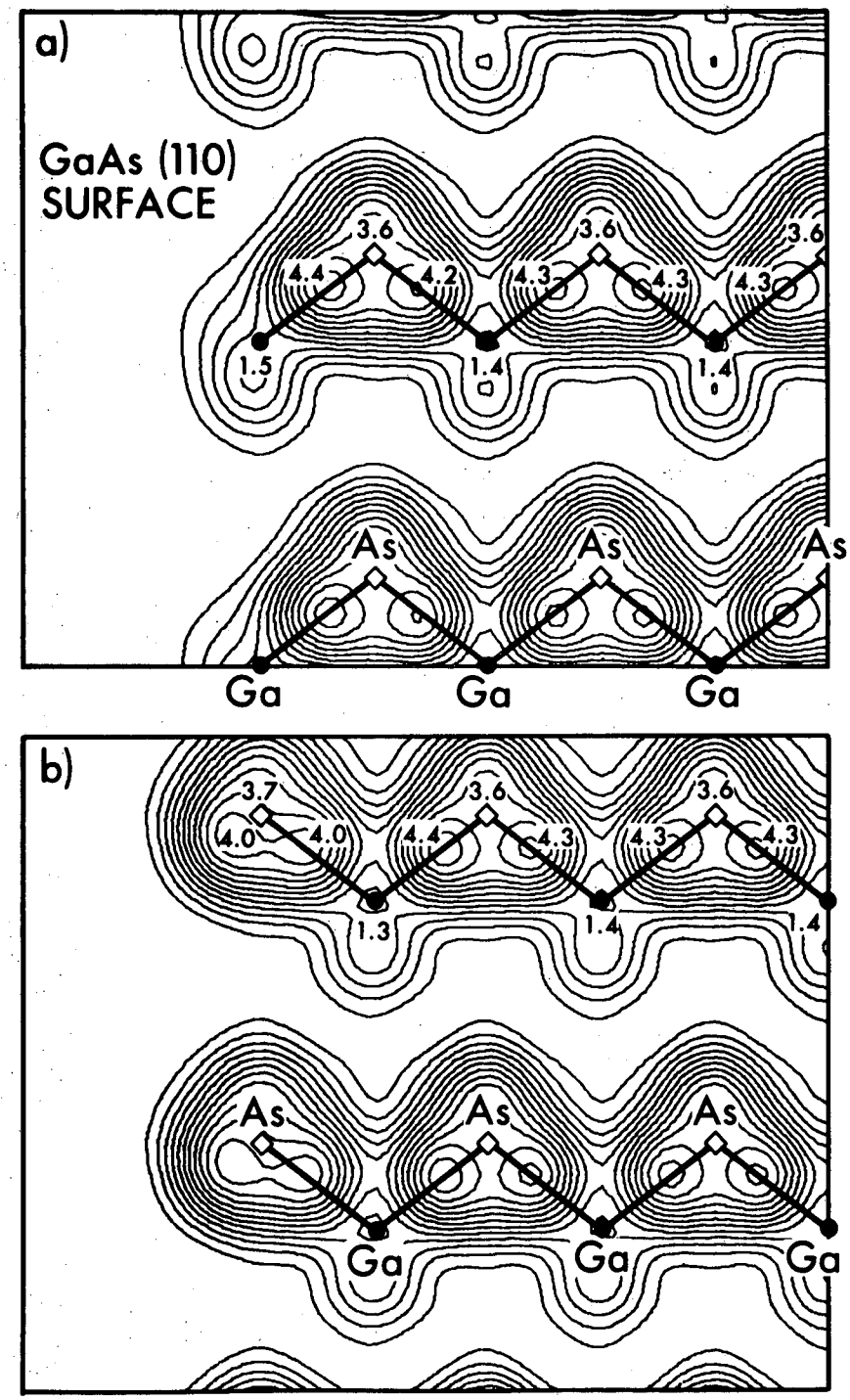

XBL 758-6956

Fig. 81.

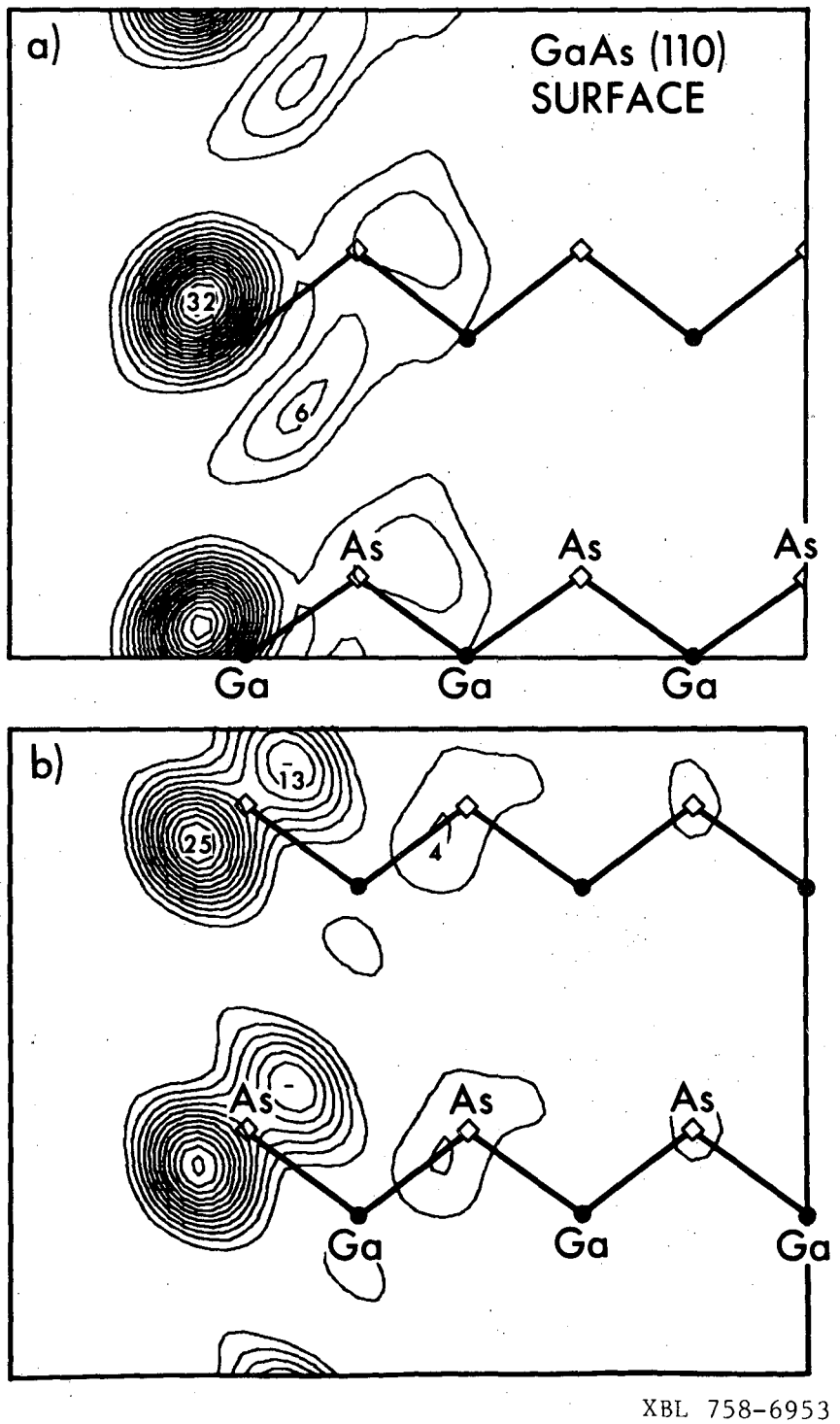

XBL 758-6953

Fig. 82.

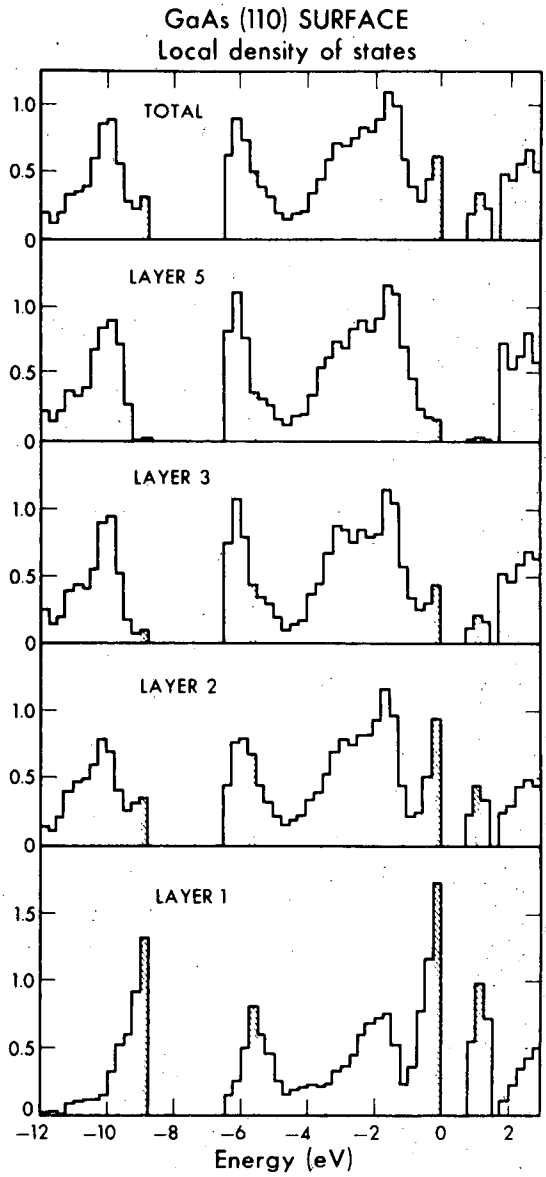

XBL 758-6967

Fig. 83.

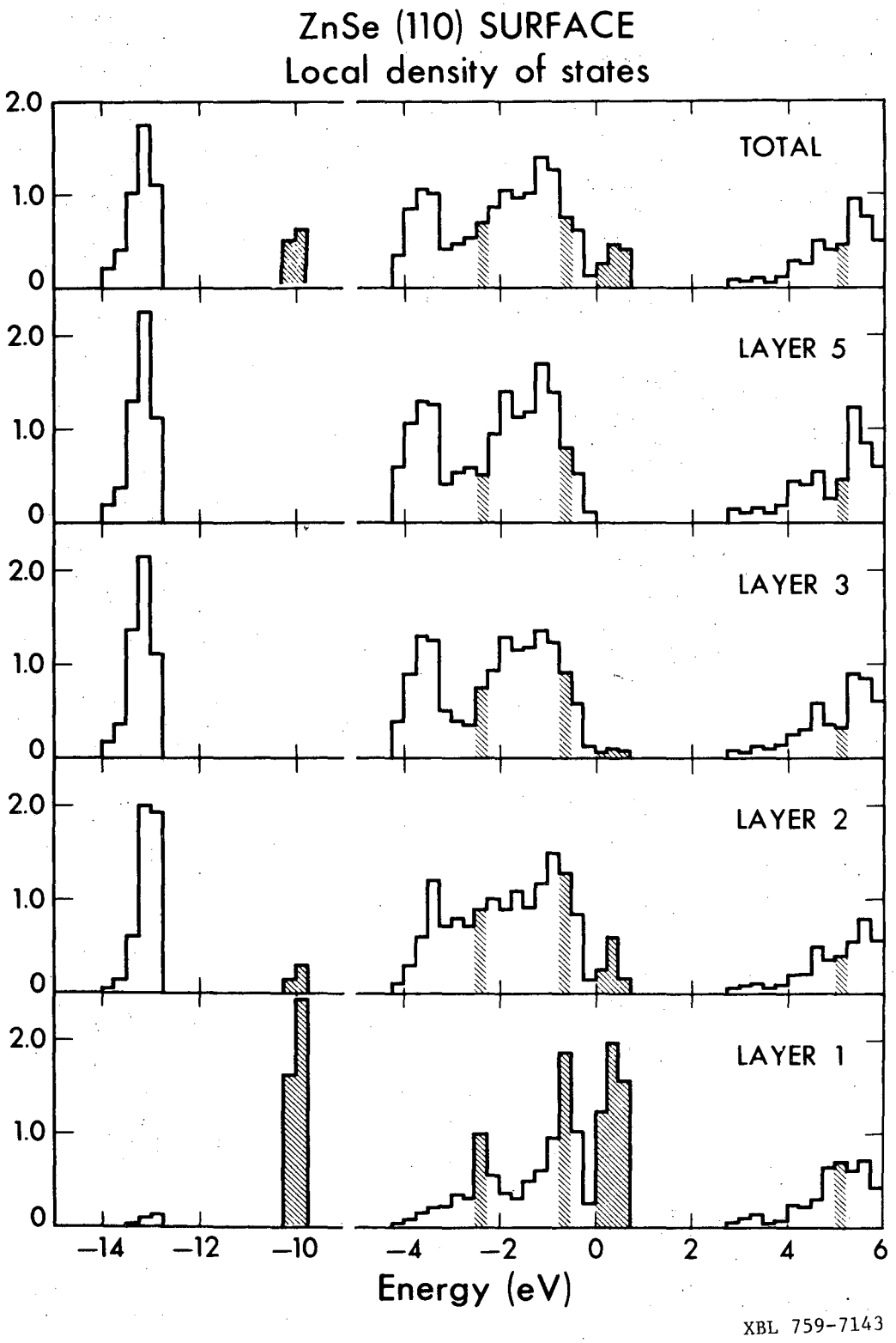
ZnSe (110) SURFACE
Local density of states
TOTAL
LAYER 5
LAYER 3
LAYER 2
LAYER 1
2.0
1.0
0
−14
−12
−10
−4
−2
0
2
4
6
Energy (eV)
XBL 759-7143

Fig. 85.

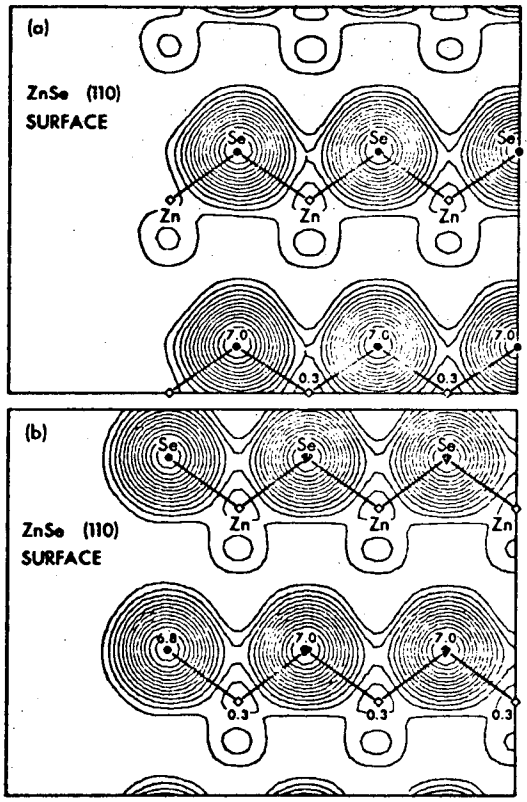

XBL 759-7139

Fig. 84.

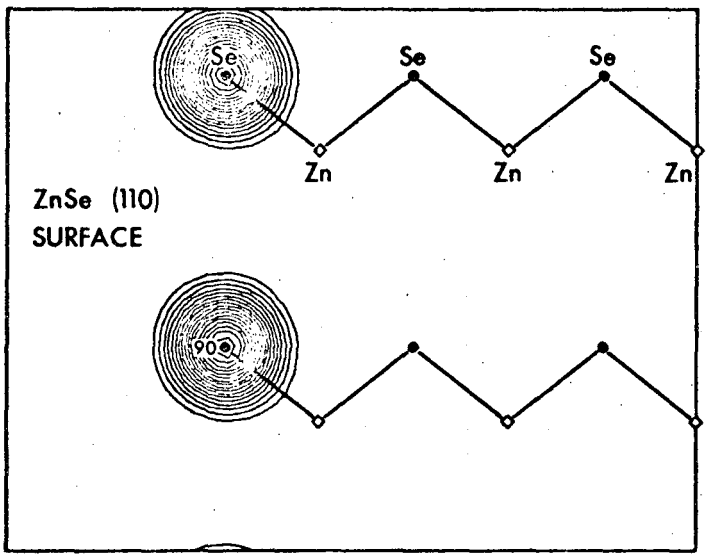

XBL 759-7128

Fig. 86.

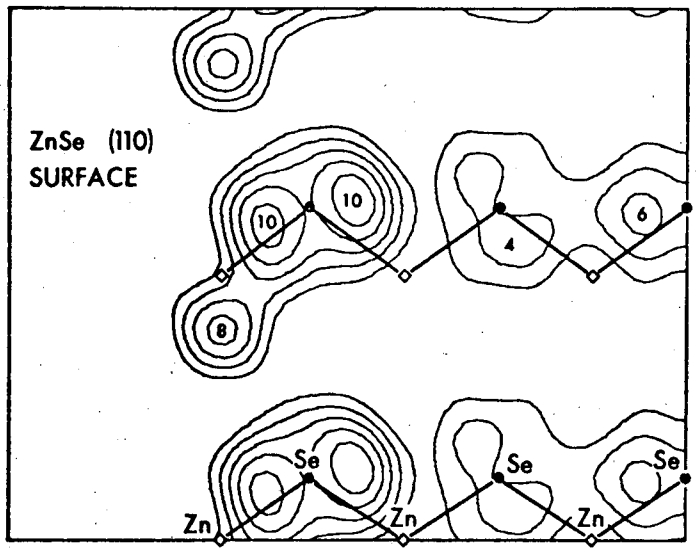

XBL 759-7129

Fig. 87.

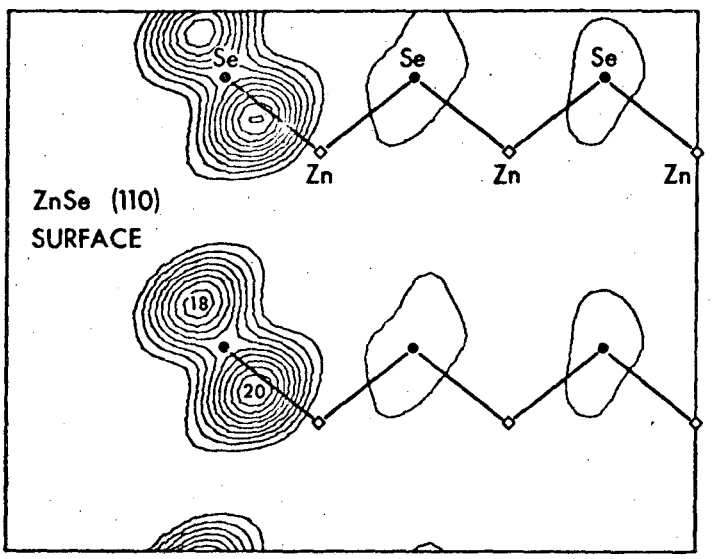

XBL 759-7133

Fig. 88.

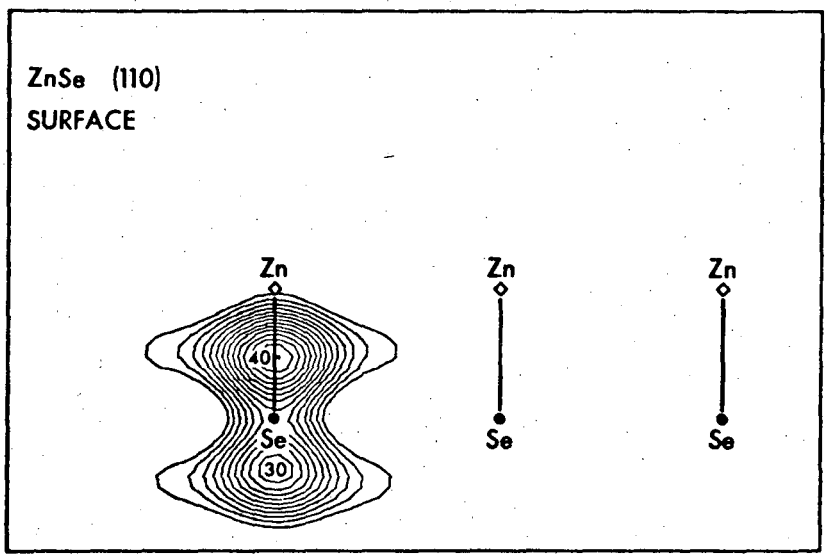

XBL 759-7130

Fig. 89.

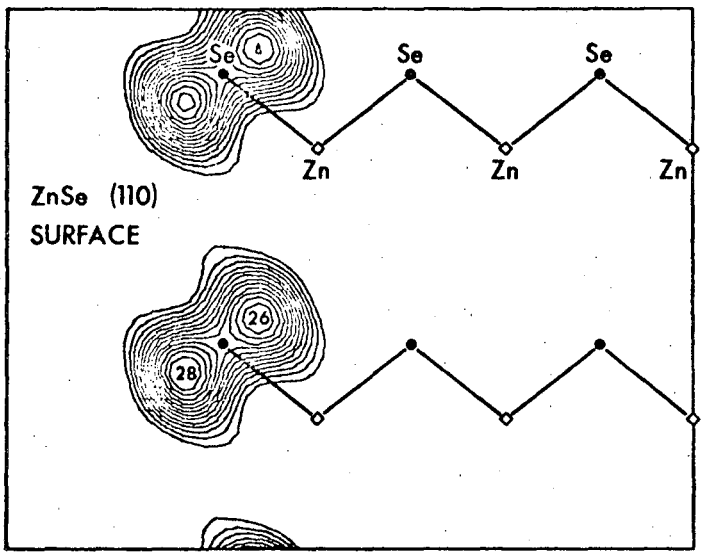

XBL 759-7132

Fig. 90.

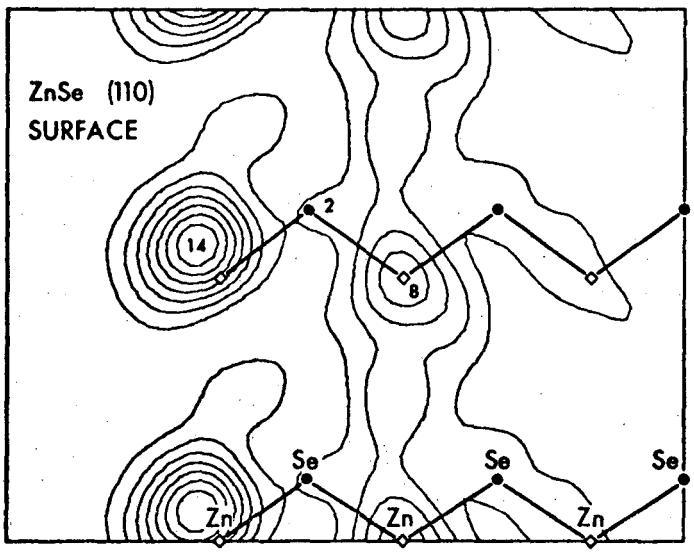

XBL 759-7137

Fig. 91.

TECHNICAL INFORMATION DIVISION
LAWRENCE BERKELEY LABORATORY
UNIVERSITY OF CALIFORNIA
BERKELEY, CALIFORNIA 94720